

A STUDY OF FLOW UNSTEADINESS DUE TO AN IMPINGING OBLIQUE SHOCK-
WAVE BOUNDARY LAYER INTERACTION

by

AMRUTHKIRAN HEGDE

SEMIH M. ÖLÇMEN, COMMITTEE CHAIR
JAMES PAUL HUBNER
MUHAMMAD ALI ROB SHARIF
THANG N. DAO
DENIS ASLANGIL

A DISSERTATION

Submitted in partial fulfillment of the requirements for the degree of Doctor of Philosophy in the
Department of Aerospace Engineering and Mechanics in the Graduate School of The University
of Alabama

TUSCALOOSA, ALABAMA

2022

COPYRIGHT Amruthkiran Hegde 2022
ALL RIGHTS RESERVED

ABSTRACT

This campaign was undertaken with a primary objective of understanding the characteristics of wall static pressure in a 3D oblique impinging shock-wave boundary layer interaction (IOSWBLI) generated by a wedge in a rectangular channel. This is important from the perspective of understanding the factors that lead to unstart and unsteady loading due to IOSWBLIs in engine inlets of aircraft which operate in high Mach number regime. In this regard, an IOSWBLI was generated in the UA Supersonic Wind Tunnel test section, at a free stream Mach number of 2.9, using an oblique shock-wave generated by a 12° isosceles wedge installed on the base of the test section. Oil flow visualization was conducted on the wall opposite the wedge (top-wall) and one of the side walls. Unsteady pressure measurements were acquired on the same top and side walls utilizing pressure transducers. The results revealed a decreasing value of peak pressure rise past the shock-wave on moving from tunnel centerline towards the sidewall which indicates the presence of a 3D IOSWBLI, and energy content concentrated mostly in the frequency range of 200-1000 Hz in the interaction region. Concurrently, a steady-state 3D and unsteady 2D IOSWBLI (at tunnel centerline) were simulated in the software ANSYS (FLUENT), with the same experimental boundary conditions and test section geometry. The results from the 3D and 2D simulations captured pressure rise trends and frequency content of the flow in the interaction region that aligned with the experimental results. Additionally, 3D simulation also predicted a vortical flow near the walls that is opposite in value, maintaining symmetry about the tunnel centerline and the plane of impinging shock-wave.

The secondary objective was to capture the pressure and strain effects an IOSWBLI impresses on a thin structure. This is a fluid structure interaction that can be detrimental to aircraft panels. In this experiment, a dual-layer luminescent coating was used to measure the pressure and strain on a thin, circular clamped plate subjected to an IOSWBLI in the same facility, using a 12° right angled wedge. The two-coating technique uses a fast-response pressure sensitive paint (PSP) applied over a photo-elastic Coating (PEC) adhered to the surface of the plate. The results using a low-speed micropolarizer camera with four polarization orientations show that the technique is sensitive to pressure and strain, measuring a pressure field topography that overlaps with the oil flow visualization conducted separately and a strain field where the maximum shear strain is along the clamped edge of the plate.

DEDICATION

This journey would not have been possible without the blessings of my parents, Gajanana and Anitha G. Hegde. I am thankful to them for teaching me to always chase my dreams. They have lived and breathed this endeavor with me. I also cannot imagine reaching this stage without the emotional support from my wife, Vindhya Hegde. Her faith and pride in me has been a great motivation. I will always be indebted to her. I thank my sister Shama Hegde and brother-in-law Adarsh Bellad, my father-in-law Dr. S.B. Hegde and mother-in-law Anuradha Hegde, my friends Mayank Vaish, M.K. Prajwal, and Vivek Nair, for their unwavering support.

I would like to thank the people who helped me reach the US in the first place. The Late Mr. Victor Monteiro, Mr. Ganapathi Bhat, Mr. Madhav Rao, and my uncle Arun Hegde and his family who provided me financial support, were the reason behind me receiving education in the US initially, my friend Ishan Mandhan who helped me put together strong applications to the US universities, the professors from my university and colleagues back home who provided me letters of recommendation. I would also I would like to thank my former graduate advisor Dr.Venkateswaran Narayanaswamy who introduced me to the area of research in high-speed aerodynamics.

Finally, I thank my school teacher Ms. Philomena Pushparaj who taught me to read and write in the first place. I am thankful for the unconditional love from Venkatramana Bhat and family and Chandrakala Gowda and family that has been my talisman over the course of my career.

LIST OF ABBREVIATIONS AND SYMBOLS

a	coating absorptivity
A, B	PSP calibration coefficients
f	frequency
f_s	sampling frequency
F, G	amplitude and phase of optical strain response
$G(f)$	pressure power spectra
h	coating thickness
I	emission intensity
I_{ref}	reference emission intensity
K	photoelastic coating sensitivity
L	length of separation; length of beam (clamp to free end)
M_∞	free stream Mach number
P	pressure

\bar{P}_∞ mean upstream wall static pressure (free-stream pressure)

P_{rms} root mean square value of wall static pressure

P_{abs} absolute pressure

P_{ref} reference pressure

N fringe order

S sensitivity of the pressure transducer

U flow velocity measured by pitot probe

U_∞ free stream velocity

V voltage

X pre-gain (KSC signal conditioner)

Y post-gain (KSC signal conditioner)

Z abs (double sided spectrum)²

w width of the test section

t time

α analyzer angle or flow reattachment angle

β oblique shock angle

γ	maximum in-plane shear strain
δ_o	incoming turbulent boundary layer thickness
δ	flap angle
ε_i	principal strains
θ	principal strain direction
λ	wavelength
λ^*	effective excitation-emission wavelength
λ_{em}	coating emission wavelength
λ_{ex}	excitation wavelength
ν	poisson ratio
σ	standard deviation
ϕ	polarization efficiency
CPT	critical point theory
DDES	delayed detached eddy simulation
DL	dual-layer
IOSWBLI	impinging oblique shock-wave boundary layer interaction

LES	large eddy simulation
LP	linear polarizer
LPF	long-pass filter
LPC	luminescent photoelastic coating
OSR	optical strain response
PSD	power spectral density
PEC	photoelastic coating
PSP	pressure sensitive paint
QWP	quarter-wave plate
RANS	reynolds-averaged navier stokes
SFSC	secondary flow separation concept
SWBLI	shock-wave boundary layer interaction

ACKNOWLEDGMENTS

I would like to take this opportunity to first and foremost thank my graduate advisor Dr. Semih Olcmen, who extended a helping hand in the most difficult phase of my life, by offering me enrollment into the Ph.D. program at UA. This milestone would not have been possible without his guidance. I would like to extend my gratitude to Dr. James Hubner, who introduced me to a novel area of research halfway through the program, patiently taught me its fundamentals, and encouraged me to explore and excel in it. I would like to thank my colleague Dr. Narendra Chaganti who shared his research experience during our meetings which gave me an idea of do's and don'ts to follow. I would also like to thank Mr. Kyle Chism, Mr. Garrett Sellers, and Mr. Zach MacIntyre who helped me with my project under Dr. Hubner. I am grateful to Dr. Muhammad Sharif, Dr. Thang Dao, and Dr. Denis Aslangil for agreeing to serve as my committee members. The project discussed in Section II was supported by NSF and AFOSR Grant CBET-180299: program managers Dr. Ronald Joslin and Dr. Sarah Popkin. I would like to thank ISSI in developing PSP application techniques to PEC samples

CONTENTS

ABSTRACT.....	ii
DEDICATION.....	iv
LIST OF ABBREVIATIONS AND SYMBOLS.....	v
ACKNOWLEDGMENTS.....	ix
LIST OF TABLES.....	xiv
LIST OF FIGURES.....	xv
INTRODUCTION	1
Motivation	1
Previous Studies on SWBLI.....	4
Characteristics and Structure of 2D IOSWBLI.....	9
Characteristics of 3D IOSWBLIs.....	12
Full-Field Measurement Techniques of High-Speed FSI.....	15
Objective.....	17
Structure of Dissertation.....	18
EXPERIMENTAL AND COMPUTATIONAL SET-UP	19
Wind Tunnel Facility.....	20
Air supply.....	20

Wind Tunnel Assembly.....	21
Experimental Techniques	25
Oil flow visualization.....	25
Static pressure measurements.....	25
Computational Model: Steady-state Simulation.....	30
Computational Model: Unsteady Simulation	30
RESULTS AND DISCUSSION.....	32
Experimental Results.....	32
Flow visualization.....	32
Pressure port locations	35
Uncertainty estimation	37
Pressure rise.....	40
Pressure fluctuations	42
Spectral analysis.....	44
Computational Results (Unsteady Simulation)	56
Pressure rise.....	57
Pressure fluctuations	58
Computational Results (Steady-State Simulation)	68
Co-ordinate system & axes normalization	68
Grid independence study.....	68

Floor flow visualization	70
Side-wall flow visualization.....	72
Discussion of 3D SWBLI interior flow field	74
CONCLUSIONS AND FUTURE WORK.....	109
REFERENCES	112
APPENDIX-I	119
Pressure and Strain Measurement on a Thin Clamped Plate in Supersonic Flow using a Dual Layer Luminescent Coating.....	119
Background and theory	119
Experiment.....	126
Experimental facility and set-up	126
Oil flow visualization technique	129
Results and Discussion	130
PSP calibration.....	130
Flow visualization	131
Pressure response: baseline flow	134
Pressure response: SWBLI.....	135
Measurement of strain using strain gage.....	137
Strain response	139
Interpretation of phase.....	142

PSP and PEC temperature sensitivity	142
Conclusions and Future Work.....	143
APPENDIX-II.....	145
Procedure to Setup 3D Steady-state Simulation of IOSWBLI in ANSYS (FLUENT).....	145
Geometry	145
Mesh Generation	145
Setup.....	146
Procedure to Setup 2D Unsteady Simulation of IOSWBLI in ANSYS (FLUENT).....	153
Geometry	153
Mesh Generation	153
Setup.....	154
APPENDIX-III	162
APPENDIX-IV	163
APPENDIX-V.....	194
APPENDIX-VI.....	199

LIST OF TABLES

Table 3.1. Port location comparison	36
Table 3.2. Mach number uncertainty	38
Table 3.3. Static pressure measurement uncertainty.....	39
Table A.1.1. Structural response of the clamped plate	128
Table A.1.2. Tests of the clamped plate.....	130
Table A.1.3. Pressure rise across the ports	134
Table A.1.4. Mean strain during steady run.....	139
Table A.2.1. Inflation layer parameters (steady)	146
Table A.2.2. Inflation layer parameters (unsteady)	154

LIST OF FIGURES

Figure 1.1. SWBLIs on high-speed aircrafts (Dolling (1993)).....	2
Figure 1.2. Canonical geometries to study SWBLI (Gaitonde (2015))	4
Figure 1.3. Structures of 2-D SWBLIs (a) Normal SWBLI (b) IOSWBLI (Delery et al. (2000) (c) Compression corner SWBLI (Verma et al. (2015)).....	7
Figure 1.4. Single-fin interaction (Kubota & Stollery (1982)).....	8
Figure 1.5. Double-fin interaction	9
Figure 1.6. Flow organization in 3D normal SWBLI (Bruce et al. (2011))	13
Figure 1.7. Flow organization in 3D IOSWBLI (Eagle and Driscoll (2014))	14
Figure 2.1. Free stream static pressure (left) and stagnation pressure (right) during the wind tunnel run	19
Figure 2.2. Free stream Mach number variation during wind tunnel run	19
Figure 2.3. (a) air dryer (b) storage tank and air compressor	20
Figure 2.4. UA small supersonic wind tunnel facility (top) and its schematic (bottom).....	21
Figure 2.5. Schematic of 3D IOSWBLI created by a triangular wedge	22
Figure 2.6. (a) schematic of test section set-up (b) actual set-up.....	23

Figure 2.7. (a) pressure transducer inserted into #6-32 screw (b) transducers installed on ports of top-wall (c) transducer installed on ports of side-wall	26
Figure 2.8. (a) pressure ports on top wall (b) schematic showing the distance between the spanwise locations	28
Figure 2.9. (a) pressure ports on side wall (b) schematic showing the dimensions of the port locations used for side-wall measurements.....	29
Figure 3.1. Top-wall oil flow visualization	32
Figure 3.2. Side-wall flow visualization.....	34
Figure 3.3. Top-wall flow pressure transducer locations (b) Side-wall pressure transducer locations.....	35
Figure 3.4. Stream-wise pressure rise (a) centerline (b) vortex (c) corner (d) side-wall.....	40
Figure 3.5. Prms comparison	42
Figure 3.6. LP6P Pulse mode low-pass filter response.....	44
Figure 3.7. Power spectral density-centerline.....	49
Figure 3.8. Power spectral density - vortex	51
Figure 3.9. Power spectral density-corner	54
Figure 3.10. Power spectral density- side-wall.....	55
Figure 3.11. Mach number contour (unsteady simulation).....	56
Figure 3.12. Pressure data points on the wall	57

Figure 3.13. Pressure rise - bottom wall	57
Figure 3.14. Data points Prms.....	59
Figure 3.15. Power spectral density (unsteady simulation)	62
Figure 3.16. Data points in the flow-field.....	64
Figure 3.17. Power spectral density of points in the flowfield (unsteady simulation)	67
Figure 3.18. Cartesian coordinate system	68
Figure 3.19. Boundary layer profile (a) normalized velocity (b) log-law	69
Figure 3.20. Floor flow visualization top-view (a) experimental (b) ANSYS (FLUENT)	71
Figure 3.21. Side-wall flow visualization (a) experimental (b) ANSYS (FLUENT).....	73
Figure 3.22. Evolution of boundary layer through SWBLI (floor mid-span).....	75
Figure 3.23. Stream-wise velocity contours superimposed with velocity streamlines (a) $z/\delta_o = 5.442$ (b) $z/\delta_o = 7.257$ (c) $z/\delta_o = 9.978$	78
Figure 3.24. X-component wall shear stress – span-wise locations	78
Figure 3.25. Wall static pressure measurements – steady state simulation	80
Figure 3.26. Evolution of Mach number and velocity streamlines in the stream-wise direction (a) collective isometric view (b) separate normal view	83
Figure 3.27. Total pressure variation-centerline	84
Figure 3.28. Evolution of total pressure in the stream-wise direction (a) collective isometric view (b) separate normal view.....	86

Figure 3.29. Reynolds stress in the span wise centerline plane (a) uu-RS (b) vv-RS (c) uv-RS.	88
Figure 3.30. Z-Component vorticity	89
Figure 3.31. Evolution of uu-RS at $y/\delta_o =$ (a) 0.10 (b) 0.15 (c)0.20 (d) 0.25 (e) 0.30 (f) 0.40 (g) 0.50 (h) 0.75.....	91
Figure 3.32. Evolution of vv-RS at $y/\delta_o =$ (a) 0.10 (b) 0.15 (c)0.20 (d) 0.25 (e) 0.30 (f) 0.40 (g) 0.50 (h) 0.75.....	92
Figure 3.33. Evolution of ww-RS at $y/\delta_o =$ (a) 0.10 (b) 0.15 (c)0.20 (d) 0.25 (e) 0.30 (f) 0.40 (g) 0.50 (h) 0.75	93
Figure 3.34. Evolution of uw-RS at $y/\delta_o =$ (a) 0.10 (b) 0.15 (c)0.20 (d) 0.25 (e) 0.30 (f) 0.40 (g) 0.50 (h) 0.75	94
Figure 3.35. Evolution of Y-Component vorticity at $y/\delta_o =$ (a) 0.10 (b) 0.15 (c)0.20 (d) 0.25 (e) 0.30 (f) 0.40 (g) 0.50 (h) 0.75	95
Figure 3.36. Evolution of uu – rs in the stream-wise direction (a) collective isometric view (b) separate normal view	98
Figure 3.37. Evolution of vv-Reynolds Stress in the stream-wise direction (a) collective isometric view (b) separate normal view.....	100
Figure 3.38. Evolution of ww-Reynolds Stress in the stream-wise direction (a) collective isometric view (b) separate normal view.....	102
Figure 3.39. Evolution of vw-Reynolds Stress in the stream-wise direction (a) collective isometric view (b) separate normal view.....	104
Figure 3.40. Evolution of X-vorticity in the stream-wise direction (a) collective isometric view (b) separate normal view	106
Figure 3.41. Vortices calculated by the Q-Criterion.....	108

Figure A.1.1. Schematic of the dual-LED/single-camera configuration; the red and blue LEDs are pulsed out-of-phase with each other	123
Figure A.1.2. Experimental set-up.....	127
Figure A.1.3. Schematic of the flow environment over the thin plate.....	127
Figure A.1.4. Variation of strains from center to edge of a clamped plate.....	128
Figure A.1.5.(a) intensity ratio contour for thick plate at $P/P_{ref} = 0.16 - 1.0$ (b) intensity ratio contour for thin plate at $P/P_{ref} = 0.15 - 1.0$ (c) Stern-Volmer plot-thick plate (d) Stern-Volmer plot-thin plate.....	131
Figure A.1.6. 5 mm thick plate (left) oil flow visualization (right) P/P_{ref} after 2 seconds of wind tunnel run with the wedge.....	133
Figure A.1.7. Time dependent pressure contours at $\Delta t = 71 \text{ ms}$ for baseline flow	134
Figure A.1.8. Location of pressure ports	134
Figure A.1.9. Time dependent pressure contours at $\Delta t = 71 \text{ ms}$ with the wedge- Thin plate (continuous blue light)	135
Figure A.1.10. Time dependent pressure contours at $\Delta t=14 \text{ ms}$ with the wedge (a) continuous blue light (b) alternating light.....	136
Figure A.1.11. Centerline pressure rise at steady state condition (2.25 s) (a) thick plate (b) thin plate.....	136
Figure A.1.12. Experimental set-up to acquire strain on PEC mounted thin plate.....	137
Figure A.1.13. Measured strain at $r/a=0.44$	138
Figure A.1.14. Time dependent strain (upper) and phase (lower) contours at $\Delta t=7 \text{ ms}$ intervals of the thick and thin clamped plate in the absence of the wedge (continuous red light)	140

Figure A.1.15. Time dependent strain (upper) and phase (lower) contours at $\Delta t=7$ ms intervals of the thick and thin clamped plate in the presence of the wedge (continuous red light).....	140
Figure A.1.16. Centerline strain at steady state condition (2.25 s) - thin plate.....	141
Figure A.1.17. Phase vectors superimposed on strain contours (left) and phase contours (right)– thin plate for start-up load without wedge	142
Figure A.2.1. CAD model (a) wind tunnel fluid domain (b) test-section.....	145
Figure A.2.2. ANSYS (Fluent) test-section fluid domain grid (a) side-view (b) front-view (c) inflation layer to resolve boundary layer and SWBLI	146
Figure A.2.3. Reynolds transport equation	147
Figure A.2.4. Reynolds stress model parameters.....	148
Figure A.2.5. Material properties.....	149
Figure A.2.6. Velocity inlet values	150
Figure A.2.7. Pressure outlet values	150
Figure A.2.8. Reference values.....	151
Figure A.2.9. (a) solution methods (b) solution controls.....	151
Figure A.2.10. Residual monitors.....	152
Figure A.2.11. Test-section.....	153
Figure A.2.12. ANSYS (Fluent) test-section fluid domain grid (a) side-view (b) front-view (c) inflation layer to resolve boundary layer and SWBLI	154

Figure A.2.13. (a) DDES model parameters (b) model constraints hidden in (a)	155
Figure A.2.14. Material properties.....	156
Figure A.2.15. Velocity inlet values	156
Figure A.2.16. TUI commands for periodicity	157
Figure A.2.17. Pressure outlet values	157
Figure A.2.18. Reference values.....	158
Figure A.2.19. (a) solution methods (b) solution controls.....	158
Figure A.2.20. Report definitions	159
Figure A.2.21. Residual monitors.....	159
Figure A.2.22. (a) report file definitions (b) report plot definitions	160
Figure A.2.23. Autosave of data files	160
Figure A.2.24. Run calculation parameters	161
Figure A.3.1. KSC-2 signal conditioner settings	162
Figure A.5.1. Switch to turn on the compressor	194
Figure A.5.2. Compressor panel	194
Figure A.5.3. Dryer humidifier panel	195
Figure A.5.4. Storage tank panel	196

Figure A.5.5. (From left to right) butterfly valve pneumatic line, filters and pressure gauge....	196
Figure A.5.6. Pressure regulator	197
Figure A.5.7. Storage tank valve	197
Figure A.5.8. (From left to right) control console and butterfly valve	198
Figure A.6.1. Picoscope and KSC-2 signal conditioner	199
Figure A.6.2. KSC-2 signal conditioner (top); KSC-2 software control panel (bottom).....	200
Figure A.6.3. Picoscope software panel.....	201

INTRODUCTION

Motivation

Since the advent of the age of aviation, there has always been a constant effort to push the boundaries of flight speed, as flying at high speeds provides several benefits. Particularly, in the area of defense, missiles and aircrafts, flying at high speeds provide a considerable advantage over the adversaries. Missiles gain higher penetration capability without the necessity of a separate ballistic head and can reach a target before being detected. Aircraft can conduct rapid surveillance.

Flight speed is often measured in Mach number (M), with $M=1$ being equal to the speed of sound. As an object approaches and travels beyond $M=0.3$, compressibility effects become important. Transonic ($0.8 < M < 1.2$), supersonic ($M > 1$), and hypersonic flight regimes ($M > 5$) respectively, are common designations. At these higher speeds, the shock waves form and interact with the aircraft.

Shock-wave boundary layer interaction (SWBLI) occurs when a shock-wave meets a boundary layer (Viswanath (1988), Dolling (2001)). Shock-waves and expansion fan are generated as the object traveling in transonic, supersonic, and hypersonic flight regimes obstruct and change the direction of fluid flow. Shock-waves also occur due to sudden changes in the back pressure, as observed in the combustor of scramjet engines. Simultaneously, as the fluid flows over the surfaces of an aircraft, a thin region develops over the surface where the viscous effects of the fluid are dominant. This region is known as the boundary layer. Hence, in high speed flight, as a shock-wave is generated from a surface or approaches a surface, it has the potential to interact and alter the characteristics of a boundary layer. This is the essence of SWBLI. Apart from aircraft, SWBLI

also commonly occurs in rocket nozzles and fin-body junctions of supersonic and hypersonic missiles.

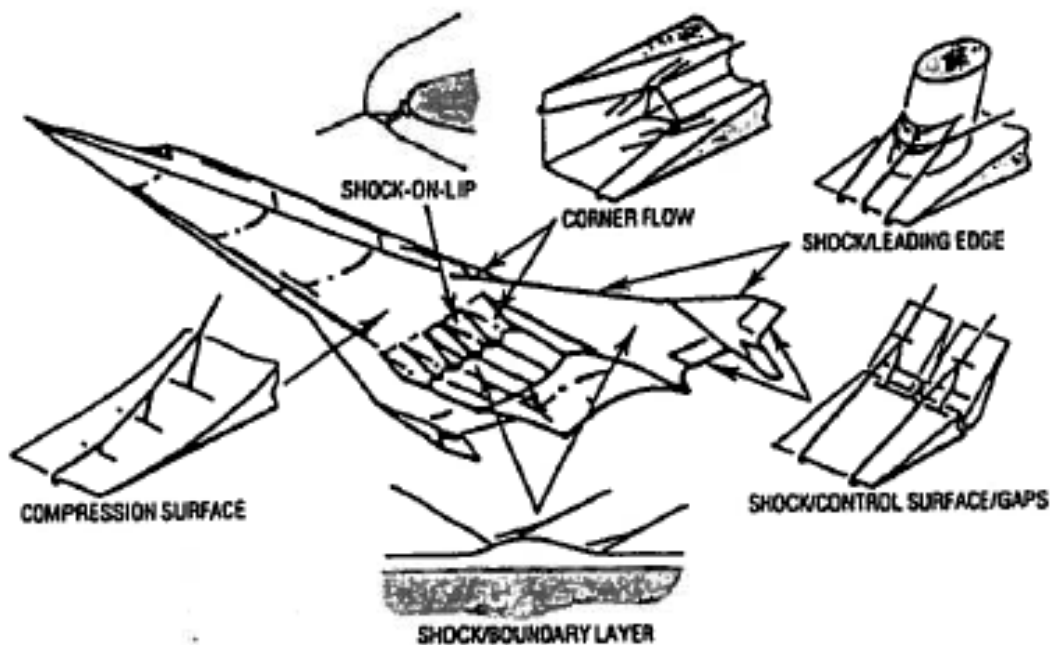


Figure 1.1. SWBLIs on high-speed aircrafts (Dolling (1993))

A shock-wave leads to a rise in temperature and pressure of the fluid. Additionally, by acting as an adverse pressure gradient, it also thickens the incoming boundary layer. If the shock-wave is strong enough, the low momentum layer of the fluid at the base of the boundary layer eventually lifts from the surface leading to flow separation, thus resulting in reversed flow or separation bubble near the wall surface. The structure is further discussed in the next section.

A relevant challenge posed by SWBLI occurs in the engines of ram and scramjet engines. As oblique shock-waves are deployed successively to decelerate the incoming flow of air in the engine inlet diffuser for efficient combustion with the fuel, they interact with the boundary layers that grow on the walls and corners of the inlet. In addition to leading to a rise in pressure and temperature of the fluid, the shock-waves may result in the separation of the boundary layers, thus

disrupting the flow uniformity and choking the entrance of the inlet. If this couples with the additional pressure rise in the combustor due to heat release, the blockage/pressure increase caused by the downstream components creates a sufficient back pressure which may cause large recirculating regions adjacent to the walls that can propagate upstream to the inlet. This leads to the upstream travel of the shock system and formation of a shock-wave outside the inlet, which is known as ‘unstart’. This is especially true for scramjets at flight Mach numbers less than 7 (Riggins et al. (2006)). This eventually results in drastically reduced mass flow through the engine, loss of thrust, and high transient pressure loading (Curran et al. (1996)).

To lower the weight of a high-speed aircraft, its body is made of thin panels supported by an interior structure. During high speed flight, the control surfaces are subjected to a harsh environment that results in severe thermal and mechanical loading. The control surfaces, as a result of the fluid shear forces and complex field of adverse pressure gradients, may deform non-uniformly. Additionally, owing to their orientation and geometry, the control surfaces naturally generate shock and expansion waves that result in SWBLIs to form either partially or completely over them. These can further accelerate the fatigue loading of the panels, due to the unsteady motions of the separation shock foot that can couple with the structural resonant frequencies of the panels.

All of the above events establish the fact that SWBLIs can have a detrimental effect on the aircraft due to localized heating and severe levels of pressure and strain which can even result in compromising structural integrity of the vehicle. Hence, it is imperative that there is a comprehensive understanding of SWBLIs and FSI induced by SWBLI for the development of flow control techniques accordingly.

Previous Studies on SWBLI

SWBLI has been studied for over eighty years since its initial observation which can be traced back to Ferri (1939) who observed it during the tests on an airfoil. His study was focused on flow over curve bodies. During his experiments, Ferri found that the flow over an airfoil accelerated from near sonic velocities to supersonic speeds and terminated in the form of quasi-normal shock. Since then, focus has been on studying SWBLIs in canonical geometries (shaded regions in Fig. 1.2). Comprehensive reviews that present the progress made in the understanding of SWBLIs include Green (1970), Adamson Jr. and Messiter (1980), Delery and Marvin (1986), Dolling (1993), Smitts and Dussauge (1996), Zheltovodov (1996, 2006), Andreopoulos et al. (2000), Dolling (2001), Knight et al. (2003), Edwards (2008), Clemens et al. (2013), and Gaitonde (2015).

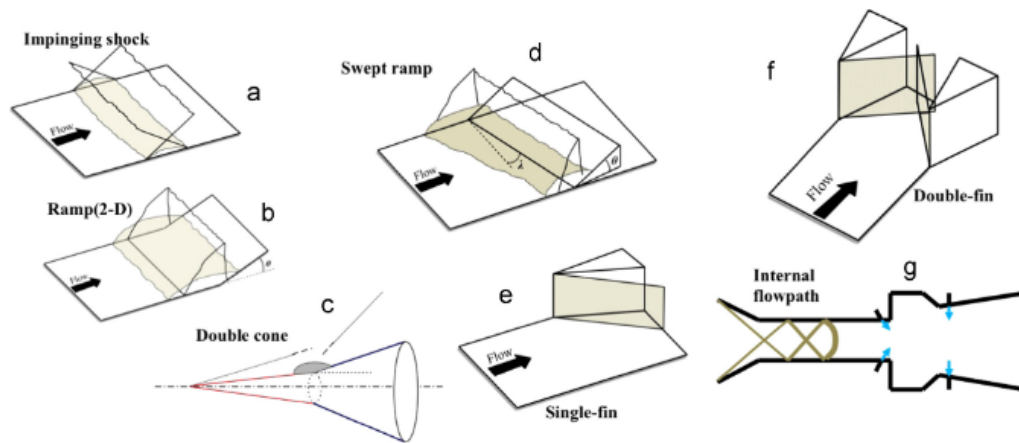


Figure 1.2. Canonical geometries to study SWBLI (Gaitonde (2015))

Dolling (2001), Delery (1985), and Delery et al. (1994) discuss how the flow structure inside an inlet or on a transonic airfoil can be significantly affected by the interaction between the boundary layer and the inviscid outer layer. Settles et al. (1994) presents SWBLI data and results with an importance given to factors such as base-line applicability, simplicity, specific applicability,

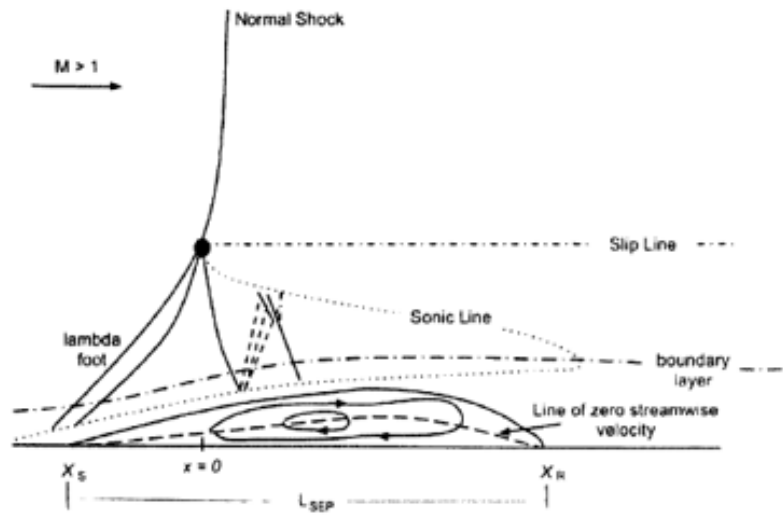
consistency, and adequate data with respect to turbulence, test conditions, and flow conditions suitable to be used in computational studies of the shock wave boundary layer analysis.

Based on their behavior, SWBLI are categorized into one of the five types: impinging oblique shock, compression corner, normal shock, single fin, and double fin. The first three are grouped into 2D interactions while the remaining two are studied as 3D interactions. A boundary layer ‘free interaction’ first described by Chapman et al. (1957) explains the principal mechanism occurring in a two-dimensional SWBLI. The length scale of the interaction L_o and the overall pressure rise imposed by the shock strength due to incoming Mach number M_o , normal to the wave in the boundary layer, determine the threshold pressure gradient that affects the interaction. Despite no one predictive theory to explain the interactions, Lapsa (2009) notes that:

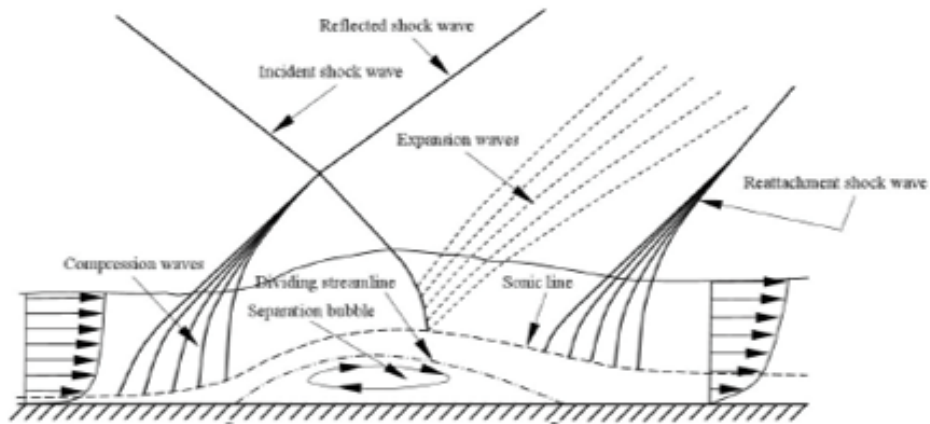
- Separation length increases with increased wedge angle for a fixed Mach number.
- Separation length decreases with increasing Mach number for a fixed wedge angle.
- The incompressible shape factor H is an appropriate characterization of the incoming boundary layer for scaling of the upstream interaction length L_o .

The essence of normal (Fig 1.3(a)), impinging (Fig 1.3(b)), and compression corner (Fig. 1.3(c)) SWBLI is as follows. The part of the boundary layer near the surface of any high Mach number flow is always subsonic. This part of the flow is unable to support the abrupt pressure rise due to a shock-wave. This is the reason why the shock-wave terminates at the sonic line even in a high Mach number flow. Viswanath (1988) explained the mechanism of interaction without separation. In a supersonic flow, the shock-wave imparts pressure disturbances that travel both upstream and downstream of the flow. In reaction, the subsonic stream tubes thicken and generate compression waves that travel in the supersonic part of the boundary layer. These waves result in additional pressure rise and readjust the subsonic part of the boundary layer. This cycle continues

until there is a compatibility between the gradual pressure rise in the subsonic region of the boundary layer with the abrupt pressure rise in the outer inviscid flow.



(a)



(b)

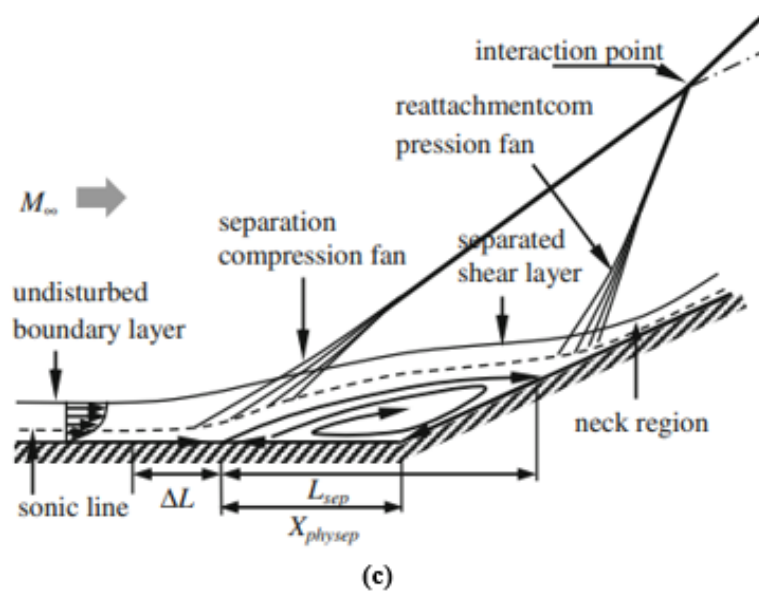


Figure 1.3. Structures of 2-D SWBLIs (a) Normal SWBLI (b) IOSWBLI (Delery et al. (2000) (c) Compression corner SWBLI (Verma et al. (2015))

If the pressure rise is below a certain threshold value, then the boundary layer can resist the adverse pressure gradient without separation. In the case of an impinging shock-wave, when the interaction does not result in separation, a secondary set of waves are formed due to the refraction of the incident shock wave. In the case of a compression corner, the secondary waves are formed partly due to the streamline curvature of the stream tubes and partly due to the compression waves which generate waves that are reflected at the sonic line of the boundary layer.

As the strength of the adverse pressure gradient imposed on the turbulent boundary layer increases, it results in the increase of pressure across the shock wave. This affects the low momentum flow near the wall which lifts from the surface leading to boundary layer separation. The separating boundary layer reattaches downstream once the pressure gradients are relaxed and forms a separation bubble.

Fin-plate and double-fin SWBLIs are inherently 3D. The former has been well characterized by several authors (Korkegi (1973), Kubota and Stollery (1982), Lu (1983), Lu and Settles (1990, 1991), Alvi and Settles (1992), Schmisser and Dolling (1992)). In a 3D single fin configuration, (Fig. 1.4), a semi-infinite fin is attached at a 90-degree angle to a flat plate. The main characteristic of the fin-plate interaction is the growth of a vortex structure under the shock foot producing a quasi-conical interaction structure. The secondary cross flow in this type of SWBLI skews the approach boundary layer in a manner that characteristically distinguishes it from 2D flow.

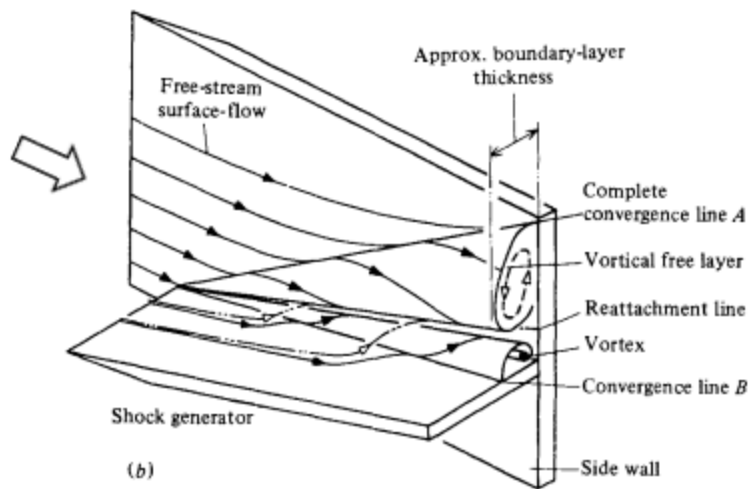


Figure 1.4. Single-fin interaction (Kubota & Stollery (1982))

The double-fin interaction is the most complex of the five types of SWBLIs. In the double fin model, two semi-infinite fins are in close proximity and attached to a flat plate (Fig. 1.5). However, this geometry is the most realistic type as it would be expected to be found in scramjet engine inlets. While Knight et al. (1986), Ketchum et al. (1989), Narayanswami et al. (1991), Hingst and Williams (1991), Knight et al. (1995, 1986), Zheltovodov et al. (2001) and Derunov et

al. (2008) are some of the notable experimental works in this area, Gaitonde et al. (1994, 1995, 1996, and 1999) developed numerical techniques to reproduce the three-dimensionality in these interactions. For strong (or fully-separated) interactions the principal elements of this type of interaction are described in terms of four flow regimes: the separated boundary layer, vortex interaction, centerline vortices, and entrainment. Each regime has a distinct footprint, and the lines of coalescence and divergence mark the boundaries between the various regimes.

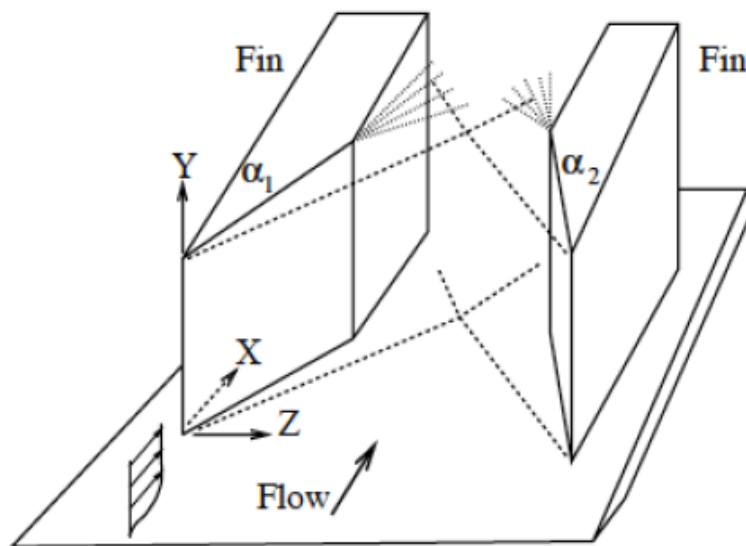


Figure 1.5. Double-fin interaction

Characteristics and Structure of 2D IOSWBLI

IOSWBLIs have been the subject of numerous experimental and computational studies. Measurements were performed by Dupont et al. (2005), Dussauge et al. (2006), Dussauge and Piponniau (2008) at $M_\infty = 2.3$, using 7 to 9.5° shock generator angles, Oskam et al. (1976) at $M_\infty = 3$ using 10° shock generator angle, Humble et al. (2009) at $M_\infty = 2.1$, using 8° shock generator angle. Direct numerical simulation codes have been used by Pirozzoli and Grasso (2006) to study

the unsteadiness of the IOSWBLI in a flow at $M_\infty = 2.25$, where the impinging oblique shock wave angle was 33.2° .

A recent review conducted by Clemens and Narayanaswamy (2014) and Gaitonde (2015) summarizes the research completed in the area of shock induced separation with unsteady motions, which are characterized by a range of frequencies. A summary of the combined results indicate that the reflected shock wave and the compression waves oscillate at low frequencies and move with a low average speed of a few meters per second, the separation bubble successively contracts and dilates. The shockwave acts as a low pass filter separating the shock fluctuation frequency from the characteristic high frequencies present in the incoming boundary layer (>10000 Hz). The separation bubble and eddies in the separated region are considered as the origin of the unsteadiness. The mass balance within the separation bubble affected by the eddies forming within the shear layer between the subsonic reversed flow and the high speed flow over the separation bubble results in the separation bubble changing its size in time, causing an unsteady flapping of the separation shock. The dominant frequencies result in the Strouhal numbers in the range of $S_t = 0.03 - 0.05$. The Strouhal number is defined as dimensionless shock frequency,

$$S_t = (f_s)(L)/U_\infty \quad 1.1$$

where f_s is the characteristic shock frequency, L is the length of separation defined as the distance on the wall between the intersection of the extrapolated incident and the reflected shocks with the wall and U_∞ the free stream velocity. These results agree with the values obtained in experiments conducted by Erenkil and Dolling (1991), Dolling and Brusniak (1989) and Wu and Martin (2008) under different configurations. A direct numerical simulation study by Pirozzoli and Grasso (2006) indicated the causes of low-frequency unsteadiness are due to (a) vortex-shedding near the separation point together with downstream propagation of the vortical structures in the mixing

layer over the separation bubble (b) generation of feedback pressure waves due to shock interaction at the foot of incident shock, and (c) upstream propagation of acoustic frequencies of cavity tones. It was also observed that when a shock wave interacts with a boundary layer without inducing separation, the shock motion was dominated by the structure of inflow turbulence.

Delery and Dussauge (2009) discussed the mechanism of flow separation in a 2D IOSWBLLI. As the oblique shock-wave impinges the boundary layer that forms on the opposite wall, it acts as an adverse pressure gradient on the subsonic portion of the flow near the wall. This affects the low momentum flow near the wall which lifts from the wall, forming a reversed flow region. The reversed flow region acts as an obstacle to the incoming flow, which gets deflected and flows over the separation bubble, leading to the formation of a separation shock. The incident shock and the separation shock interact at a distance away from the wall above the approaching boundary layer. The incident shock penetrates into the viscous rotational flow region over the separation bubble leading to a further downstream pressure rise. However, the static pressure and the direction of flow in the region between the penetrating shock (also called as transmitted shock) and the reflected shock needs to be the same considering the inviscid flow theory. Hence, downstream of the transmitted shock, expansion waves are formed that reduce the pressure and turn the flow towards the wall, thus closing the separation bubble and equalizes the pressure within the separation bubble and the region over the aft section of the bubble. After the flow reattaches, it turns to follow the wall contour which generates compression waves that coalesce to form the reattachment shock.

Characteristics and Structure of 3D IOSWBLLs

In rectangular/square channels, in addition to the 2D boundary layers that grow along the walls, boundary layers also develop along the junction where two walls form a right angled corner. These boundary layers are formed due to the overlapping of the individual 2D boundary layers and exhibit a 3D behavior. For a long time IOSWBLLs, compression corner and normal SWBLLs were explained assuming 2D behavior. However, with the exploration of the role of the corner boundary layer in SWBLL, there is sufficient evidence that these too are 3D depending on the width of the channel.

Study on 3D aspect of SWBLLs in the past has been conducted in channels with low aspect ratios of 1:1.5 (normal SWBLL) and 1:1.25(IOSWBLL). Experiments conducted by Chris et al. (1989) and Titchener & Babinsky (2011) have shown that flows along centerline are affected by flows along corners. Burton & Babinsky (2012), Bruce et al. (2011) and Burton et al. (2010), studied corner flows in a normal SWBLL setting. The objective of their experiments was to determine the role of the corner separation in driving the centerline separation. In this regard, corner flows were manipulated by corner suction and vortex generators. Their experiments were restricted to surface measurement techniques such as flow visualization and pressure measurements. The major conclusions from their experiments were that there was a reduction in the span-wise corner separation marked by a centerline separation due to corner suction, while

increased corner separation without any centerline flow separation was seen when corner vanes acting as vortex generators were positioned upstream of the flow.

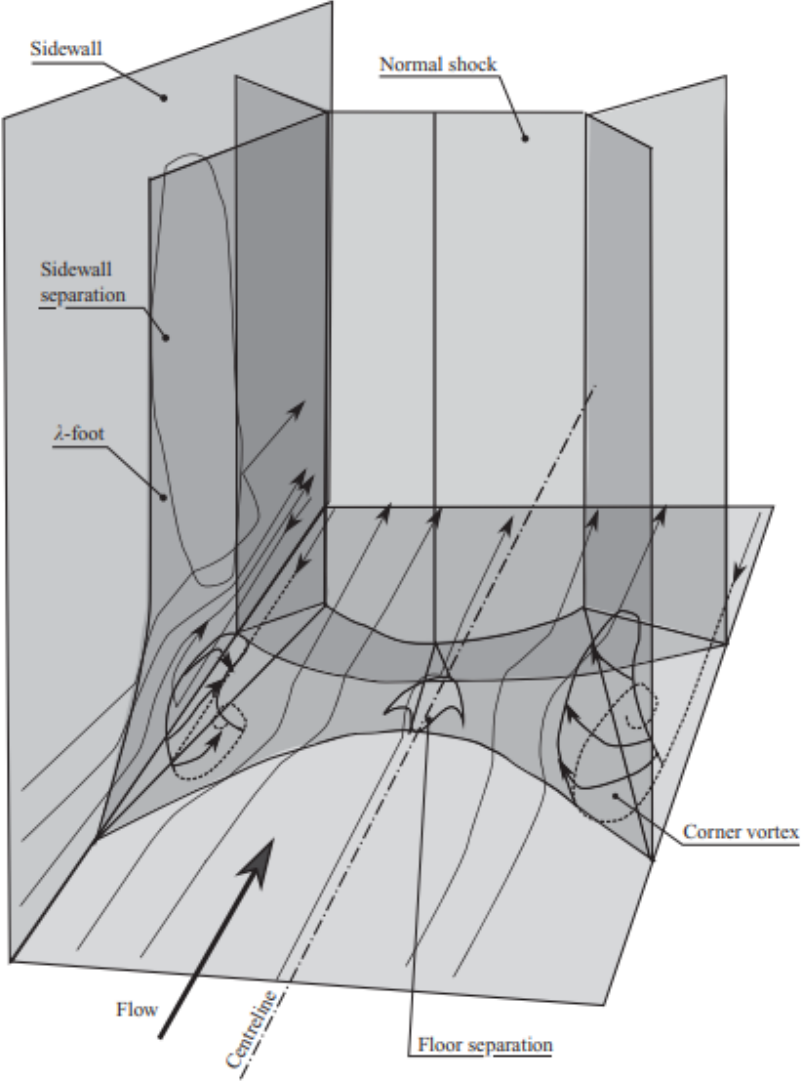


Figure 1.6. Flow organization in 3D normal SWBLI (Bruce et al. (2011))

Eagle et al. (2011), Eagle (2012), Eagle and Driscoll (2014), Morajkar et al. (2015, 2016), and Morajkar and Gamba (2016) described corner separation in an IOSWBLI based on oil flow visualization and PIV measurements. They concluded that the 3D IOSWBLI is composed of three unit physics problems: (a) oblique-incident SWBLI on the bottom wall, (b) swept/fin type SWBLI on the sidewalls, and (c) corner flows on the corners of sidewall and bottom wall. They utilized critical point theory (CPT) and proposed a new concept named secondary flow separation concept (SFSC) to explain the behavior of corner separation. According to them, there are two types of separations, namely, primary and secondary. The assumption of SFSC is that the flow first separates due to disturbances to the ‘primary flow’. Then, downstream of these primary separations, topological features and the vorticity associated with them interact to form new global separations. Hence, in an IOSWBLI, the wedge and the corner are the primary source of separations. Horse-shoe vortices that are formed due to centerline separation and a vortex that

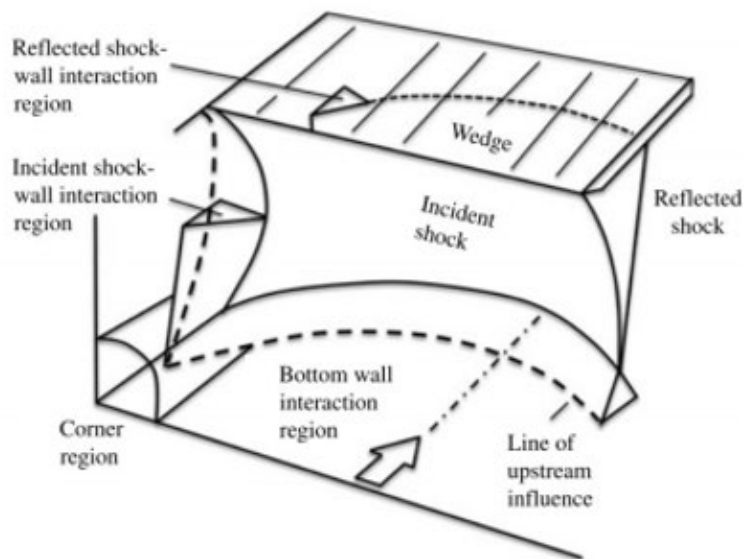


Figure 1.7. Flow organization in 3D IOSWBLI (Eagle and Driscoll (2014))

grows along the root of the glancing shock-wave on the side-wall interact downstream and lead to secondary separation.

Full-Field Measurement Techniques of High-Speed FSI

As discussed earlier, a characterization of the FSI in the high-speed flow regime is critical in the design of the aircraft as it results in understanding of load margins and response of the structure. FSI can be driven by IOSBWLI. Over the years, a considerable amount of effort has been invested in describing the fatigue caused due to these loads, through experimentation on thin panels. The main source of fatigue in high Mach number flows is the turbulent boundary layer noise and SWBLIs. The SWBLIs further result in thermal heating and mechanical loading due to oscillating shock fronts and separating vortices that can potentially couple with structural resonant frequencies of the panels.

Validation of unsteady theoretical and computational fluid-structure interaction models requires high temporal and spatial resolution data and corresponding measurement techniques. Acquisition of this data is often compromised by traditional surface and off-surface probes that can interfere and distort the airflow, necessitating substantial correction techniques. Pointwise techniques such as pressure taps, accelerometers, and strain gauges, while highly accurate, can have insufficient spatial resolution or add significant time and cost to instrument the model. PSPs and temperature sensitive paints (TSPs) have proven to be effective alternative measurement techniques as they overcome the above obstacles and provide full-field map of pressure and temperature respectively. These techniques have been utilized on both rigid and compliant surfaces in various studies over the years. A few of these studies have been highlighted in the following to draw out the capabilities of these techniques.

Spottswood et al. (2019) were successful in detecting the fundamental modes on a PSP coated panel subjected to an IOSWBLI, using digital image correlation (DIC). Mears et al. (2019) studied the effects of forced perturbations on a single fin SWBLI by coating the wall with PSP and found that both upstream and downstream forcing of perturbations have an impact on the flow. Liu et al. (2022) investigated the effects of a sidewall by coating the SWBLI region with PSP. They used correlation analysis and proper orthogonal decomposition analysis to extract the large-scale unsteady flow patterns and found asymmetry in the instantaneous pressure distribution induced by the sidewalls and spanwise differences of the pressure fluctuation amplitudes in the interaction zones.

A recent project inspired by the Joint Computational/Experimental Aerodynamics Program (JCEAP) aimed at studying FSI on a thin panel. In the set of experiments, the panel was clamped on a wedge, installed on a longitudinal slice at the aft end of a 7° slender cone and subjected to a compression corner SWBLI at various hypersonic Mach numbers (Anshuman et al. (2020 and 2021), Sadagopan et al. (2022)). TSPs and pressure transducers were utilized to acquire measurements. However, it must be noted that transducers (installed underneath the panel) captured the pressure fluctuations on the panel while TSPs were employed to study the characteristics of the SWBLI on a rigid wedge in place of the panel in a prior experiment. The tests revealed that the transitional regime affected the panel vibrations the most due to the convective shock undulations induced by the boundary layer disturbance. Shear layer flapping at appropriate frequencies excited select panel modes. Further, the heating of the panel led to a downward shift of the resonant frequencies of the panel. TSPs results showed that the peak heating occurred during the transitional flow.

A separate experiment focused on the development of a technique to measure full-field pressure and strain of high-speed FSI. However, this is not a focus of this dissertation and is discussed in Appendix-I and published papers.

Objectives

The knowledge of flow physics in a 3D IOSWBLI is important as it is more realistic from the perspective of operating conditions of engine inlets of high speed aircraft (Dolling (2001)). This demands gathering and interpreting data in 3D IOSWBLIs that involve flow separation at high Mach numbers and various shock strengths in channels with low aspect ratios. The Mach numbers in wind tunnel test sections and their geometry offer an environment where a 3D IOSWBLI can be generated through the choice of an appropriate wedge angle. In the experiment, the width and height of the tunnel test section had a 1:1 aspect ratio. The 12° shock generating wedge that spanned the width of the test section has been shown to generate a flow separation in IOSWBLI in the past (Chaganti (2017)) in the same facility. With this setup, it could be extrapolated from literature that a 3D IOSWBLI would be formed. As there is currently no information regarding the characteristics of wall static pressure field for such a setup, this investigation created experimentally and computationally a 3D IOSWBLI. The investigation aimed at specifically understanding

- a) The pressure fluctuations and spectral content of wall static pressure under the interaction region, both on the opposite and side-walls through the experiment and comparing the spectral content of wall static pressure at centerline with a simulation of 2D IOSWBLI.
- b) The evolution of the vortical nature of the flow field and Reynolds stresses near the walls in the interaction region through the simulation of a 3D IOSWBLI.

Structure of Dissertation

This dissertation focuses on the experimental and computational approaches adopted to study the 3D IOSWBLI which was generated using the 12° wedge in a 1:1 aspect ratio channel at $M = 2.9$. The chapter titled 'Experimental Setup' describes the UA supersonic wind tunnel facility and techniques used to acquire the flow structure and pressure profiles. The chapter titled 'Results and Discussion' first discusses the experimental results followed by the computational results. The chapter titled 'Conclusion and Future Work' lists the key observations from the two approaches. Appendix-I discusses the experiment conducted to achieve the secondary objective. This experiment demonstrated the application of a new luminescent technique in high speed flow to measure full-field pressure and strain. The approach combined fast-response PSP with thin PEC to create a fast luminescent pressure and strain measurement technique. In this campaign, circular clamped plates of two different thicknesses were subjected to baseline flow (absence of any shock-wave) and an IOSWBLI at Mach 2.9 flow. The pressure and strain fields that developed on the plates were analyzed. Appendix-II discusses the processes of setting up 3D steady and 2D unsteady computational grids using ANSY (FLUENT). Appendix-III shows the KSC-2 signal conditioner settings for the experiment. Appendix-IV highlights the MATLAB code setup to process the wall static pressure data. Appendices V and VI discuss the procedure to run the UA small supersonic wind tunnel facility and acquire the pressure measurements using KSC-2 signal conditioner and Picoscope respectively.

EXPERIMENTAL AND COMPUTATIONAL SET-UP

The experimental investigation was undertaken at the supersonic wind tunnel facility at the Department of Aerospace Engineering and Mechanics in The University of Alabama (UA), to

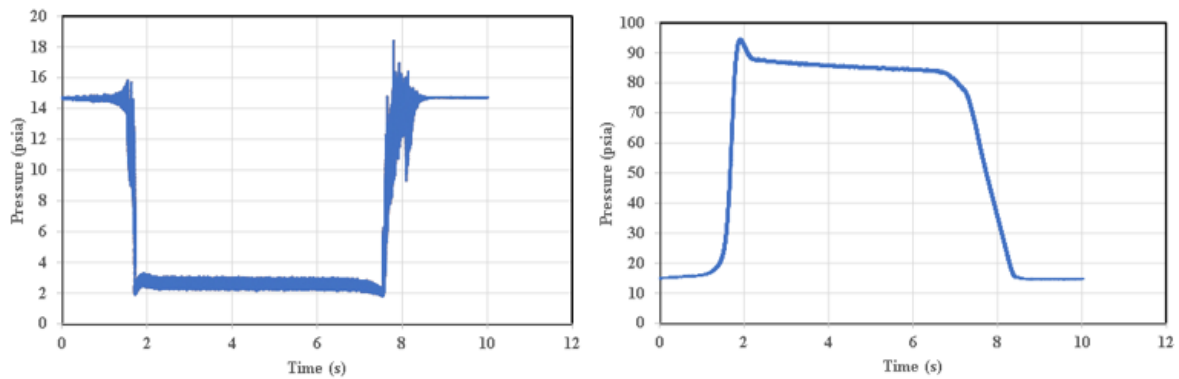


Figure 2.1. Free stream static pressure (left) and stagnation pressure (right) variation during the wind tunnel run

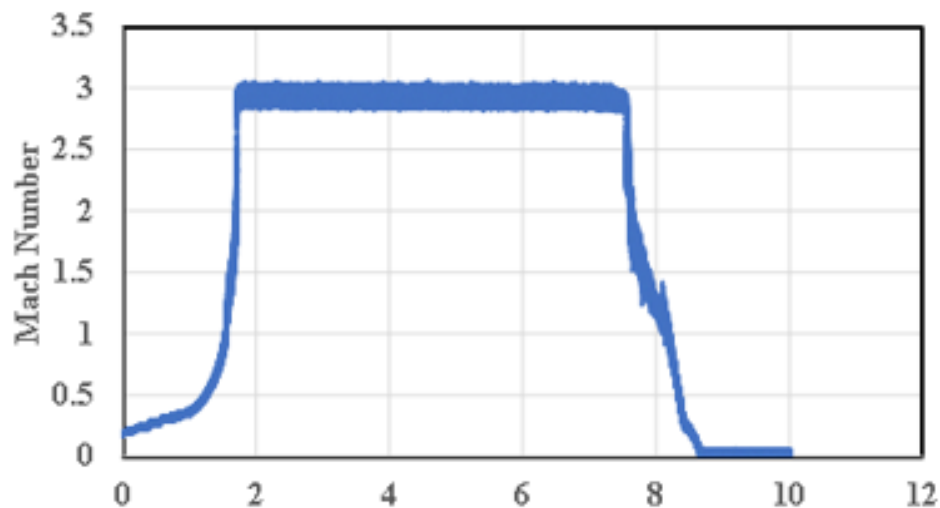


Figure 2.2. Free stream Mach number variation during wind tunnel run

acquire qualitative (oil flow visualization) and quantitative (pressure measurements) data. The Mach number of the blowdown facility is 2.9.

Wind Tunnel Facility

Air supply

The blow-down air supply system is comprised of compressors, dryer, and storage tank (Fig 2.3.). Air is pressurized by a couple of compressors from Ingersoll Rand with a rated operating pressure of 1.37 MPa (198.9 psia) and a capacity of 288.83 cubic m/hr (170 cubic ft/min). The compressors are run using a 3 phase, 60 Hz, 3.73 kW (50 HP) motor. An automatic air-cooled Ingersoll – Rand dryer dries the air using activated alumina as a desiccant. The desiccant has a dew point of -73°C (-100°F). The pressurized air is stored in a tank of wall thickness 12.7 mm and a volume of 28 m^3 , with a maximum allowable design pressure of 1.38 MPa (200 psia). During the experiments, the storage tank is usually charged up to 1.34 MPa (194.54 psia). The air flow from the storage tank to the regulator is controlled by a butterfly valve. A Leslie pressure regulator of diameter 76.2 mm regulates the operating pressure of the wind tunnel and compresses the air from the storage pressure to 0.55 MPa (79.77 psia).



Figure 2.3. (a) Air dryer (b) Storage tank and air compressor

Wind Tunnel Assembly

The wind tunnel assembly (Fig. 2.4) is comprised of stagnation chamber, nozzle, test section, and diffuser. The stagnation chamber contains a flow straightener, damping screen, and a pitot probe. The flow straightener is made up of circular steel tubes that are 101.6 mm long and 12.7 mm in diameter. For the experiments, an in house manufactured aluminum nozzle was used to expand the flow to the design Mach number in the test section. The nozzle is 254 mm in length

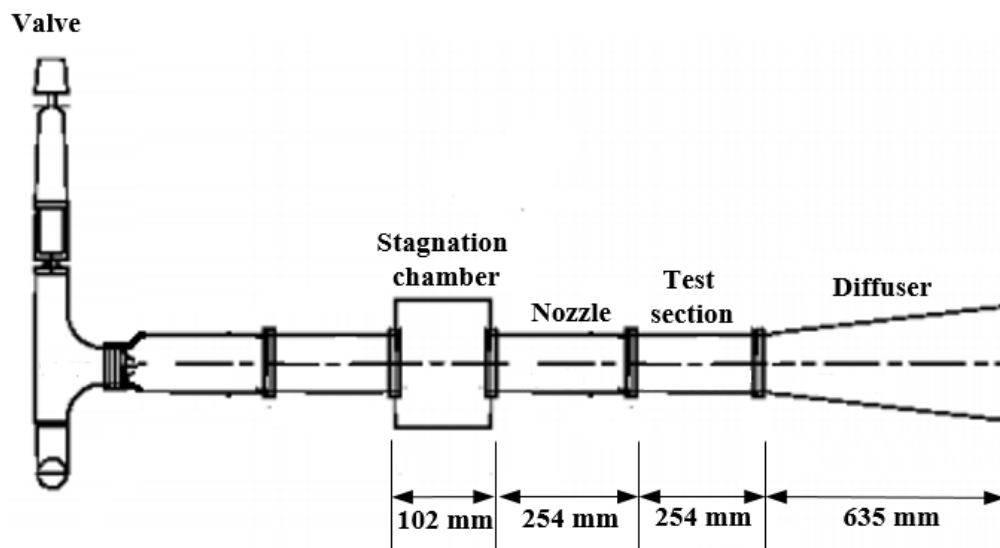


Figure 2.4. UA small supersonic wind tunnel facility (top) and its schematic (bottom)

with a throat area of 16.5 mm x 76.2 mm. It is followed by the test section. Figure 2.4 shows the schematic of the 3D IOSWBLI. During the operation of the wind tunnel, 2D and 3D turbulent boundary layers grow on the walls and corners of the tunnel, respectively. A 12° isosceles triangular wedge (12.7 mm in height) installed on the top wall of the test section results in an oblique shock-wave that impinges the bottom and side walls of the test section and forms the 3D IOSWBLI. Fig 2.5 (b) shows the actual test-section set up which is inverted in comparison to the schematic in Fig. 2.4. However, this did not affect the data acquisition as the test section was a square channel and the nozzle had a symmetric contour in the stream wise direction.

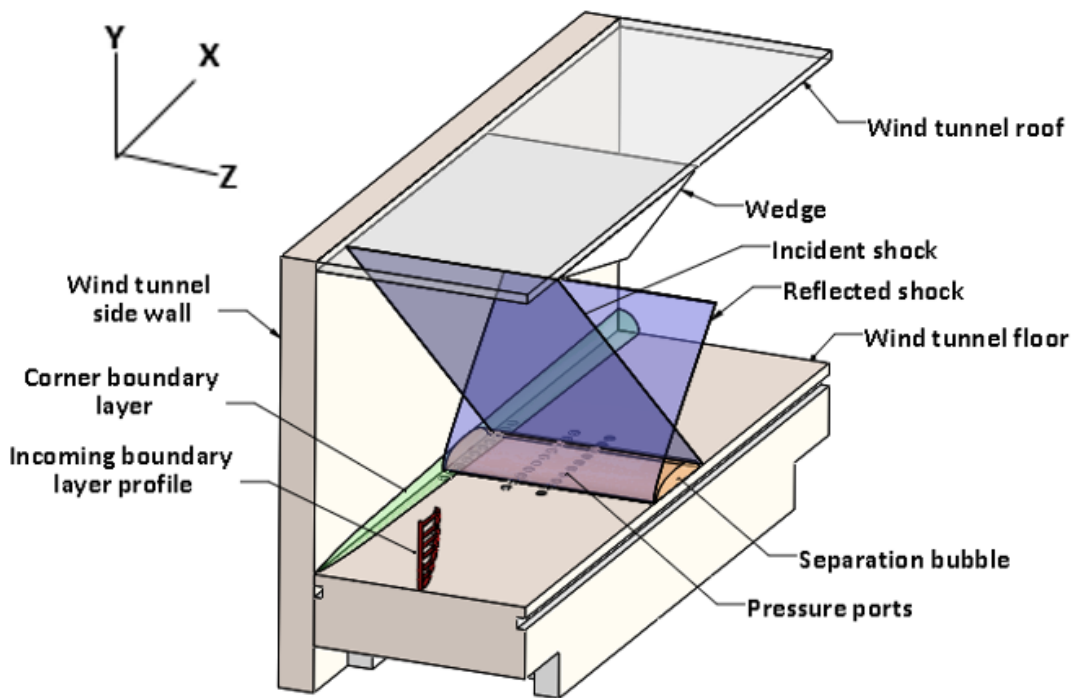


Figure 2.5. Schematic of 3D IOSWBLI created by a triangular wedge

Four separate walls formed the test section. The four walls were assembled using screws to form the test section that is 254 mm long x 76.2 mm wide x 76.2 mm high. The side walls were made of aluminum of dimensions 152.4 mm long x 254 mm wide x 25.4 mm thick. Each sidewall was machined to accommodate a circular optical glass with dimensions of 108 mm diameter x 19 mm thick to have optical access. The top and bottom walls, fabricated from aluminum, were 254 mm long x 76.2 mm wide x 25.4 mm thick.

The incoming tunnel boundary layer profile was determined through pitot tube sweeps using a hypodermic needle at a stream-wise distance of 53 mm, from the end of flow expansion in the nozzle, beginning at a distance of 1 mm in the wall normal direction from the lower wall of the test section, up to 35 mm. This yielded a mean Mach number of 2.9, and a boundary layer of thickness 7 mm. The wedge was installed in a manner such that the leading-edge of the wedge was located at the same stream-wise distance where the boundary layer was measured. The free stream velocity for the experiments was calculated to be 620 m/s. The unit length Reynolds number was determined to be $4.6 \times 10^6 \text{ m}^{-1}$. Stagnation pressure, static pressure, and temperature are nominally

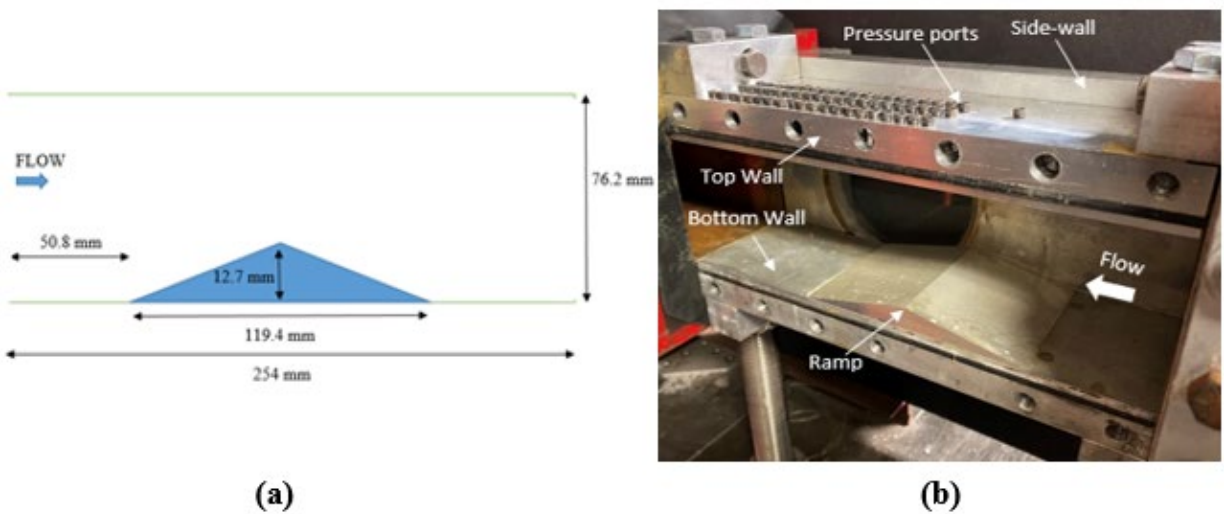


Figure 2.6. (a) schematic of test section set-up (b) actual set-up

between 482-544 kPa, 16-18 kPa, and 290-300 K respectively. A variable area supersonic diffuser downstream of the test section is used to recover pressure to reduce the total pressure required to run the tunnel. A 635 mm long diffuser with an inlet area 76.2 mm x 76.2 mm and the outlet area of 127 mm x 76.2 mm is used. The walls of the diffuser include a hinged plate, which can be adjusted to work with the different Mach numbers in the test section.

Experimental Techniques

Oil flow visualization

Oil-flow visualization was conducted on the top-wall and on one of the side-walls of the wind tunnel. Wall shear force developing due to velocity gradients on the wall transports the pigment as the fluid flows over the surface and hence provides a time averaged image of the interaction. The flow mixture consisted of aluminum oxide and kerosene oil mixed in the ratio of 1:8 by weight. To obtain the maximum contrast between the white oil flow and the surface, an adhesive matte black paper was applied on the surfaces of the top and side-wall. The mixture was then applied uniformly over the paper, and the tunnel was run for 10 seconds. After the run, the mixture was allowed to dry for 10 minutes. It was then preserved by coating with the spray 'Krylon Workable Fixatif'.

Static pressure measurements

Fluctuating wall-pressure measurements were made in the regions of IOSWBLI. The pressure fluctuation measurements were acquired using two high frequency response transducers from Kulite (XCE-062-100A and XCS-062-15D). The probe diameter is 1.7 mm. The natural frequencies of the membranes of XCE-062-100A and XCS-062-15D are 380 kHz and 200 kHz, respectively. Perforated screens above the diaphragms protect the transducers from being damaged by the dust particles in the flow. To install the transducers, pressure ports were drilled into the top wall. These ports were tapped holes for #6-32 screws. A 2.54 mm through hole was drilled through the length of the #6-32 socket head bolt. The transducer was then inserted into this hole, and the probe was adhered to the insides of the screw using an adhesive in such a manner that the sensing face of the probe was flush with the end of the body of the screw (Fig. 2.7(a)). This assembly allowed the transducers to be easily installed into and removed from any of the ports.



(a)



(b)



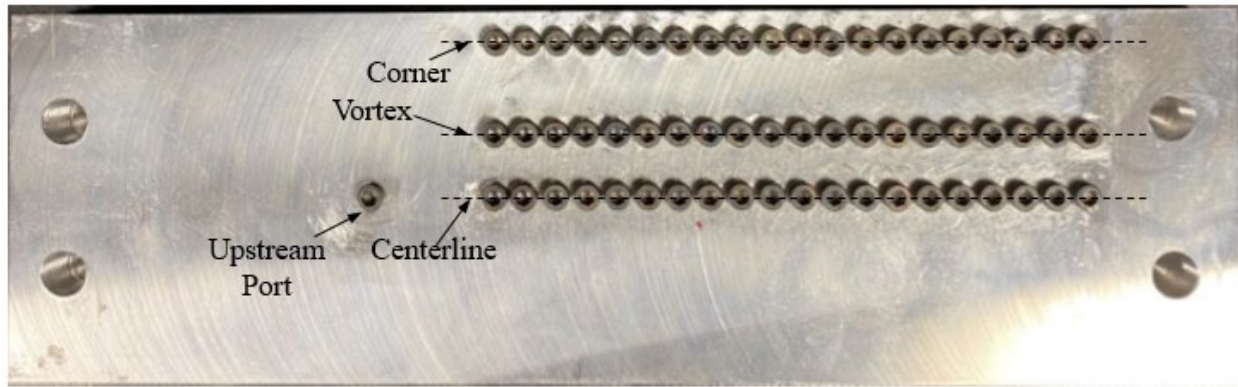
(c)

Figure 2.7. (a) pressure transducer inserted into #6-32 screw (b) transducers installed on ports of top-wall and (c) transducer installed on a port of side-wall

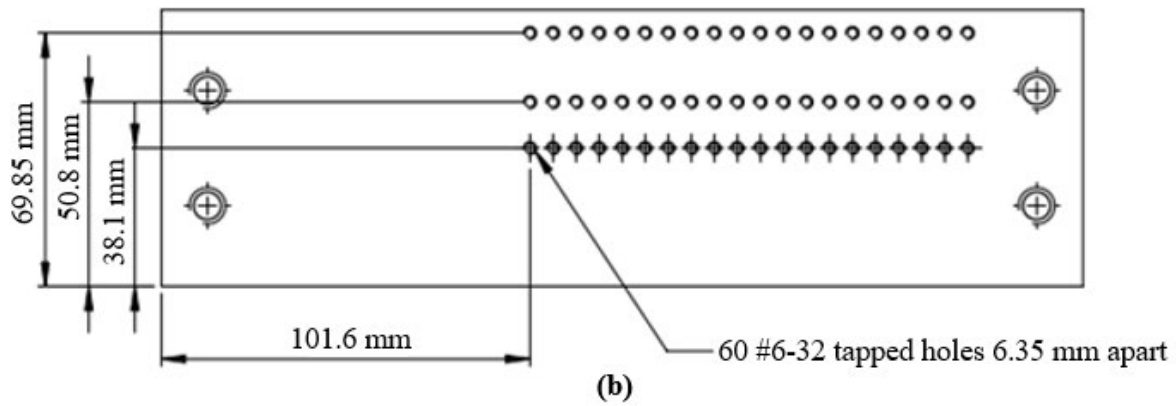
During the wind tunnel runs, the rest of the ports were plugged with blank screws the ends of which were flush with the surface of the wall. As seen in figs. 2.8 and 2.9, a total of 61 and 12 pressure ports were drilled on the top and side-walls respectively, with the guidance of the flow visualization (underneath and in the vicinity of the flow structures).

On the top wall, one port was located upstream to measure the static pressure underneath the incoming undisturbed boundary layer. The remaining ports were drilled along three span-wise locations that were named as centerline, vortex, and corner, as the ports were located under these flow structures. The transducer XCS-062-15D was placed in the most upstream port and XCE-062-100A was used to acquire the data from the rest of the ports.

The signals from the pressure transducers were conditioned using a Kulite KSC-2 signal conditioner. Fig. A.3.1 in Appendix-III shows the settings used on the signal conditioner for the two transducers. The signal conditioner allows three separate filter settings (flat, pulse, and no filter) to acquire the data. For every port, pressure signals were acquired at a rate of 50 kHz for 10 seconds per run at every filter setting and repeated twice, which resulted in a total of six measurements at every port. However, the pressure measurements that were of interest and discussed in this dissertation are from those acquired with the pulse filter settings as this setting was the best suited for the transient analysis which is the characteristic nature of the IOSWBLI. The data was then passed through a Picoscope 4262 digital oscilloscope from Pico Technology, which made it possible to visualize and store the measurements on a computer using its Picoscope 6 software.

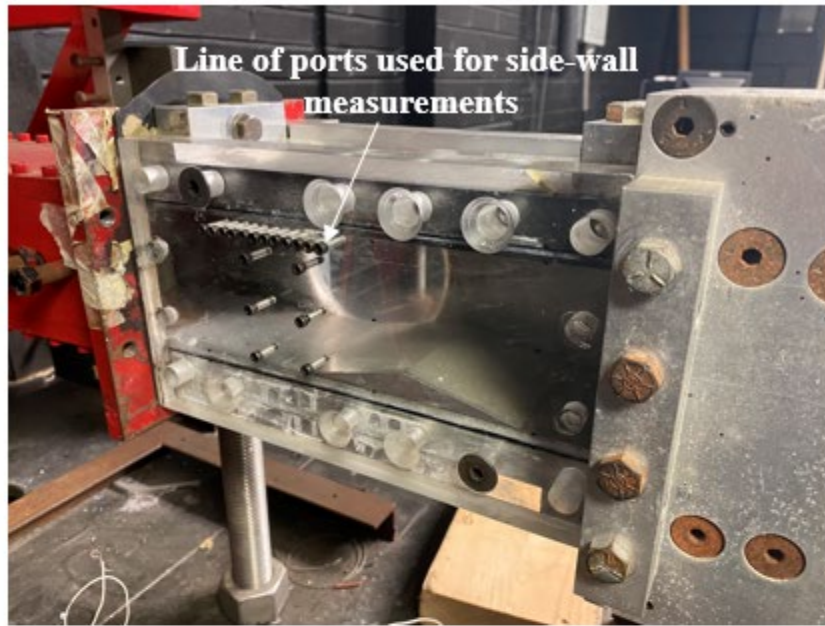


(a)

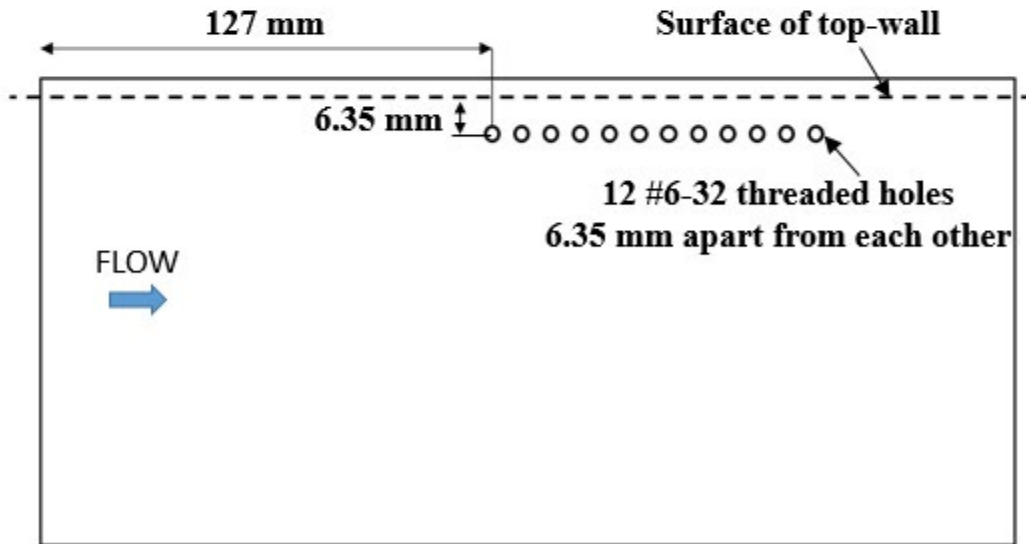


(b)

Figure 2.8. (a) pressure ports on top wall (b) schematic showing the distance between the spanwise locations



(a)



(b)

Figure 2.9. (a) pressure ports on side wall (b) schematic showing the dimensions of the port locations used for side-wall measurements

Computational Model: Steady-state Simulation

A steady-state 3D IOSWBLI was simulated in ANSYS (FLUENT), with inlet and outlet conditions the same as those in the experiment. The SWBLI region is characterized by high degrees of anisotropic turbulence (velocity components and their derivatives are dependent on the direction), flow separation, zones of re-circulation and flows influenced by mean rotational effects. The eddy viscosity models are incapable of capturing this behavior as they assume turbulence isotropy. The Reynolds-Stress (R-S) model however is advantageous in this scenario as it computes all the components of the Reynolds stresses directly and can be implemented for a steady state simulation. Friedlander et al. (2022) demonstrated this through investigation of diffusive flow fields in subsonic in S-duct diffuser and transonic flow in a two-dimensional diffuser. Hence, the R-S model available in ANSYS was utilized for this simulation. Although the 3D OSWBLI generated in the experiment was unsteady, the simulated steady-state 3D IOSWBLI helped in the comparison of mean static pressure results.

Computational Model: Unsteady Simulation

Results from an unsteady 3D IOSWBLI simulation would more likely compare to the experimental results for the given test configuration. In this regard, to begin with, an unsteady 2D IOSWBLI was simulated on ANSYS (FLUENT), under inlet and outlet conditions similar to those in the experiment, with an objective of calculating the time-dependent static pressure values at a rate of 15 kHz on the floor (20 points corresponding to the pressure port locations in the experiment) and compare them with the experimental data acquired along the centerline. It was found that the data acquisition required two weeks to acquire data for a duration as small as 0.25s. Hence, it was quite evident that with the available computational resources it would be time intensive to acquire the same data if the simulation was extended to three dimensions. Therefore,

only a 2D unsteady IOSWBLI was simulated and studied, and has been discussed in this dissertation. Further, on observing the unsteady behavior of the flow-field, several locations of interest were further identified within the flow-field, such as within the separation bubble, expansion fan, re-attachment shock. Time-dependent static pressure values were acquired at these additional locations (31 additional points).

Delayed detached eddy simulation (DDES) turbulence model was utilized for this simulation because it combines RANS modeling with LES for applications such as high-Re external aerodynamics simulations. In the detached eddy simulation (DES) approach, the unsteady RANS models are employed in the boundary layer, while the LES treatment is applied to the separated regions. Large unsteady turbulence scales play a dominant role in core turbulent region, and LES region is normally associated with this region. The cost of a near-wall resolving LES would be prohibitive in high Reynolds number wall bounded flows, and, hence, DES models have been specifically designed for such flows. In this region, the DES models recover LES-like subgrid models. The difference with the LES model is that it relies only on the required resolution in the boundary layers. In the near-wall region, the respective RANS models are recovered. Although this model is implemented for a 3D case, it was implemented for the simulation under consideration by assigning periodic boundary conditions to the two side-walls of the 3D fluid domain, which resulted in effectively a quasi 2D simulation (*ANSYS Documentation**).

*<https://www.afs.enea.it/project/neptunius/docs/fluent/html/th/node88.htm>

RESULTS AND DISCUSSION

All the images and plots have been assigned Cartesian coordinates and have been normalized by the thickness of the incoming boundary layer measured at the centerline of the top-wall ($x/\delta_0 = 0$ corresponds to the edge of the wedge). The abscissa and the ordinate represent the stream-wise and span-wise/wall normal directions, respectively. In all the images and plots, flow direction is from left to right.

Experimental Results

Flow visualization

Top wall flow visualization

Figure 3.1 shows the top-wall oil flow visualizations. For the purpose of illustration, the regions $0 < z/\delta_0 < 5.4$ and $5.4 < z/\delta_0 < 10.8$ in the image are denoted as upper and lower halves respectively.

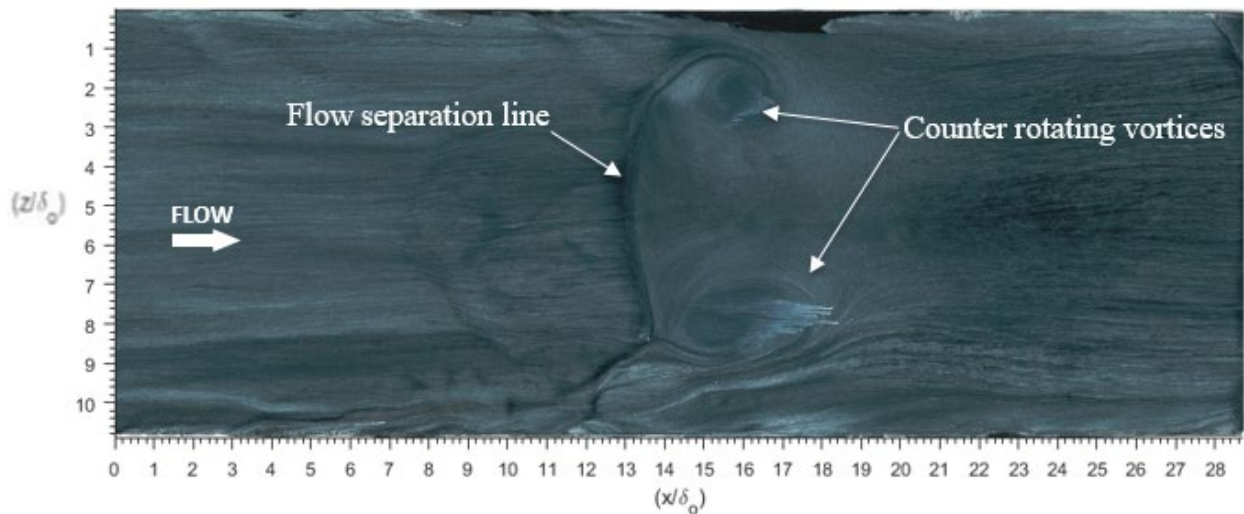


Figure 3.1. Top-wall oil flow visualization

In the figure, the streamlines of the incoming flow runs parallel along the surface, indicating minor distortion in the span-wise direction. The observed flow features have also been recorded in literature (Morajkar et al. (2014), Burton et al. (2012), Stanbrook (1960)). The line of flow separation is observed at $x/\delta_o \approx 13$, marked by the accumulation of pigment due to the collapse of the x-component wall shear stress to a negative value at this location. If the flow separation was 2D, then the line of separation would have spanned the test section width. However, away from the centerline, the separation lines curves downstream in the flow direction indicating the occurrence of a 3D IOSWBLL.

Oval patterns representing counter-rotating vortices are observed on opposite sides of the streamwise centerline. According to Dolling et al. (2006), these vortices grow upwards from the surface and spiral in the downstream direction. Bookey et al. (2005) studied IOSWBLLs at the same Mach number and shock strength. They observed similar oval patterns in their experiments and concluded that the flow separation is three dimensional which can be extended to the experiment under consideration.

An additional observation is a line of separation emanating from the corner in the lower half region, at $x/\delta_o \approx 11.4$ well ahead of the centerline separation. It extends at an angle into the flow and meets the primary separation line at $x/\delta_o \approx 13.6$, $y/\delta_o \approx 8.6$. This separation is due to a bifurcated shock system (Morajkar et al. (2014)). However, this is not prominently captured in the upper half region, probably due to the non-uniformity in the application of the oil mixture.

Side-wall flow visualization

Figure 3.2 shows the oil flow visualization for the side-wall of the test section. The boundary of the wedge extends on the upper wall between $x/\delta_o \approx 0$ to $x/\delta_o \approx 16.7$. At the leading edge the streamlines of the incoming flow and the flow past the Shock-wave - I follow its path. At

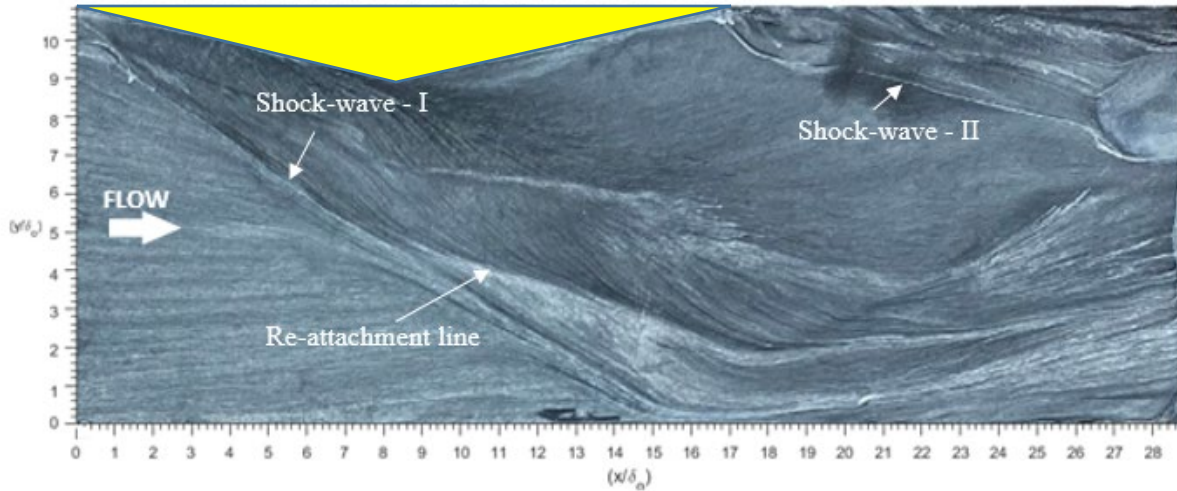
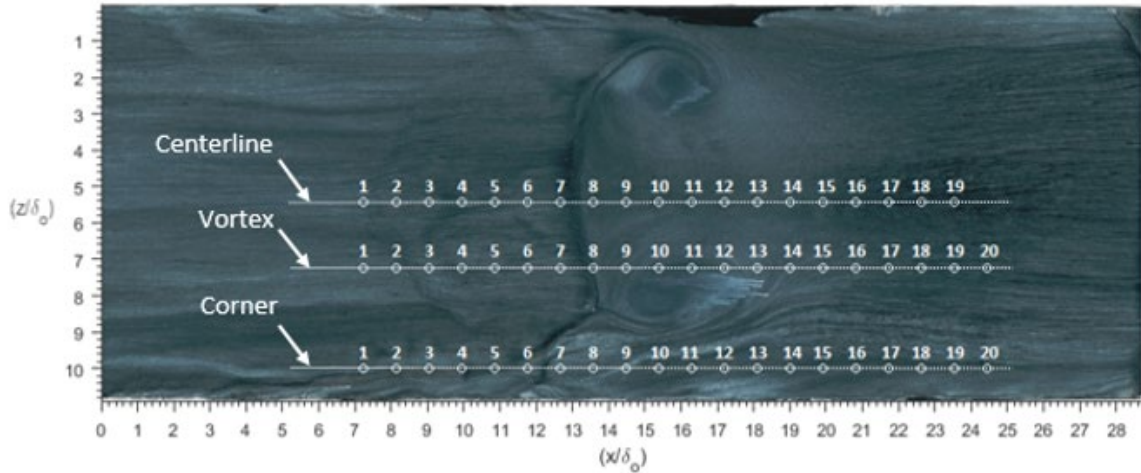


Figure 3.2. Side-wall flow visualization

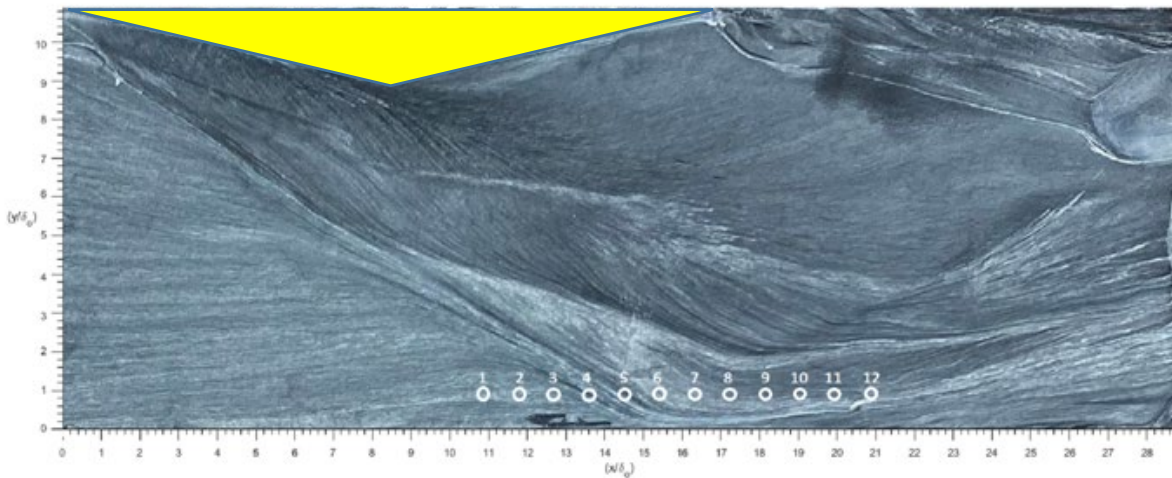
the root along this shock wave, a vortex (not visualized) is expected to develop. The fluid away from the side-wall wraps around this vortex, forming the re-attachment line as shown. Emanating from the trailing edge of the wedge is Shock-wave - II. The visualization is not however clear enough to view whether the flow follows its path. If the SWBLI was 2D then the flow separation would have occurred even on the side-wall. However, there does not appear to be accumulation of pigment in the vicinity of the point where the shock-wave meets the opposite wall (top-wall). This indicates that the separation bubble spans only to a limited extent and is inhibited by the corner separation.

Pressure port locations

Figure 3.3 (a) and (b) show the flow visualizations overlaid with pressure transducer locations for the top-wall and left side-wall, respectively. As discussed in Chapter 2, the flow



(a)



(b)

Figure 3.3. (a) Top-wall flow pressure transducer locations (b) Side-wall pressure transducer locations

visualizations guided the placement of the ports. For the top wall, all the ports were at the same distance from each other in the stream-wise location for the centerline, vortex and corner locations. The port locations were located to capture pressure data under the different flow topographies,

beginning with the incoming boundary layer and extending downstream of the SWBLI interaction. Table 3.1 shows the ports on the side-wall that are at the stream-wise locations with their counterparts on the top wall. This has been shown for easier reference of the ports in the chapter ‘Results and Discussion’.

Table 3.1. Port location comparison

Side-wall	Centerline/Vortex/Corner
Port - 1	Port - 5
Port - 2	Port - 6
Port - 3	Port - 7
Port - 4	Port - 8
Port - 5	Port - 9
Port - 6	Port - 10
Port - 7	Port - 11
Port - 8	Port - 12
Port - 9	Port - 13
Port - 10	Port - 14
Port - 11	Port - 15
Port - 12	Port - 16

Uncertainty estimation

An uncertainty analysis was carried out to ascertain that the repeatability of the experiments and that there was no extreme deviation of the values measured at different locations. Holman (1978) discusses a method for this calculation which implements Chauvenet's criterion. In this regard, the mean value of a variable (\bar{X}) from all the trials is subtracted from its mean value at every trial (\bar{X}_i) in order to obtain a deviation value. The maximum deviation value (d_{max}) is then divided by Chauvenet's standard deviation value (T) that is assigned based on the number of trials/samples and read from the Chauvenet's Criterion table. The resulting value (σ) is converted to the uncertainty (U). Equations 3.1 – 3.3 show this process:

$$d_{max} = \max (\bar{X}_i - \bar{X}) \quad 3.1$$

$$\sigma = d_{max}/T \quad 3.2$$

$$U = \pm 2\sigma \quad 3.3$$

The number of samples considered to calculate the uncertainties for the variables were 3, 5 or 6. Hence, as per the Chauvenet's criterion table, T values of 1.383, 1.645, or 1.732 were respectively used. All the static pressure values have been normalized by the average value of the static pressure (21403.61 Pa) measured by the *Upstream Port* while acquiring the static pressure at every transducer location and the stagnation pressure has been normalized by the average value of the stagnation pressure for three runs (509.54 kPa) as discussed in the next section.

Mach number uncertainty

To ascertain the Mach number of the incoming flow, three runs were conducted without the wedge in the test section. The Kulite XCS-062-15D acquired the wall static pressure, and the

Omega transducer PX-302 was acquired the tunnel stagnation pressure. The data was acquired at 1000 Hz. Table 3.2 shows the static pressure, stagnation pressure and Mach number uncertainty

Table 3.2. Mach number uncertainty

Variable	Uncertainty
Static Pressure	± 0.01
Stagnation Pressure	± 0.02
Mach Number	± 0.003

Static pressure measurement uncertainty

The static pressure uncertainty at the locations where the data was acquired was again calculated using equations 3.1, 3.2, and 3.3, and is shown in Table 3.3. For all the span-wise locations, Kulite transducer XCS-062-15D was used to acquire wall static pressure at the *Upstream port* and XCE-062-100A was used to acquire wall static pressure at the rest of the ports. For the side-wall, only XCS-062-15D was used to acquire wall static pressure at all the ports. Pressure was not acquired at the *Upstream port* during the side-wall pressure measurements.

Table 3.3. Static pressure measurement uncertainty

Location	Uncertainty			
	Centerline	Vortex	Corner	Side-wall
Upstream Port	± 0.03	± 0.04	± 0.04	-
Port-1	± 0.04	± 0.04	± 0.05	-
Port-2	± 0.05	± 0.05	± 0.06	-
Port-3	± 0.05	± 0.04	± 0.06	-
Port-4	± 0.04	± 0.05	± 0.05	-
Port-5	± 0.05	± 0.04	± 0.05	± 0.02
Port-6	± 0.05	± 0.04	± 0.05	± 0.07
Port-7	± 0.03	± 0.05	± 0.03	± 0.05
Port-8	± 0.05	± 0.03	± 0.08	± 0.04
Port-9	± 0.07	± 0.07	± 0.09	± 0.06
Port-10	± 0.09	± 0.08	± 0.06	± 0.05
Port-11	± 0.10	± 0.13	± 0.09	± 0.08
Port-12	± 0.10	± 0.10	± 0.12	± 0.12
Port-13	± 0.12	± 0.14	± 0.13	± 0.27
Port-14	± 0.15	± 0.20	± 0.13	± 0.33
Port-15	± 0.16	± 0.16	± 0.12	± 0.20
Port-16	± 0.17	± 0.16	± 0.13	± 0.20
Port-17	± 0.14	± 0.18	± 0.13	-
Port-18	± 0.17	± 0.12	± 0.11	-
Port-19	± 0.13	± 0.11	± 0.12	-
Port-20	-	± 0.11	± 0.17	-

Pressure rise

Figures 3.4 (a), (b), (c), and (d) show the mean wall static pressure for centerline, vortex, corner, and side-wall regions respectively, normalized by the free stream mean wall static pressure

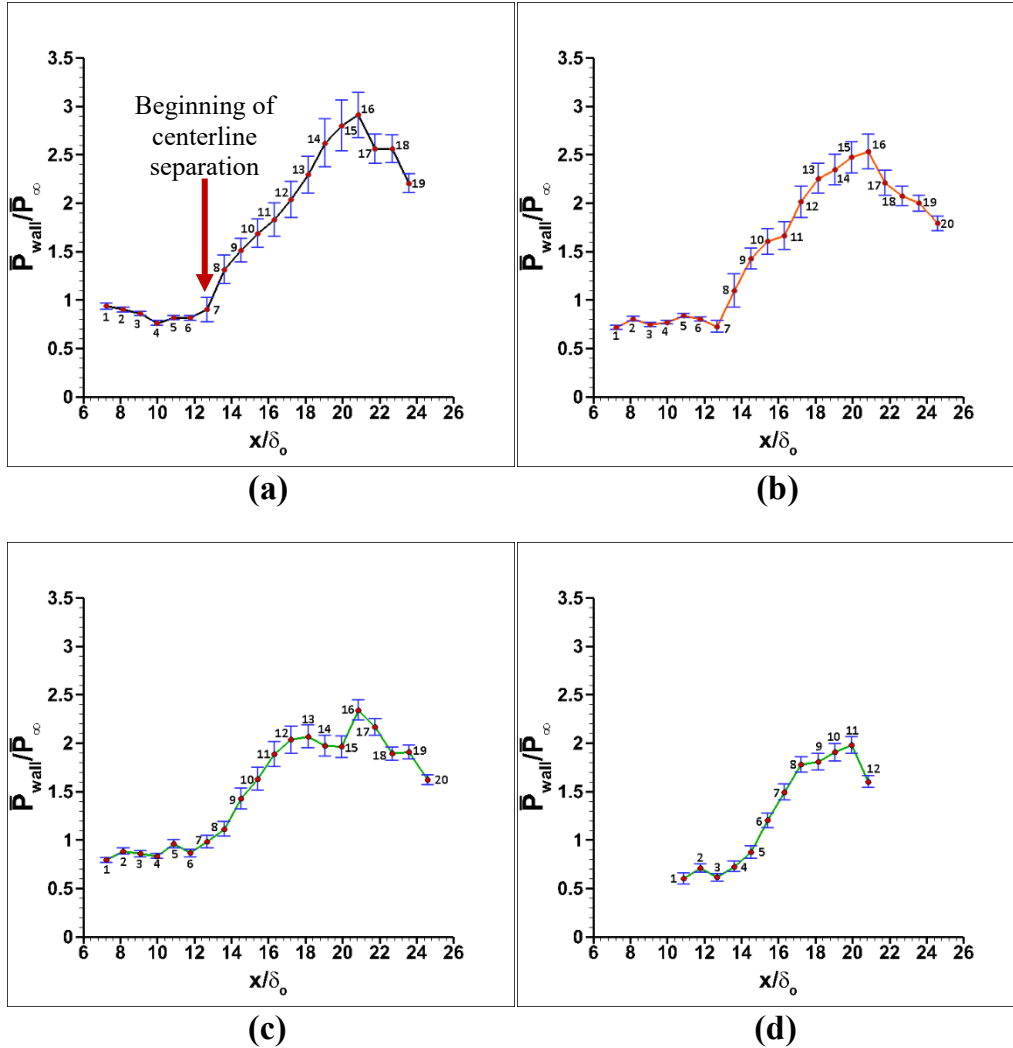


Figure 3.4. Stream-wise pressure rise (a) centerline (b) vortex (c) corner (d) side-wall measured at the ‘Upstream Port’. This is assumed to be under the undisturbed incoming boundary layer. As the free stream pressure is imposed on the boundary layer, the wall pressure would be the same as the free-stream static pressure. The static pressure decreased along centerline, and remained approximately the same for vortex and corner below the free stream value, up to port 4. This could be the upstream influence of the IOSWBLI. Therefore, the pressure ratios for the initial

set of ports, before the detected rise in pressure due to the shock-wave, are lower than 1 for all the locations. In fig. 3.4 (a), the initial rise in pressure at $x/\delta_o \approx 12.7$ is as expected due to the onset of flow separation as seen from the flow visualization images. In fig. 3.4 (b), the locations of initial pressure rise for the vortex is the same as centerline. However, the behavior of pressure rise deviates from this point onwards. In fig. 3.4(c), the pressure rises earlier at $x/\delta_o \approx 11.7$. This is may be due to the fact that the incoming boundary layer in the corner being a result of two overlapping boundary layers, has a lower global Mach number which makes it more susceptible to earlier separation. In fig 3.4(d), the rise in pressure on the side-wall is detected at the same stream-wise location ($x/\delta_o \approx 12.7$) as centerline, vortex, and corner. The pressure rise reaches a peak value of $\bar{P}_{wall}/\bar{P}_\infty \approx 1.94$ at port 11. The gradient between $x/\delta_o \approx 12$ and $x/\delta_o \approx 18$ is the same for all the locations. At $x/\delta_o \approx 18$, the pressure ratio is ~ 2 . It is past this location that the traces differ, leading to different peaks. Except for the side wall, the peak pressure rise values, 2.91, 2.53, and 2.34, for centerline, vortex, and corner respectively are observed to be at Port 16. Further, it is also observed that the peak value of pressure rise decreases as the corner is approached. As argued by Hegde et al. (2015), this is because of the 3D nature of the flow separation that results in the flow facing a slightly swept shock of lower strength on moving away from the centerline. Also, the low global Mach number of the fluid in the corner boundary layer results in a low pressure rise.

Pressure fluctuations

Figure 3.5 shows the mean rms of the experimental pressure values along the centerline, vortex, corner and side-wall locations. These values are again normalized by the free stream mean wall static pressure measured at the ‘Upstream Port’. Ports at the same stream-wise location have

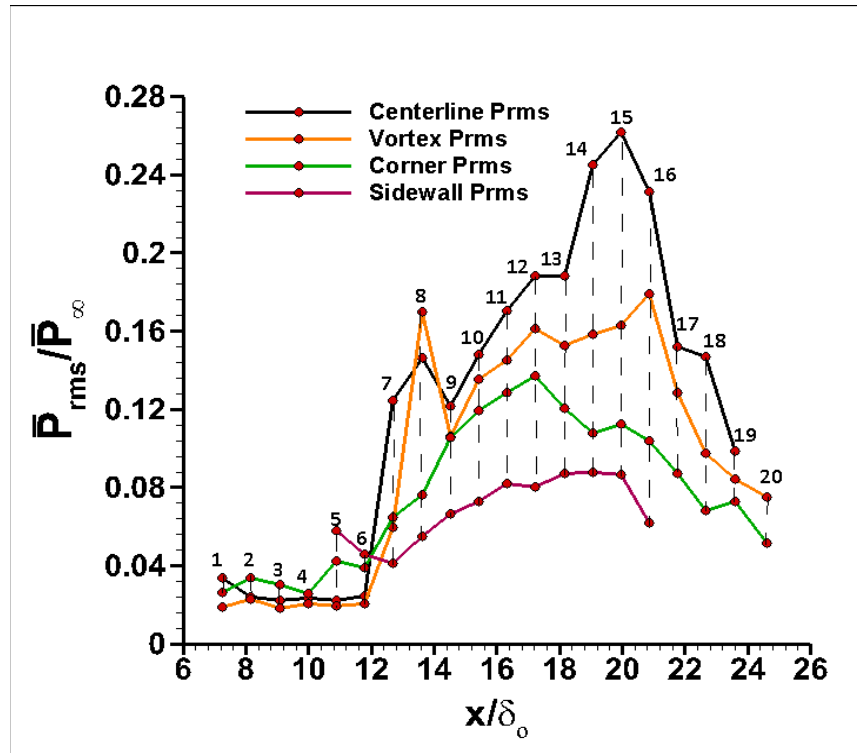


Figure 3.5. P_{rms} comparison

been connected with dashed lines at all the locations for easier identification. For all the locations on the top wall low flow unsteadiness exists up to Port 4 (<0.04).

At centerline, the rms value reaches two maxima, first at Port 8 ($\bar{P}_{rms}/\bar{P}_\infty \approx 0.15$) and second at Port 15 ($\bar{P}_{rms}/\bar{P}_\infty \approx 0.26$). From Dolling (1993) we know that the locations of maximas correspond to flow separation and reattachment, respectively, and result due to the contraction and expansion of the separation bubble. Using proper orthogonal decomposition and rainbow schlieren deflectometry, Chaganti (2017) found that the length of the interaction region along the centerline in the same facility was 41.4 mm. This would approximately correspond to the distance between

Port 8 and 15. Hence, it can be deduced that these ports correspond to the locations of flow separation and reattachment.

At the vortex, although the rms begins increasing at Port 6, the peak rms is reached at Port 8 ($\bar{P}_{rms}/\bar{P}_\infty \approx 0.17$). This value is greater than the rms of the centerline separation. A hypothesis over here is that given the fact that Port 8 lies in the upstream periphery of the vortex, along with the intermittent region, the unsteadiness of the vortex is contributing towards the higher value of rms. The measurements at ports 9, 10, 11, and 12 evolve in a manner similar as their corresponding centerline separation values. Similar to the centerline, a third maxima is observed at the vortex. However, this location is further downstream in comparison. For the corner and side-wall Prms, a considerably high Prms is detected at $x/\delta_o \approx 10.89$ in comparison to the other locations. This rise could be particularly due to the fact that these locations lie in the vicinity of the corner shock foot. Again for the side-wall and corner, unlike the other regions, a sharp rise and fall in the rms value is not observed as compared to the centerline and vortex. The peaks occur at Port 12 ($\bar{P}_{rms}/\bar{P}_\infty \approx 0.14$) and Port 14 ($\bar{P}_{rms}/\bar{P}_\infty \approx 0.09$). All these observations further strengthen the argument that the SWBLI is 3D with the separation bubble extending to a limited distance from the centerline on both sides.

Spectral analysis

Figures 3.7 – 3.10 show the PSDs of pressure traces at centerline, vortex, corner, and side-wall locations. Data was collected for a period of 10 s and filtered using a 6-pole low pass (LP6P) pulse filter setting with a cut-off frequency of 50 kHz. As seen in Fig. 3.6, this mode has little overshoot (fig. 3.6(a)) and a sharper roll-off slope (fig. 3.6(b)). It was desirable to set the sampling frequency to as high a value as possible to ensure the capturing of pressure fluctuations across a broad frequency range. Since the maximum cut-off (sampling frequency) frequency recommended by Kulite for both the transducers was 50 kHz, this sampling frequency was chosen for all the experiments. In all the figures, PSD is plotted on the y-axis and has been normalized by the square of the mean Prms of the ‘Upstream Port’ for all the locations. The frequency is plotted on the x-axis on a semi-log scale. The PSD values were fit with polynomials of different orders on MATLAB to identify the peaks for the frequencies in the Nyquist range. While the polynomials of low order did not capture the easily seen peaks on the PSD plots, those of high order overlapped the PSD plots. Hence, a polynomial fit of 25th order for each PSD curve was adopted as it helped in reasonably identifying the peaks. Further, Fig. 3.1, which was used to identify the flow separation and reattachment points, was again used to help explaining the spectral characteristics

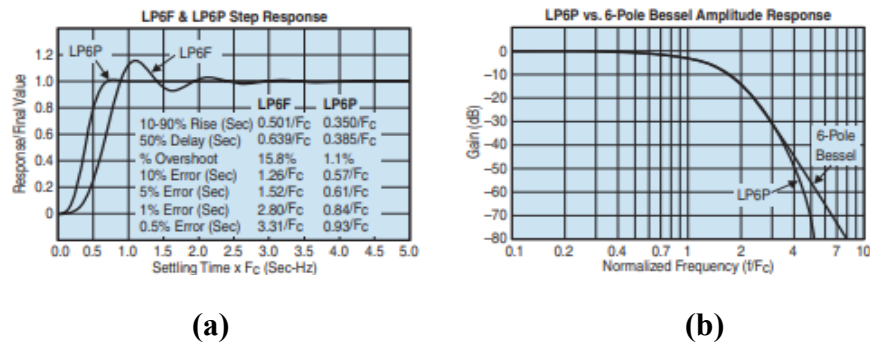


Figure 3.6. LP6P pulse mode low-pass filter response

of different regions of the flow. The difference in the power content of the flow structures is also clearly observed.

Signal processing procedure

To process the pressure signal (which is in the form of voltage) from any transducer, the pressure signals were processed using the ‘*fft*’ function in MATLAB. This function determines the double-sided discrete fast fourier transform using the equation shown below:

$$Y(k) = \sum_{j=1}^n X(j)W_n^{(j-1)(k-1)} \quad 3.4$$

The MATLAB code to determine the PSD is available in the Appendix-IV. Key parameters that resulted in the final PSDs are as follows:

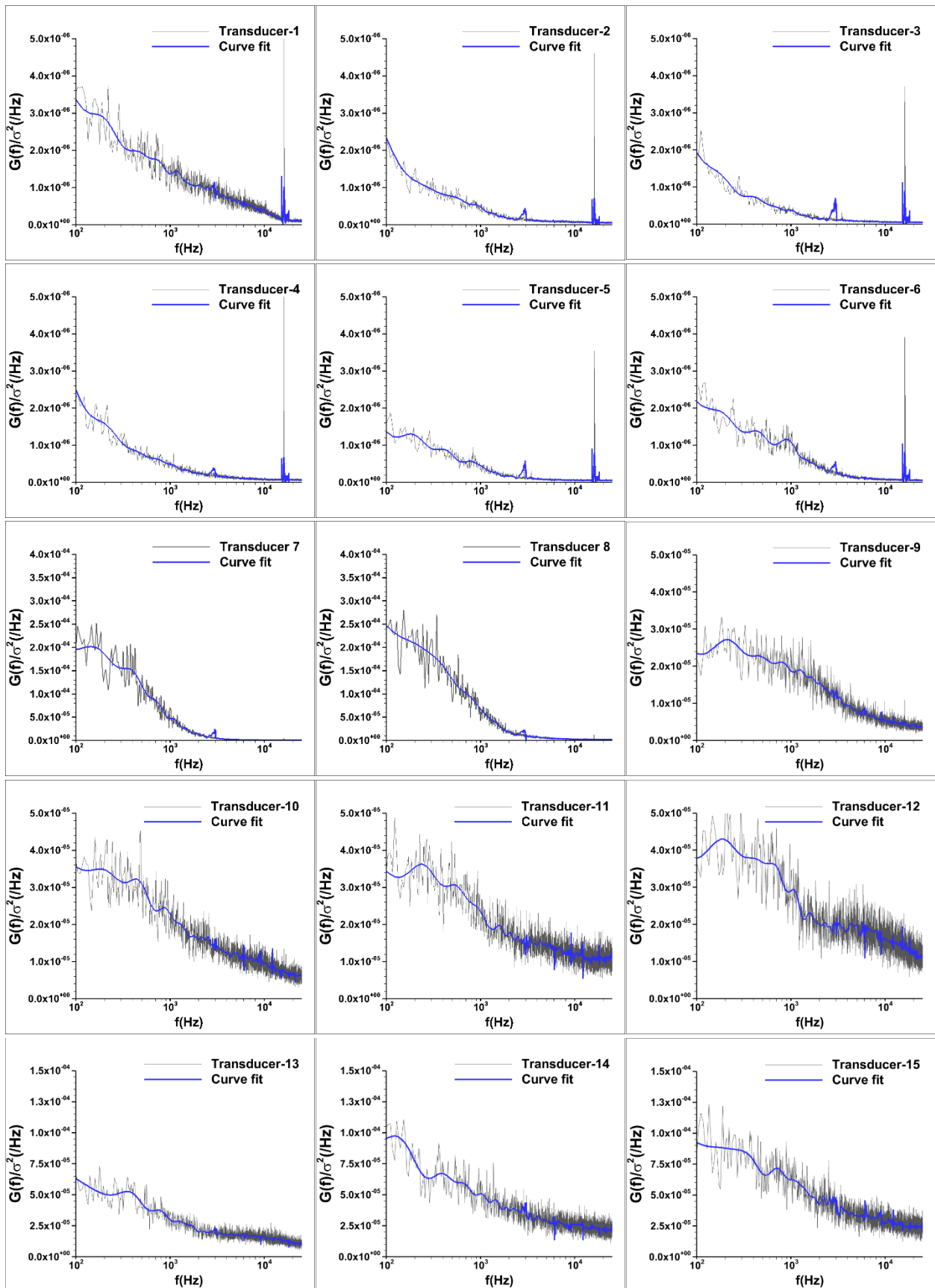
- (a) The signal was first converted into the corresponding pressure (psia) using the following

$$\text{equation } P_{abs} = \frac{V}{(X)(Y)(S)} + 14.7$$

- (b) The mean of the signal was calculated and subtracted from the original signal.
- (c) The transfer coefficients of a 7th order High-pass Butterworth filter with a cut-off frequency of 100 Hz were calculated.
- (d) The signal was further passed through *filtfilt* function using the coefficients calculated in Step in order to remove phase distortion, minimize start up and ending transients and match initial conditions.
- (e) No segment overlap was assigned.
- (f) A block size of $B1 = 8932$ was chosen; a step size was calculated as the product of the block size and difference of ‘1-Overlap’. This was assigned a *Hann* window.
- (g) A new input length that is the next power of 2 from the original signal length was identified in order to pad the signal with trailing zeros to improve the performance of *fft*. This was assigned to a variable *NP1*.
- (h) Variables $N1 = \text{round}\left(\frac{NP1}{B1}\right)$ and $\text{Step1} = \text{round}(B1)$ were calculated

- (i) An array named *Blocks1* of size $N1 \times B1$ was generated where in pressure signal values were collected into $N1$ columns and $B1$ such rows were formed. Every element of the array of then multiplied with the *Hann* window value
- (j) The fft of the array *Blocks1* was calculated which resulted in a double sided spectrum. This was converted into PSD values by the equation $1/(f_s)(B1)(Z)$ and was stored in array *P2*. Half of the values from *P2* were doubled and were stored onto array *P1*.
- (k) The fft values of every frequency in *P1* were then summed up, divided by $N1$ (64) to obtain the final PSD array *Av*.
- (l) The frequency array was formed by the equation $frequency = f_s (0:\frac{B1}{2})/B1$

Figure 3.7 shows the power spectral density (PSD) of the pressure traces at centerline. The orders of PSDs of transducers 1-6, 7 and 8, 9-12, and 13-19 are 10^{-6} , 10^{-4} , 10^{-5} , and 10^{-4} . Transducers 1-4 do not exhibit any low frequency activity, which is as expected for the incoming boundary layer. However, transducers 5-16 show several broad peaks between 100-1500 Hz. Transducers 5 and 6 marginally detect the shock motions as their power content is still of the same order as the incoming boundary layer. However, transducers 7 and 8 whose power content is two orders of magnitude higher than the upstream transducers appear to truly capture the low frequency oscillations of the separated shock-wave. Further downstream, the power content of transducers 9-13 is in between the incoming boundary layer and the separated shock. These ports are located underneath the separation bubble. Transducers 14 and 15 again exhibit a power content similar to the separated shock motion. These locations correspond to the reattachment region. The good agreement between the centerline SWBLI and a nominally 2D SWBLI result further indicates that the shock unsteadiness remains unaffected by the corner separation.



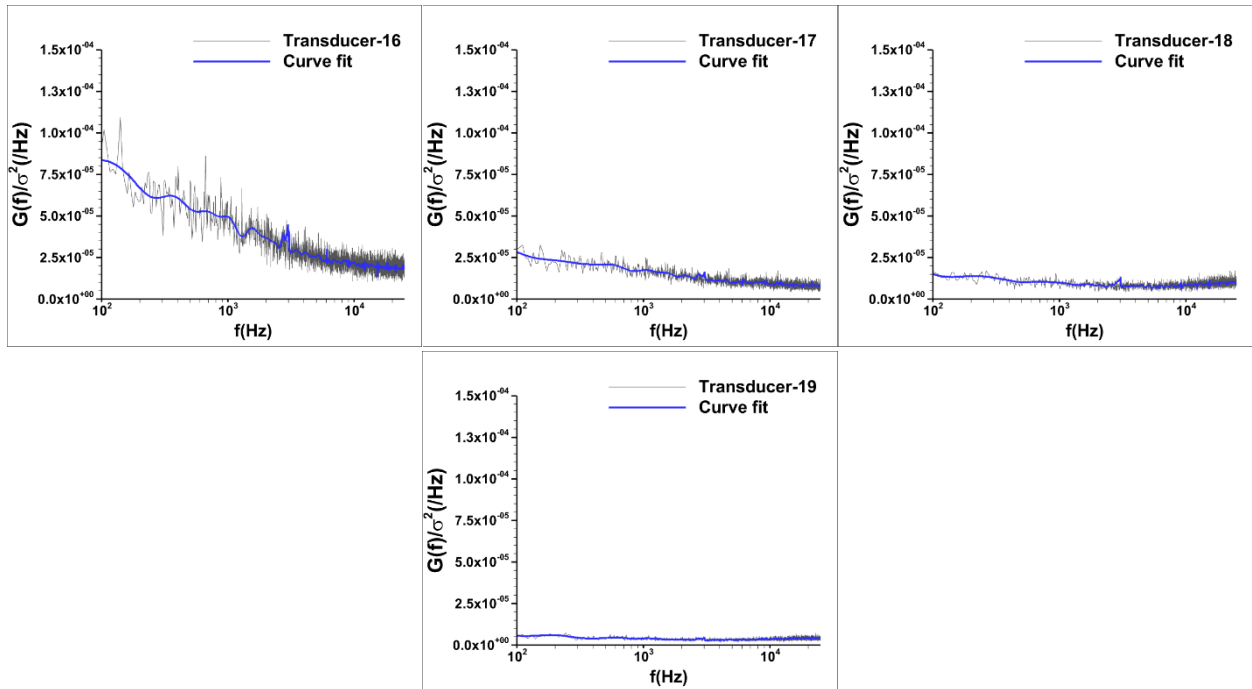
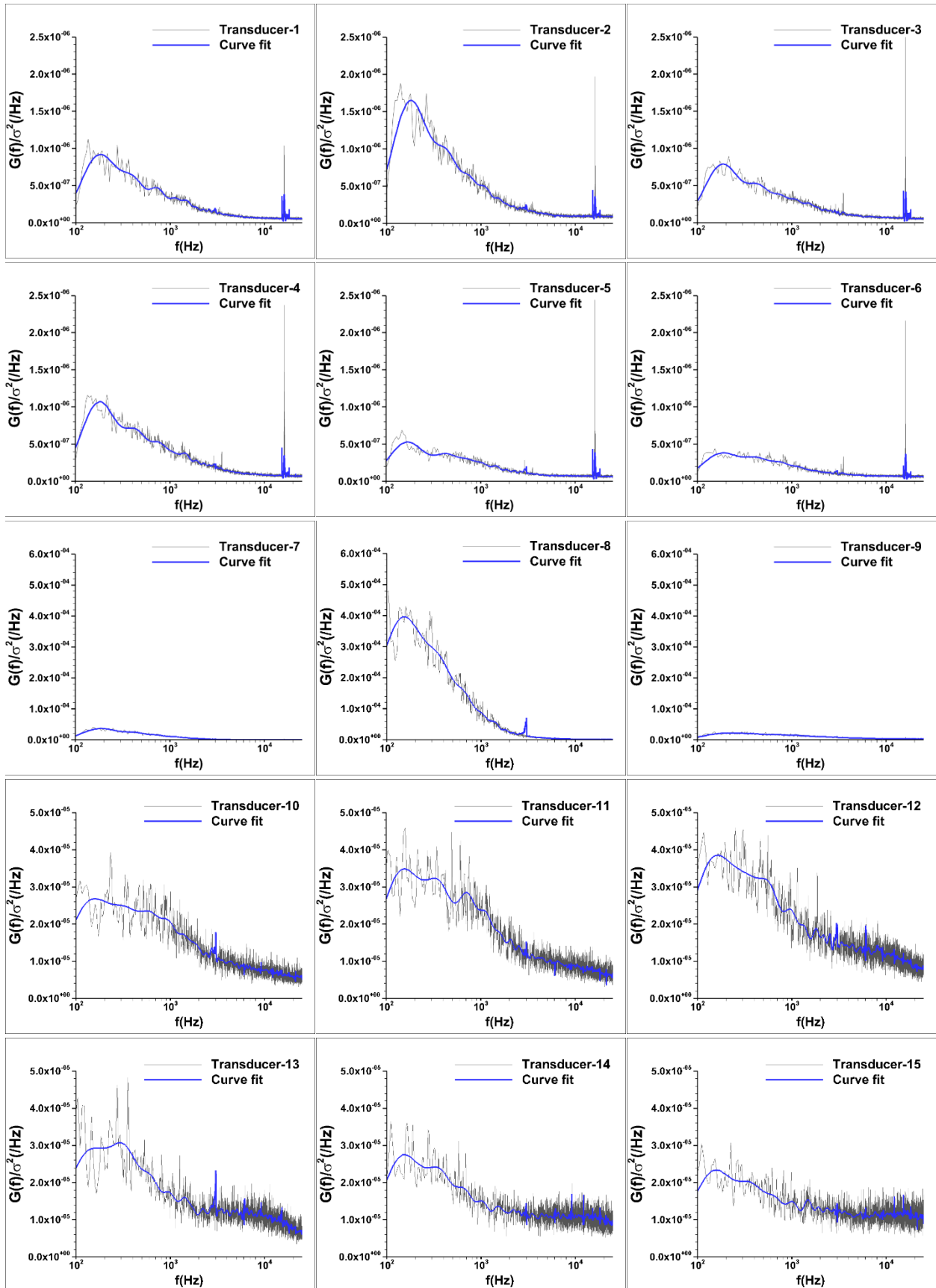


Figure 3.7. Power spectral density-centerline

Figure 3.8 shows the power spectral density (PSD) of the pressure traces at the vortex. The orders of PSDs of transducers 1-6, 7-9, and 10-20 are 10^{-6} , 10^{-4} , and 10^{-5} respectively. Given that their power content is significantly low, it can be assumed that transducers 1-7 are under the incoming boundary layer. Transducer 8 shows broad peaks of short frequency bands. It has a PSD that is a couple of orders of magnitude larger than those of the upstream transducers as it is closest to the flow separation line. Transducers 9-12 have a broad peak that covers the frequency range of 150-600 Hz. However, the energy content of this band is again very small in comparison with that of transducer 8. As these transducers are located underneath the vortex (fig 3.3(a)), this band could be associated with it. Transducers 13 and 14 could be in the vicinity of flow reattachment that leads them to have similar PSD as transducer 8. Although transducers 15-17 show a decaying PSD, transducers 18-20 again show peaks of low frequencies, especially in 200-600 Hz. These concentrated ranges could be frequencies being picked up as the flow meets the expansion fan from the wedge downstream.



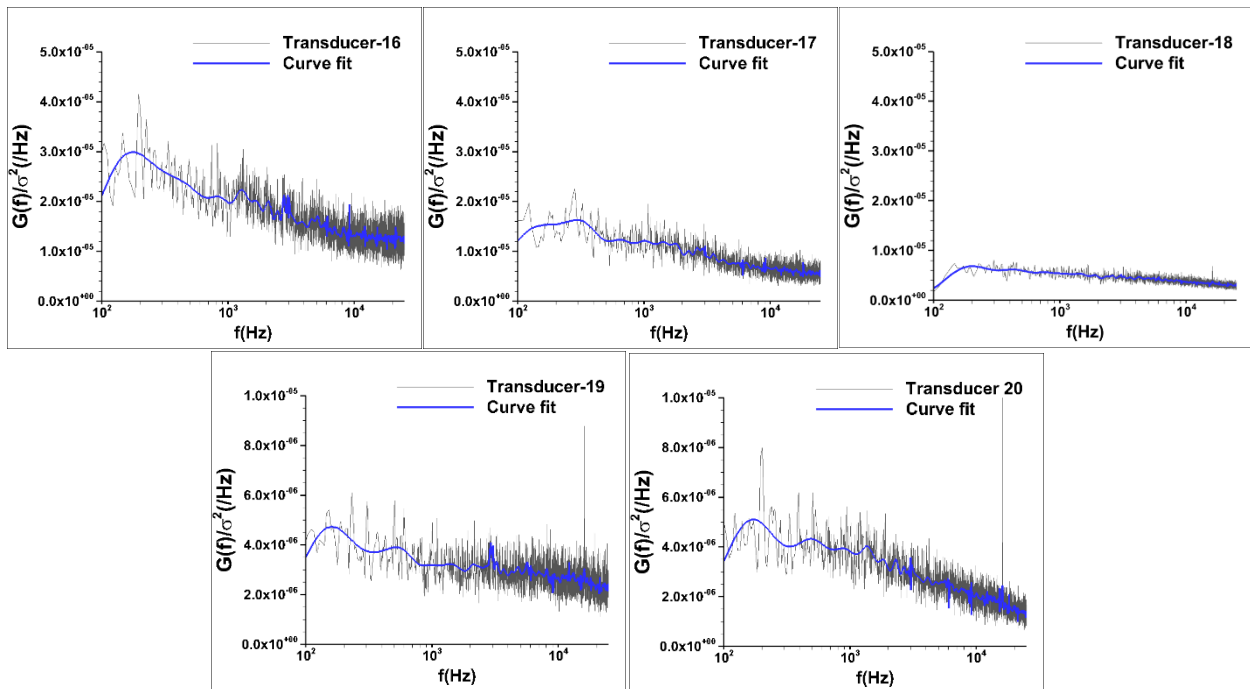
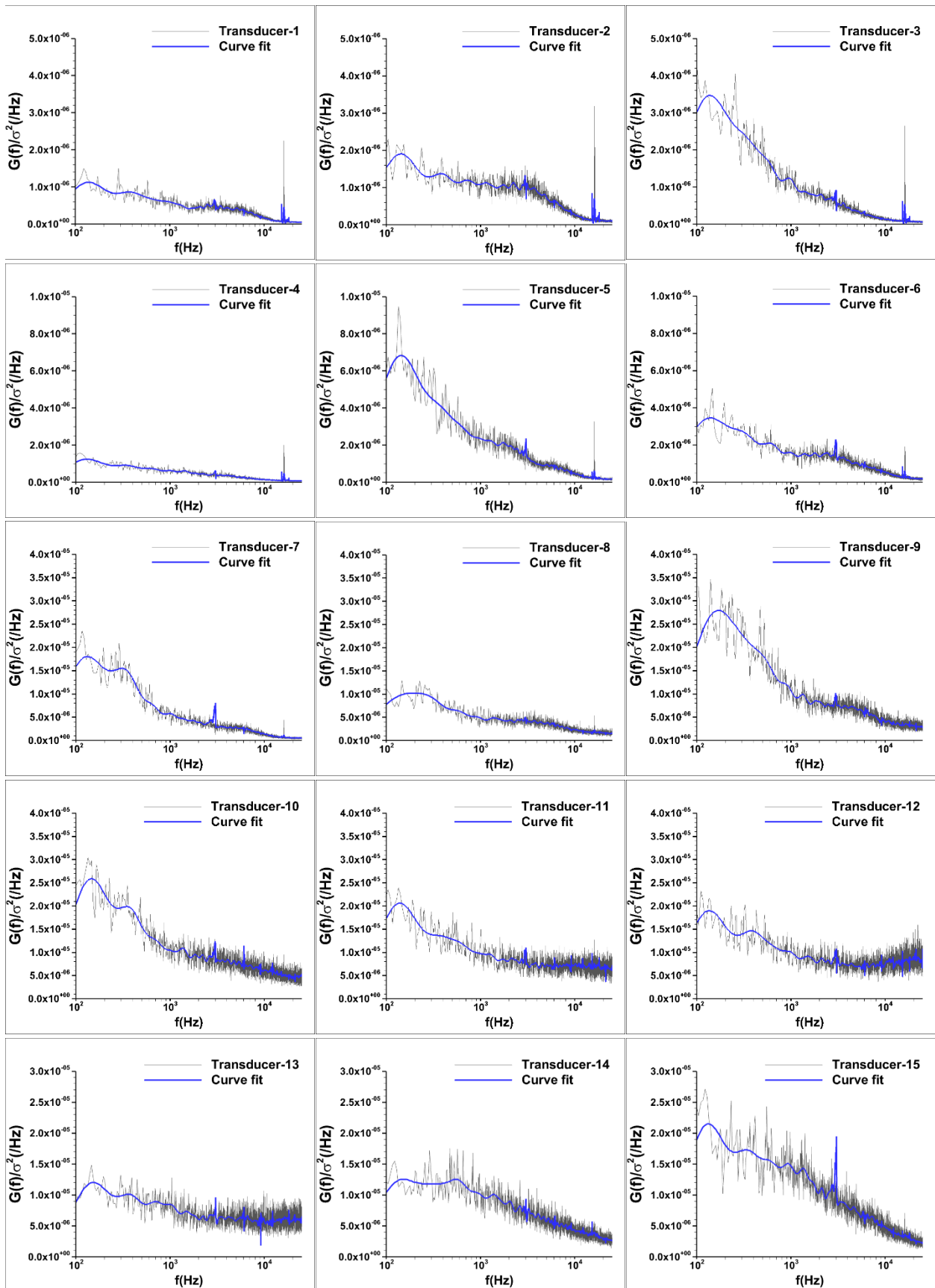


Figure 3.8. Power spectral density - vortex

Figure 3.9 shows the power spectral density (PSD) of the pressure traces at the corner. The orders of PSDs of transducers 1-3 and 4-20 are 10^{-6} and 10^{-5} respectively. Although ports 1 and 2 appear to show peaks for several frequency ranges, these appear to be extraneous jitters, as it can be seen that the PSD of the incoming boundary layer is exhibited even at the downstream location of transducer 5. Hence, transducers 1-5 can be assumed to be underneath the incoming boundary layer. The first indications of low frequency flow oscillations are observed by transducer 6 which would be expected on comparison with fig 3.3 (a), probably due to the swept corner shock. Transducers 6-16 contain several bands of low frequency content. Transducer 17 appears to show a quick decay of spectral content which indicates the recovery of the boundary layer from here onwards. However, transducers 18-20 again indicate low frequency flow oscillations which could be again extraneous as seen in the upstream transducers. It can be observed that unlike their centerline counterparts, the maximum value of power content of PSDs do not change by orders of magnitude at any transducer location and all the PSDs have a comparatively low value of power

content for all the frequencies. This indicates that overall the spectral content of flow unsteadiness at the corner is lower than that at the centerline.



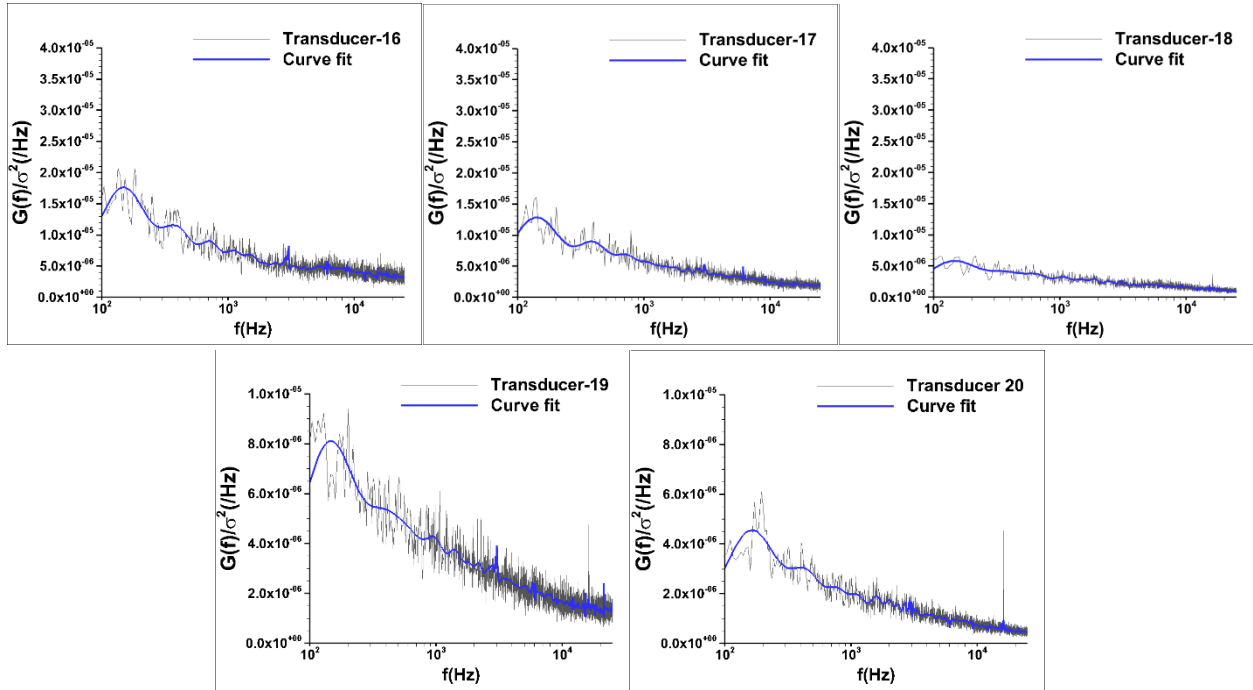


Figure 3.9. Power spectral density-corner

Figure 3.10 shows the power spectral density (PSD) of the pressure traces on the side wall. The orders of PSDs of transducers 1-6 and 7-12 are 10^{-6} and 10^{-4} respectively. From Fig. 3.3 (b), transducers 1-4 are upstream of the shock-wave. However, all these transducers contain energy in the frequency band of $\approx 300 - 1300 \text{ Hz}$. Although, these locations could be experiencing an influence from the corner separation, as discussed in the previous section, the corresponding corner locations do not appear to exhibit the same PSDs. Hence, measurements away from the wall could throw more light on the factors behind this behavior. The PSDs between transducers 5-12 are similar in appearance, with a couple of peaks for frequency bands of $300 - 500 \text{ Hz}$ and $600 - 900 \text{ Hz}$. Amongst them, $300 - 500 \text{ Hz}$ appears in all the above locations and has similar low energy content. A reason behind the low energy content could be that, the adverse pressure gradient effects of the glancing shock on the side-wall induces relatively lesser perturbations in the side-wall boundary layer in comparison to the top wall centerline.

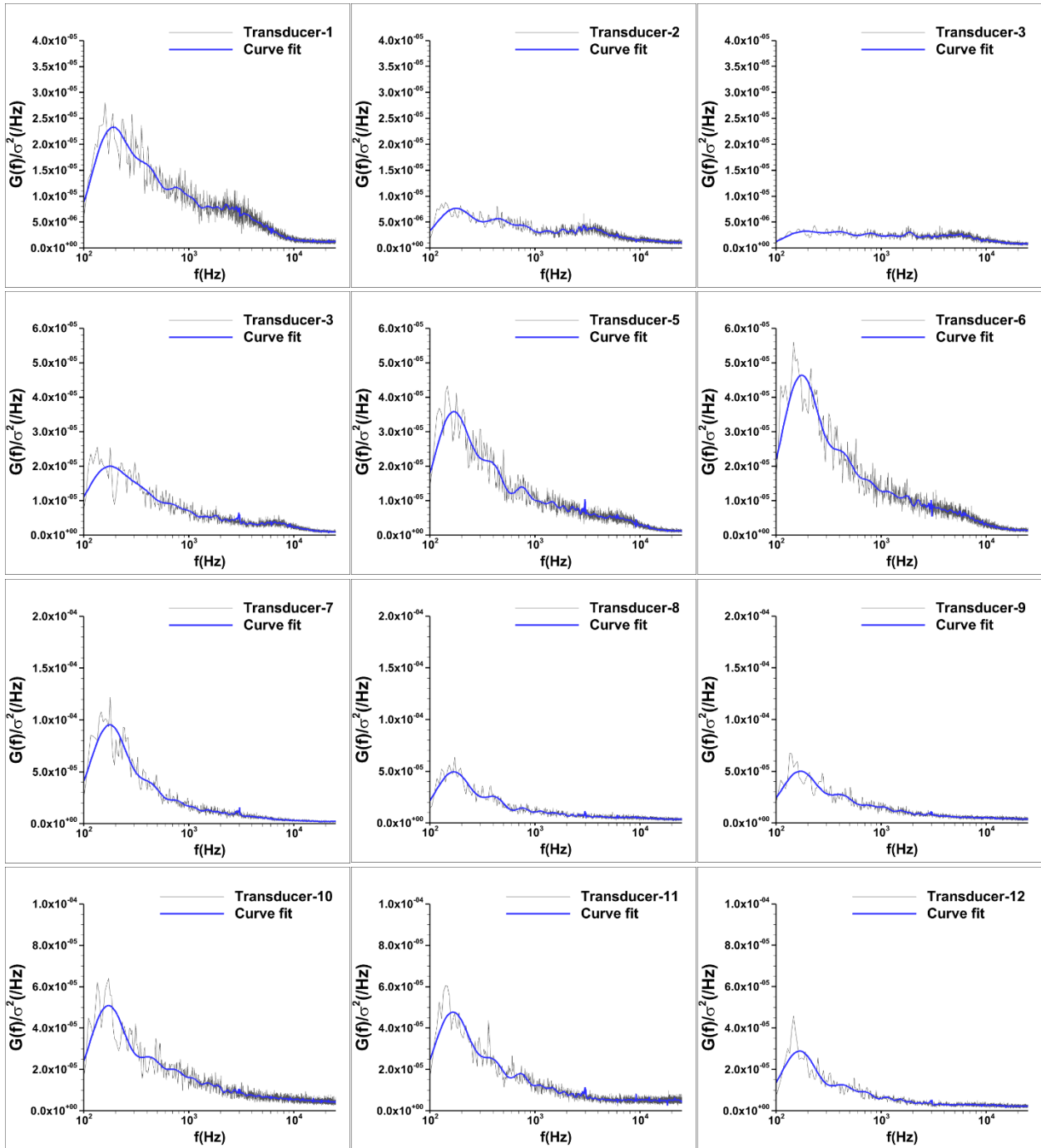


Figure 3.10. Power spectral density- side-wall

Computational Results (Unsteady Simulation)

Figure 3.11 shows a snapshot of the Mach number contours from the unsteady simulation of IOSWBLI under consideration. It can be observed that key flow features are predicted well by

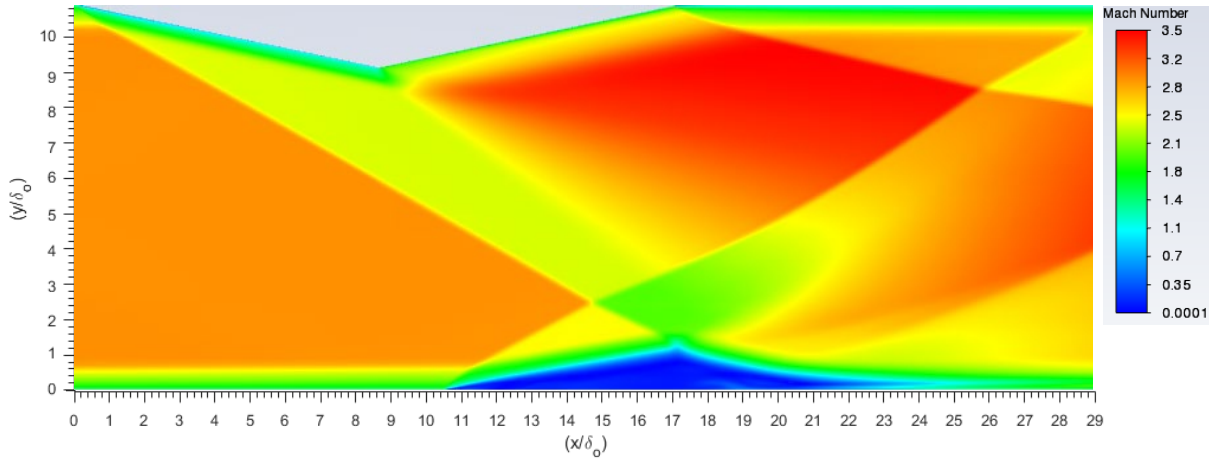


Figure 3.11. Mach number contour (unsteady simulation)

the simulation. However, it must be noted that as the simulation is unsteady, these features oscillate spatially in a periodical/apperiodical manner with progression in time. This kind of flow organization manifests at the mid-span of the wind tunnel test section. The boundary of the wedge again extends on the upper wall between $x/\delta_0 \approx 0$ to $x/\delta_0 \approx 17$. The change in the Mach number indicated by the change in color, on progressing in the downstream direction is the evidence of the formation of oblique shock-wave at the leading edge of the wedge, which decelerates the flow (green color) and expansion fan that forms at the apex of the wedge, which again accelerates the flow (red color). The separation bubble on the bottom wall is bound upstream at $x/\delta_0 \approx 10.6$ on the lower wall in the figure. However, it was found to execute a flapping motion instead of reattaching at a downstream location. This is a key observation made in literature. This simulation was advantageous because it not only allowed to analyze the static pressure on the bottom wall but anywhere in the flow-field which is difficult to realize experimentally.

Pressure rise

Data points were created at locations similar to those of the centerline transducers in the experiments. This is illustrated in Fig. 3.12. Figure 3.13 shows the pressure rise at these data

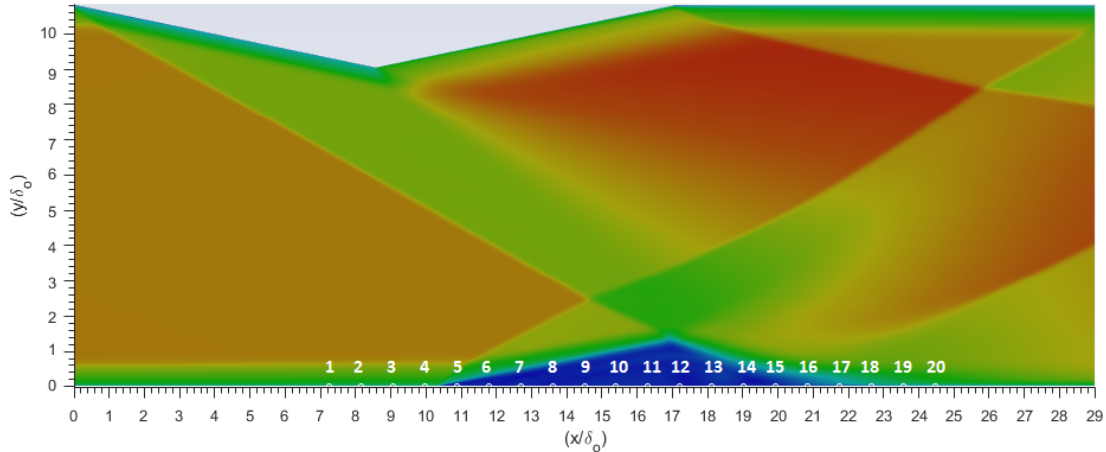


Figure 3.12. Pressure data points on the wall

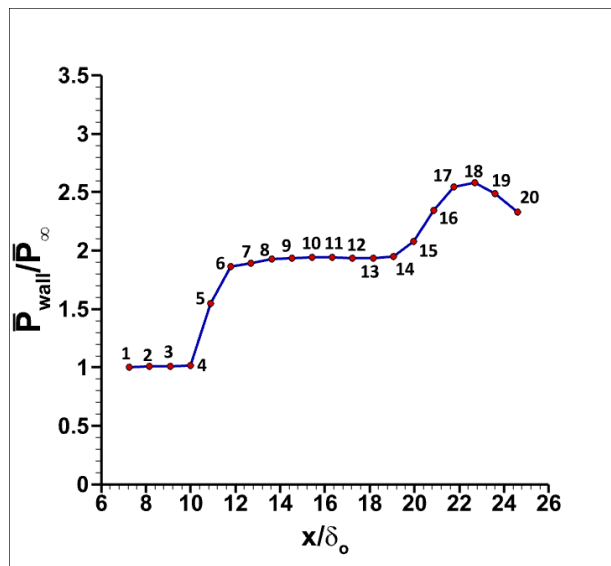


Figure 3.13. Pressure rise - bottom wall

points. All the mean pressure values have been normalized by the mean pressure value at Port-1 which is denoted as free-stream pressure. The pressure rise is initially detected at Port-4. This increases to a value of $\bar{P}_{wall}/\bar{P}_{\infty} \approx 1.9$ at Port-6. However, the rise in pressure is not as sharp as observed in the steady simulation but is gradual over a distance of $x/\delta_0 \approx 2$ between Ports 4-6.

This is expected as it appears to be the region of unsteady shock motion. Past Port-6, the pressure rise plateaus and the pressure remains fairly constant up to Port 14. Ports 6-14 are clearly seen to be under the separation bubble and hence exhibit this behavior. The pressure again rises between Ports 14-18 up to $\bar{P}_{wall}/\bar{P}_{\infty} \approx 2.5$. As these ports lie in the reattachment region, the pressure rise is expected with the flow sensing a second adverse pressure gradient. This value is considerably lower than the maximum pressure rise observed at the centerline in the experiments. The pressure falls between Ports 18-20. This could be the region affected by the expansion fan from the apex of the wedge.

Pressure fluctuations

Figure 3.14 shows the mean rms of the pressure values at the Ports. These values are again normalized by the free stream mean wall static pressure measured at Port-1. The curve generally follows the same trend as the corresponding experimental P_{rms} values. However, these values are significantly higher than the corresponding experimental P_{rms} values. It is observed that the rms value reaches two maxima, first at Port-5 ($\bar{P}_{rms}/\bar{P}_{\infty} \approx 1.3$) and second at Port-17 ($\bar{P}_{rms}/\bar{P}_{\infty} \approx 1$). As concluded from Fig. 3.13, Port-5 lies in the region of unsteady shock motion. Hence, this strongly appears to be the reason for it to exhibit the highest P_{rms} . From Fig. 3.13, it is also observed that Port-17 is in the region of reattachment and hence, this would be the cause for a P_{rms} higher than those of its neighboring ports.

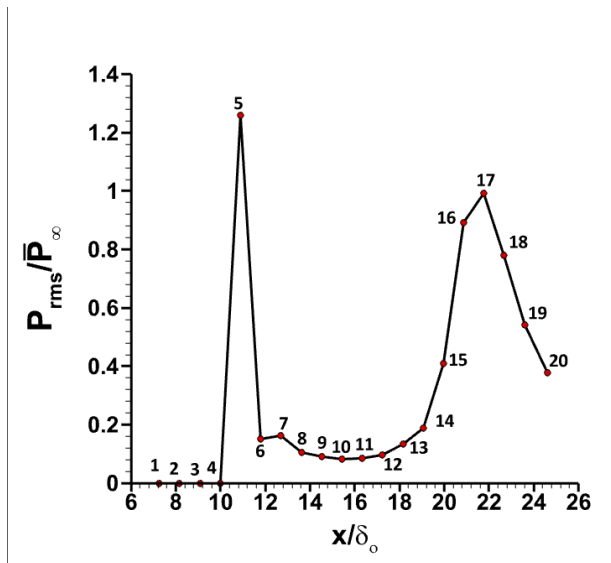
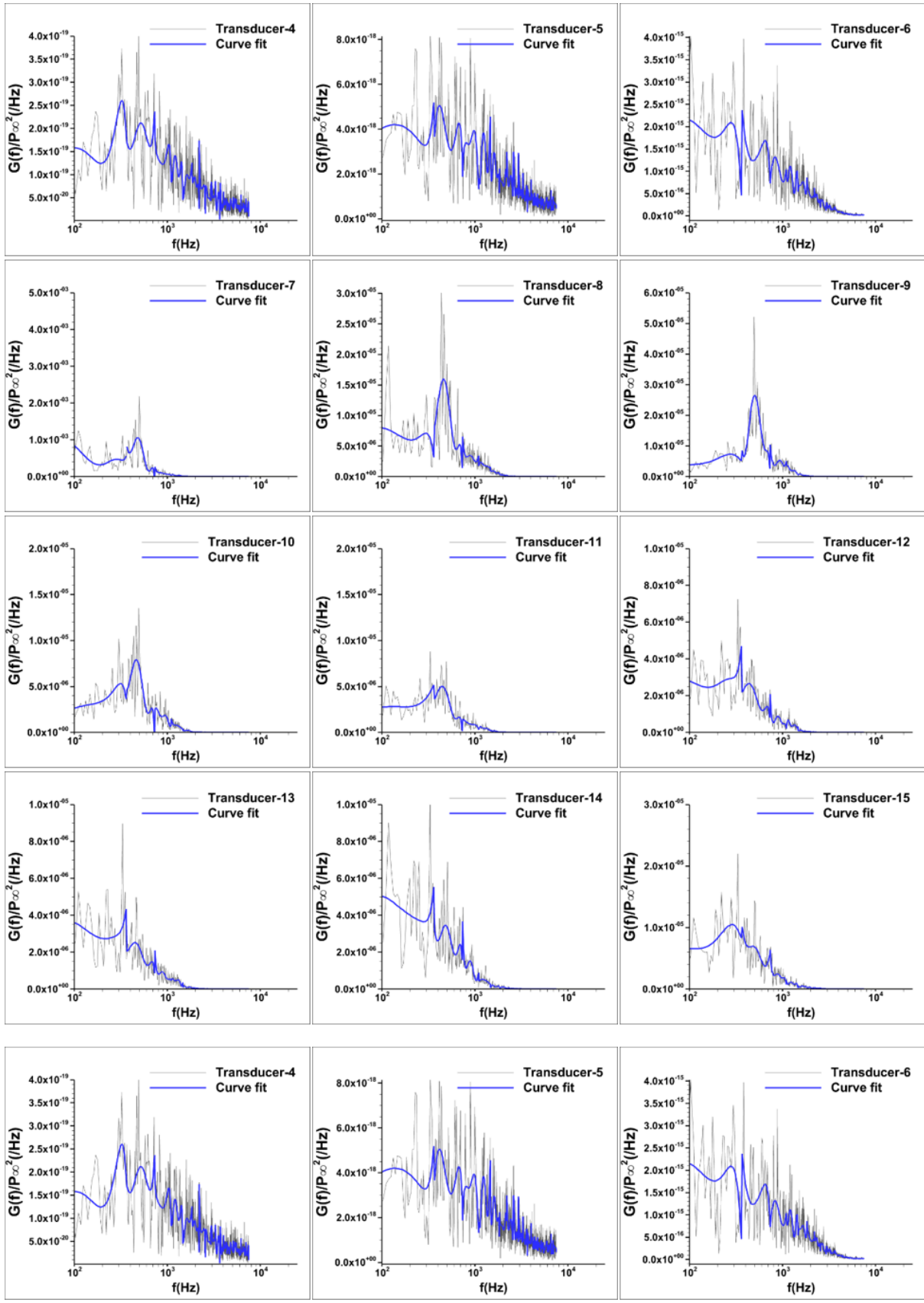


Figure 3.14. Data points Prms

Spectral analysis of wall pressure measurements

Figure 3.15 shows the PSDs of the pressure traces on the wall. These locations are analogous to the ones on the centerline in the experiments. All the PSDs were normalized by the mean wall static pressure of the undisturbed incoming boundary layer which was assumed to equal to the free stream static pressure. It should be noted that the order of the magnitude of the PSDs is different from PSDs of the centerline. A polynomial curve of 5th order was fit onto each PSD curve in order to identify the peaks for the frequencies in the Nyquist range. PSDs of transducer-4 onwards is shown as the order of the PSDs of locations upstream of it was very low which made it difficult to represent them. At transducer 7, the effects of the separation shock-wave are initially detected with the presence of a peak of a narrow band of frequency $\approx 300 - 400 \text{ Hz}$. This peak is present between transducers 7-11 and is then replaced by a sharp peak $\approx 200 \text{ Hz}$ between transducers 12-14. Between transducers 15-16, this peak spreads around 200 Hz. From transducer 17 onwards, it again moves downstream to $\approx 400 \text{ Hz}$. Hence, it can be concluded that the DDES model under consideration, predicts low frequency oscillations under separation shock and bubble and reattachment regions.



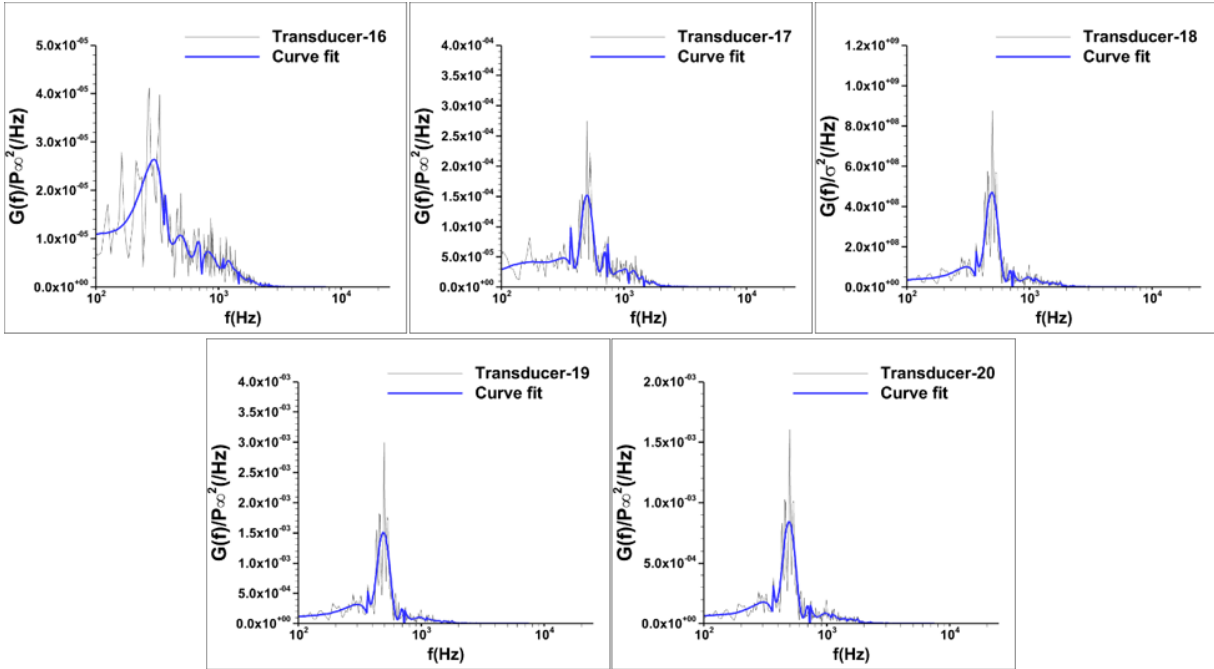


Figure 3.15. Power spectral density (unsteady simulation)

Flow field spectral analysis

As mentioned earlier, simulation provides the opportunity to analyze data in the flowfield in addition to the surface, which is difficult with the experimental approach as probes disturb the flowfield resulting in erroneous measurements. This opportunity was made use of by laying a set of 41 points of interest in the flowfield. Figure 3.16 shows these points overlaid on the Mach number contours. These points have been named in a manner such that it is a combination of a number (corresponding stream-wise location on the wall) and a letter (named progressively in the wall normal direction; distance between two successive letters being $x/\delta_o = 0.907$). The only exception is Port 9_1j which does not have a corresponding port on the wall and is at $x/\delta_o = 0.226$ from Port-9. The objective of selecting these locations was to understand the spectral characteristics at different locations in the flow structures.

Figure 3.17 shows the PSDs of the pressure traces on the selected points in the flow-field. They were calculated in the same manner as those calculated for the floor. PSDs for ports 9e, 19f, and 20h are not shown as their predicted values were negligible. Ports 6c, 7b, 8b, 13d, 14c, 14e, 14q, 15d, 15k, 16a, 16c, 16f, 16u, 17a, 17c, 18c, 18n, 20a, and 20b exhibit a sharp peak at 500 Hz. Port 10b, 11d, 11f, 12i, 12n, 13f, 13i, 14j, and 16l exhibit a broad peak centered at 100 Hz. Ports 5b, 7f, 8e, 9_1j, 12e, 12b, and 15b exhibit both the broad (centered at 100 Hz) and sharp (400 Hz) peaks. Ports 7d 9c, and 18a have a broad band frequency peak that extends between 10-1000 Hz. This indicates that the interaction region as a whole is dominated by low frequency unsteadiness.

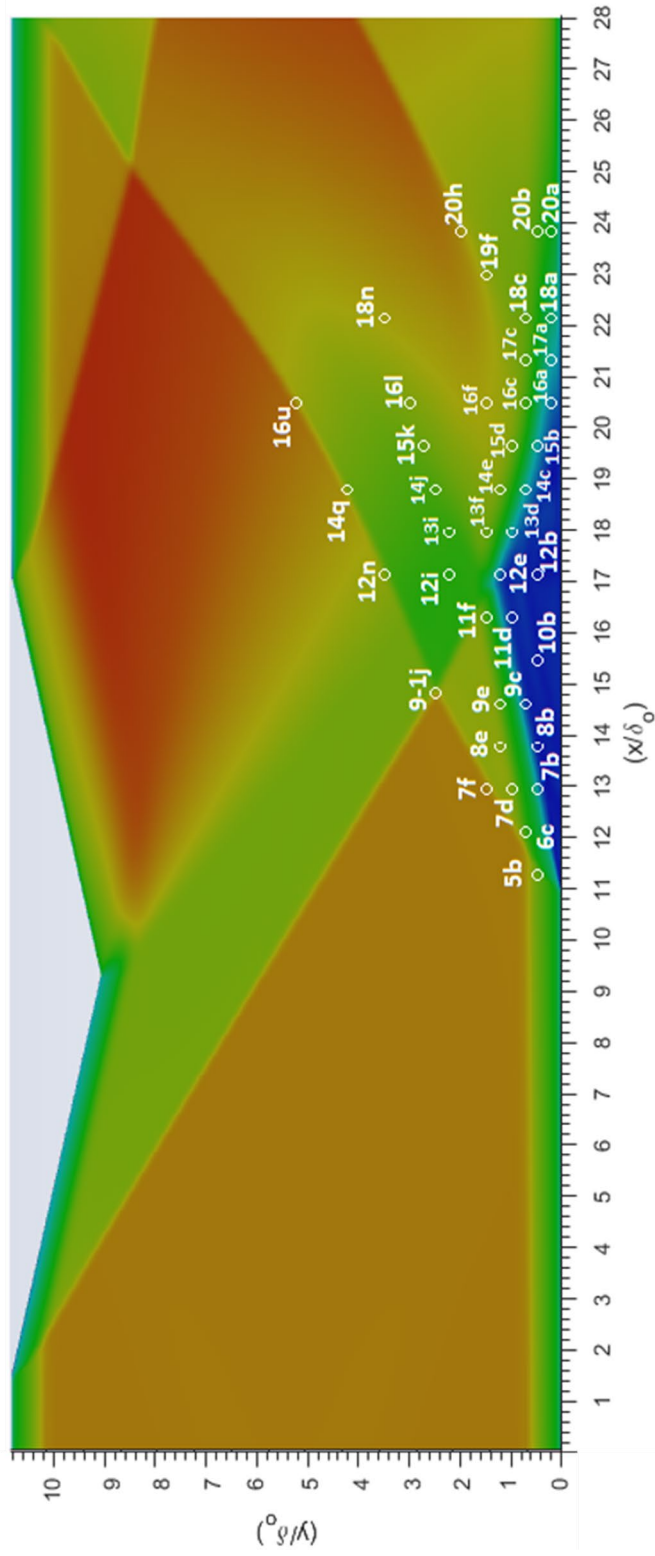
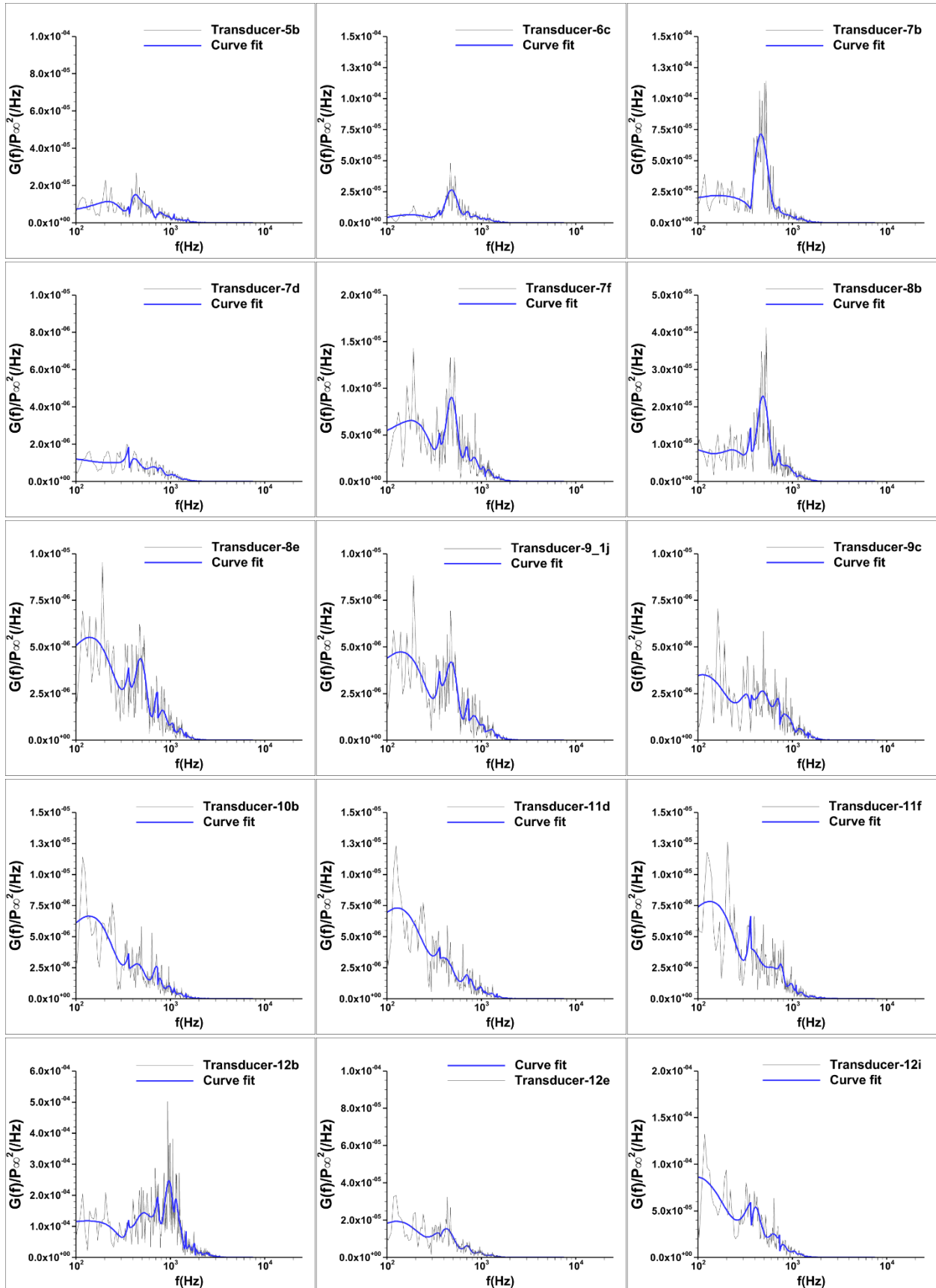
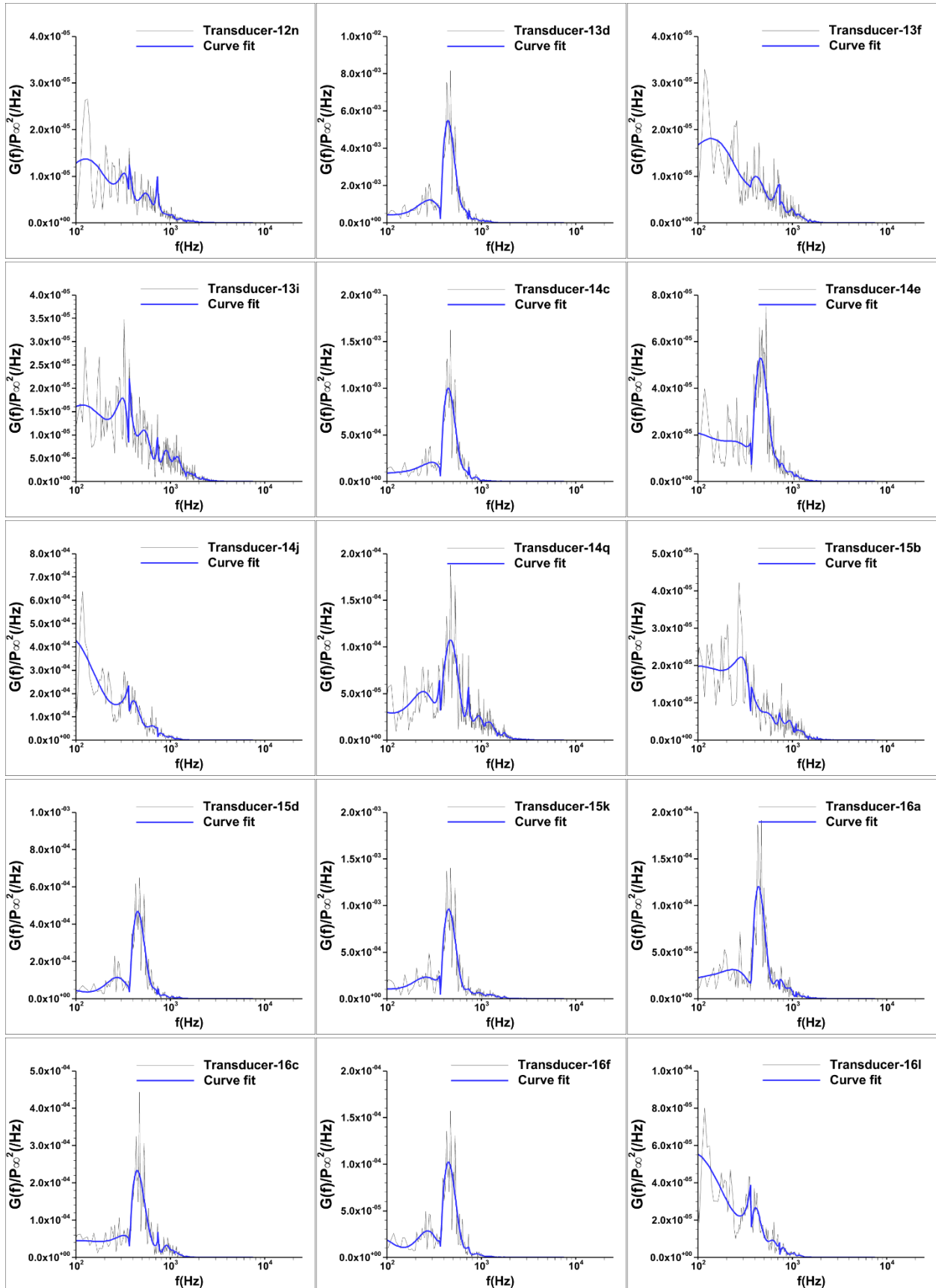


Figure 3.16. Data points in the flow-field





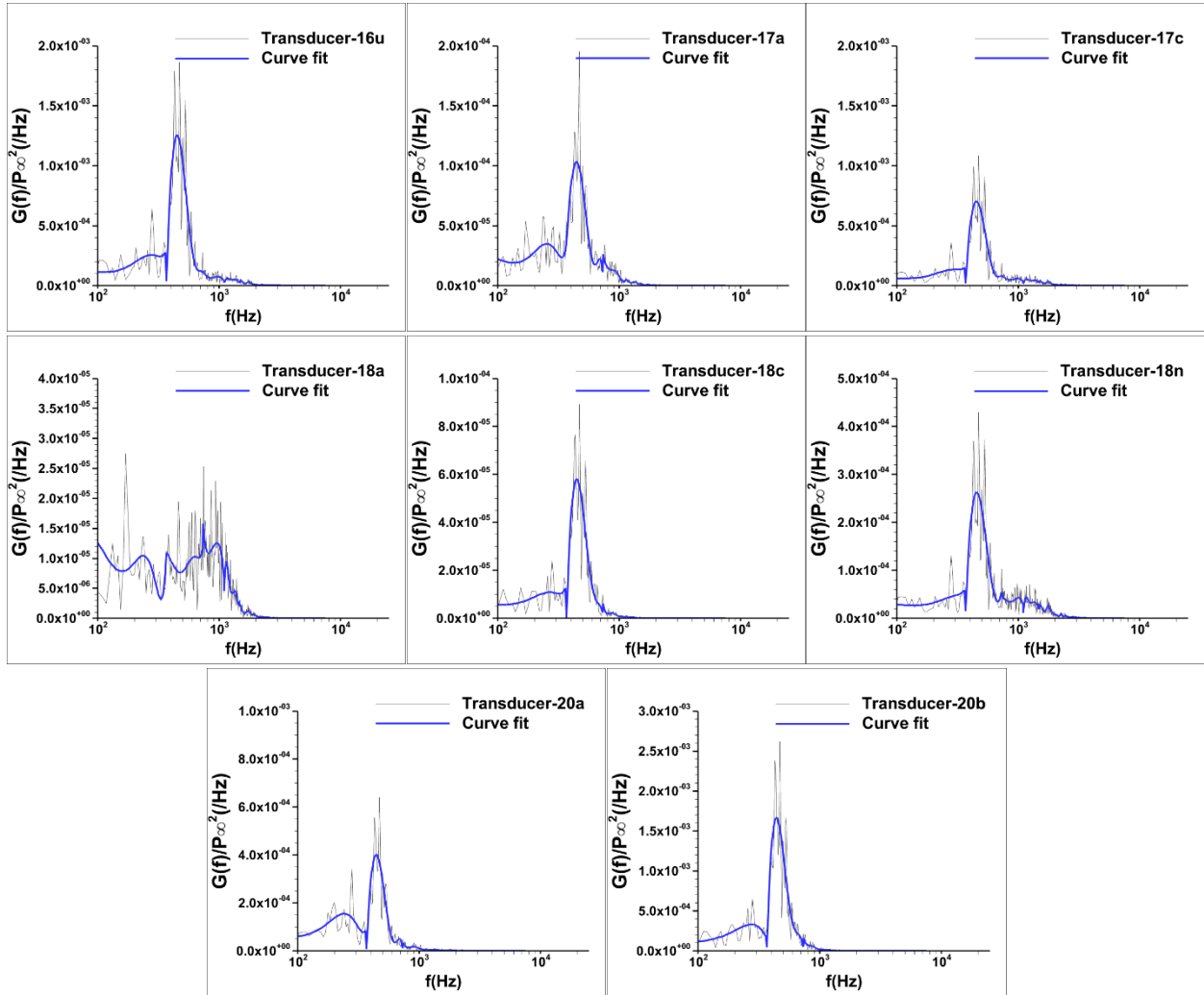


Figure 3.17. Power spectral density of points in the flow field (unsteady simulation)

Computational Results (Steady-State Simulation)

Co-ordinate system & axes normalization

The section of the fluid domain that will be discussed in this section is shown in Fig. 3.18. This domain represents the wind tunnel test section. The domain size is 300 mm x 76.2 mm x 76.2 mm. Also shown in the same figure is the assigned Cartesian co-ordinate system. All the three axes have been normalized by the thickness of the incoming boundary layer ($\delta_0 = 7 \text{ mm}$) measured experimentally at the mid-span of the test section.

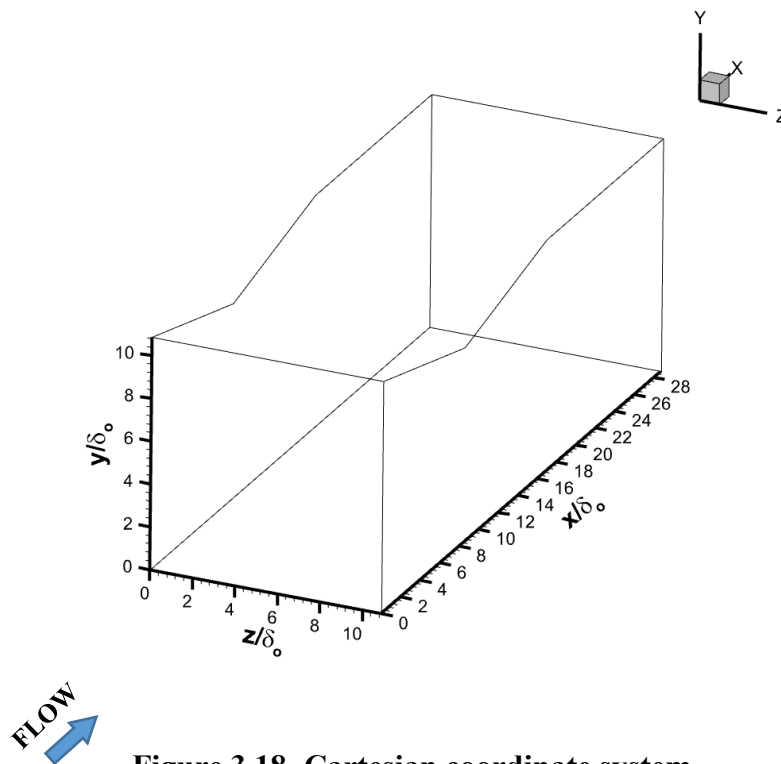


Figure 3.18. Cartesian coordinate system

Grid independence study

A grid independence study was conducted in order to ascertain that the convergence of the solution did not depend on the number of the cells in the domain. In this regard, simulations were run on four grids of different cell count. The incoming boundary layer profiles acquired mid-span

at the entrance of the test section entrance have been compared in Fig. 3.19. The flow at mid-span is assumed to be fairly 2-D.

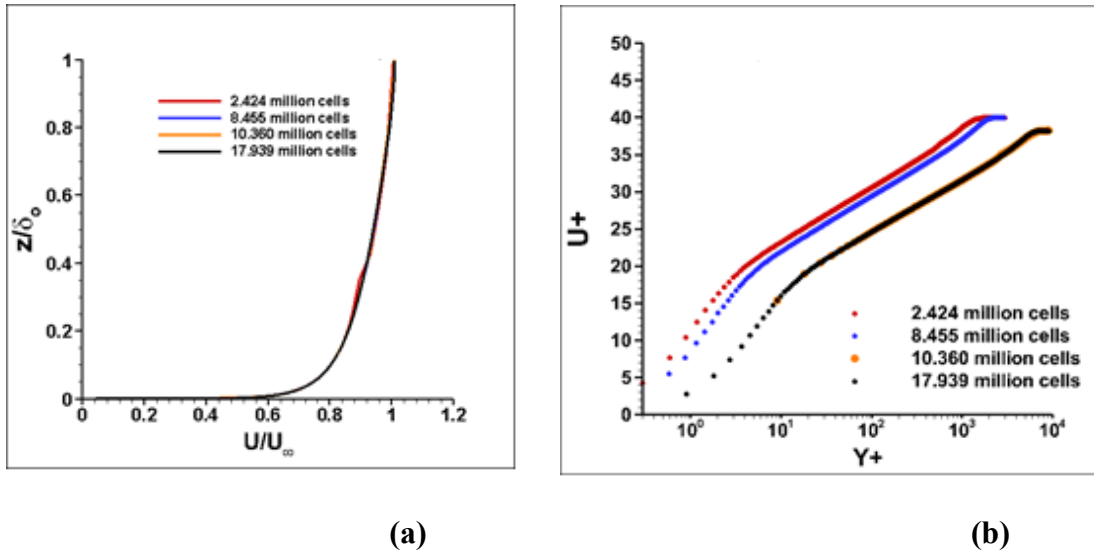


Figure 3.19. Boundary layer profile (a) normalized velocity (b) log-law

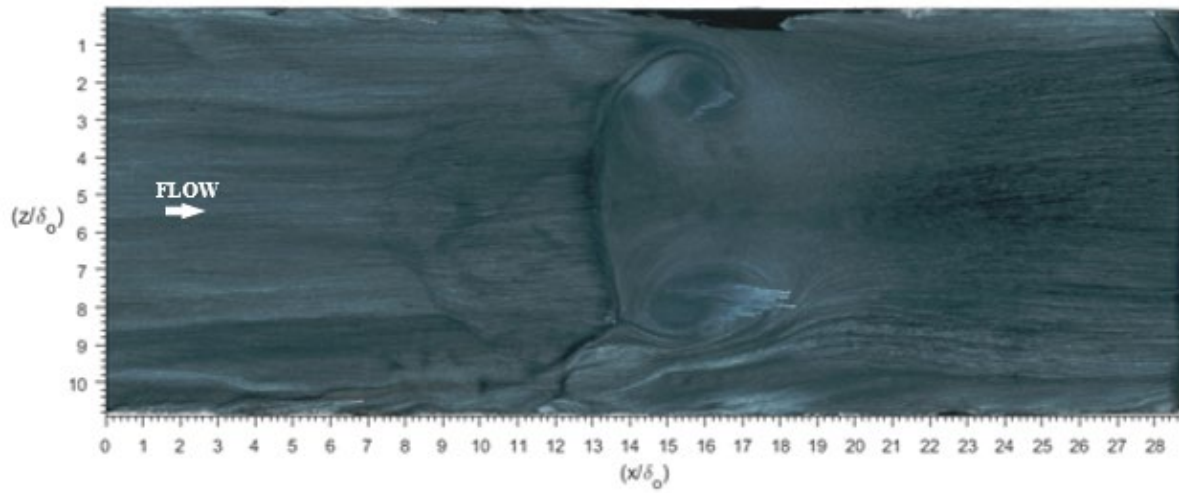
Although the normalized velocity profiles in Fig. 3.19 (a) appear to collapse over each other, the effect of grid refinement is observed clearly in Fig. 3.19 (b). It is seen that as the grid size is increased from 2.42 to 10.36 million cells, the log-law profile of the incoming boundary layer shifts downward in such a manner that the viscous sublayer region can be extrapolated nearer to the origin. On further increasing the grid size to 17.94 million cells, no change is observed in the profile and it collapses over the previous profile. Hence, in this manner, grid convergence of the solution was achieved. The solution obtained with the grid size of 17.94 million cells was used to study the mean-flow field of the SWBLI. The results presented here onwards are for this grid size.

Floor flow visualization

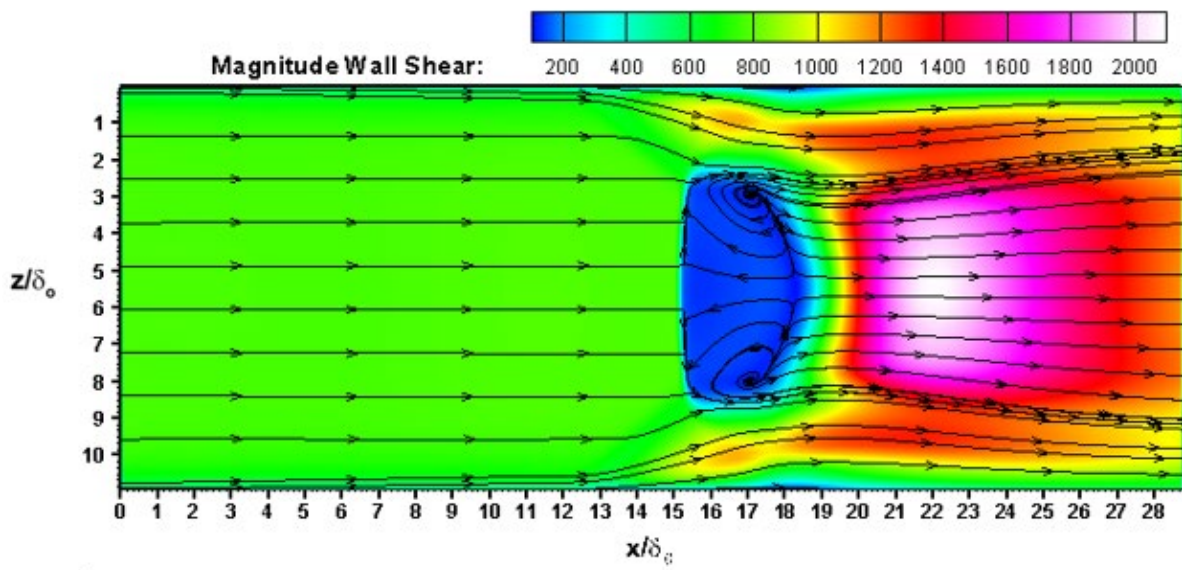
Figure 3.20 compares the experimental and computational floor flow visualizations. Floor flow visualization has been obtained by overlaying the magnitude of shear stress with the limiting streamlines. Similar to the experimental oil flow visualization, for the purpose of illustration, the regions $0 < z/\delta_o < 5.4$ and $5.4 < z/\delta_o < 10.8$ in the computational flow visualization are denoted as lower and upper halves respectively.

In Fig. 3.20 (b), Fluent predicts a primary flow separation boundary at $x/\delta_o \approx 15.2$, marked by a separation saddle point. Similar to the oil flow visualization result, the boundary of separation ceases to extend the complete span, its extent being $2.4 < y/\delta_o < 8.6$. This behavior is again indicative of 3D structure of the SWBLI. The length of separation appears to be $3\delta_o$ and the flow reattaches at $x/\delta_o \approx 18.6$.

Similar to Fig. 3.3(a) oval patterns representing counter-rotating tornado vortices are observed by a couple of foci on opposite sides of the centerline. Their extents are $2.4 < y/\delta_o < 5$; $15.4 < x/\delta_o < 18.4$ and $5.8 < y/\delta_o < 8.6$; $15.4 < x/\delta_o < 18.4$. The corner separation happens at both the walls at $x/\delta_o \approx 12.4$, as the streamlines deviate from the corner.



(a)



(b)

Figure 3.20. Floor flow visualization top-view (a) experimental (b) ANSYS (FLUENT)

Side-wall flow visualization

Figure 3.21 compares the flow visualizations determined experimentally and computationally for the side-wall of the test section. The boundary of the wedge extends on the upper wall between $x/\delta_o \approx 0$ to $x/\delta_o \approx 16.7$ in both the figures.

The Fluent flow visualization captures the key features such as leading and trailing edge shock-waves, and the fluid flow paths near them. Further, Fluent predicts low magnitude of wall shear in these projected paths. However, it does not capture the attachment line seen in the experimental results. A low momentum fluid, which appears to be the corner separation flow, is observed between $x/\delta_o \approx 13$ and $x/\delta_o \approx 21$ near the lower wall in Fig. 3.21(b). An interesting observation that is made is that unlike the mid-span flow separation, the recirculation of fluid is absent in the plane. This corroborates the experimental result regarding the three-dimensionality of the interaction and that the separation bubble is confined to a limited span at the center of the test section

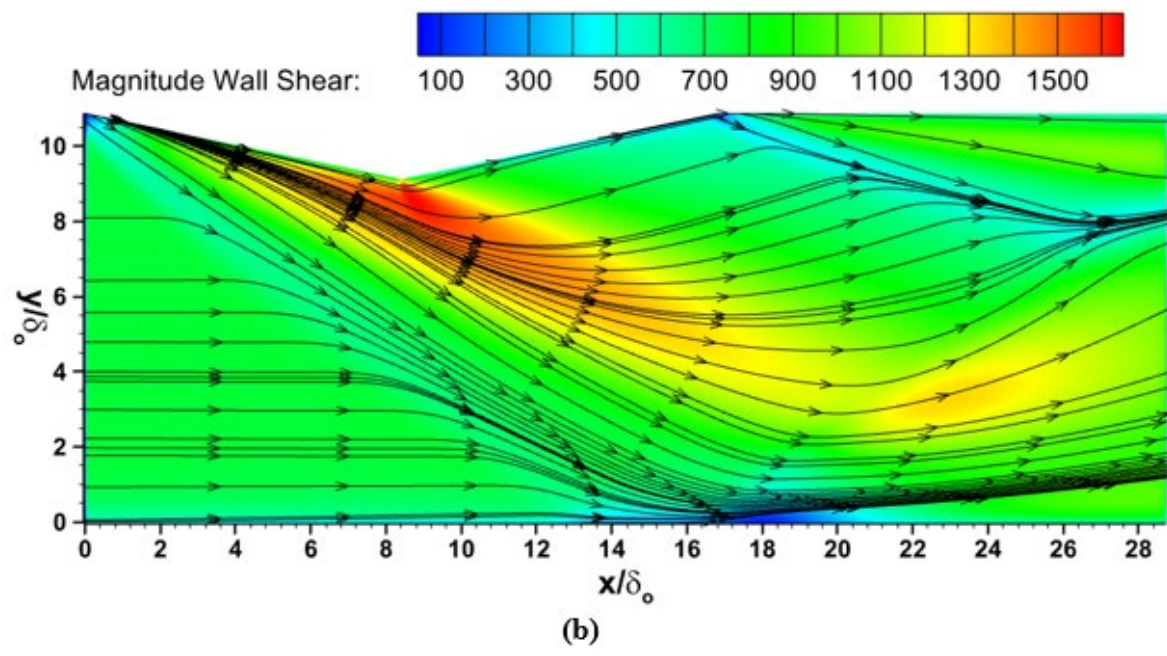
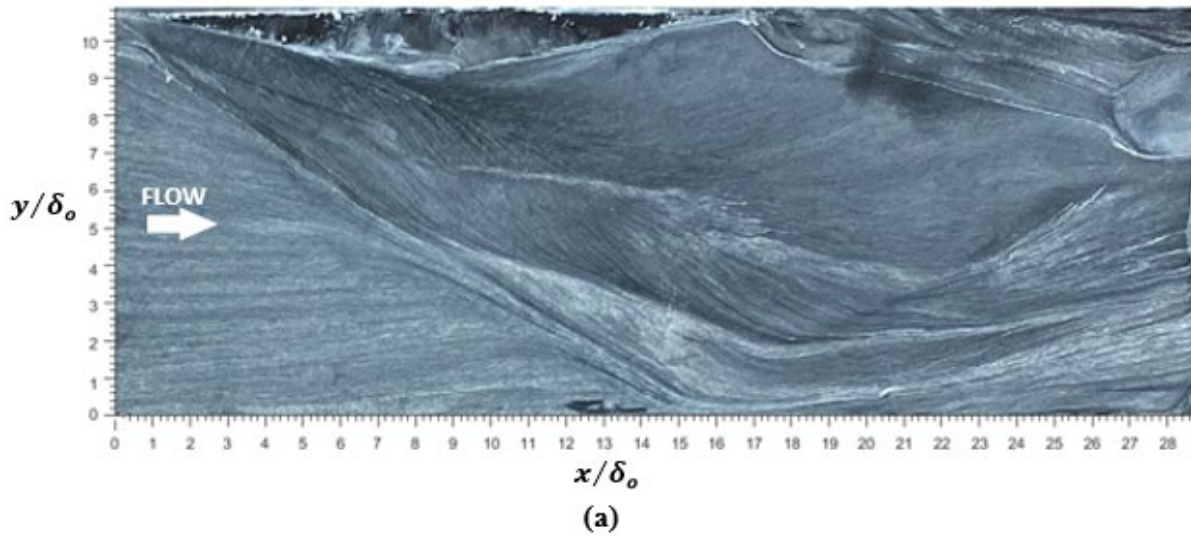


Figure 3.21. Side-wall flow visualization (a) experimental (b) ANSYS (FLUENT)

Discussion of 3D SWBLI interior flow field

A major portion of the following section discusses the flow behavior inside fluid domain. Wherever possible, the discussion has been made with the help of stream-wise (varying x/δ_o), wall-normal (varying y/δ_o) or span-wise centerline, vortex, and corner contour plots. The behavior of various flow parameters in the stream-wise direction have been discussed at $x/\delta_o = 15, 16, 17, 18, 19, 20, 21, 22, 23, 24,$ and 25 and in the wall-normal direction at $y/\delta_o = 0.10, 0.15, 0.20, 0.25, 0.30, 0.40, 0.50$ and 0.75 . For all the parameters studied in the stream-wise, a contour plot at $x/\delta_o = 0$ is shown as a reference and to judge the deviation of the flow behavior.

Span-wise centerline boundary layer evolution

Figure 3.22 shows the evolution of the boundary layer through SWBLI at mid-span. The $x/\delta_o = 1$ is the reference boundary layer profile here. In the simulation under consideration, it can be clearly seen that beginning at $x/\delta_o \approx 16$, the near wall fluid attains negative velocity, indicating a reversal of flow. This results in an inflection point, where the portion of the boundary layer lower than the inflection point has negative momentum and the portion above it has positive momentum. The behavior is exhibited by locations upto $x/\delta_o \approx 18$. The maximum flow reversal is measured to be 7.30 % of U_∞ . As the adverse pressure gradient relaxes downstream, the fluid again begins attaining a positive velocity ($x/\delta_o \approx 19$) and recovers its profile. However, even at $x/\delta_o \approx 26$ (not shown), it was seen that the fluid was yet to recover its full profile, which may be indicative of a prolonged effect of the SWBLI downstream of the flow. The falling of the shear stress to a negative value and its recovery, and the behavior of the boundary layer through the SWBLI corroborates the flow separation and reversal.

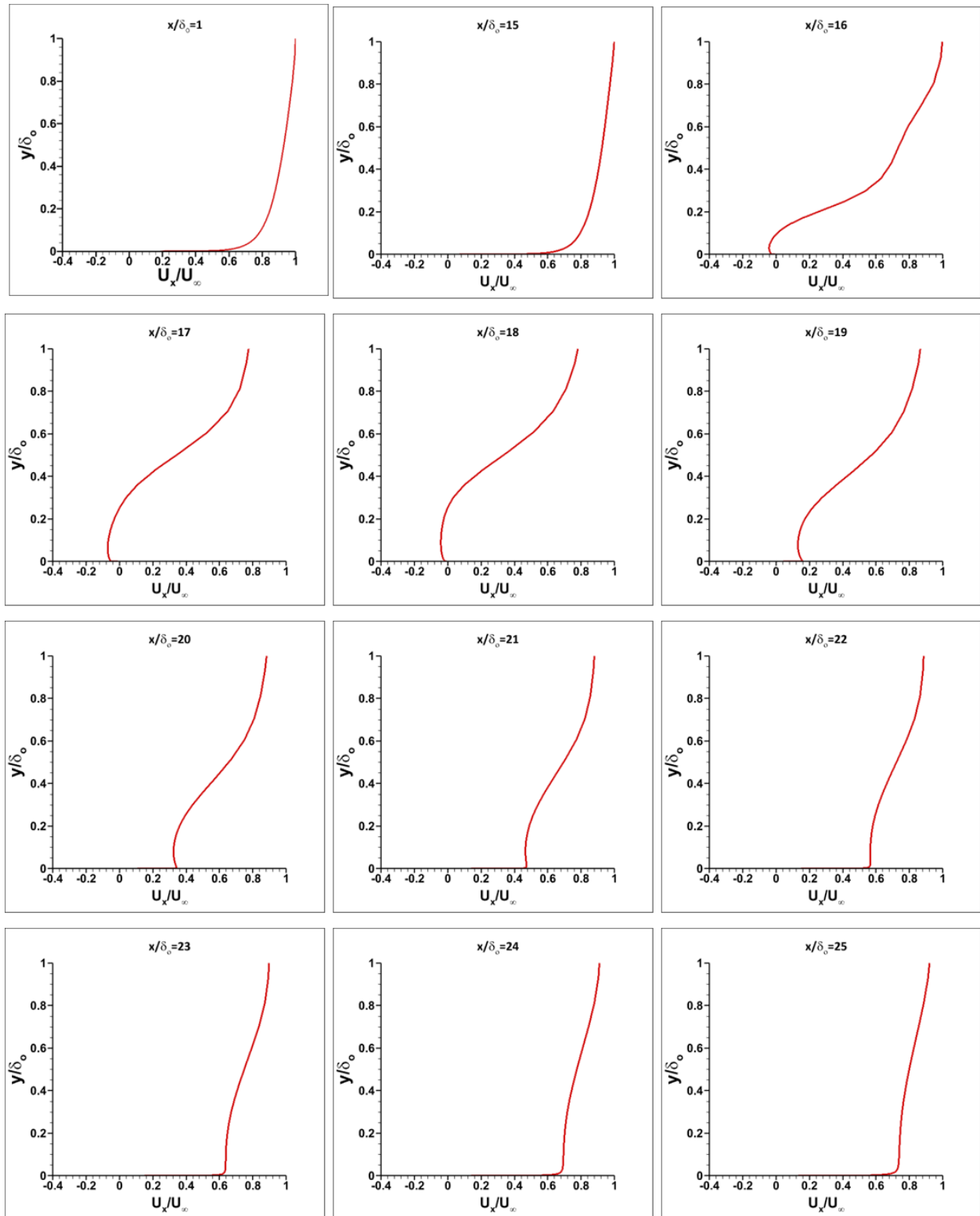
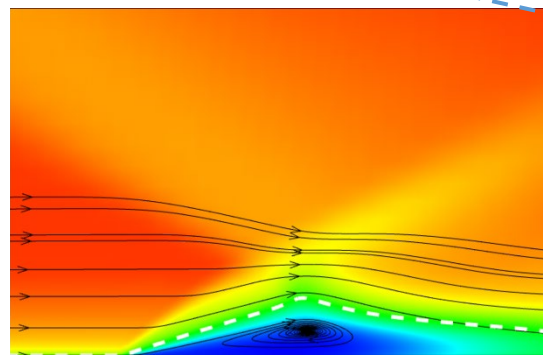
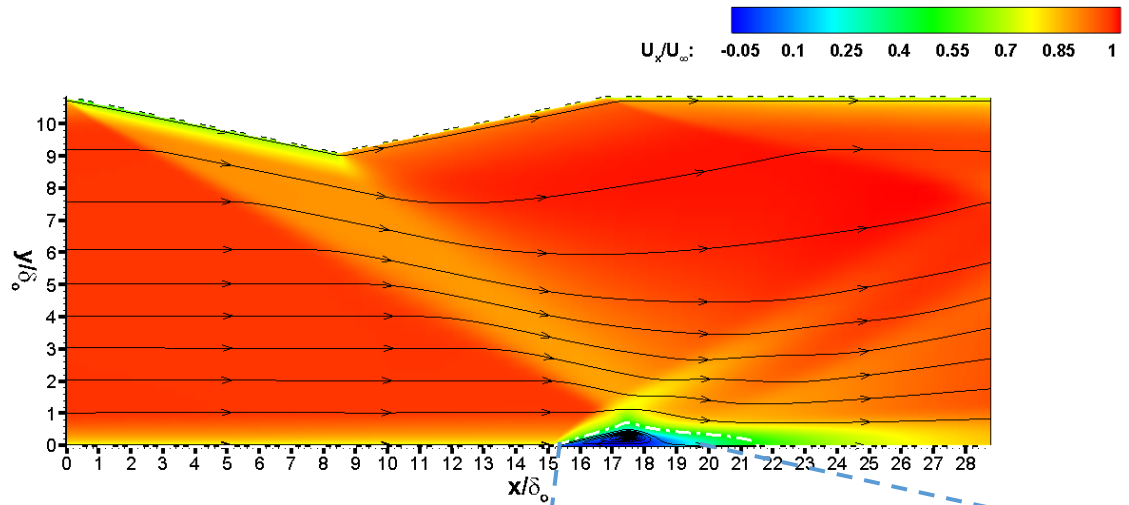


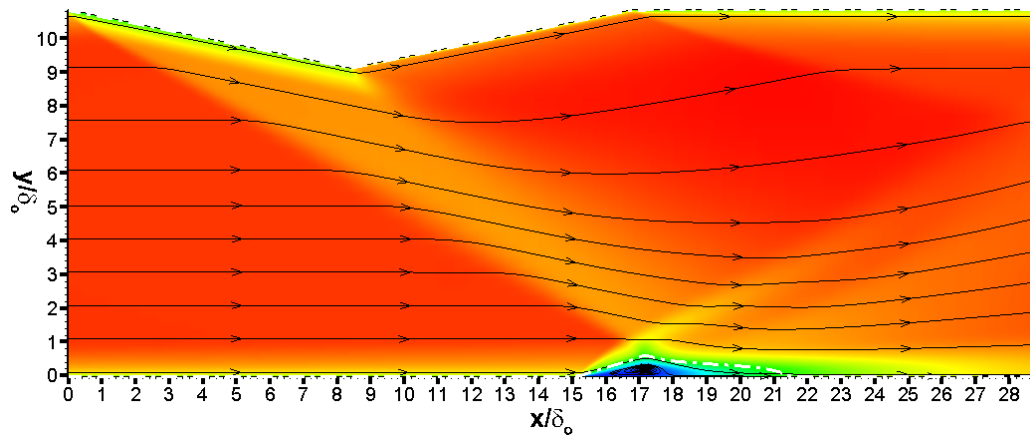
Figure 3.22. Evolution of boundary layer through SWBLI (floor mid-span)

Floor flow separation

Figure 3.23 shows the x-velocity contours overlaid with velocity streamlines at the spanwise locations where pressure measurements have been acquired. Further, the sonic line (in white) has been utilized to illustrate the extent of the separation bubble. Figure 3.24 shows the variation of the x-component of the wall shear stress along the mid-span. The change in velocity in all the three figures which is indicated by the change in color, on progressing in the downstream direction, is the evidence of the formation of oblique shock-wave at the leading edge of the wedge. This shock-wave decelerates the flow. The expansion fan that forms at the apex of the wedge again accelerates it. It is easily observed that the streamlines also change their directions to follow the shape of the wedge, past the oblique shock-waves and expansion fan. In Fig. 3.23 (a), in the top image, the growing boundary layer that forms on the lower wall appears to grow in the wall normal direction beginning at $x/\delta_o \approx 15$. This is the location where it begins to respond to the adverse pressure gradient imposed by the incident oblique shock-wave. This layer of fluid flows over a drastically low momentum fluid (dark blue) that is observed between $x/\delta_o \approx 15$ and $x/\delta_o \approx 21$ near the lower wall. This is the separation bubble which is a salient feature of a strong SWBLI observed consistently in literature. We see that its height is $\approx 0.8\delta_o$ (the apex of sonic line). Further, the recirculation of the fluid within the separation bubble is illustrated by a streamline forming a focus further illustrated in the bottom image. In Fig. 3.24, after remaining fairly constant, the value of X-component wall shear stress begins dropping at $x/\delta_o \approx 15.2$ and goes past zero to a minimum value of -108.087 Pa at $x/\delta_o \approx 17.26$, which is located underneath the separation bubble. Past this location, the shear stress value again begins increasing and recovers past the zero value at $x/\delta_o \approx 18.225$. However, the extent of the separation bubble ($x/\delta_o \approx 3.023$) predicted is considerably smaller than the observation made by Chaganti (2017).



(a)



(b)

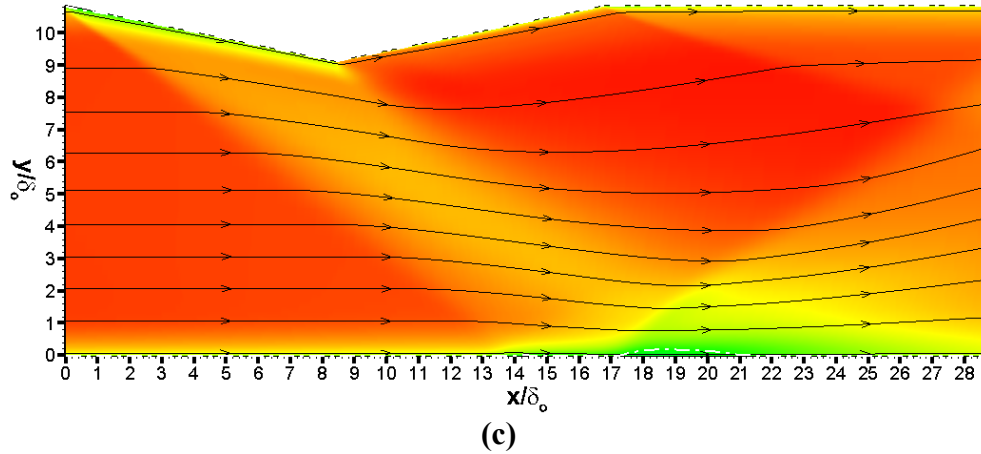


Figure 3.23. Stream-wise velocity contours superimposed with velocity streamlines
 (a) $z/\delta_o = 5.442$ (b) $z/\delta_o = 7.257$ (c) $z/\delta_o = 9.978$

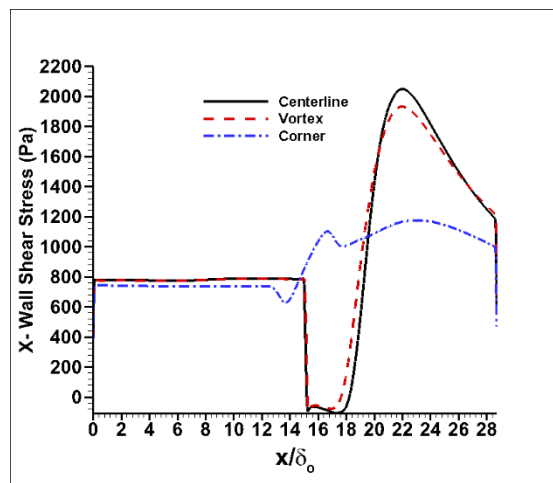


Figure 3.24. X-component wall shear stress – span-wise locations

The flow structure deviates considerably on moving away from the centerline. In Fig 3.23 (b), the height of the separation bubble is lower (the apex of sonic line $\approx 0.6\delta_o$) in comparison to that at in the centerline. In Fig 3.24, the X- wall shear stress under the vortex begins dropping slightly earlier at $x/\delta_o \approx 15.26$ and goes past zero to a minimum value of -93.14 Pa at $x/\delta_o \approx 15.36$. It recovers back to a non- zero value at $x/\delta_o \approx 17.642$. Thus, the extent of the bubble ($x/\delta_o \approx$

2.382) at the vortex is lower than that at the centerline. At the corner in Fig. 3.23 (c), the boundary layer separation bubble appears to be non-existent with only a smearing of the pressure gradient (yellow to green) over a considerable distance downstream and away from the floor. This region is most probably influenced by the corner separation. The shear stress trend supports the observation of a bifurcated shock-wave that is discussed in the literature (Morajkar et al. (2016)) This is because the shear stress exhibits two local minimum values which could be due to the flow encountering the two legs of the bifurcated shock-waves. The first minima is observed at $x/\delta_o \approx 13.67$ (626.71 Pa) and the second is observed at $x/\delta_o \approx 17.84$ (1000.65 Pa). The location of the first minima is also one of the evidences that the corner separation precedes the primary separation. However, unlike the centerline and vortex, the shear stress for the corner does not fall below zero, which further indicates that the interaction of the shock waves with the boundary layers growing on the bottom and the side wall does not cause separation very near the wall.

Wall mean static pressure measurements – steady-state simulation

Wall static pressure measurements extracted along the locations where the experimental data was acquired have been plotted in Fig. 3.25. Although the predicted trends at every location show a deviation from their experimental counterparts, the trends still show expected trends on comparison with each other there. There is an overall reduction in the maximum pressure on moving from the centerline towards the corner. The side-wall pressure rise is the minimum. The rise in pressure at the corner ($x/\delta_o \approx 13$) occurs well ahead of the centerline and the vortex ($x/\delta_o \approx 15$). Flow separation at the side-wall occurs further upstream in comparison to the corner ($x/\delta_o \approx 11$). There also is a smearing of the pressure gradient at the corner and the side-wall as the pressure rise occurs over a large distance in comparison with the centerline and vortex.

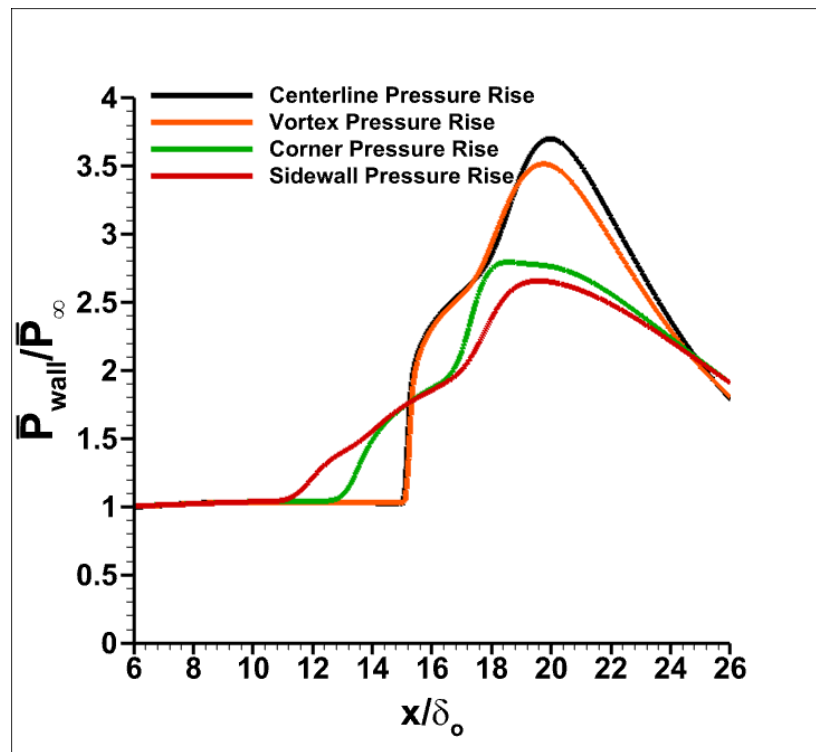
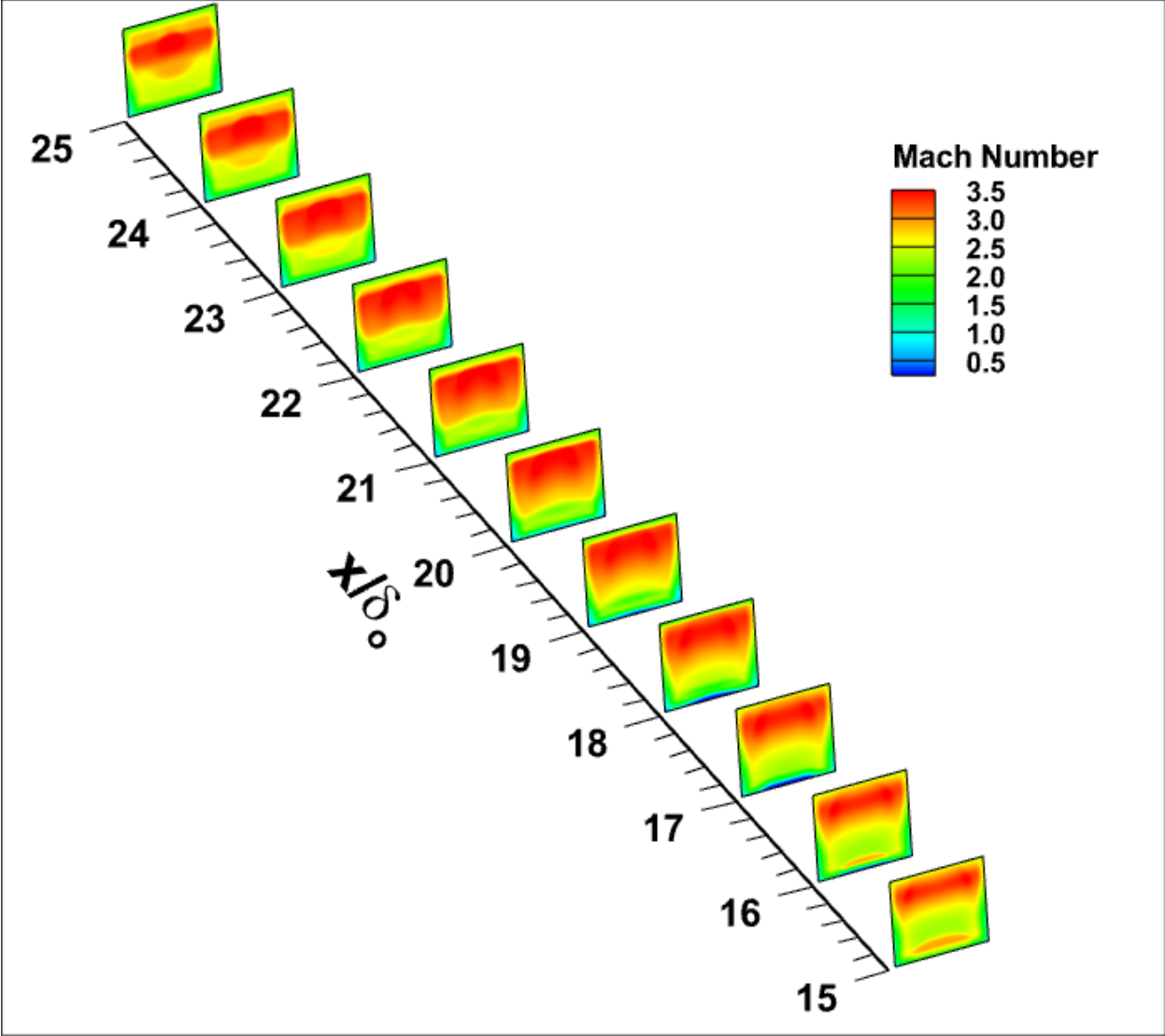


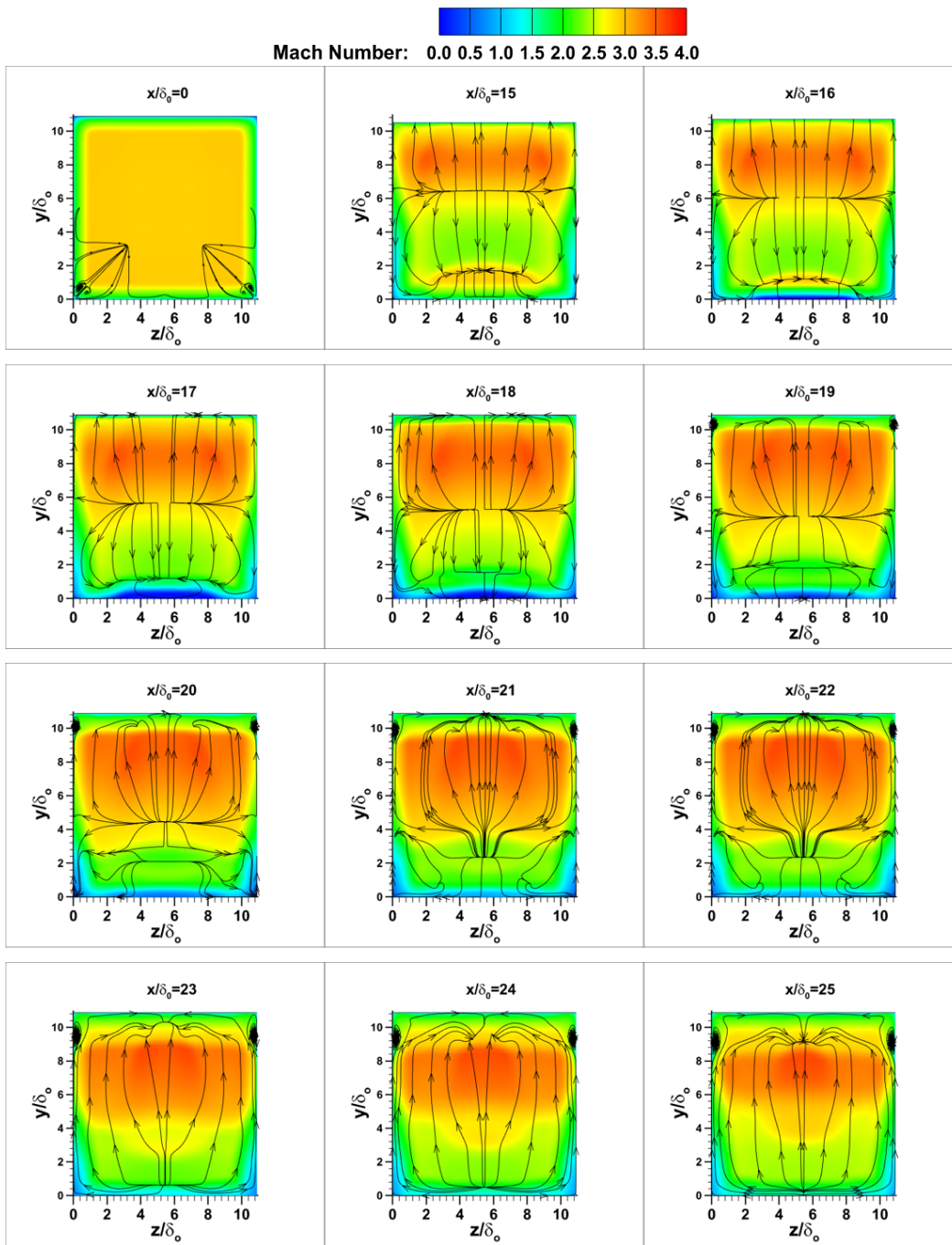
Figure 3.25. Wall static pressure measurements – steady state simulation

Variation of Mach number and velocity streamlines - stream-wise direction

Figure 3.26 shows the variation of Mach number overlaid with velocity streamlines on stream-wise planes. In Fig. 3.26 (b), at the location $x/\delta_0 = 0$, a pair of counter rotating vortices can be observed at both the left and right bottom corners which are a salient feature of corner flows. These vortices occur due to the effects of the right-angled corners on the flow. However, they are not observed in the upper corners. This is probably due to the fact that this plane lies at the leading of the wedge. Hence, the flow at the upper corners are distorted by the wedge. The streamlines show a combination of saddle points and nodes at various locations in all the planes. In Fig. 3.26 (b), the saddle point that spans the plane $x/\delta_0 = 15$ at $y/\delta_0 \approx 6.5$ shifts downward on moving in the stream-wise direction. A couple of vortices appear $x/\delta_0 = 15$ at the left and right upper corners of the side-walls beginning at $x/\delta_0 = 19$ and is present in the all the planes then onwards.



(a)



(b)

Figure 3.26. Evolution of Mach number and velocity streamlines in the stream-wise direction (a) collective isometric view (b) separate normal view

Total pressure – centerline

Figure 3.27 shows the total pressure variation at the centerline plane. The total pressure of the flow remains constant in the free-stream and decreases on moving closer to the wall in the boundary layer. This is due to a decrease in the dynamic pressure. Similar to the fluid velocity, it becomes negligible inside the separation bubble. As expected, it first drops past the leading edge shock-wave and further past the reflected shock-wave. It smears over a greater region between the apex of the wedge and the trailing edge due to the formation of the expansion fan that lowers the static pressure.

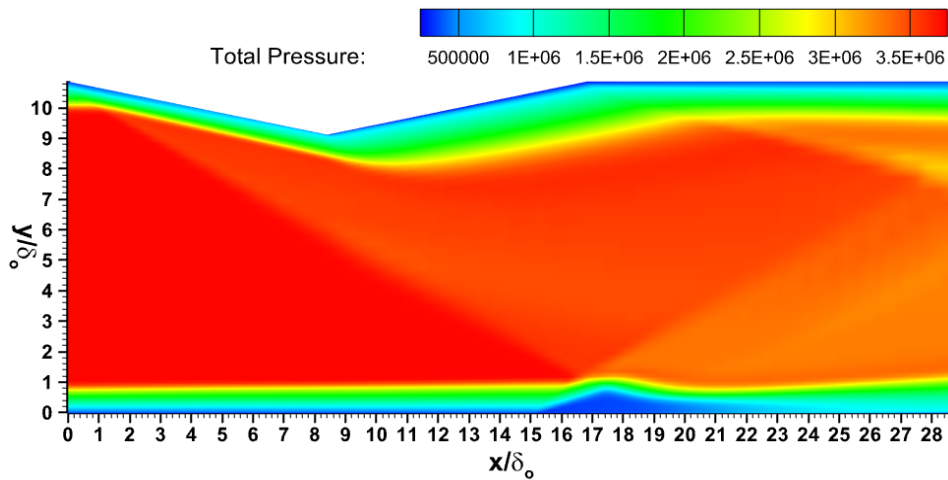
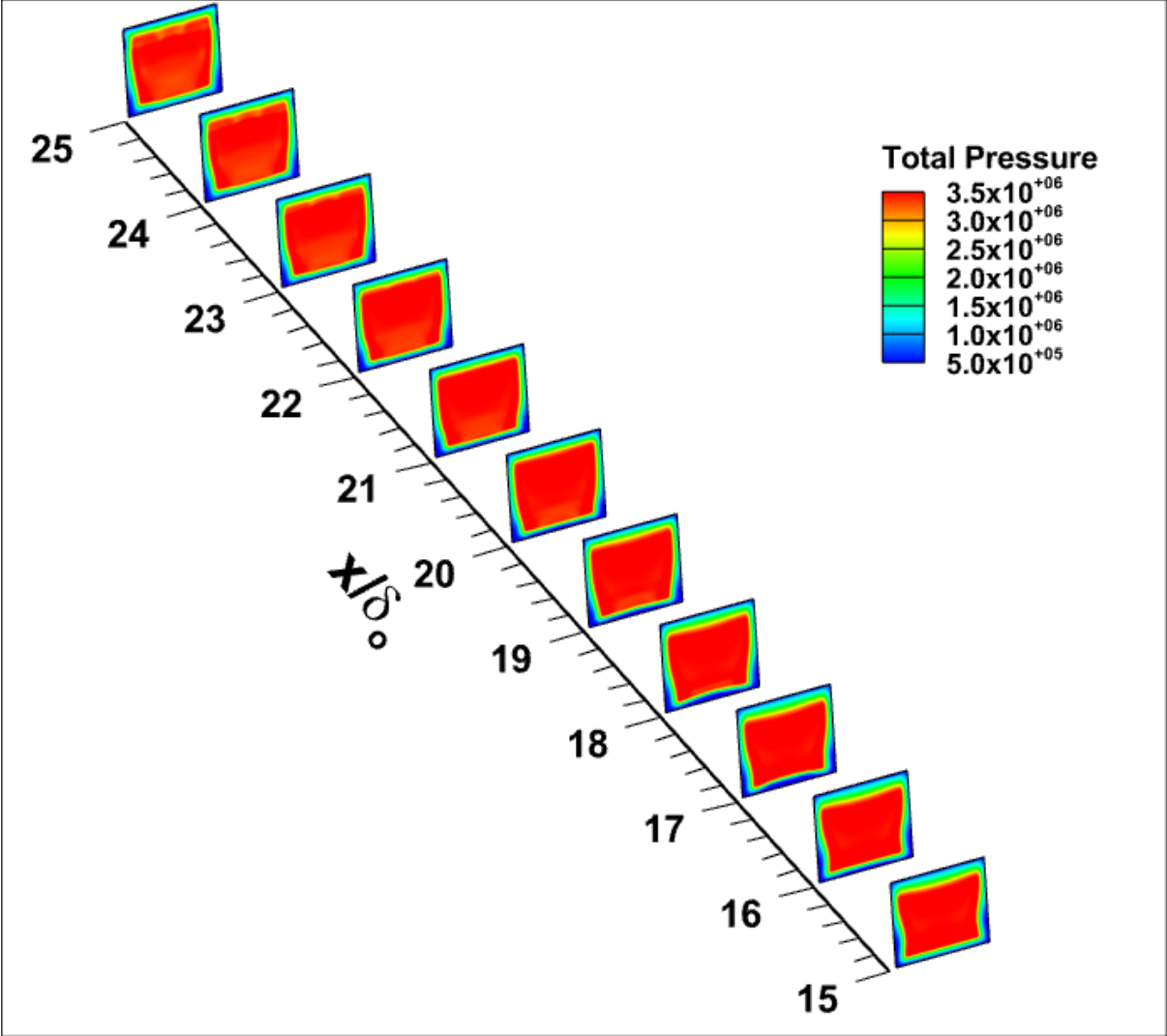


Figure 3.27. Total pressure variation-centerline

Variation of total pressure –Stream-wise direction

In Fig. 3.28, the total pressure also follows a similar but that of a decreasing trend, i.e., the total pressure decreases first and then increases in the separation region in the downstream direction. This aligns with the observation made in Fig. 3.28. This is accompanied with a couple of low values of the total pressure move down the side-walls.



(a)

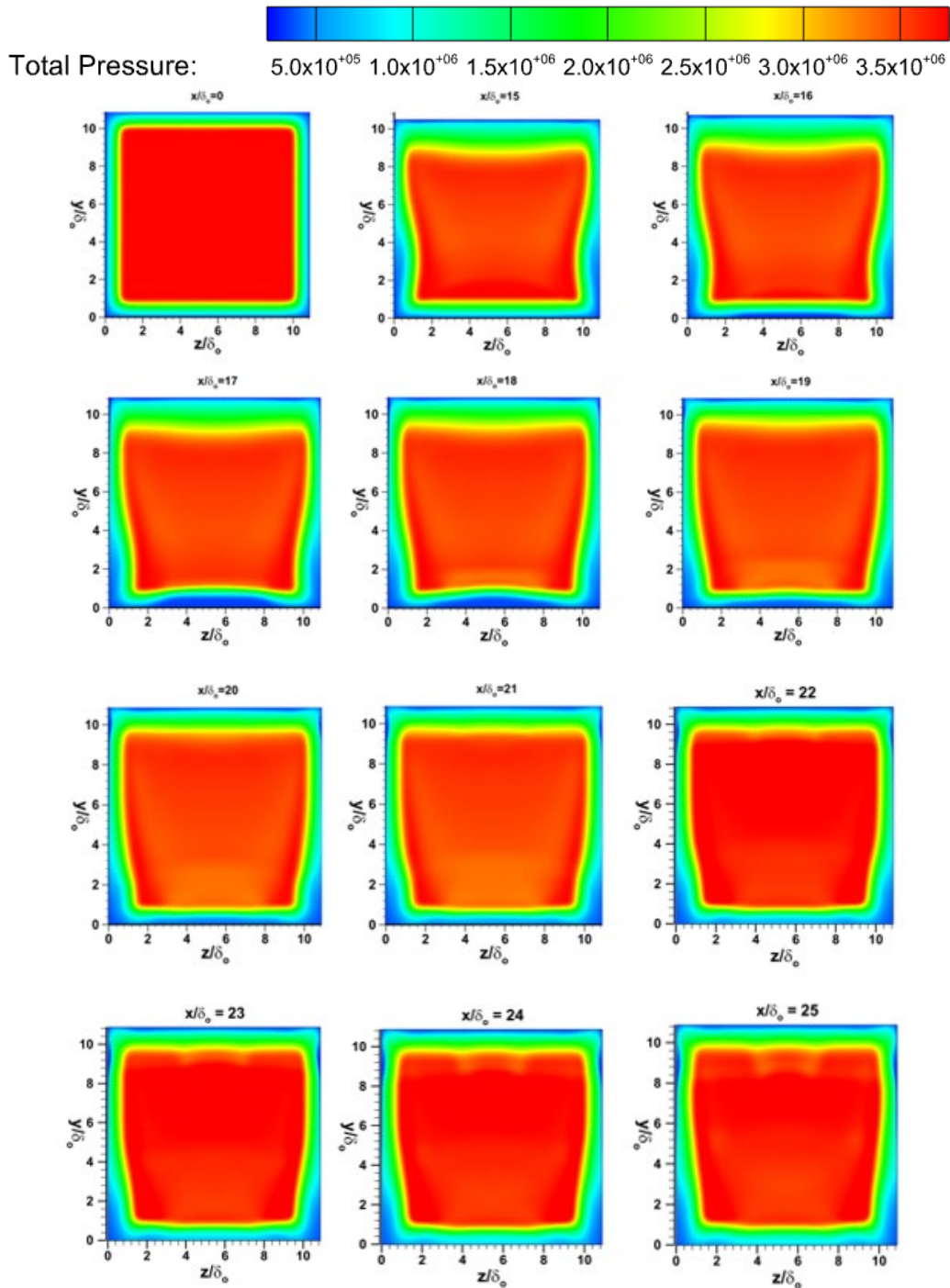
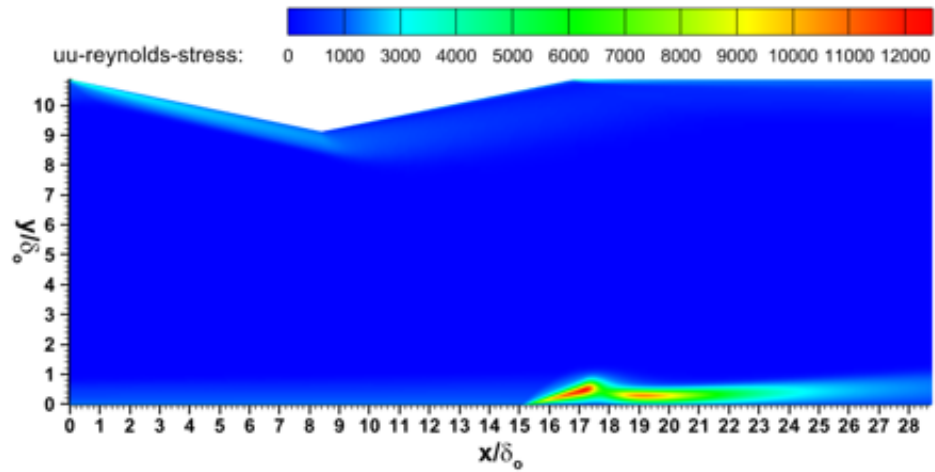


Figure 3.28. Evolution of total pressure in the stream-wise direction (a) collective isometric view (b) separate normal view

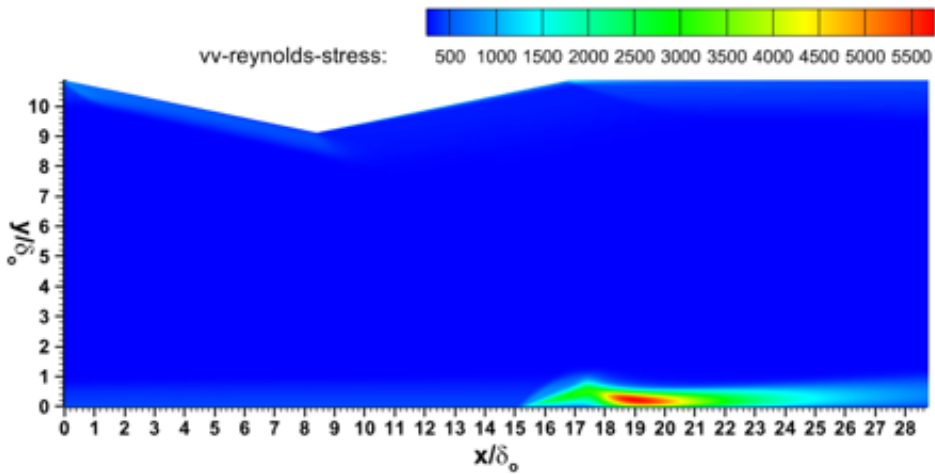
Variation of Reynolds stresses – centerline

Figure 3.29 (a), (b), and (c) show the variation of uu -, vv - and uv - Reynolds Stresses in the centerline plane. All the three stresses are expectedly negligible in the flowfield except for the separation region. In Fig. 3.29 (a), the maximum normal uu -RS is concentrated in regions both in the front and rear end of the bubble. In Fig. 3.29 (b), the maximum normal vv -RS is concentrated at the rear end of the bubble. In Fig. 3.29 (c), the maximum shear uv -RS is again concentrated at the rear end of the bubble. However while both the normal stresses are positive, the shear stress is negative in the separation region. The maximum shear stress occurs between $x/\delta_o \approx 18$ and $x/\delta_o \approx 21$.

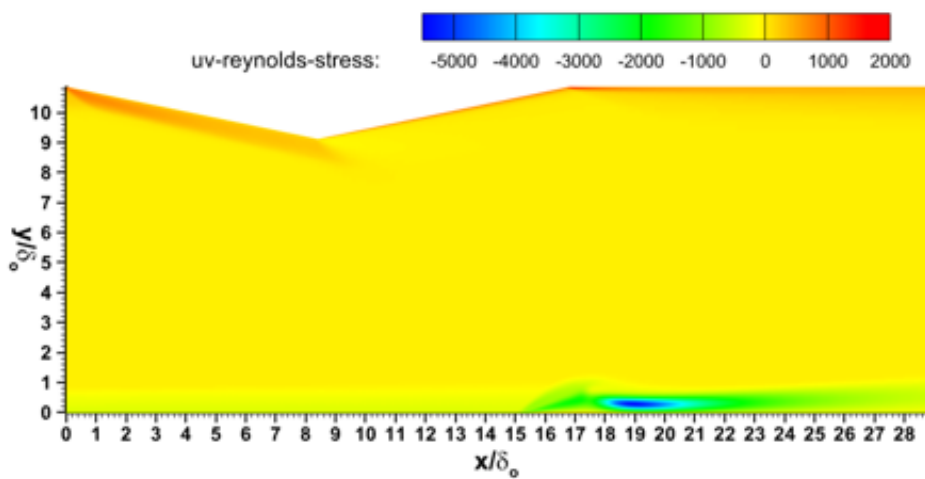
Results indicate that the u -fluctuating velocity is increased as the flow encounters the separation and near the end of the separation. The bubble, the front and the back end of the bubble oscillate as it was shown previously by Chaganti (2017) using schlieren movies. The v -fluctuating velocity increase near the back end of the separation bubble is due to the flapping motion of the flow while reattaching to the wall. This motion also results in large negative uv stresses, indicating that the positive u velocity fluctuations occur together with negative v velocity fluctuations.



(a)



(b)



(c)

Figure 3.29. Reynolds stress in the span wise centerline plane (a) uu-RS (b) vv-RS (c) uv-RS

Variation of Z- component vorticity in the span-wise direction

Figure 3.30 shows the variation of Vorticity on the span-wise centerline plane. The Z- vorticity appears to be several orders of magnitude higher than the X and Y- Vorticity magnitudes. All the vorticities are concentrated either in the separation region or aft of the shock-wave past the trailing edge of the wedge. In Fig. 3.30 (a), the separation region is layered with X-vorticity of opposite senses. In Fig. 3.30 (b), a high degree of Y-vorticity on the floor is formed only after the separation while in Fig. 3.30 (c), Z-vorticity remains in the incoming boundary layer and the separation bubble.

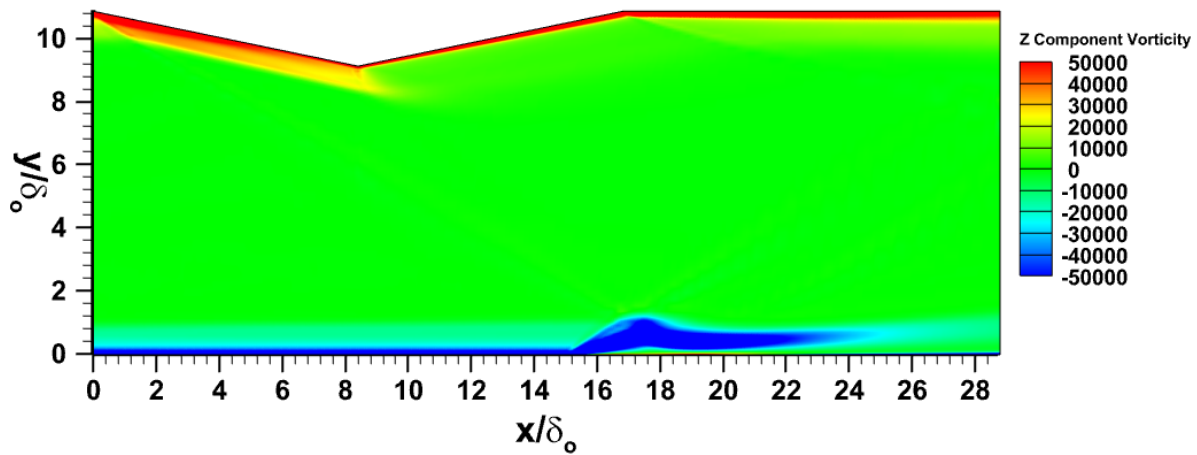


Figure 3.30 Z-component vorticity

Variation of Reynolds stresses and vorticity – wall normal direction

Figures 3.31, 3.32, 3.33, 3.34, and 3.35 show the variation of uu -, vv -, ww -, uw - Reynolds Stresses and Y -Vorticity respectively on wall normal planes. In Figs. 3.31 (a), 3.32 (b), it is observed that the stresses are concentrated in the region of interaction, fore and aft of the separation. Their magnitudes begin decreasing on moving away from the wall. The uw -Reynolds Stress (Fig. 3.34) and Y -vorticity (Fig. 3.35) behave in a manner such that each of them are of opposite senses on moving from the upper end to lower end of the span within each image.

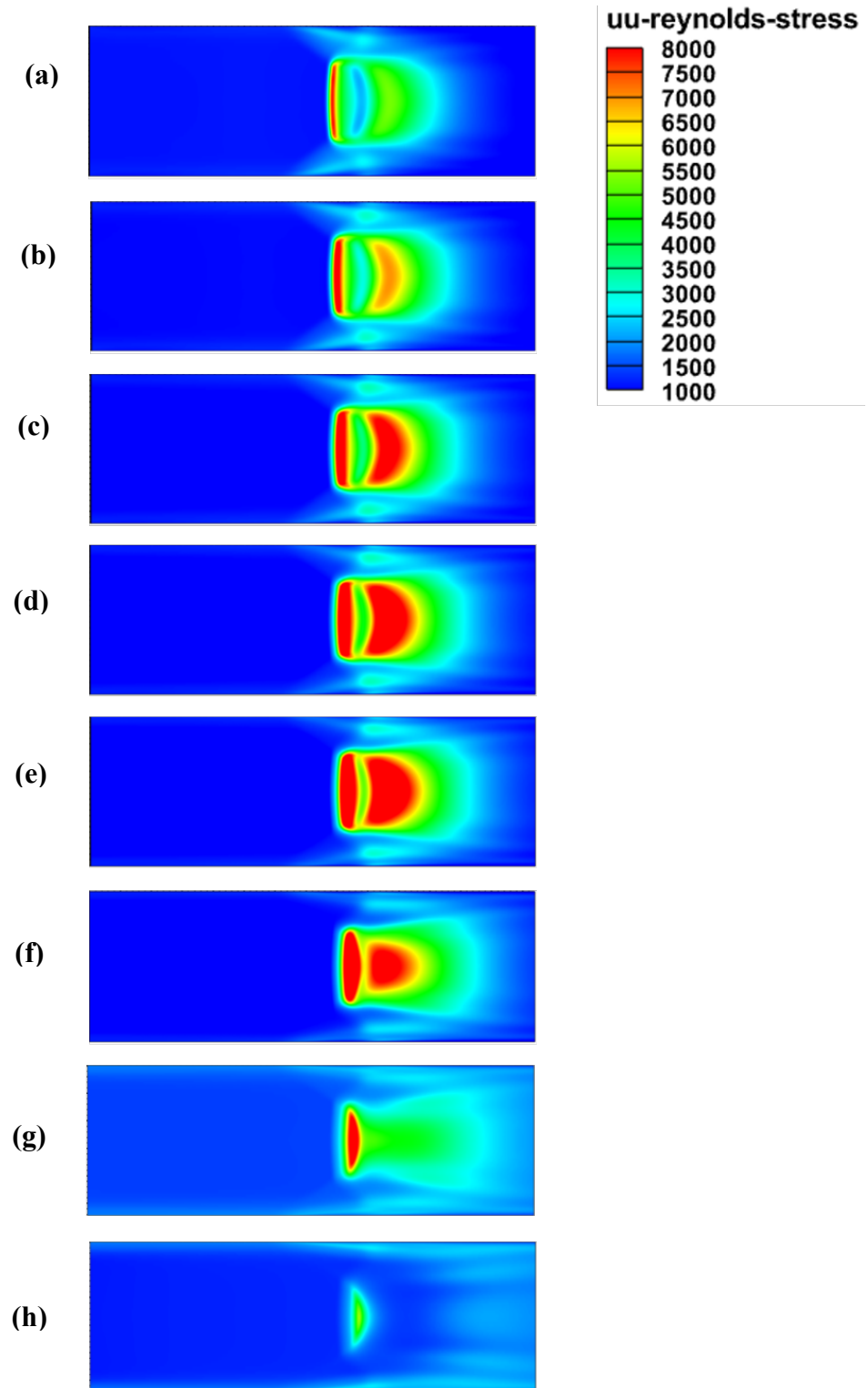


Figure 3.31. Evolution of uu -RS at $y/\delta_o =$ (a) 0.10 (b) 0.15 (c) 0.20 (d) 0.25 (e) 0.30 (f) 0.40 (g) 0.50 (h) 0.75

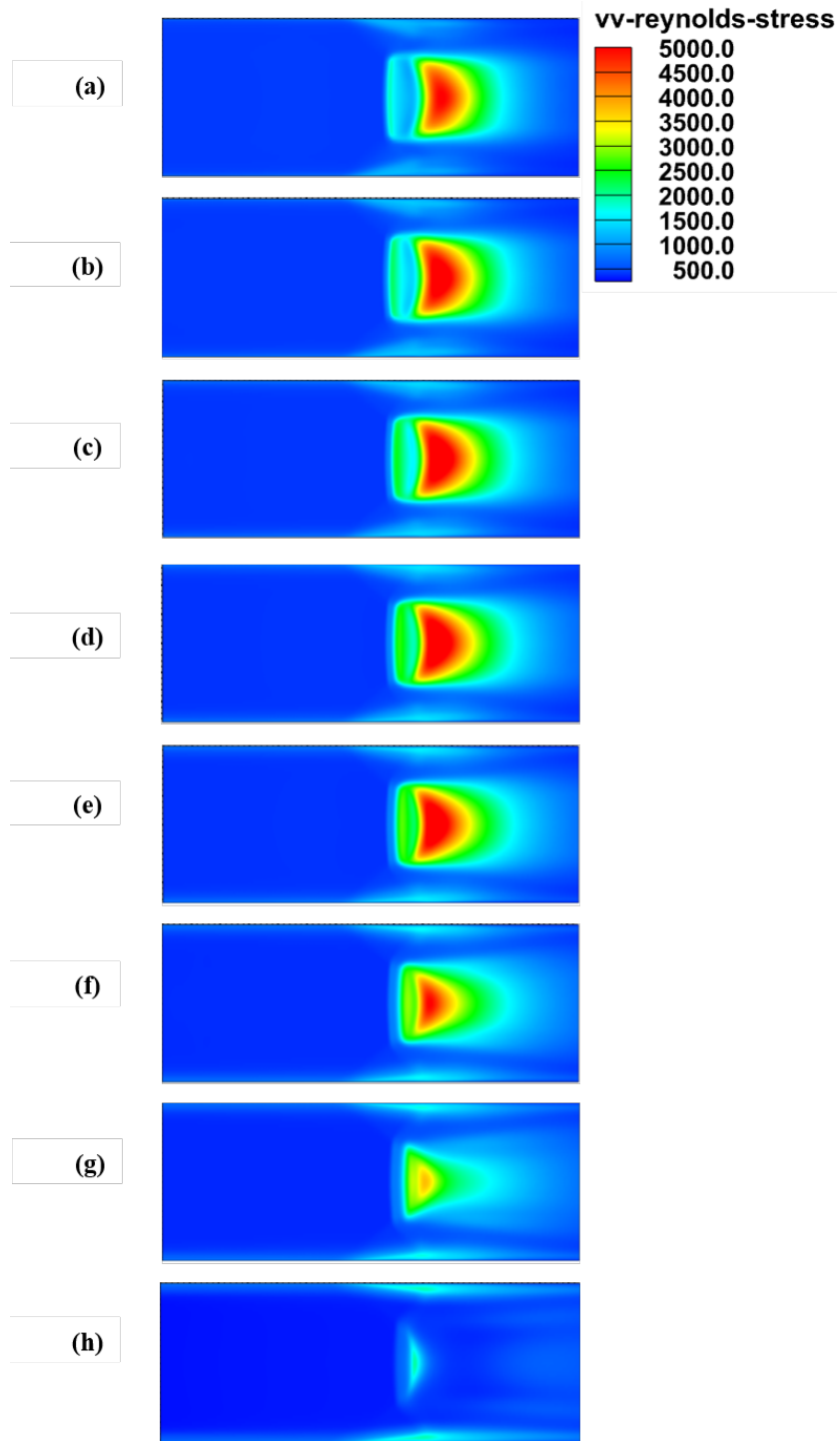


Figure 3.32. Evolution of vv-RS at $y/\delta_o =$ (a) 0.10 (b) 0.15 (c) 0.20 (d) 0.25 (e) 0.30 (f) 0.40 (g) 0.50 (h) 0.75

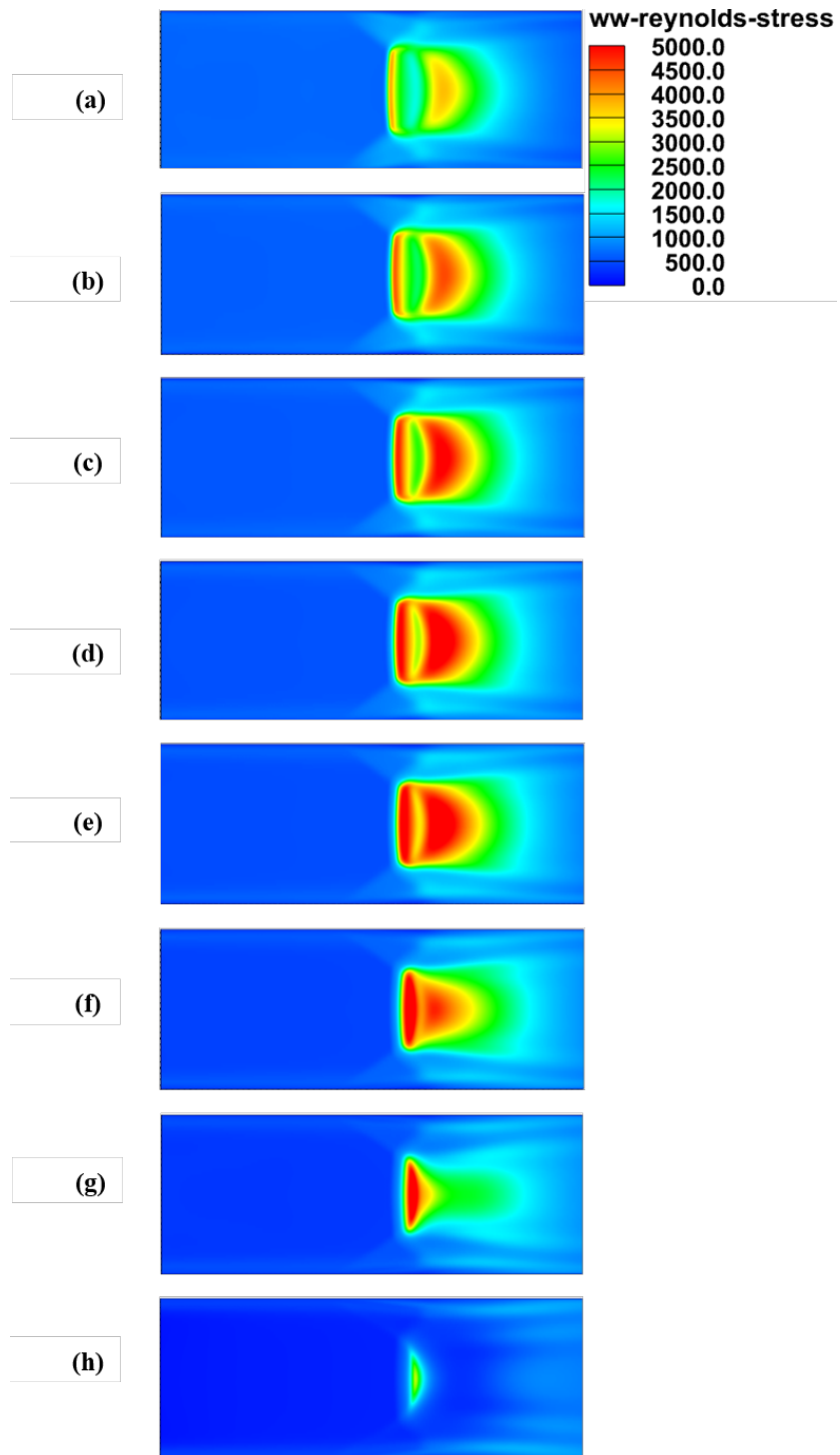


Figure 3.33. Evolution of ww-RS at $y/\delta_o =$ (a) 0.10 (b) 0.15 (c) 0.20 (d) 0.25 (e) 0.30 (f) 0.40 (g) 0.50 (h) 0.75

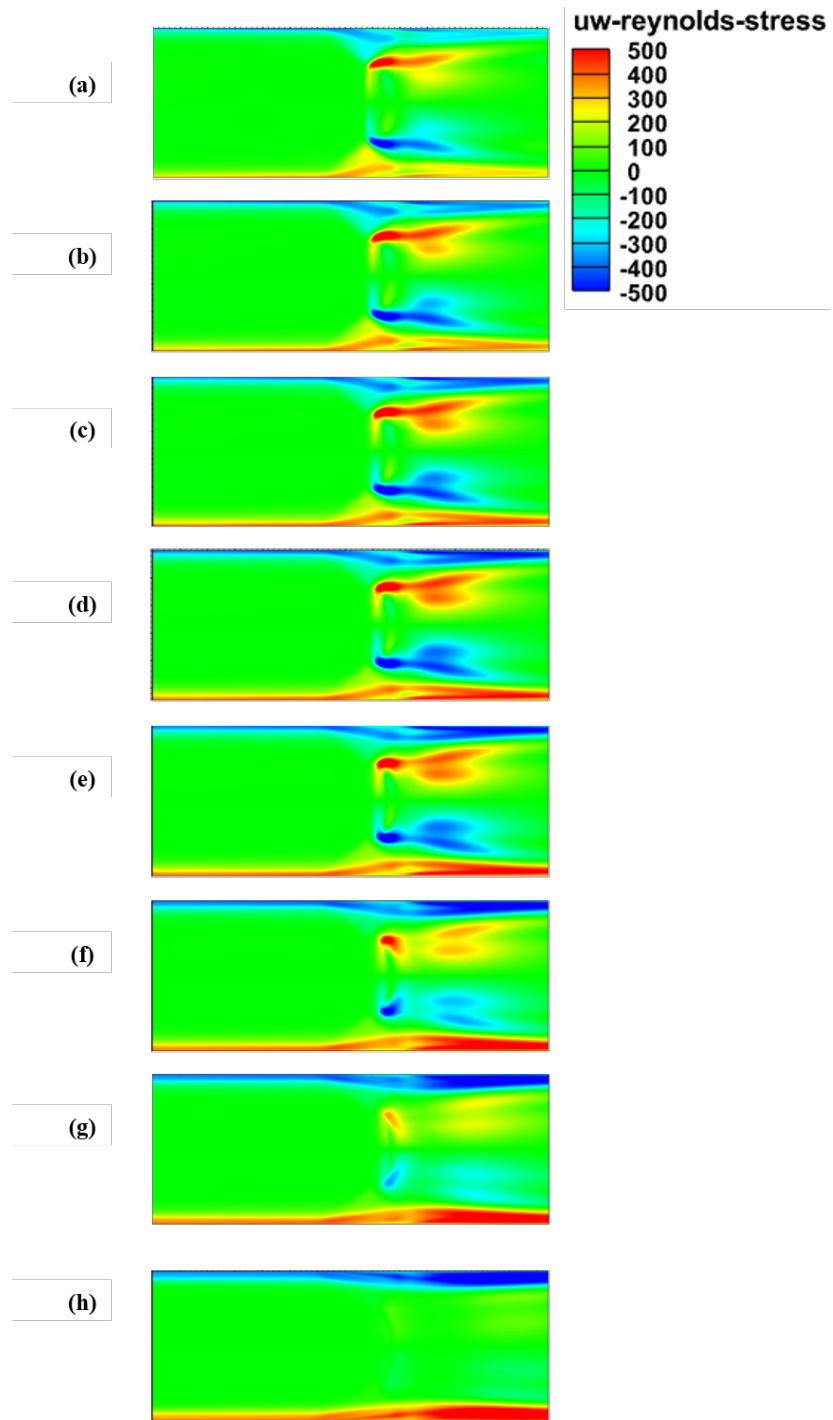


Figure 3.34. Evolution of uw -RS at $y/\delta_o =$ (a) 0.10 (b) 0.15 (c) 0.20 (d) 0.25 (e) 0.30 (f) 0.40 (g) 0.50 (h) 0.75

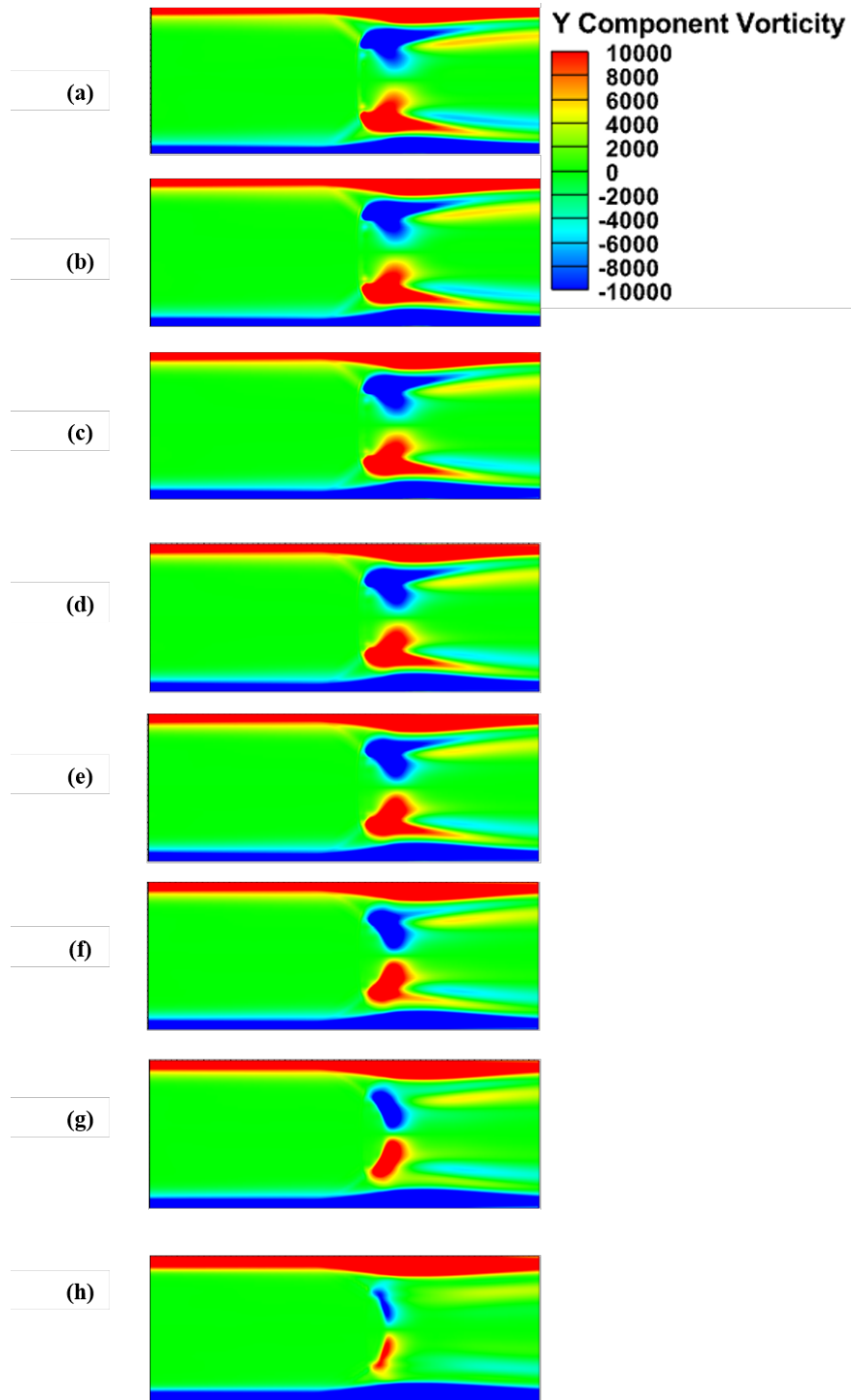


Figure 3.35. Evolution of Y-Component vorticity at $y/\delta_o =$ (a) 0.10 (b) 0.15 (c) 0.20 (d) 0.25 (e) 0.30 (f) 0.40 (g) 0.50 (h) 0.75

Variation of Reynolds stresses and X-component vorticity - stream-wise direction

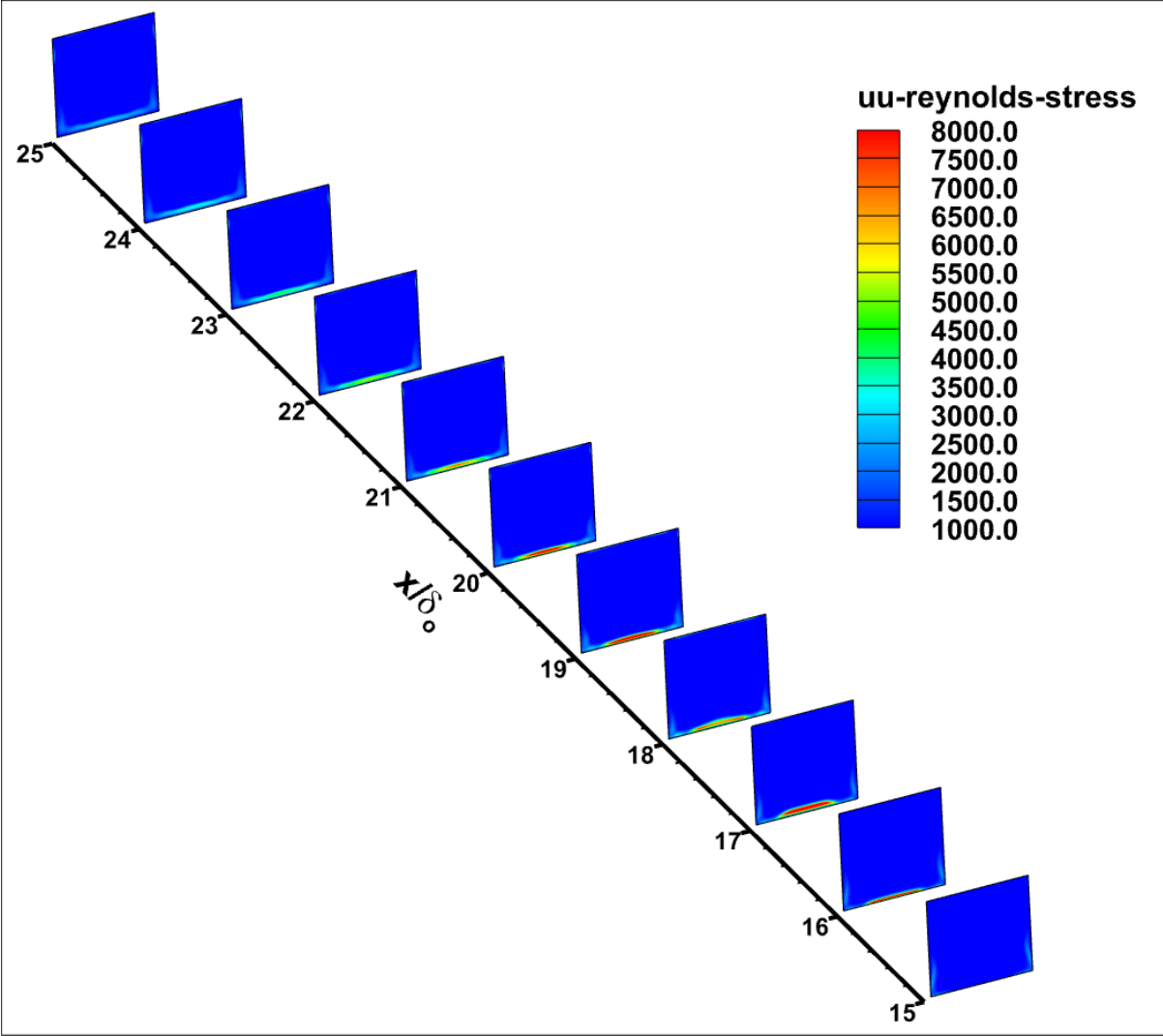
Figures 3.36, 3.37, 3.38, 3.39, and 3.40 shows the variation of uu -, vv -, ww -, and vw - Reynolds Stress, and X-Component Vorticity respectively on stream-wise planes.

In Fig. 3.39 and 3.40, the vw -Reynolds Stress and X- Vorticity act in opposite directions consecutively across the walls within each plane indicating a symmetric nature of the SWBLI. This shows that the flow is highly rotational leading to an increased shear stress in these regions.

The variations in figure 3.40 a and b, inserts 17, 18, and 19 show that there are multiple opposite sense rotations within the separation bubble region. These CW and CCW rotations merge to a single sign vortex proceeding downstream near the bottom wall. The sign of the vortices near the side wall show regions of opposite sign structures (inserts 23, 24, and 25)

We see similar variations for the vw stress in figure 3.39, inserts 17, 18, and 19, with opposite signs as expected.

In Fig. 3.37, and 3.38, both the vv - and ww - Reynolds Stresses on the floor first increase and then decrease in the separation region in the downstream direction. The peak value of both the stresses does not span the complete width of the test section and is confined to a certain percentage of the floor. It is interesting to also note that for both the type, high stresses develop along the side-walls and move downward with each plane. This is probably due to the interaction of the side wall boundary layer and the shock wave.



(a)

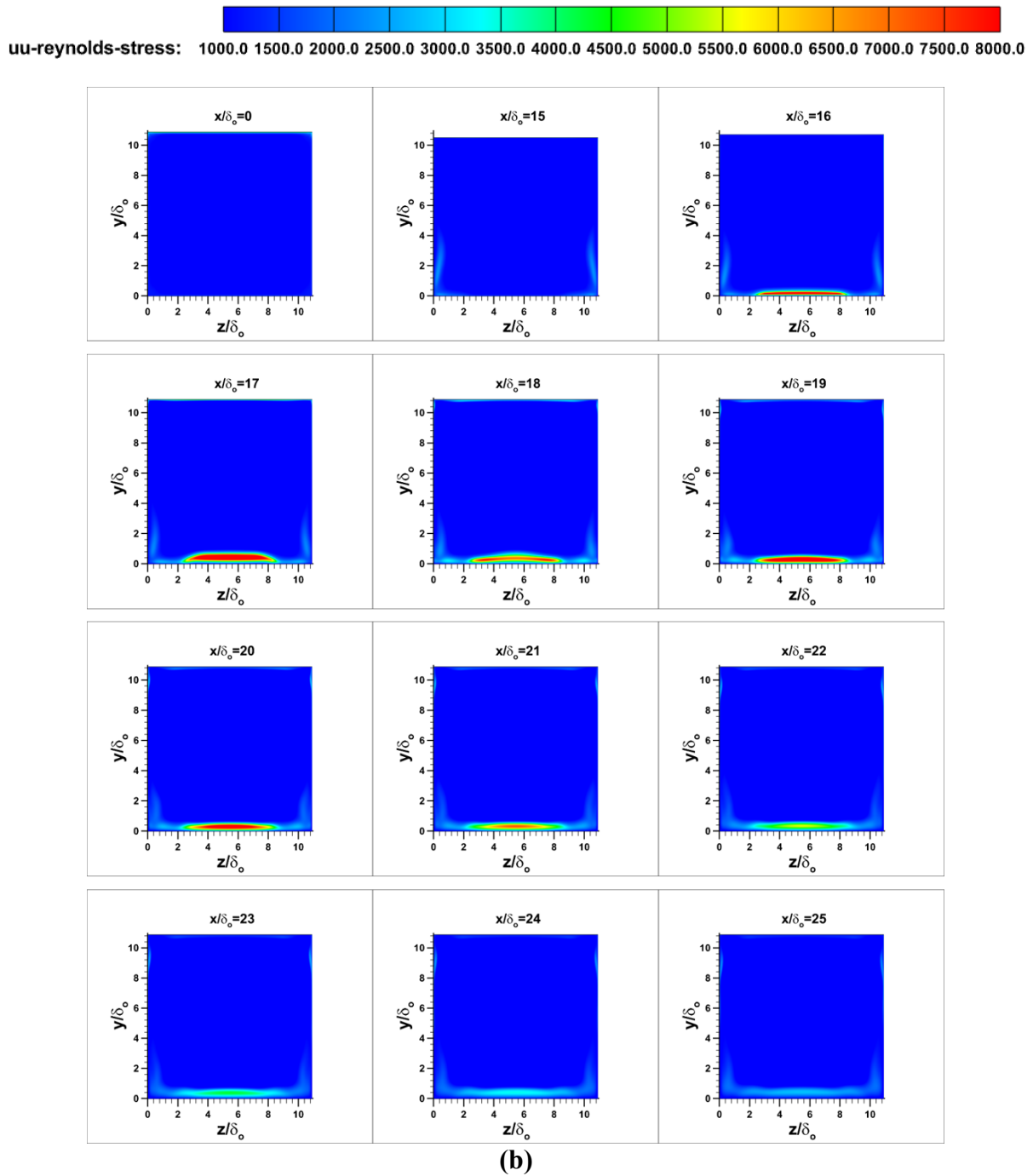
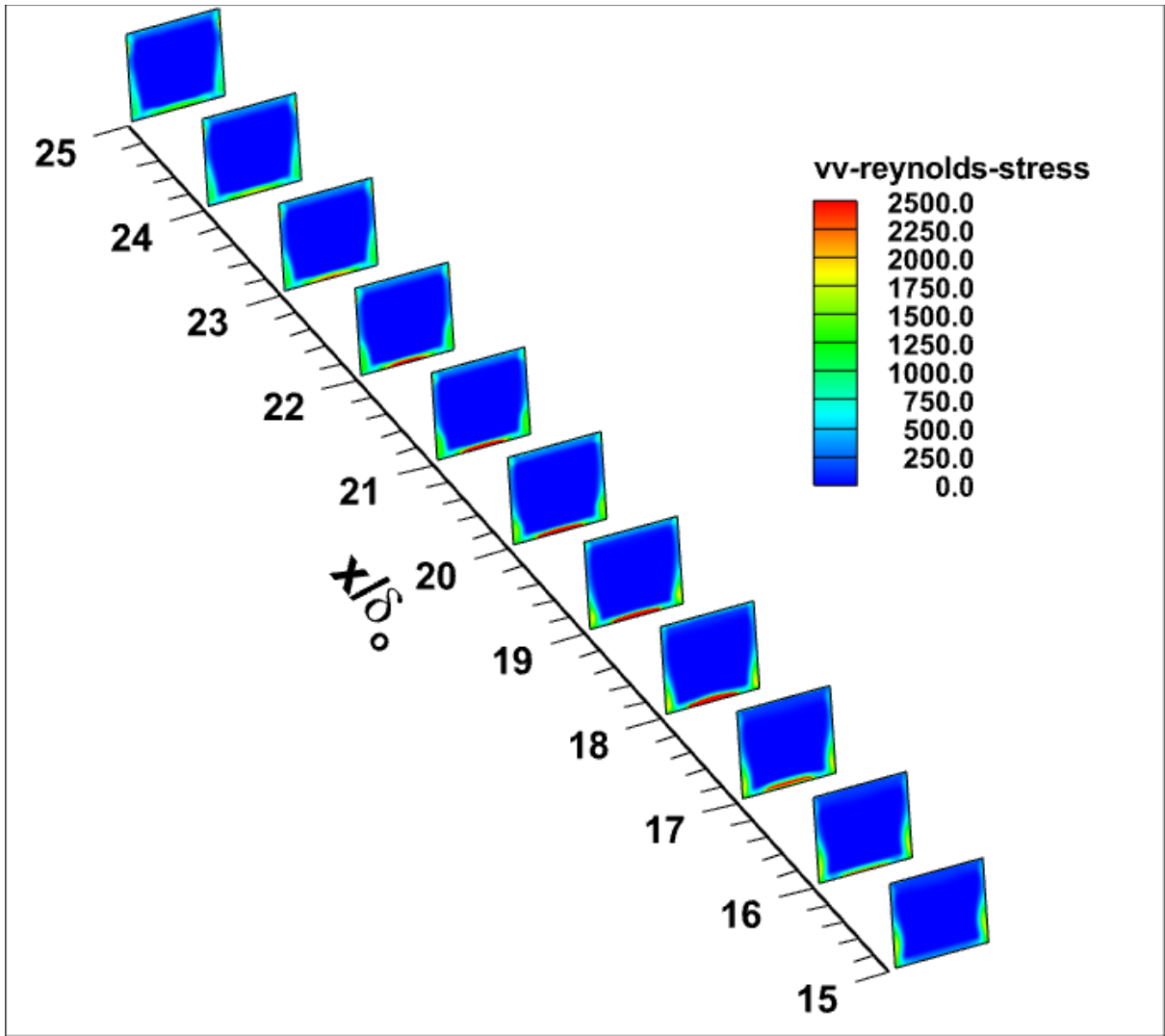
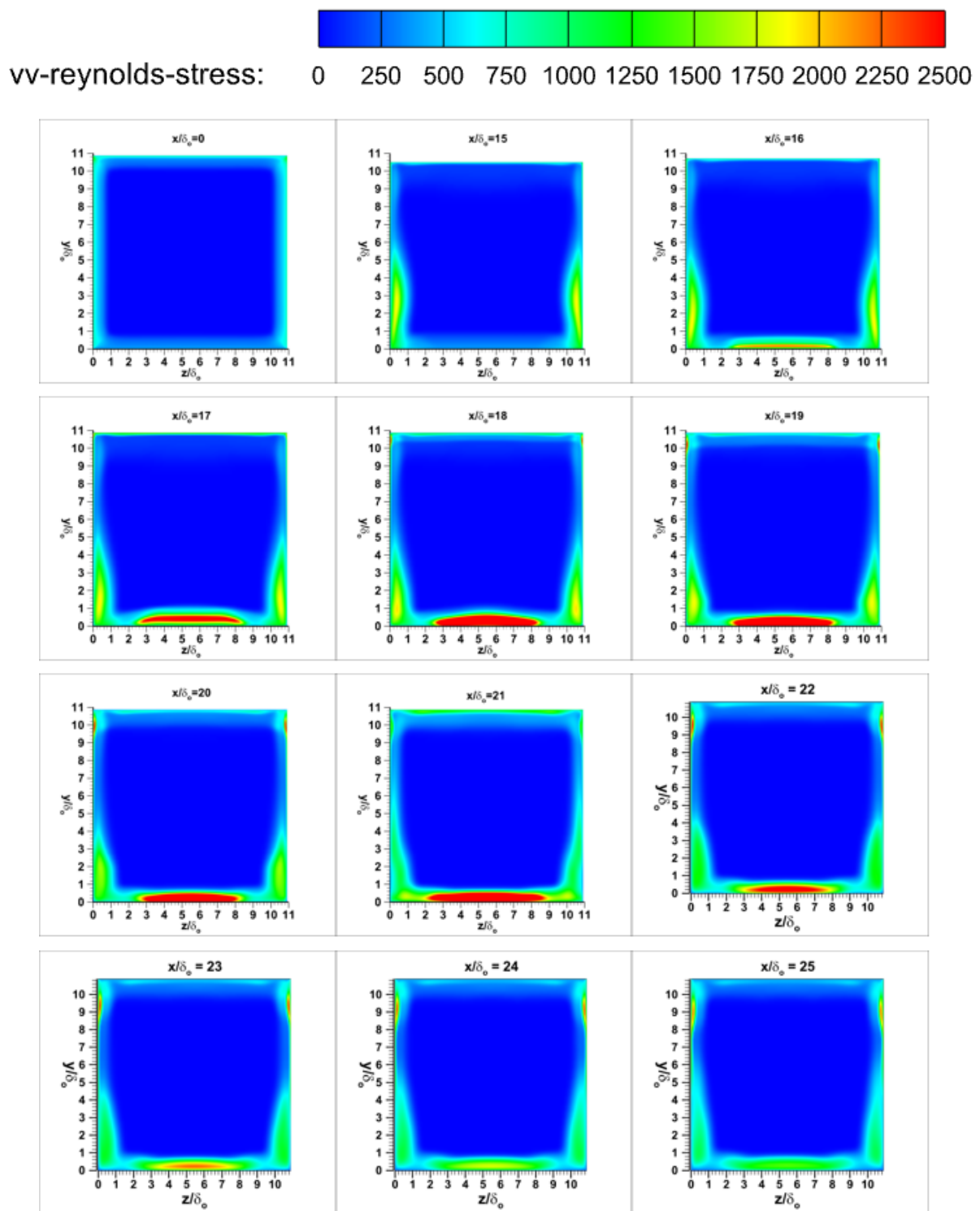


Figure 3.36. Evolution of uu – Reynolds stress in the stream-wise direction (a) Collective isometric view (b) Separate normal view

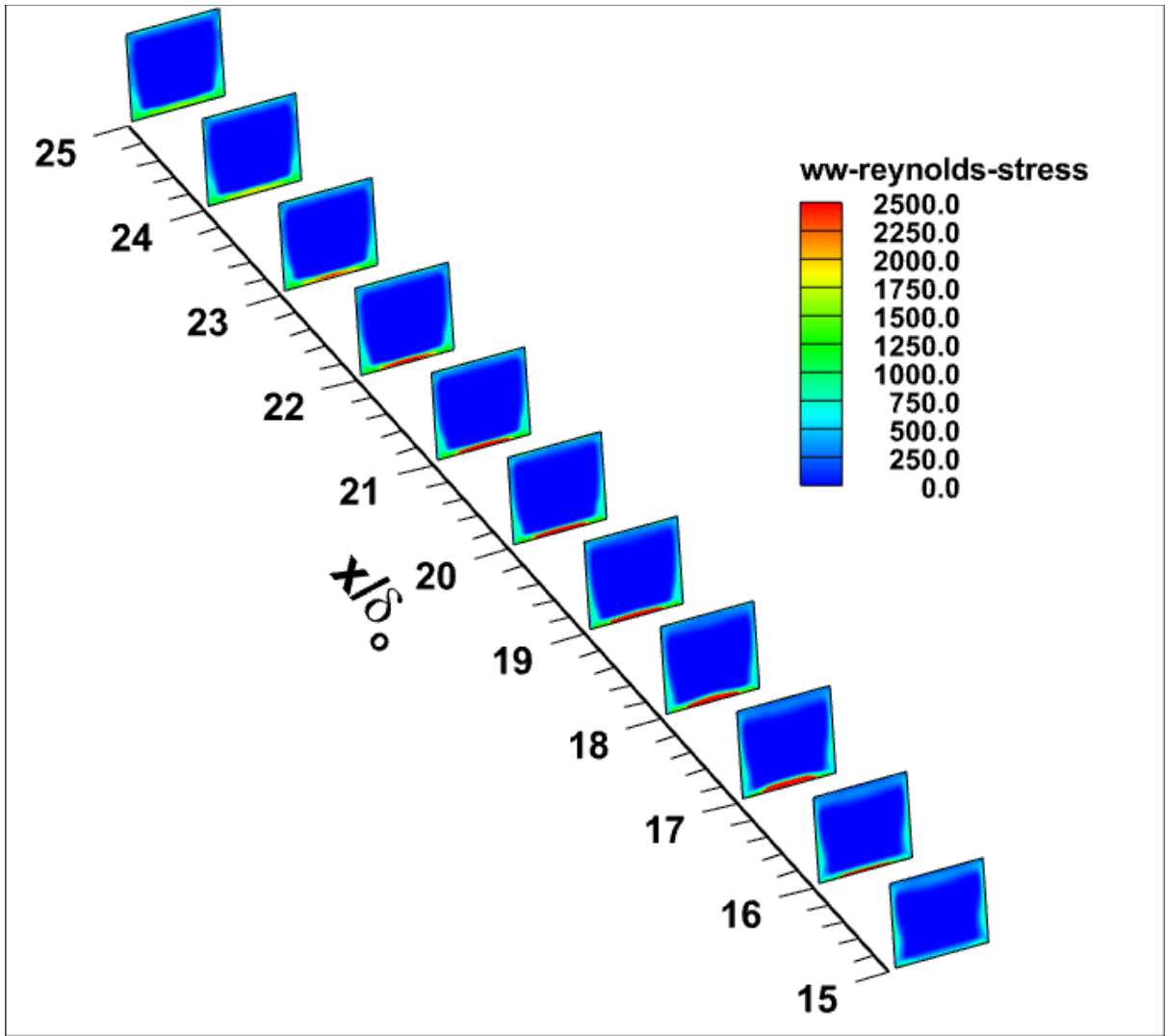


(a)



(b)

Figure 3.37. Evolution of vv-Reynolds Stress in the stream-wise direction (a) Collective isometric view (b) Separate normal view



(a)

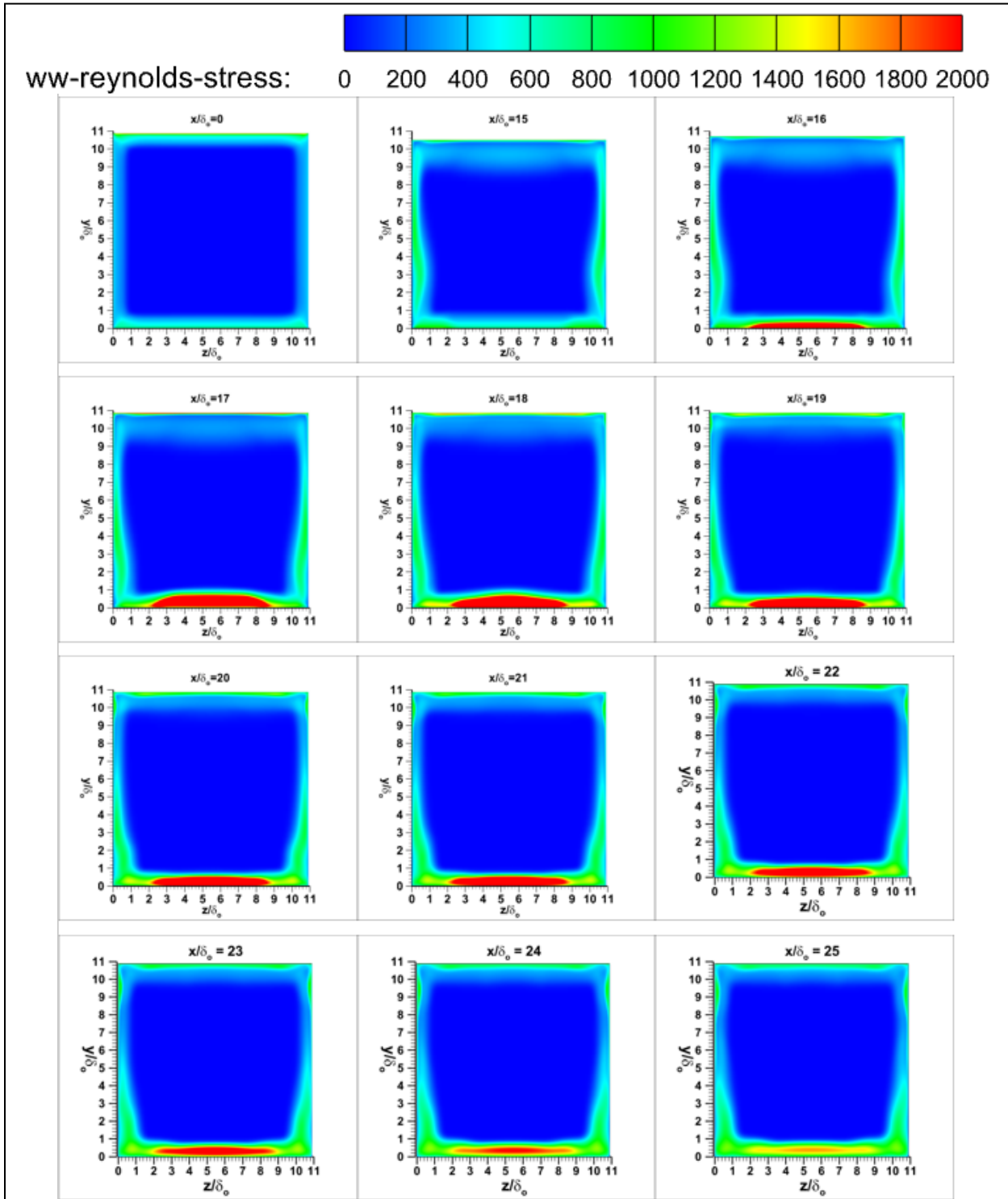
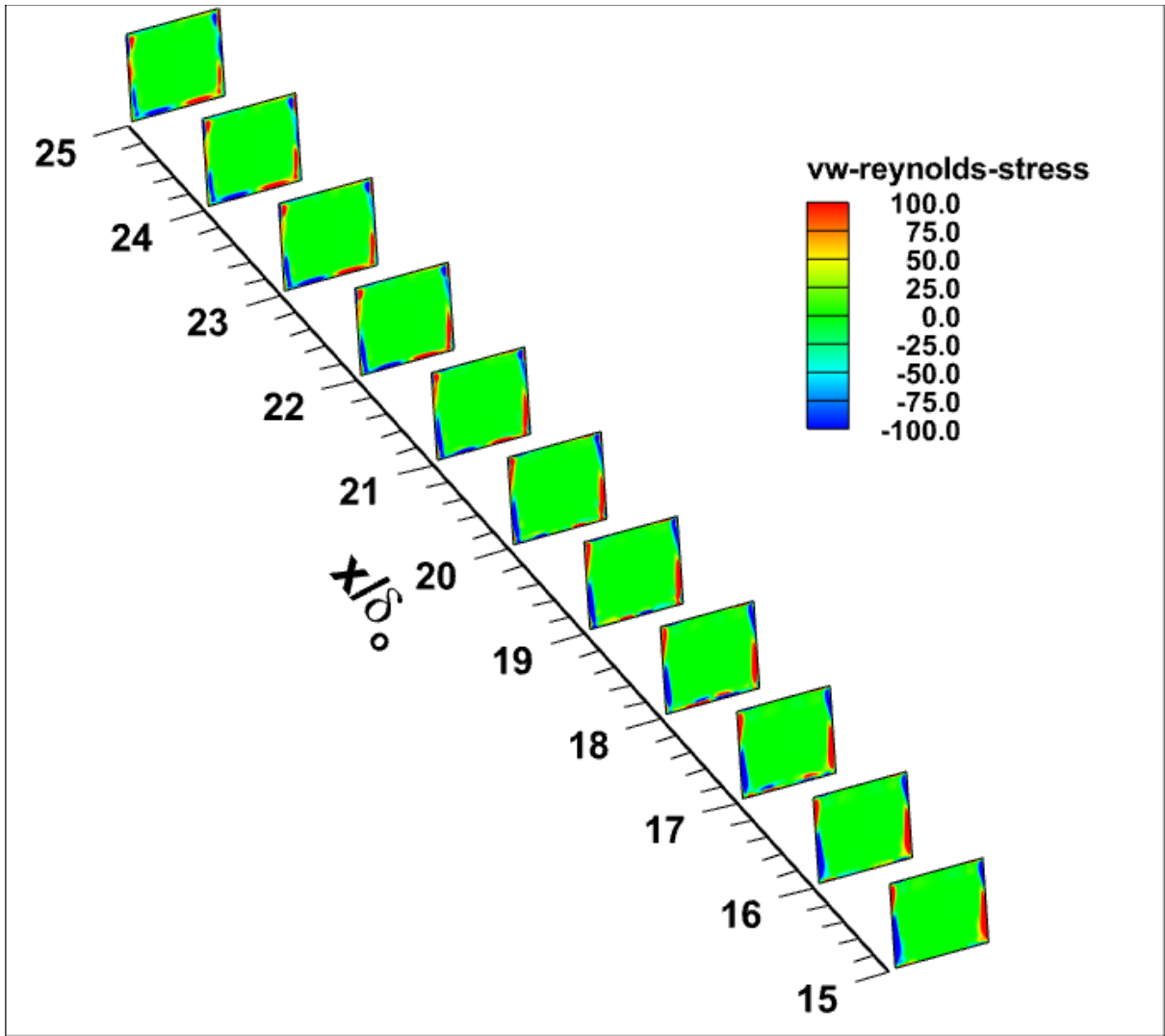


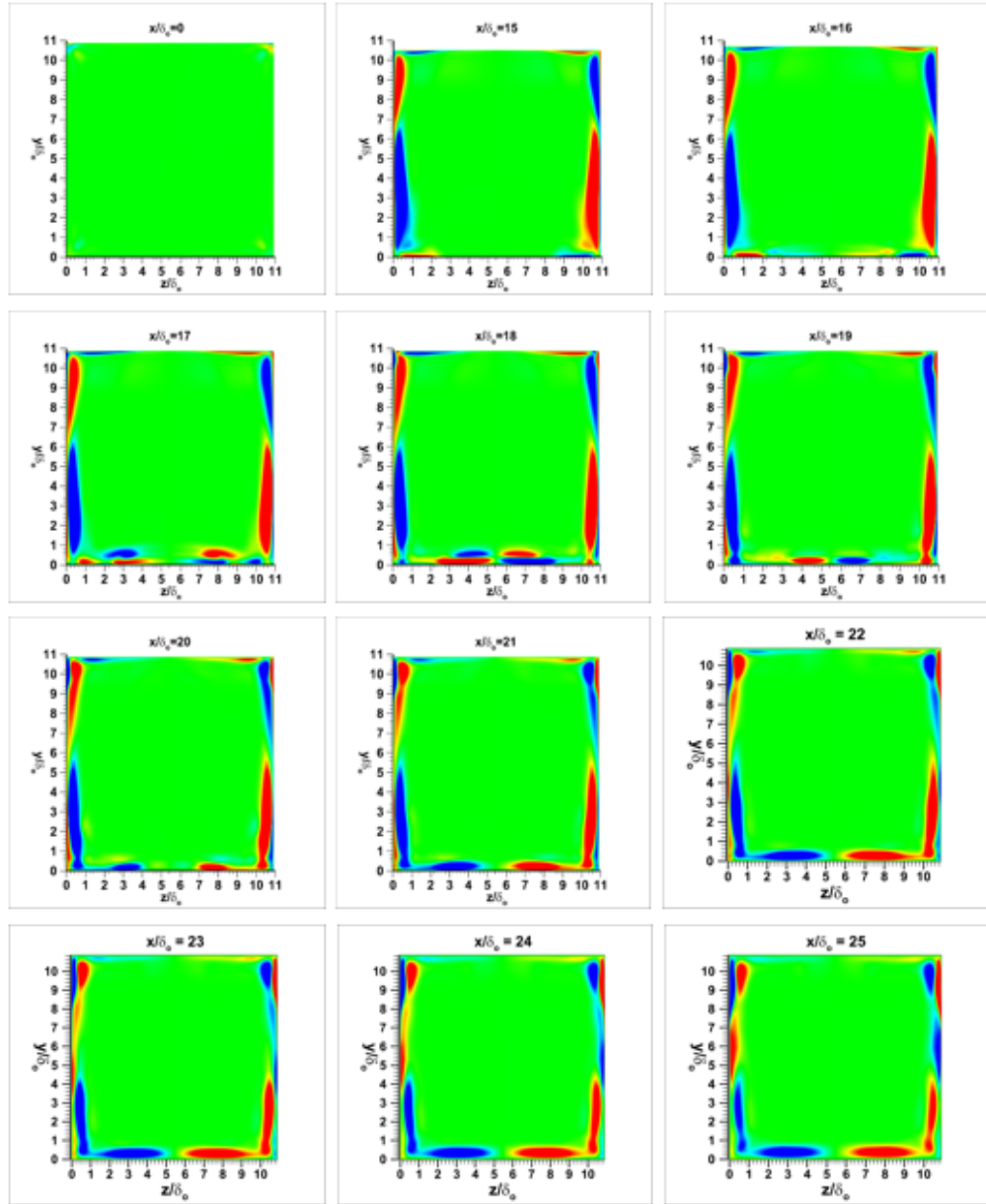
Figure 3.38. Evolution of ww-Reynolds Stress in the stream-wise direction (a) Collective isometric view (b) Separate normal view



(a)

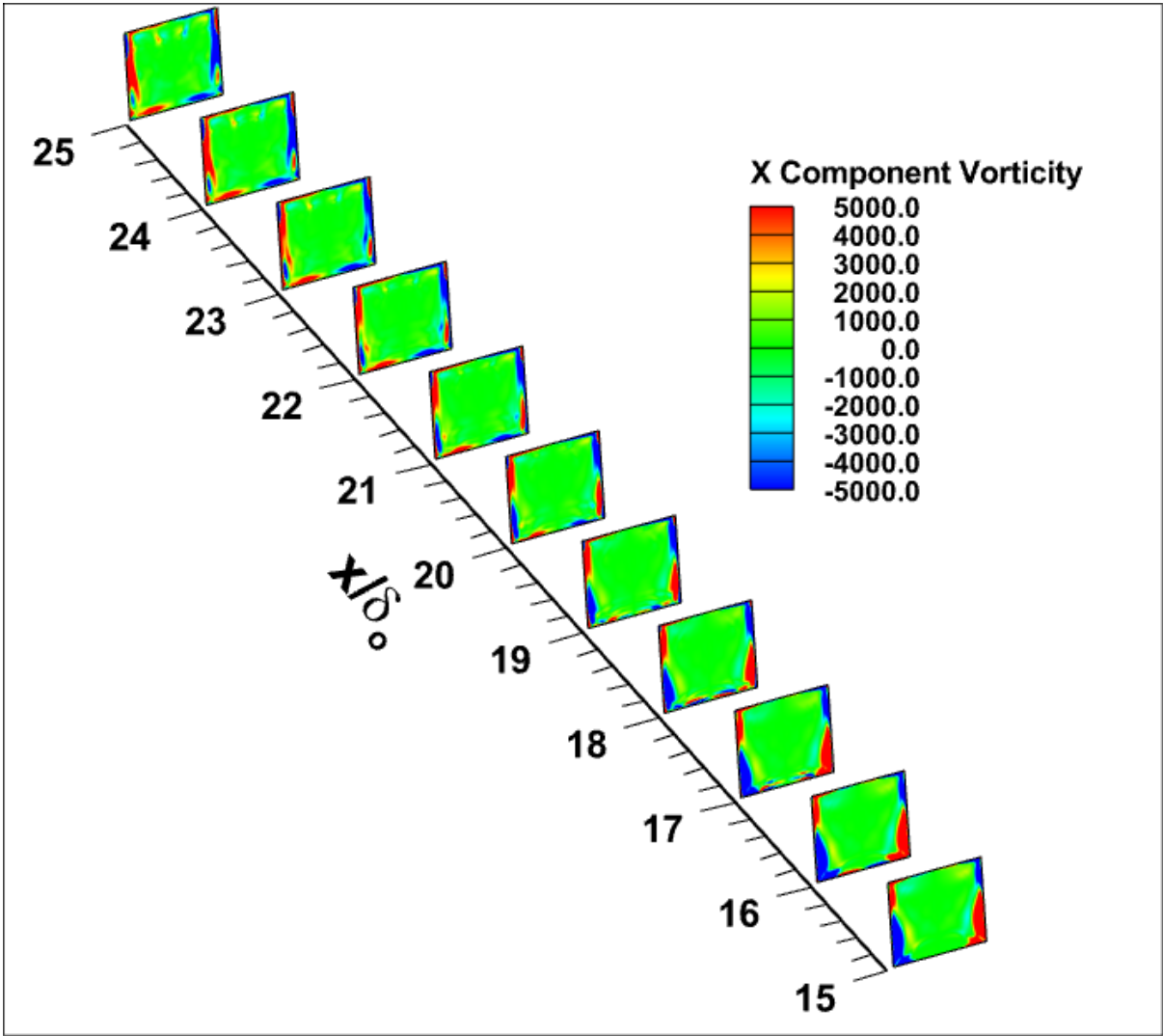


vw-reynolds-stress: -100 -75 -50 -25 0 25 50 75 100



(b)

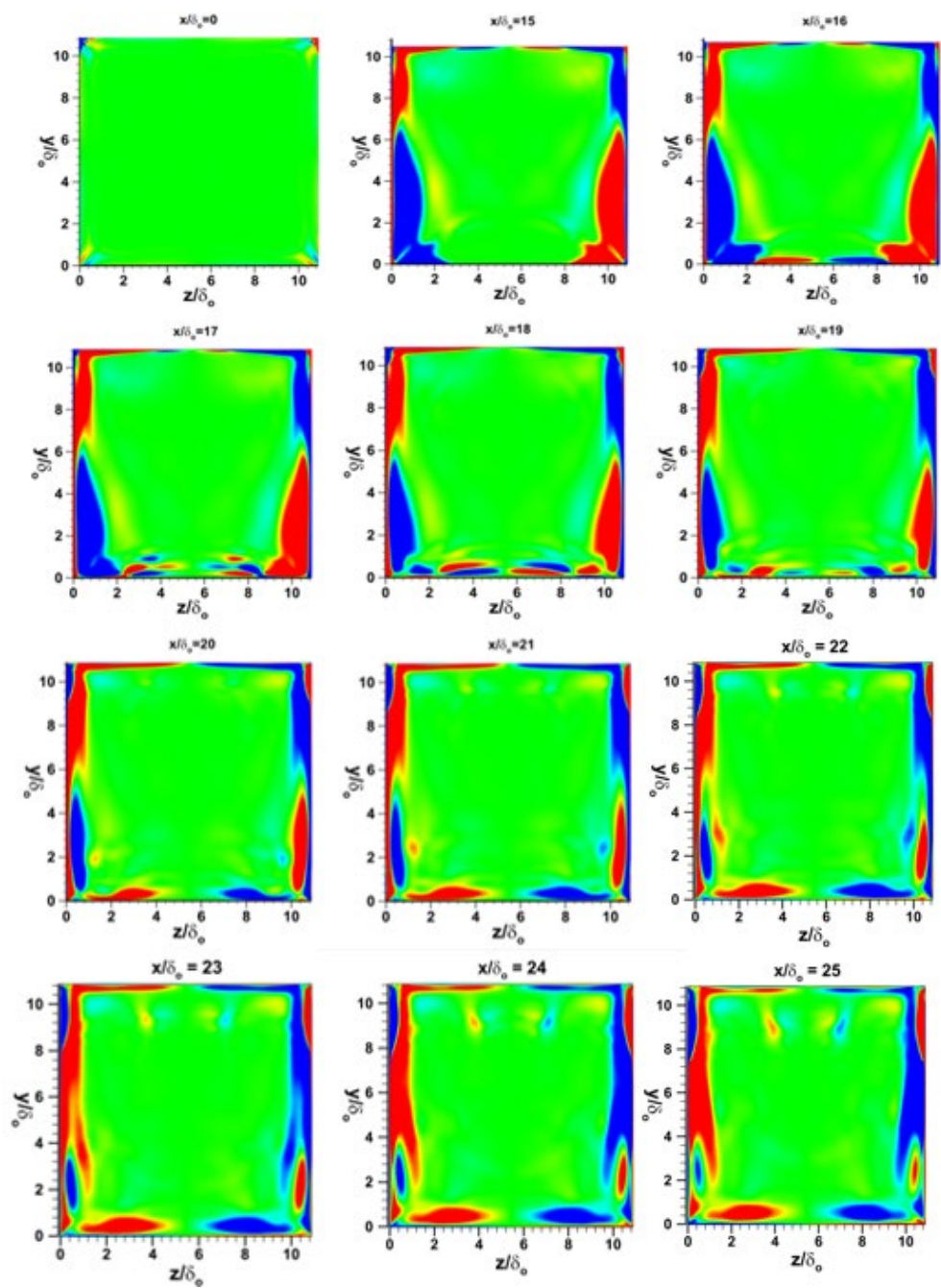
Figure 3.39. Evolution of vw-Reynolds Stress in the stream-wise direction (a) Collective isometric view (b) Separate normal view



(a)



X Component Vorticity: -5000 -4000 -3000 -2000 -1000 0 1000 2000 3000 4000 5000



(b)

Figure 3.40. Evolution of X-vorticity in the stream-wise direction (a) Collective isometric view (b) Separate normal view

Visualization of vortex cores

Figure 3.41 shows the iso-contours of the Q-Criterion, a feature available in Tecplot for viewing the vortex cores. Equations 3.4, 3.5, and 3.6 show the calculation of the Q-Criterion. Ω and S are termed as symmetric and anti-symmetric components of the velocity gradient tensor $\nabla\vec{u}$.

$$\Omega = 0.5 \times (\nabla\vec{u} - (\nabla\vec{u})^T) \quad 3.4$$

$$S = 0.5 \times (\nabla\vec{u} + (\nabla\vec{u})^T) \quad 3.5$$

$$Q = 0.5 \times (|\Omega|^2 + |S|^2) \quad 3.6$$

By setting an appropriate value of the Q-Criterion (in this case a value of 300 is chosen), key features of the SWBLI discussed earlier in the section have been made visible in the figure. The couple of vortices that originate on either side-wall and leading edge of the wedge junction can be observed to be growing under the glancing shock on the side-wall and meeting the bottom wall. The extent of the separation bubble that spans only a fraction of the span-wise length on either sides of the centerline and the tornado vortices that originate of the centerline and propagate downstream are also observed.

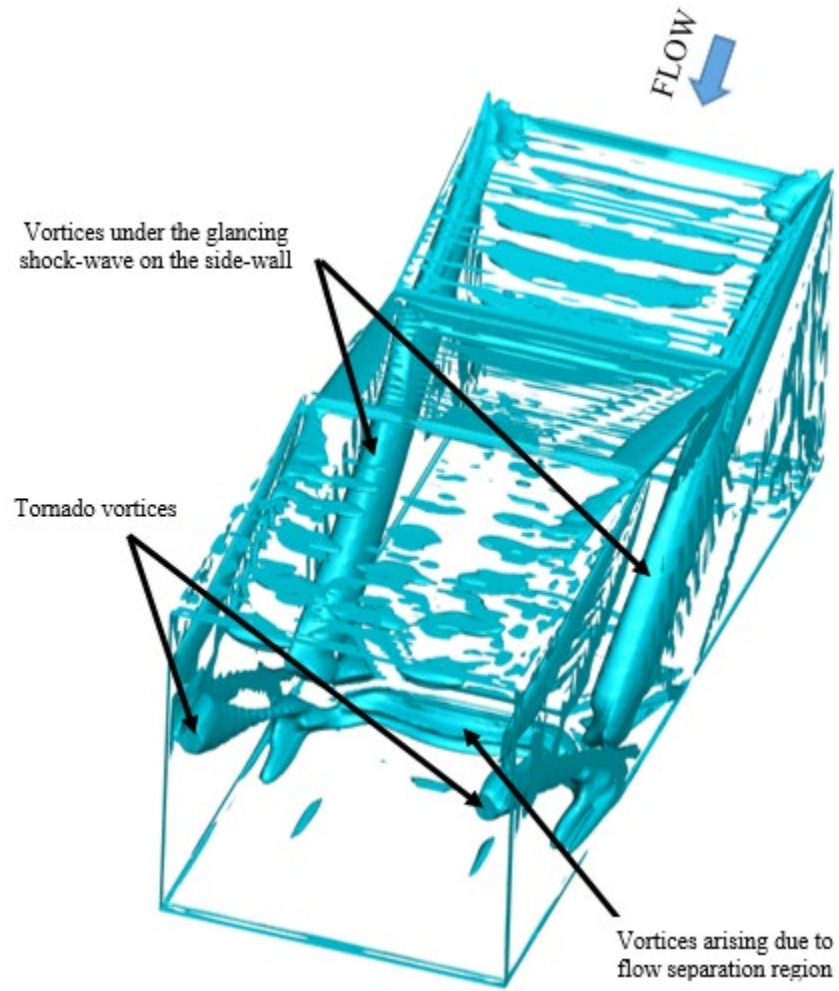


Figure 3.41. Vortices calculated by the Q-Criterion

CONCLUSIONS AND FUTURE WORK

Experimental and computational approaches were adopted to understand the characteristics of wall static pressure in a rectangular channel due to an SWBLI. In this regard, an impinging oblique SWBLI was generated at Mach 2.9 with a 12° wedge at the UA Small Supersonic Wind Tunnel facility. A similar 3D steady and 2D unsteady SWBLI was simulated utilizing ANSYS (Fluent). A qualitative analysis of the experimental SWBLI was made in the form of oil flow visualization on the floor and side-wall, and a quantitative analysis was made using wall static pressure measurements on the floor. The oil flow visualizations were compared with the Fluent solution. Following are the conclusions from this investigation:

1. Both the oil flow visualization and CFD results exhibited flow features observed in the channel flow literature. The floor flow visualization results indicated the presence of a highly 3D SWBLI with a curved primary flow separation boundary. On the same surface, two counter-rotating vortices on either sides of the centerline were also captured by both the approaches. The computational mid-span flow visualization accurately depicted the separation bubble enveloping a recirculating fluid. However, the extent of the bubble predicted by the 3D simulation is smaller than the extent measured through the experiment. In comparison to the mid-span flow visualization, the side-wall flow visualization showed a considerable departure in flow behavior which is expected, due to corner separation.
2. Pressure trends in the downstream direction from both the approaches indicated that the maximum pressure rise behind the shock-wave decreased on moving away from the centerline and approaching the corner. In addition, they also indicated early pressure rise

at the corner. These are respectively due to the swept shock from 3D SWBLI and a premature corner separation. The PSDs provide an insight into the unsteady loading in different regions of the interaction. All the span-wise locations exhibited a broad range of low frequency energy spectrum at select transducer locations. The 2D unsteady simulation exhibited a sharper low frequency peak along analogous points on the wall. It further gave insights into the spectra at key points in the flow-field by highlighting additional frequencies in the low bandwidth.

3. The 3D steady simulation predicted a Reynolds stress behavior dominant in the fore and aft regions of the separation. The predicted components of vorticities indicate a symmetry of vortical structures of opposite senses.

Although inroads have been made into understanding the flow physics in the 3D IOSWBLI through the experimental and computational measurements in this campaign, much needs to be further understood about the areas discussed in this dissertation:

1. The correlations of the side and top wall static pressure signals in the interaction region and their correlation with the static pressure signals in the incoming boundary layer need to be calculated as this will further help in understanding the interdependency of bottom and side-wall interactions.
2. Experiments need to be set up in the wind tunnel to acquire the fluctuating velocities and calculate Reynolds stresses, to validate the corresponding computational results. This can be achieved through PIV measurements.
3. An in depth study of the parameters involved in Reynolds stress and DDES turbulence models will help to explain the discrepancies in pressure rise trends and the measurement of length of separation bubble between experiments and CFD.

All the above tasks can be pursued as future research in the same facility.

REFERENCES

- Adamson Jr., T., and Messiter, A., "Analysis of two-dimensional interactions between shock waves and boundary layers", *Annual Review of Fluid Mechanics* Vol. 12, no. 1, Jan 1980, pp. 103-138.
- Babinsky, H., Oorebeek, J., and Cottingham, T., "Corner effects in reflecting oblique shock-wave/boundary-layer interactions," *51st AIAA Aerospace Sciences Meeting including the New Horizons Forum and Aerospace Exposition*, January 2013, p. 859.
- Bookey, P., Wyckham, C. and Smits, A., "Experimental investigations of Mach 3 shock-wave turbulent boundary layer interactions", *In 35th AIAA Fluid Dynamics Conference and Exhibit* June 2005, (p. 4899).
- Bruce, P., Burton, D., Titchener, N., and Babinsky, H., "Corner effect and separation in transonic channel flows," *Journal of Fluid Mechanics*, Vol. 679, 2011, pp. 247-262.
- Burton, D. M. F., and Babinsky, H., "Corner Separation Effects for Normal Shock-wave/Turbulent Boundary Layer Interactions Rectangular Channels," *Journal of Fluid Mechanics*, Vol. 707, 2012, pp. 287-306.
- Casper, K.M., Wagner, J.L., Beresh, S.J., Spillers, R.W., and Henfling, J.F., "Study of Fluid-Structure Interactions on a Tunable Store in Complex Cavity Flow", AIAA Paper 2017-3125, June 2017.
- Chaganti, N., "An experimental study of coherent structures in shock boundary layer interaction at Mach 3," Ph.D. Dissertation, Dept. of Aerospace Engg. and Mechanics, University of Alabama, Tuscaloosa, AL, 2017.
- Chapman, D. R., Kuehn, D. M., and Larson, H. K., "Investigation of separated flows in supersonic and subsonic streams with emphasis on the effect of transitions," Tech. rep., NACA Technical Note 3869, 1957.
- Clemens, N. T. and Narayanaswamy, V., "Low-frequency unsteadiness of shock wave/turbulent boundary layer interactions," *Annual Review of Fluid Mechanics*, Vol. 46, 2014, pp. 469,492.
- Curran, E. T., Heiser, W. H., Pratt, D., "Fluid phenomena in scramjet combustion systems", *Annual Review of Fluid Mechanics*, Vol. 28, no. 1, 1996, pp. 323-360.
- Dally, J., "An Introduction to Dynamic Photoelasticity," *Experimental Mechanics*, Vol. 20, No. 12, Mar. 1983, pp. 409-416.

- Delery, J.M., and Bur, R.S., "The physics of shock wave/ boundary layer interaction control: last lessons learned," *European Congress on Computational Methods in Applied Sciences and Engineering, ECCOMAS, Barcelona, 2000*.
- Delery, J., Marvin, J. G., and Reshotko, E., "Shock-wave boundary layer interactions," 1986 Andreopoulos, Y., Agui, J.H., Briassulis, G., "Shock Wave & Turbulence Interactions," *Annual Review of Fluid Mechanics*, Vol. 32, no. 1, pp. 309-345, 2000.
- Delery, J.M., "Shock wave/turbulent boundary layer interaction and its control," *Progress in Aerospace Sciences*, Vol. 22, No. 4, 1985, pp. 209-280.
- Delery, J.M., Dussauge, J.P., "Some physical aspects of shock wave/boundary layer interaction," *Shock Waves*, Vol. 19, No. 6, 2009, pp. 453-468.
- Derunov E.K., Zheltovodov, A.A., and Maksimov, A.I., "Development of three-dimensional turbulent separation in the neighborhood of incident crossing shock waves", *Thermophysics and Aeromechanics*, 2008 Mar 15 (1) : 29-54.
- Dolling, D. S., "Fifty Years of Shock-wave/Boundary Layer Interaction Research:What Next?," *AIAA Journal*, Vol. 39, No. 8, 2001, pp. 1517,153.
- Dolling, D. S., "Fluctuating Loads in Shock-wave/Turbulent Boundary Layer Interaction: Tutorial and Update," *31st Aerospace Sciences Meeting & Exhibit*, Jan 1993, p 284.
- Dolling, D. S., "Unsteady phenomena in shock wave/boundary layer interaction," *In AGARD, Special Course on Shock-Wave/Boundary-Layer Interactions in Supersonic and Hypersonic Flows*, Vol. 1, 1993.
- Dolling, D. S., and Brusniak, L., "Separation shock motion in fin, cylinder, and compression ramp-induced turbulent interactions," *AIAA journal*, Vol. 27, No. 6, 1989, pp. 734-742.
- Dupont P., Haddad C., Ardisson J.P, and Debieve J.F., "Space and time organisation of a shock wave/turbulent boundary layer interaction," *Aerospace Science and Technology*, Vol. 9, No. 7, 2005, pp. 561-572.
- Dussauge, J.P., and Piponniau, S., "Shock/boundary-layer interaction: Possible sources of unsteadiness," *Journal of Fluids and Structures*, Vol. 24, 2008, pp. 1166–1175.
- Dussauge, J. P., Saric, W. S., Smith, R., Smits, A., Fernholz, H., Finely, P., and Spina, E., "Turbulent boundary layers in subsonic and supersonic flow," 1996.
- Dussauge, J.P., Dupont, P., and Debieve, J.F., "Unsteadiness in shock wave boundary layer interactions with separation," *Aerospace Science and Technology*, Vol. 10, 2006, pp. 85-91.
- Eagle, W. E. and Driscoll, J. F., "Shock wave boundary layer interactions in rectangular inlets: three-dimensional separation topology and critical points," *Journal of Fluid Mechanics*,

Vol. 756, Sep 2014, pp. 328–353.

Eagle, W., Driscoll, J. and Benek, J., “Experimental investigation of corner flows in rectangular supersonic inlets with 3D shock-boundary layer effects”, *In 49th AIAA Aerospace Sciences Meeting including the New Horizons Forum and Aerospace Exposition*, 2011, p. 857.

Eagle, W.E., “An experimental study of three-dimensional inlet shock-boundary layer interactions”, Doctoral dissertation, University of Michigan, 2012.

Edwards, J. R., "Numerical simulations of shock/boundary layer interactions using time-dependent modeling techniques: A survey of recent results," *Progress in Aerospace Sciences*, Vol. 44, No. 6, 2008, pp. 447-465.

Erengil, M. E., Dolling, D. S., “Unsteady wave structure near separation in a Mach 5 compression ramp interaction,” *AIAA journal*, Vol. 29, No. 5, 1991, pp. 728-735.

Ferri, A., “Experimental Results with Airfoils Tested in the High-speed Tunnel at Guidonia”, Natl Advisory Committee for Aeronautics, No. 17, NACA Technical Memorandum 946, Sep, 1939.

Flaherty, W.P., Reedy, T., Elliot, G.S., Austin, J.M., Schmit, R.F., and Crafton, J.W., “Investigation of Cavity Flow Using Fast Response Pressure Sensitive Paint,” *AIAA Journal*, Vol. 52, No. 11, 2014, pp 2462-2470.

Friedlander, D.J., Dudek, J.C., and Liou, M.F., “Prediction of Turbulent Diffusing Flows Using FUN3D”, *AIAA SCITECH 2022 Forum* (p. 1168).

Gaitonde, D. V., “Progress in shock wave/boundary layer interactions,” in 43rd Fluid Dynamics Conference, 2013.

Gaitonde, D., and Shang, J. S., “The Structure of a Double-Fin Turbulent Interaction at Mach 4,” *AIAA Paper 94-2810*, June 1994.

Gaitonde, D., Shang, J. S., and Visbal, M. R., “Structure of a Double-Fin Turbulent Interaction at High Speed,” *AIAA Journal*, Vol. 33, No. 2, 1995, pp. 193–200.

Gaitonde, D. V., and Shang, J. S., “On 3-D Shock-Wave/Turbulent Boundary Layer Interactions at Mach 4,” *AIAA Paper 96-0043*, Jan. 1996.

Gaitonde, D., Shang, J. S., Garrison, T. J., Zheltovodov, A. A., and Maksimov, A. I., “Evolution of the Separated Flow Field in a 3-D Shock Wave/Turbulent Boundary Layer Interaction,” *AIAA Paper 97-1837*, June 1997.

- Gaitonde, D., Shang, J. S., Garrison, T. J., Zheltovodov, A. A., and Maksimov, A. I., “Three-Dimensional Turbulent Interactions Caused by Asymmetric Crossing-Shock Configurations,” *AIAA Journal*, Vol. 37, No. 12, 1999, pp. 1602–1608.
- Green, J., “Interactions between shock waves and turbulent boundary layers”, *Progress in Aerospace Sciences* Vol. 11, Jan 1970, pp. 235-340.
- Gregory, J.W., Asai, K., Kameda, M., Liu, T., and Sullivan, J.P., “A Review of Pressure-sensitive Paint for High Speed and Unsteady Aerodynamics,” *Proceedings of the Institution of Mechanical Engineers, Part G, Journal of Aerospace Engineering*, 1 Feb. 2008, Vol. 222 , No.-2, pp. 249-290.
- Hegde, A., Funderburk, M., Hill, J., and Narayanaswamy, V., “Experimental Investigation into Shock Induced Corner Boundary Layer Separation,” *45th AIAA Fluid Dynamics Conference*, 2015, p. 2934.
- Hegde, A., Sellers, G., Ölçmen, S. M., and Hubner, J.P., “Pressure and Strain Measurement on an Inclined Flap in Supersonic Flow Using a Dual-Layer Luminescent Coating,” *AIAA Paper 2020-2969*, June 2020, <https://doi.org/10.2514/6.2020-2969>.
- Hegde, A., Chen, M., Olcmen, S., Hubner, J.P., Crafton, J. and Ryan, C., “Pressure and Strain Measurement on a Thin Clamped Plate in Supersonic Flow using a Dual-Layer Luminescent Coating”, *AIAA Aviation Forum 2021 Forum* (p. 2920).
- Hildebrand, N., Dwivedi, A., Nichols, J.W., Jovanović, M.R., and Candler, G.V., "Simulation and stability analysis of oblique shock-wave/boundary-layer interactions at Mach 5.92." *Physical Review Fluids*, Vol. 3, No. 1, 26 Jan. 2018, pp. 013906.
- Hingst, W.R. and Williams, K.E., “Interaction of two glancing, crossing shock waves with a turbulent boundary-layer at various Mach numbers”, 1991, (No. E-6566).
- Holman, J.P., “ *Experimental Methods for Engineers*”, McGraw-Hill Book Company, New York, 1978.
- Hubner, J.P., Hegde, A., Chism, K., Ölçmen, S.M. and Crafton, J., “Full-Field Pressure and Strain Measurement Technique Using a Dual-Layer Luminescent Coating”, *AIAA Journal*, pp.1-11, 2020, <https://doi.org/10.2514/1.J060058>.
- Humble, R. A., Elsinga, G. E., Scarano, F., and Van Oudheusden, B. W., “Three-dimensional instantaneous structure of a shock wave/turbulent boundary layer interaction,” *Journal of Fluid Mechanics*, Vol. 622, 2009, pp. 33-62.
- Kelly, P.A., “*Mechanics Lecture Notes: An Introduction to Solid Mechanics*”, The University of Auckland 2013.

- Ketchum, A., Bogdonoff, S., and Fernando, E., "Preliminary study of the interactions caused by crossing shock waves and a turbulent boundary layer", 27th Aerospace Sciences Meeting 1989, Jan 9, (p. 359).
- Knight, D., Yan, H., Panaras, A. G. and Zheltovodov, A. A., "Advances in CFD Prediction of Shock-wave Turbulent Boundary Layer Interactions," *Progress in Aerospace Sciences* (39), 2003, pp 121-184.
- Kubota, H. and Stollery, J. L., "An experimental study of the interaction between a glancing shock-wave and a turbulent boundary layer, *Journal of Fluid Mechanics*, Vol. 116, 2014, pp. 431-458.
- Lapsa, A. P., "Experimental Study of Passive Ramps for Control of Shock Boundary Layer Interactions" Ph.D. thesis, University of Michigan, 2009.
- Lesniak, J.R., and Zickel, M.J., "Applications of Automated Grey-field Polariscope," *Proceedings of Society of Experimental Mechanics*, 1 Jun. 1998, pp. 298-301.
- Liu, X., Zhang, L., Ji, Y., He, M., Liu, Y., and Peng, D., "Fast PSP measurement of three-dimensional low-frequency unsteadiness in sidewall-confined shock wave/turbulent boundary layer interaction," *Experimental Thermal and Fluid Science*, Jan 17:110599, 2022.
- Liu, T, and Sullivan, J.P., *Pressure and Temperature Sensitive Paints*, Springer-Verlag, Berlin, 2004.
- Mears, L., Arora, N., and Alvi, F.S., "Flowfield response to controlled perturbations in swept shock/boundary-layer interaction using unsteady PSP, " *AIAA Scitech 2019 Forum*, p. 0094. 2019.
- Morajkar, R. R., D., Klomparens, R. L., Eagle, W. E., Driscoll, J. F., and Gamba, M., "Flow Separation Associated with 3-D Shock-wave Boundary Layer Interaction (SBLI)," *AIAA SciTech Forum 52nd Aerospace Sciences Meeting*, January, 2014.
- Morajkar, R. R., and Gamba. M., "Turbulence characteristics of supersonic corner flows in a low aspect ratio rectangular channel." 54th AIAA Aerospace Sciences Meeting, 2016, pp. 1590.
- Morajkar, R. R., Klomparens, R.L., Eagle E.W., Driscoll, J.F., Gamba, M., and Benek, J.A., "Relationship between intermittent separation and vortex structure in a three-dimensional shock/boundary-layer interaction." *AIAA Journal*, Vol. 54, No. 6, Jun. 2016, pp. 1862-1880.
- Narayanswami, N., Knight, D., Bogdonoff, S., and Horstman, C., "Crossing shock wave-turbulent boundary layer interactions", 29th Aerospace Sciences Meeting, 1991, Jan 1, (p. 649).
- Oskam, B., I. E. Vas, and S. M. Bogdonoff, "Oblique Shock wave/Turbulent Boundary-Layer Interactions in Three Dimensions at Mach 3," Pt. I. Air Force Flight Dynamics, Wright-Patterson Air Force Base, OH, AFFDL-TR-76-48, June 1976.

- Pandey, A. and Casper, K.M., "Hypersonic fluid-structure interaction on the control surface of a slender cone", *AIAA Scitech 2021 Forum*, p. 0909.
- Pandey, A., Casper, K.M., Spillers, R., Soehnel, M. and Spitzer, S., "Hypersonic shock wave-boundary-layer interaction on the control surface of a slender cone", *AIAA Scitech 2020 Forum*, p. 0815.
- Piponniau, S., Dussauge, J.P., Debieve, J.F., Dupont, P., "A simple model for low-frequency unsteadiness in shock-induced separation," *Journal of Fluid Mechanics*, Vol. 629, 2009, pp 87-108.
- Pirozzoli, S., Grasso, F., "Direct numerical simulation of impinging shock wave/turbulent boundary layer interaction at $M=2.25$," *Physics of Fluids*, 18(6), 2006, p.065113.
- "Porous, Fast Responsive Pressure Sensitive Paint: FP-XXX," Innovative Scientific Solutions, Inc., Dayton, OH.
- Riggins, D., Tackett, R., Taylor, T., Auslender, A., "Thermodynamic analysis of dual-mode scramjet engine operation and performance", *AIAA Paper*, Vol. 8059, 2006, p. 2006.
- Ringuette, M. J., Wu. M., Martin, M. P., "Low Reynolds Number Effects in a Mach 3 Shock Turbulent Boundary Layer interaction," *AIAA Journal*, Vol. 46, No. 7, 2008.
- Sadagopan, A., Huang, D., Jirasek, A., Seidel, J., Pandey, A. and Casper, K.M., "An Experimental and Computational Correlation Study for Fluid-Thermal-Structural Interaction of a Control Surface in Hypersonic Flow", *AIAA SciTech 2022 Forum*, p. 0291.
- Settles, G.S., and Dodson, L.J., "Supersonic and Hypersonic Shock/Boundary-Layer Interaction Database," *AIAA Journal*, Vol. 32, No. 7, 1994, pp. 1377-1383.
- Stanbrook, A., "An Experimental Study of a Glancing Interaction between a Shock-wave and a Boundary Layer," in *British ARC CP-555*, July 1960.
- Timoshenko, S. and Woinowsky-Krieger, S. "*Theory of plates and shells*", McGraw-Hill New York, 1959
- Tech Note TN-706-1, "Corrections to Photoelastic Coating Fringe-Order Measurements," Micro-Measurements, Rayleigh, NC, August 2015.
- Vishwanath, P., "Shock wave-turbulent-boundary-layer interactions and its control: A survey of recent developments," *Sadhana*, Vol. 12 Part 1 & 2, 1 Feb. 1988, pp. 45-104.
- Wang, B., Sandham, N., Hu, Z., and Liu, W., "Numerical study of oblique shock-wave/boundary-layer interaction considering sidewall effects", *Journal of Fluid Mechanics*, Vol. 767, Mar 2015, pp. 526-561.

- Wu, M., Martin, M. P., "Analysis of shock motion in shockwave and turbulent boundary layer interaction using direct numerical simulation data," *Journal of Fluid Mechanics*, Vol. 594, 2008, pp. 71-83.
- Zandman, Redner, F.S., and Dally, J.W., *Photoelastic Coatings*, Iowa State University Press, Ames, IA, 1977.
- Zheltovodov, A. A., and Maksimov, A. I., "Hypersonic Crossing Shock-waves / Turbulent Boundary Layer Interactions," Russian Academy of Sciences, TR Final Rept., EOARD Contract F61775-98-WE091, Novosibirsk, Russia, April 1999.
- Zheltovodov, A., "Shock waves/turbulent boundary-layer interactions--fundamental studies and applications," *AIAA paper*, vol. 1977, p. 1996.
- Zheltovodov, A. A., "Some Advances in Research of Shock-wave Turbulent Boundary Layer Interactions," *44th AIAA Aerospace Sciences Meeting and Exhibit*, AIAA Paper 2006-496, January, 2006.

APPENDIX-I

Pressure and Strain Measurement on a Thin Clamped Plate in Supersonic Flow using a Dual Layer Luminescent Coating

Background and theory

Pressure sensitive paints

The PSP technique (Liu (2004)) has become a common measurement technique in the aerodynamic community and successful implementation of fast pressure sensitive paints (Fast-PSP) have followed due to improvements in paint formulations, ultra-bright light-emitting diodes (LEDs) and high-quantum-efficiency, high-speed digital cameras. A typical PSP is composed of two parts: an oxygen-sensitive fluorescent molecule and an oxygen permeable binder. When a luminescent molecule absorbs a photon, it transitions to an excited energy state. The molecule then typically recovers to the ground state by the emission of a longer-wavelength photon (loss of energy due to thermal relaxation). In some materials, oxygen can interact with the molecule such that the transition to the ground state is non-radiative; this process is known as oxygen quenching. The rate at which these two processes compete is dependent on the partial pressure of oxygen, with a higher oxygen pressure increasing the quenching of the molecule and decreasing the measured luminescence.

Image-based pressure measurements using PSP are accomplished by coating the model surface with the paint and illuminating the surface with light of the appropriate wavelength (usually in the UV to blue range) to excite the luminescent molecules within the coating. The surface is imaged through a bandpass or long-pass filter (LPF) to separate the luminescent signal from the excitation light. The luminescent signal from the paint is not only a function of pressure

but also varies with illumination intensity, probe concentration, paint layer thickness, and detector sensitivity. These spatial variations result in a non-uniform intensity map from the painted surface. The spatial variations are usually eliminated by taking the ratio of the luminescent intensity of the PSP at an unknown test condition, I , and a known reference condition, I_{ref} . Most PSPs are modeled following the linear Stern-Volmer relationship (Liu (2004)), as shown in Eq. 1

$$\frac{I_{ref}}{I} = A + B \frac{P}{P_{ref}} \quad \text{A.1.1}$$

a second order polynomial, or a nonlinear dual-sorption model. For Eq. 1, A and B are temperature dependent coefficients and P is pressure.

Conventional PSP formulations typically use a polymer as a binder material. Polymer binders enable the diffusion of oxygen into the embedded dye molecules. Hybrid paint formulations use ceramic particles in the paint, creating a porous structure that decreases the effective thickness, increases the effective diffusivity, and extends the pressure range. This results in a fast-response system with favorable signal-to-noise ratio. Hybrid PSP formulations are capable of detecting pressure fluctuations up to 20 kHz, and unsteady pressure measurements have been demonstrated on a variety of models (Crafton et al. (2015), Flaherty et al. (2014), Gregory et al. (2008), Casper (2017)). Fast-PSP has also been paired with stereo-photogrammetry techniques to measure pressure and deformation (Spottswood et al. (2013)).

For this approach, a custom fast-response PSP formulation was developed by ISSI. The purpose of this new formulation is to facilitate fast response from the PSP, while allowing polarized light to pass through the PSP layer into the underlying strain-sensitive optical coating. The porous media in the PSP was selected to maximize transmission of light at 620-nm while maintaining the polarization of the lighting.

Photoelastic coatings

Photoelastic coatings (PEC) (Zandman et al. (1977)) have been used in the structural testing community for many years, primarily for static testing but applicable to dynamic testing related to stress wave propagation and impact (Dally (1983)). The dynamic response of photoelastic coatings is high due to the propagation of wave speeds through the thin coatings. Typical PEC density and elastic modulus are approximately 1000 kg/m^3 and 1 GPa , respectively. For a 1 mm thick coating, the theoretical response time based on wave propagation would be approximately $1 \mu\text{s}$.

Photoelastic coatings work on the principle of birefringence: the ability of a material to transmit light at different velocities relative to the polarization and propagation of the incoming light. In application, a reflective photoelastic coating is adhered to the surface of the model of interest and illuminated with circular polarized light (a combination of a linear polarizer (LP) and achromatic quarter-wave plate (QWP) rotated 45° relative to the polarizer). The stress induced change in the polarization as light passes into and reflects out of the coating is measured using a second linear polarizer, often called an analyzer, and a camera (Lezniak and Zickel (1998)). As with all birefringent coatings, the change in polarization is related to the maximum shear strain, γ , in the plane perpendicular to the path of the polarized light passing through the specimen. To quantify the strain field, a sequence of images at different analyzer angles is necessary. The development of micropolarizer masks attached to the imager chip eliminates the need of an exterior rotating analyzer and allows multiple analyzer states, typically four, to be acquired with each image.

The emission intensity of a PEC after it passes through the analyzer is characterized by Eq. 2 [17],

$$\frac{I_{\alpha}}{I_{avg}} = 1 + F \sin(2\alpha - 2G) \quad \text{A.1.2}$$

where I_{α} is the emission intensity at a pixel for a specific analyzer (or micropolarizer) orientation, I_{avg} is the average measured emission intensity over 180° analyzer rotation, α is the analyzer (or micropolarizer) angle, F is the magnitude of the optical strain response (OSR, shown as I_{amp} in Fig. 1) and G is the phase of the OSR. The phase is related to the principal strain direction relative to the 0° analyzer (or pixel) angle. The OSR is a function of the in-plane maximum shear strain, γ .

For a single-layer, reflective PEC, the OSR is

$$F = \phi \sin\left(\frac{\gamma}{\eta}\right), \quad \eta = \frac{\lambda_{ex}}{4\pi h K} \quad \text{A.1.3}$$

where ϕ is the polarization efficiency and η is the coating characteristic which is a function of the coating thickness, h , the coating optical sensitivity, K , which is a material property of the coating, and the excitation wavelength, λ_{ex} . The polarization efficiency and coating characteristic are determined through *in situ* or *a priori* calibration. While the latter is easier to implement if known, the former is more accurate, assisting in the elimination of systematic errors that can arise from batch variance, surface reflectance, optical interference and environmental dependencies. Polarization efficiency, ϕ , can account for attenuation effects such as the depolarization of excitation and non-ideal polarization extinction ratio of the camera pixels. The coating characteristic, η , can be thought of as a characteristic strain value that affects the curvature and sensitivity of the OSR amplitude. A larger coating characteristic decreases the OSR sensitivity but extends its range. This is important to reduce the difficulty in determining a unique solution for the strain. For strain values beyond the first OSR peak of $\gamma \geq \eta\pi/2$, the relationship is multi-valued requiring fringe counting and phase-unwrapping techniques. There are multiple approaches

to extend OSR range: decrease the coating thickness, use a PEC with lower optical sensitivity, K , or increase the excitation wavelength.

Dual-layer technique

The technique used in this investigation is a two LED approach: one blue LED without polarization optics used to excite the PSP (pressure response) and a red LED with polarization optics (LP/QWP pair) used to detect stress-induced polarization of the PEC (strain response) (Hegde et al. (2020, 2021), Hubner et al.(2021)). Figure A.1.1 is a schematic of the two LED approach. The reflective PEC is first adhered to the surface. Then, PSP is applied on top of the PEC without an opaque, white undercoat. The camera and two LEDs are triggered with an external source. The camera is triggered at twice the frequency of the LEDs. The LEDs are triggered 180° out-of-phase with each other, and their duty cycle is less than 50% to synchronize with the camera

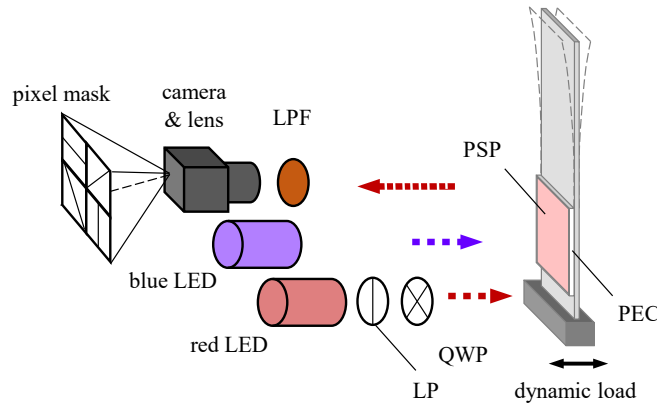


Figure A.1.1. Schematic of the dual-LED/single-camera configuration; the red and blue LEDs are pulsed out-of-phase with each other

exposure time. A long-pass (or bandpass) optical filter is necessary to block the blue excitation and allow the PSP emission and the PEC reflection to pass through to the imager. The light is imaged through a pixelated polarizer mask on the digital camera. Each pixel measures an intensity relative to the polarization orientation of that pixel. A typical micropolarizer array has four discrete orientations in a 2×2 pattern: $0/45/90/135^\circ$. The group of four pixels is called a superpixel.

The PSP emission and PEC reflection intensities recorded by each pixel are dependent on pressure, strain, excitation intensity and coating thickness/concentration. The pressure information is tracked by the average of the four pixel orientations, and the strain information is modeled by the variance of the pixel orientations. However, the information is separated by alternating images from blue and red LED pulses. For a superpixel exposed to the blue LED,

$$\bar{I}_b = \frac{\Sigma I_{b,\alpha}}{4} \quad \text{A.1.4}$$

In terms of the Stern-Volmer pressure response (blue LED image),

$$\frac{\overline{I_{b,ref}}}{\bar{I}_b} = A + B \frac{P}{P_{ref}} \quad \text{A.1.5}$$

The strain response for the two-layer coating exposed to the red LED is modeled by

$$\frac{I_{r,\alpha}}{\overline{I_{r,\alpha}}} = 1 + \phi \sin\left(\frac{\gamma}{\eta}\right) \sin(2\alpha - 2G) \quad \text{A.1.6}$$

where $I_{r,\alpha}$ is the intensity of each pixel for $\alpha = 0/45/90/135^\circ$. Relative to the pixel orientation, α , the measured intensity follows a sinusoidal curve $\sin(2\alpha - 2G)$. The amplitude of the corresponding curve fit, or the OSR, is $\sin\left(\frac{\gamma}{\eta}\right)$. The variance across the four pixels is referenced to the average of the four pixels. To calculate OSR and the phase, and hence strain and principal direction, the standard deviation of $\frac{I_{r,\alpha}}{\overline{I_{r,\alpha}}}$ for a superpixel can be used,

$$\text{OSR} = \phi \sin\left(\frac{\gamma}{\eta}\right) = \sqrt{\frac{2(n-1)}{n}} \text{stdev}\left(\frac{I_{r,\alpha}}{\overline{I_{r,\alpha}}}\right) \quad \text{A.1.7}$$

where n is the number of evenly spaced pixel orientations (in this case $n = 4$). To calculate the phase,

$$2G = \text{atan2} \left(\frac{I_0 - I_{90}}{I_{45} - I_{135}} \right) \quad \text{A.1.8}$$

When calculating the corresponding strain from the measured OSR, multiple strain values could result. This requires fringe counting or phase unwrapping. By limiting the coating thickness to less than a quarter-fringe, then fringe counting is eliminated. The fringe order, N , is

$$N = \frac{\gamma}{2\pi\eta} \quad \text{A.1.9}$$

This corresponds to $N < \frac{1}{4}$ or $\gamma_{max} < \frac{\lambda_{ex}}{8hK}$

With PECs, the reference state is generally an unloaded state (no applied load). However, a non-zero OSR may be detected at the reference state due to the coating application, the age of the coating, a stress-induced state at the reference condition (for example the weight of the specimen inducing a load or thermal difference between application and testing) or the extent the excitation is not circular polarized. This is referred to as parasitic or residual birefringence (Micro-Measurements (2015)). This is not to be confused with a residual stress that might exist in the specimen prior to coating application. A PEC would not detect a pre-existing residual strain unless somehow the specimen was unloaded after the PEC was applied and in a manner without damaging the PEC. If a non-zero (above the noise resolution) OSR exists for the reference case, then it can be corrected by treating the load and reference states as vectors and subtracting the reference state from the load state. This is further discussed in Hubner et al. (2020).

Experiment

Experimental facility and set-up

All the experiments were conducted at the UA Mach 3 supersonic wind tunnel facility (Fig. A.1.2). The tunnel is a blow-down type that has a 76 mm x 76 mm test section. Stagnation pressure and temperature is nominally between 520 – 620 *kPa* and 300 *K* (all pressures absolute unless stated otherwise). During a typical run, the free stream static pressure is nominally 16-19 *kPa_{abs.}* Figure A.1.3 shows a schematic of the experimental set-up. A circular plate coated with PSP and PEC is mounted to a cylindrical base to form a clamped boundary condition. The side wall of the cylindrical base is fitted to the tunnel wall and sealed with an o-ring such that the coating on the clamped plate is flush with the tunnel wall. This results in a pressure difference across the clamped plate during the wind tunnel run: atmospheric pressure on the back side and sub-atmospheric pressure on the tunnel (coated) side. A 12° right-angled wedge on the opposite wall generates an oblique shock-wave that impinges the portion of the boundary layer formed on the clamped plate, generating a SWBLI. The clamped plate is visible through an optical window (108 *mm* diameter) downstream of the wedge.

For the planned tests, plates of two thicknesses, 0.0016 m and 0.005 m, made of aluminum 6061-T6 alloy were selected. The diameter of each of the plates is 70 mm. The plate with the larger thickness was sized to have negligible deflection. Assuming a uniform pressure difference across the plate, the plate experiences the maximum shear strain at the clamped edge and maximum deflection at the center. (Kelly (2013)). The theoretical principal strains and maximum shear strain, γ , distributions of a thin, clamped plate relative to the boundary values are shown in Fig. A.1.4 for an applied uniform pressure load. The maximum shear strain increases radially from the center towards the boundary. At the center, $\varepsilon_r = \varepsilon_\theta \rightarrow \gamma = 0$. Thus, because the test section pressure

during the run is sub-atmospheric, the strain profile for the thin plate is expected to be larger at the boundaries. The corresponding principal stress direction is expected to follow radial lines.

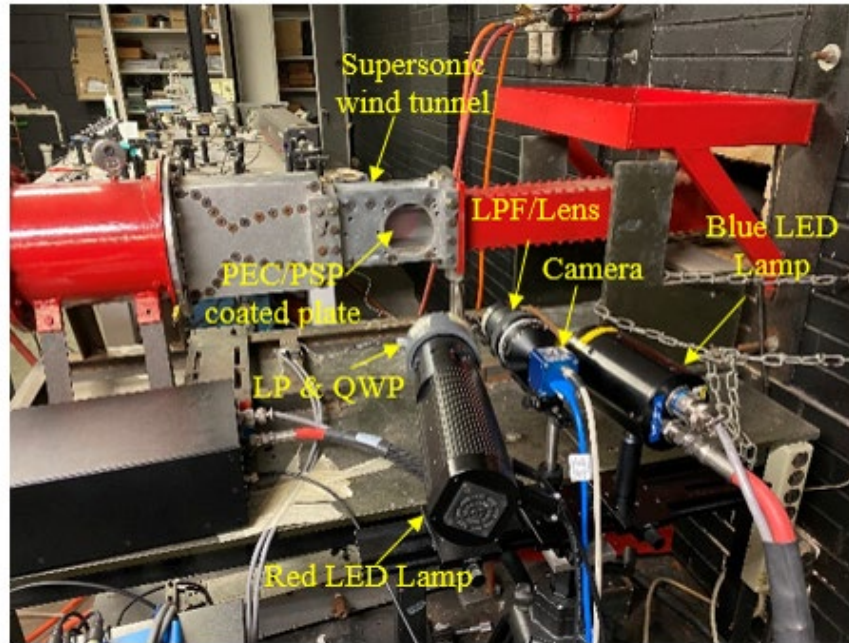


Figure A.1.2. Experimental set-up

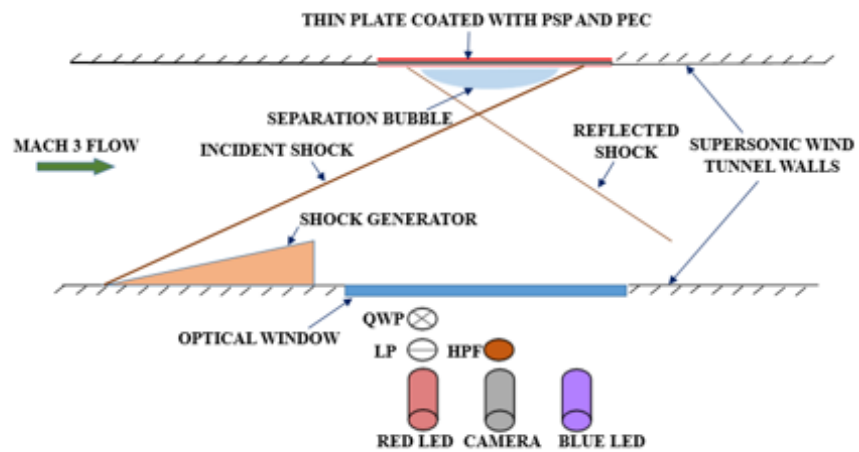


Figure A.1.3. Schematic of the flow environment over the thin plate

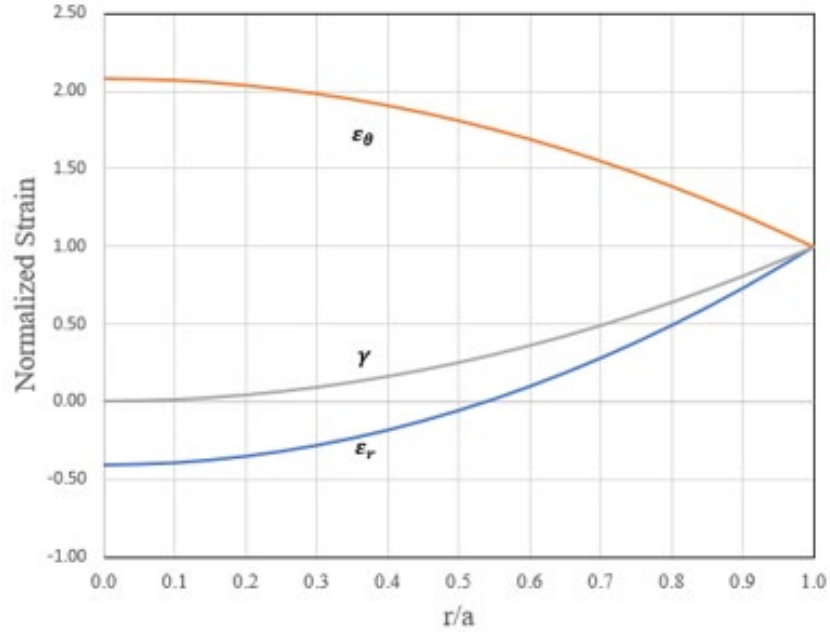


Figure A.1.4. Variation of strains from center to edge of a clamped plate

Results of the preliminary calculation for the two plates are listed in Table A.1.1.

Table A.1.1. Structural response of the clamped plates

Plate Thickness [mm]	Max Deflection [mm]	Max shear strain [$\mu\epsilon$]	Resonant Frequency [Hz]
1.6	0.07	390	1050
5	0.003	40	3140

Figure A.1.2 also shows the optical set-up of the experiment. To excite the PSP, an air-cooled ISSI LM3X 400 nm (UV, 36 W) LED lamp was used. To illuminate the PEC, an ISSI LM2 620 nm (red, 4W) LED lamp was used. Aligned in the red LED excitation path was a linear polarizer and an achromatic QWP, rotated at 45° relative to the polarizer, to create circular polarized red light. Both LEDs are placed 58 cm from the test specimen. The LEDs were triggered continuously in separate runs to separate the pressure and strain signals. The imager is a 4D-Technologies PolarCam U2 CMOS camera with a $0/45/90/135^\circ$ linear polarization mask for each superpixel. Intensity resolution is 12-bit. The maximum full-field frame rate is 164 *fps* at

full spatial resolution of 1200×1820 . Framing rate for this experiment to was set to 140 fps to acquire sufficient signal strengths. While insufficient to capture the unsteady response of the plate due to the nature of SWBLI, it facilitates in understanding the mean pressure and strain distribution over the plate and visualize start-up loads at the onset of the flow. Attached to the camera is a Nikon 50 mm lens set at an f -stop of 1.2. A 450 nm reflective LPF and 570 nm Schott glass LPF is attached to the lens when measuring PSP emission and PEC reflective intensities.

PEC (Micro-Measurement's PS-1D; $h = 0.51 \text{ mm}$) of diameter equal to that of the plate is adhered to it utilizing PC-10C adhesive. For this experiment, a value of the coating characteristic η was calculated *a-priori*. This value was $657 \mu\epsilon$. This value was used in all the proceeding calculations of strains. Next, PSP was sprayed on the surface of the PEC. First, a water-based polymer formulation was sprayed onto the PEC. This underlayer assists in protecting the PEC from the solvents of the PSP layer. The polymer included a small volume of a low refraction index porous media instead of traditionally used titanium dioxide. Increasing the concentration of the porous media diminishes the polarization retention, hence strain sensitivity, of the signal. Then, a thin layer of PtTFPP PSP (Innovative Scientific Solutions Inc.) was sprayed on the surface of the polymer until a light-pink hue of the PSP was visible, attempting to balance between the signal strength of the PSP and PEC. Pressure response of the current formulation in a calibration shock tube at ISSI was measured at 2 ms . The center absorption band of the PSP is approximately 400 nm , and the center emission band is near 650 nm .

Oil flow visualization technique

Oil-flow visualization was conducted on the tunnel side wall with an uncoated clamped plate (5 mm thick). The flow visualization mixture consisted of aluminum oxide and kerosene oil in the ratio of 1:8 by mass. To obtain the maximum contrast between the white oil flow and the

surface, the surface was coated with a matte black paint. The mixture was then applied uniformly over the surface. The tunnel was run for 10 seconds. After the run, the mixture was allowed to dry for 10 minutes. The result was a time-averaged image of the SWBLI surface flow features.

Results and Discussion

To facilitate better understanding of the oil flow visualization images, a Cartesian coordinate system is added. The abscissa and the ordinate represent the stream-wise direction and test section height, respectively. Both the axes are normalized by the incoming turbulent boundary layer thickness. In all the images, flow direction is from left to right. Table A.1.2 shows the tests of which the results have been discussed:

Table A.1.2. Tests of the clamped plate

Plate Thickness [mm]	Baseline flow (No wedge)	
1.6 (PEC/PSP)	Only pressure (continuous blue light)	Only strain (continuous red light)
5 (PEC/PSP)	Only pressure (continuous blue light)	Only strain (continuous red light)
	With wedge	
1.6 (PEC/PSP)	Only pressure (alternating lights)	Only strain (continuous red light)
5 (PEC/PSP)	Only pressure (continuous blue light; alternating lights)	Only strain (continuous red light)

PSP calibration

Figures A.1.5 (a) and (b) compares the a priori intensity ratio at the four different pressure ratios for both the plates. The plates were placed in a pressure-controlled chamber and images were acquired for $P/P_{atm} = 0.2$ to 1.0. Figures A.1.5 (c) and (d) are the corresponding Stern-Volmer plots. The linearity of the plots indicate that the behavior of PSP on both the plates is consistent with a linear Stern-Volmer relationship.

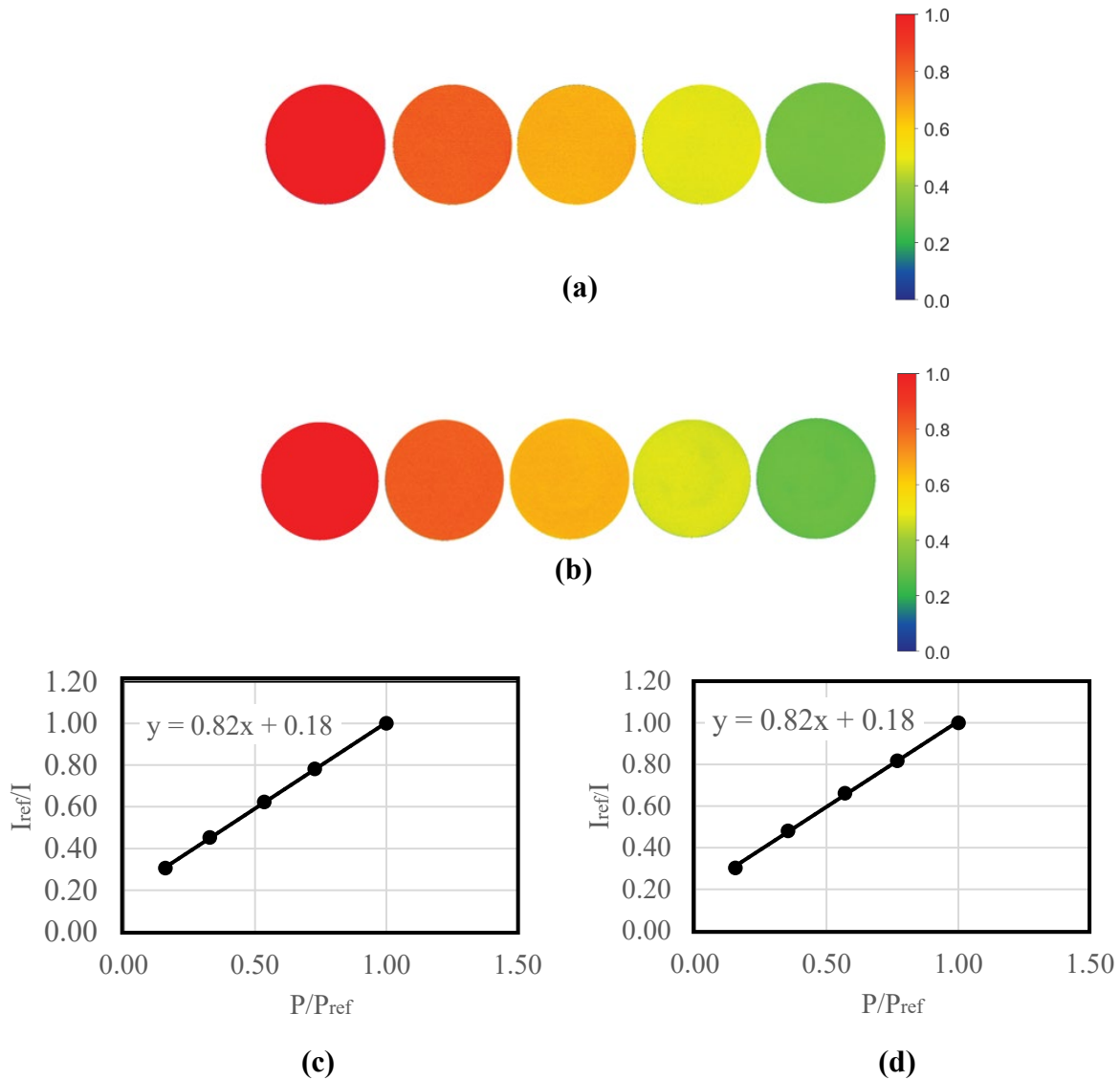


Figure A.1.5.(a) intensity ratio contour for thick plate at $P/P_{ref} = 0.16 - 1.0$ (b) intensity ratio contour for thin plate at $P/P_{ref} = 0.15 - 1.0$ (c) Stern-Volmer plot-thick plate (d) Stern-Volmer plot-thin plate

Flow visualization

The top image in Fig. A.1.6 shows the oil flow visualization of the SWBLI captured over the flat plate, confirming the 3D nature of the SWBLI for the test facility. The flow separation line is highlighted by the accumulation of oil flow mixture due to zero or low shear. This is observed as a curved region bounded by $1.5 < x/\delta_o < 4$ and $2.5 < y/\delta_o < 8.5$. In the absence of side-walls, the separation line would be expected to be straight and perpendicular to the flow. Its curved

shape suggests that the SWBLI is influenced by the corner and side-wall boundary layers. The two recirculation vortices are prominently visible downstream of the separation between $3 < x/\delta_o < 8$ and $3 < y/\delta_o < 9$. The effects of the corner boundary layer are visible starting at $x/\delta_o = 1$ (more clearly seen along the test section ceiling), indicating the separation of the corner flow. Between the primary flow and corner flow separation lines, an intrusion channel is observed. As explained by Burton et al. (2012), the intrusion channel is formed by the inhibition of the corner flow span-wise migration due to the larger adverse pressure gradient in the primary separation region. Hence, a region of increased momentum is formed due to fluid accumulation, which results in downstream displacement of the separation boundary. This has been compared with the pressure change of the PEC/PSP coated plate of the same thickness after 2 s of the wind tunnel run (bottom image). Similar flow contours as the flow visualization are captured by the PSP as depicted by the dashed splines.

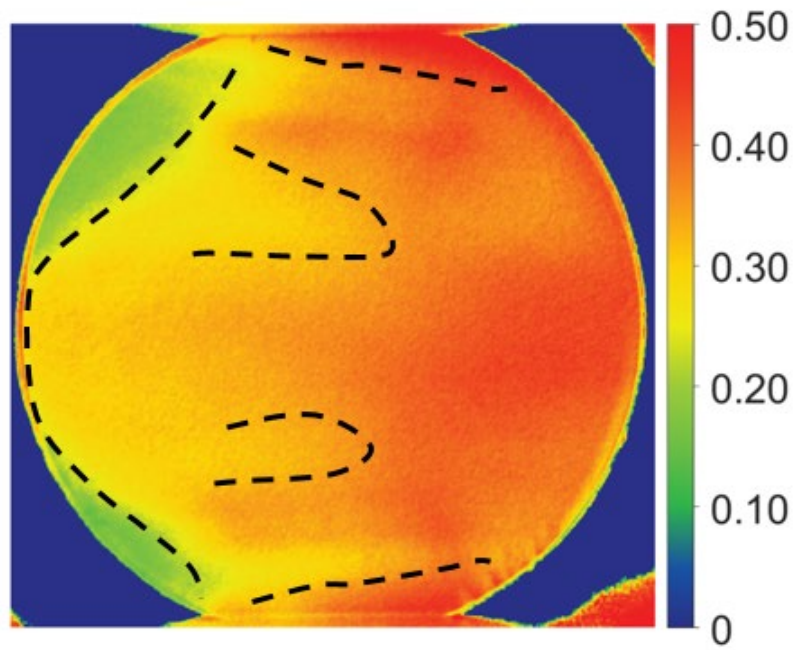
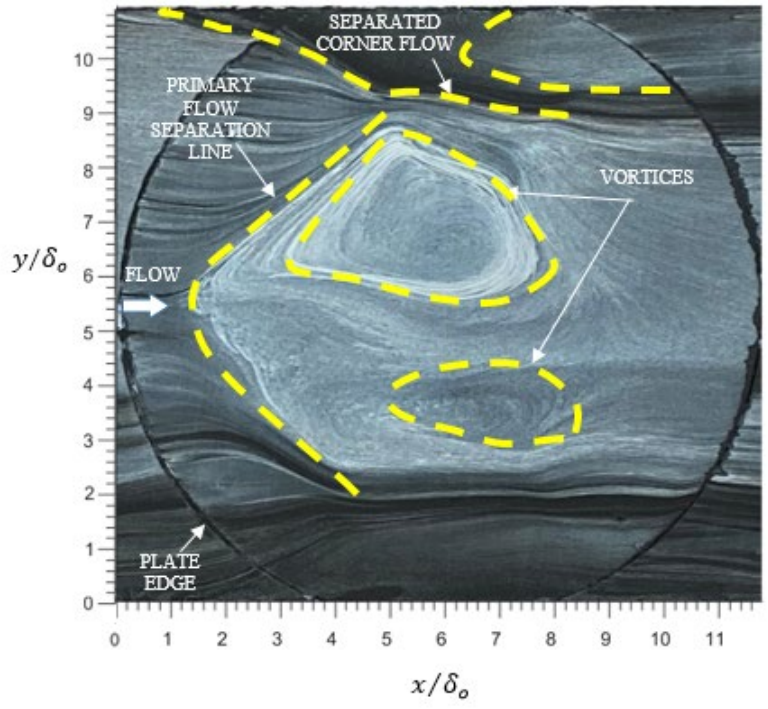


Figure A.1.6. 5 mm thick plate (left) oil flow visualization (right) P/P_{ref} after 2 seconds of wind tunnel run with the wedge

Pressure response: baseline flow

Figure A.1.7 shows the start-up flow event without the wedge installed (time increasing from left to right, the set of images for each plate are separated by a time-step of 71 ms). For both the plates, as the tunnel starts, the images indicate a pressure drop as expected. However, an undesired local pressure rise and apparent weak shock-structure during the run (Fig. A.1.8) was detected mid-span extending across the diameter during steady flow conditions for both the plates.

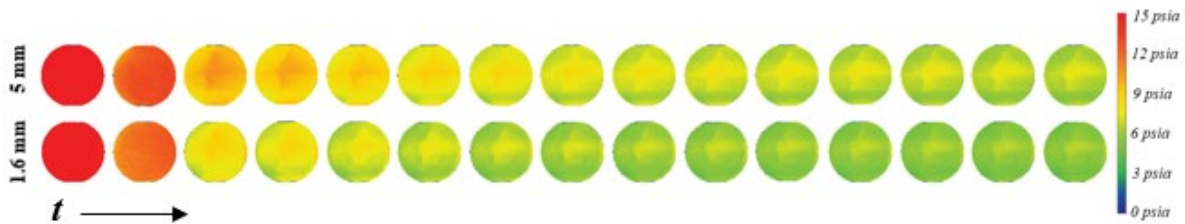


Figure A.1.7. Time dependent pressure contours at $\Delta t = 71 \text{ ms}$ for baseline flow

Surface pressure measurements using Kulite pressure transducers were acquired on an uncoated plate (Fig. A.1.8) to identify the strength of the shock structure. On analysis (Table A.1.3), the pressure port measurements confirmed a weak, uneven shock structure. The pressure

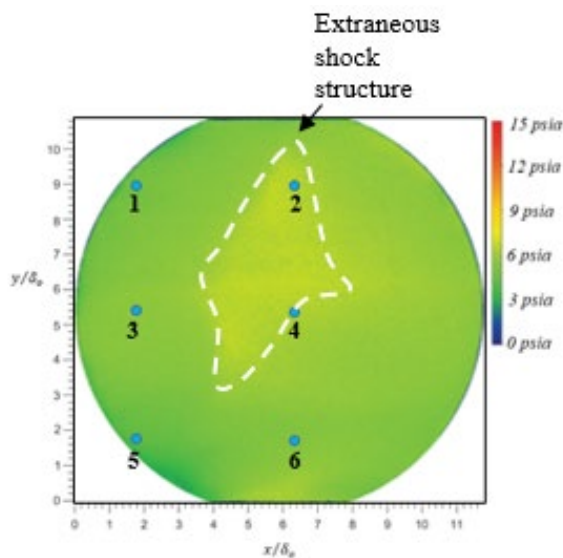


Figure A.1.8. Location of pressure ports

Table A.1.3. Pressure rise across the ports

Port combination	Pressure ratio (transducers)	Pressure ratio (PSP)
Port 1- Port 2	1.13	1.40
Port 3- Port 4	1.51	1.14
Port 5- Port 6	1.09	1.38

rise would correspond to an oblique shock at a turning angle of less than 6° , possibly indicated a side wall misalignment.

Pressure response: SWBLI

Figures A.1.9 and A.1.10 shows individual processed pressure images capturing the start-up flow event with the wedge installed for the thick plate with continuous blue light, and thick (top row) & thin (bottom row) plates with alternating lights respectively. While for Fig. A.1.9 images are shown at 71 ms time steps, for fig. A.1.10, they are shown at 14 ms time steps. As the tunnel starts, both the images indicate a pressure decrease (red to yellow-green) which is as expected due to a drop in the static pressure. As steady free stream conditions are established, the formation of a pressure rise across the plate appears. Figure A.1.11(a) and A.1.11(b) show the variation of pressure along the centerline for thick and thin plate at steady state condition, i.e., after the establishment of SWBLI. The trends for both the cases show a mean static pressure rise characteristic of flow in the separation region of a SWBLI. The gradual pressure rise in both the

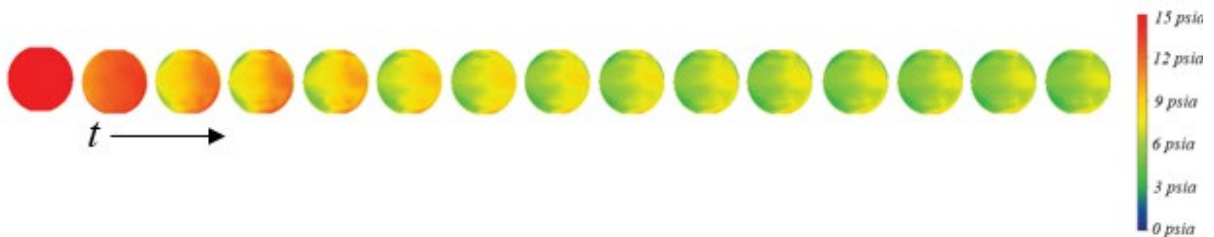


Figure A.1.9. Time dependent pressure contours at $\Delta t = 71 \text{ ms}$ with the wedge- thin plate (continuous blue light)

cases is indicative of formation of separation bubble. However, it is difficult to identify distinct peaks regions of flow separation and reattachment.

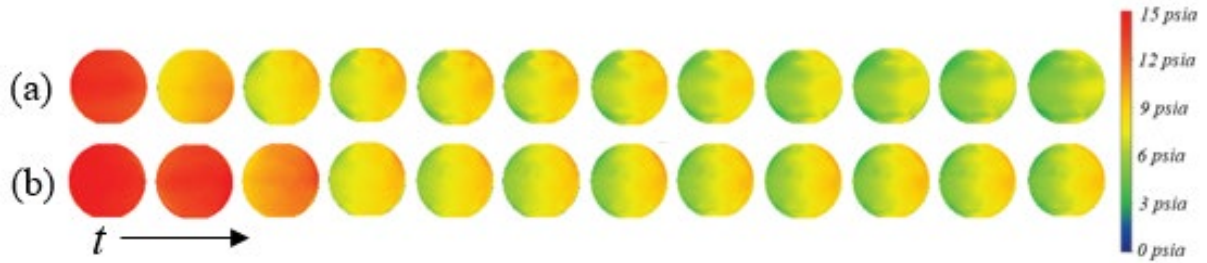


Figure A.1.10. Time dependent pressure contours at $\Delta t=14$ ms with the wedge (a) continuous blue light (b) alternating light

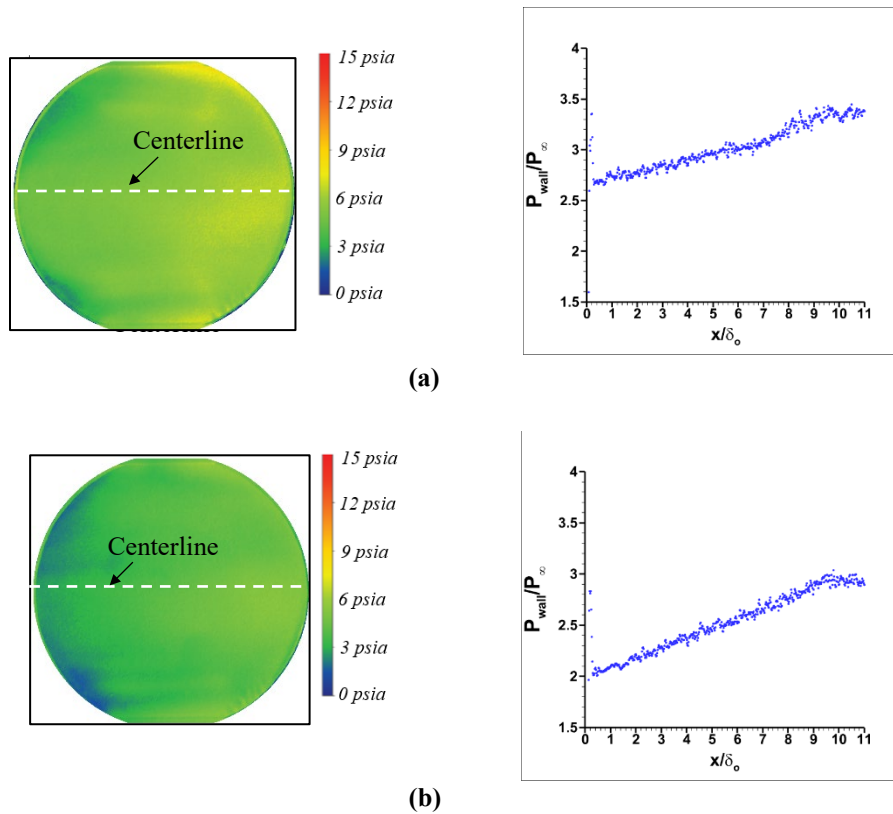


Figure A.1.11. Centerline pressure rise at steady state condition (2.25 s) (a) thick plate (b) thin plate

For both the plates, PSP also detects the fall in pressure past $x/\delta_o = 11$, which is due to the expansion fan generated at the trailing edge of the wedge meeting the opposite wall.

Measurement of strain using strain gage

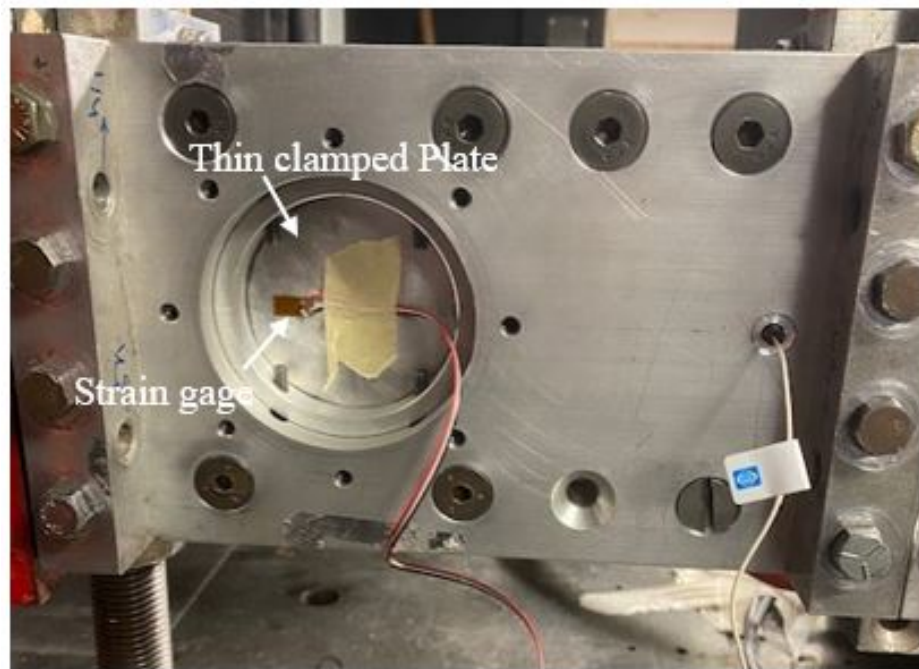


Figure A.1.12. Experimental set-up to acquire strain on PEC mounted thin plate

In addition to the luminescent technique, a supplementary experiment was conducted to measure the value of the principal strain in the radial direction and compare its value with that of the analytical solution. In this regard, PEC was mounted on the surface of the thin plate which

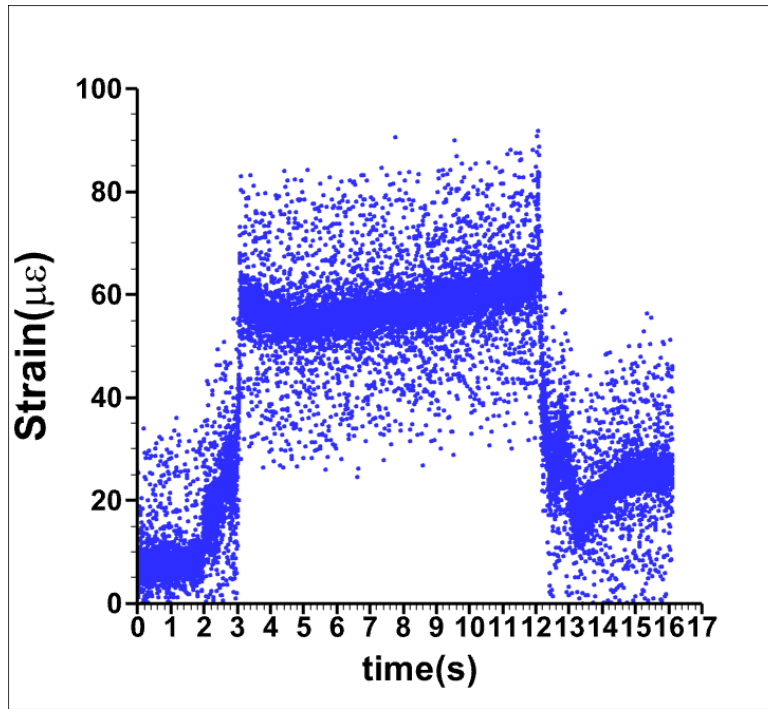


Figure A.1.13. Measured Strain at $r/a=0.44$

would be exposed to the flow. A strain gage was mounted along the diameter, at $r/a = 0.54$, (measured from the center of the plate), on the opposite surface that is exposed to ambient conditions (Fig. A.1.12). This orientation ensured that it measured the principal radial strain. Strain measurements were acquired for 16s at 1000 Hz using an NI DAQ system, for baseline flow. Figure A.1.13 shows the strain detected by the gage over the course of the run.

As the tunnel control valve was opened and closed, the gage recorded an increase and fall in the strain (between 1 – 14 s). The temperature interference on the measured strain was evident as after shut-down, instead of falling to the same value observed before the run, it decayed gradually over a period of time (not shown in the plot). The mean principal radial strains measured over the periods of 1 s intervals in the steady run time range of 5-11 s are as shown in Table A.1.4. At the same location, the value of the analytical solution is $42 \mu\epsilon$. Hence, it appears that although the gage is experiencing temperature effects, it measures a mean strain value comparable to the analytical solution. This could be due to the fact that the tank storage pressure which governs the

tunnel pressure conditions, was high enough to result in larger ambient and tunnel pressure difference than the value used for the analytical solution.

Table A.1.4. Mean strain during steady run

Time period	Strain
5 th – 6 th s	43.46 $\mu\epsilon$
6 th – 7 th s	43 $\mu\epsilon$
7 th – 8 th s	42.19 $\mu\epsilon$
8 th – 9 th s	43.09 $\mu\epsilon$
9 th – 10 th s	43.06 $\mu\epsilon$
10 th – 11 th s	43.99 $\mu\epsilon$

Strain response

Figures A.1.14 and A.1.15 show the time dependent strain and phase contours during flow start-up for the thick and thin plates in the absence and presence of the wedge, imaged with continuous red light respectively. As expected, the thick-plate configuration shows negligible strain (as indicated by the color blue) and no preferred strain direction (as indicated by the random scatter for red-white-blue where colors represent the principal strain direction in radians). This confirms the thick plate acts as an effectively-rigid side wall. From the development of the strain, it can be concluded that the flow starts at second image from the left in Fig A.1.14. For Fig. A.1.15 where the flow starts in the third image from the left, the plate experiences an initial peak strain when the starting shock-wave passes over it. The strain on the thin plate during the run in Fig. A.1.15 did not develop to the extent that was observed in Fig. A.1.14. This observation could not be explained and needs further investigation.

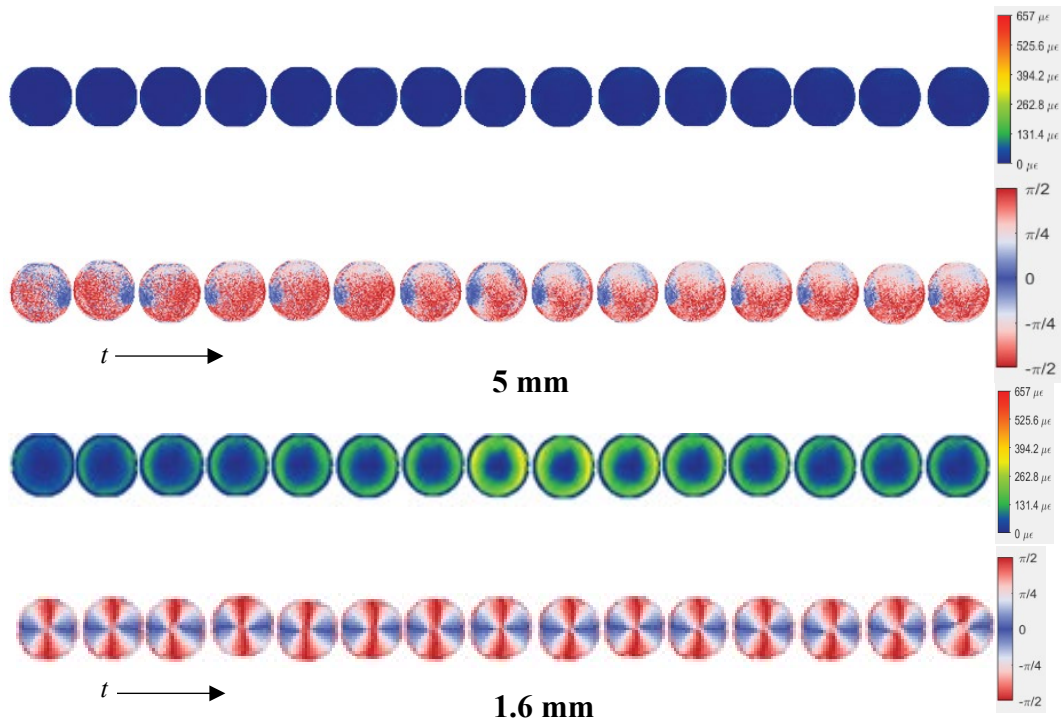


Figure A.1.14. Time dependent strain (upper) and phase (lower) contours at $\Delta t=7$ ms intervals of the thick and thin clamped plate in the absence of the wedge (continuous red light)

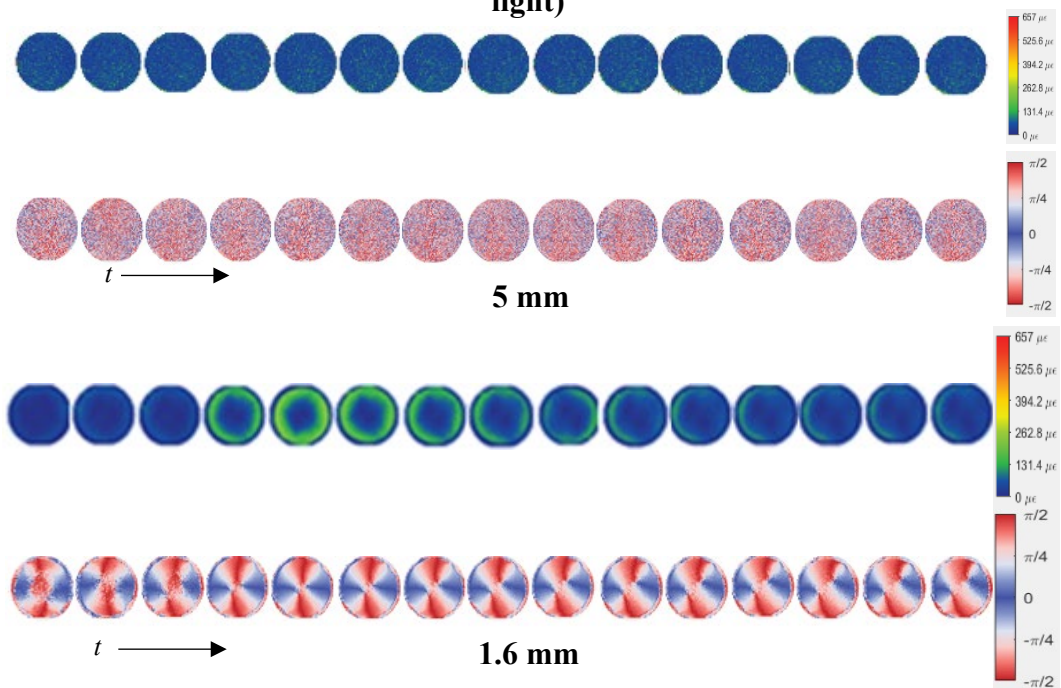


Figure A.1.15. Time dependent strain (upper) and phase (lower) contours at $\Delta t=7$ ms intervals of the thick and thin clamped plate in the presence of the wedge (continuous red light)

Figure A.1.16 shows the variation of shear strain along the centerline of the thin line at 2.25 s, in the absence of the wedge and for continuous red light. The strain trend for the thick plate is not shown due to negligible strain. It is similar to trend obtained from the analytical solution, with the strain increasing from the center of the plate to the clamped edge. However, the increase in the strain shows some asymmetry, with the maximum shear strain is found to be at the aft end of the plate ($204 \mu\epsilon$).

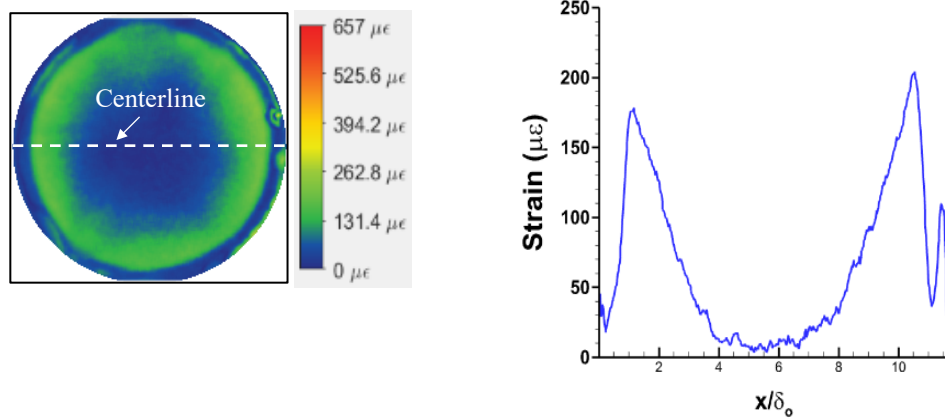


Figure A.1.16. Centerline strain at steady state condition (2.25 s) - thin plate

Interpretation of phase

Figure A.1.17 (left) shows the strain contours on the thin plate overlaid with tick marks that indicate the direction of the principal shear strain. The direction of orientation of the vectors agrees with the analytical solution and the degree of orientation agrees with the color contours. Figure A.1.17 (right) shows the corresponding phase. The determined phase alternates between the colors in the angular direction due to the fact that although ε_θ remains negative along the radial direction, ε_r changes in sign (from tension at the center to compression at the edge).

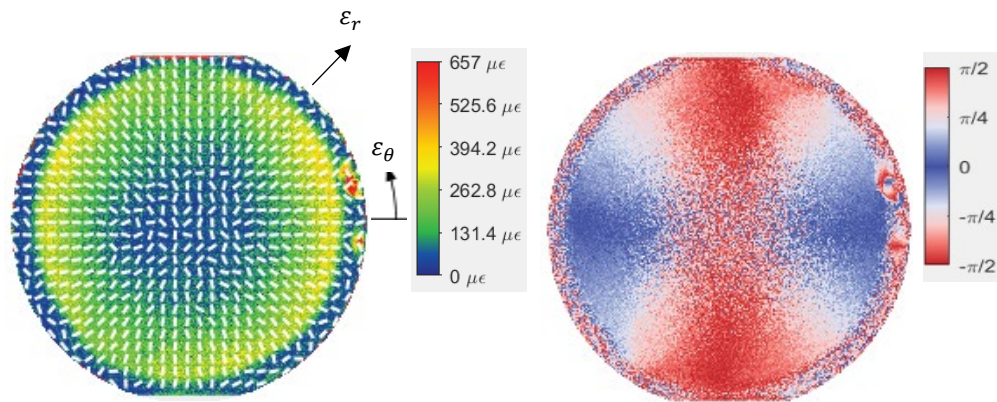


Figure A.1.17. Phase vectors superimposed on strain contours (left) and phase contours (right)—thin plate for start-up load without wedge

PSP and PEC temperature sensitivity

Errors in the measurement of both pressure and strain may arise as PSP and PEC are temperature sensitive. PECs have a glass transition nature due to the materials out of which they are fabricated. The optical sensitivity K is constant up to the point of glass transition temperature. Past the glass transition temperature the optical sensitivity can drop by as much as 80%. For the coating used in the experiments, as the glass transition temperature was $\sim 170^\circ\text{C}$, there was no temperature interference for PEC.

However, for the PSP that was used for the experiment, there is a 2-4% decrease in intensity for every 1°C which further increases as the pressure ratio increases. In the experiment, the intensity of PSP at ambient pressure and temperature was considered as the reference. Hence, it can be stated with a certain degree of confidence that the pressure detected in the images are offset and require a temperature correction. Instead of the pre-run condition, if an image of the plate immediately after the run, before the plate reaches the ambient temperature is considered as the reference, then the temperature interference can be eliminated to a great extent.

Conclusions and Future Work

The set of experiments conducted discussed the demonstration of the capability of a dual-layer luminescent coating in detecting the pressure and strain signals in a high-speed flow environment. In this regard, the specimen was prepared by initially installing a PEC over a circular clamped plate. PSP was then spraying on top of the PEC. Pressure and strain measurements were acquired on two circular clamped plates subjected to an impinging oblique SWBLI in a Mach 3 supersonic tunnel. The pressure and strain test range was $17 - 103\text{ kPa}_{abs}$ and $0 - 204\ \mu\epsilon$, respectively. Frame rates were limited to 140 fps to capture sufficient image intensities. Conclusions from this investigation are:

1. The average intensity measurements over the four-polarizer angles for each superpixel were converted to pressure using *a-priori* calibration technique. The pressure measurements for both the thin and thick plates showed a gradual pressure rise typical of a SWBLI, with the thick plate experiencing a higher pressure rise over it than the thin plate. The pressure range was $17-103\text{ kPa}_{abs}$
2. The standard deviation of intensity measurements over the four-polarizer angles for each superpixel was converted to maximum shear strain. Strain results showed the evolution of

strain on both thick and thin plates during the start-up of the flow. While the thick plate underwent negligible deformation, the thin plate developed a clear shear strain along the clamped edge. The image acquisition rate was constrained due to the capacity of the camera and the intensities of lights. Higher excitation energy and faster micro-polarizer camera should enable higher frequency testing more appropriate to analyze high-frequency SWBLI structures.

APPENDIX-II

Procedure to Setup 3D Steady-state Simulation of IOSWBLI in ANSYS (FLUENT)

Geometry

A fluid flow model (Fig. A.2.1 (a)) that captures the keys dimensions of the wind tunnel was first developed on Solidworks. The length of the inlet was iteratively determined by changing the inlet length and repeating the calculations such that the experimental boundary layer thickness was achieved at the location where the boundary layer measurements were acquired. In this manner, the experimental boundary layer thickness was established at the entrance of the test section in the CFD simulation. It was then imported into *Design Modeler* in FLUENT as the flow domain. As the IOSWBLI occurring in the test section is of interest, the discussion of the computational approach is described with a focus on the test section.

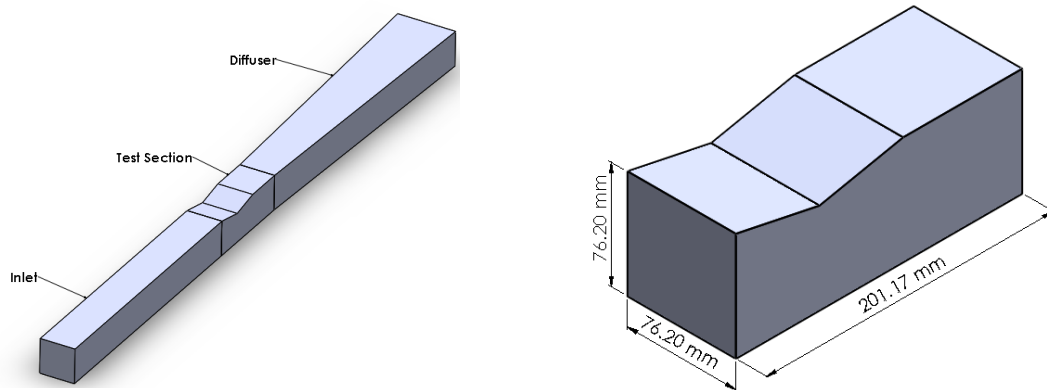


Figure A.2.1. CAD model (a) wind tunnel fluid domain (b) test Section

Mesh Generation

A mesh was generated using *Edge sizing* and *Multizone* features in such a manner that it aligned with the flow direction (Fig. A.2.2 (a)).

The *Inflation* feature was used to resolve the boundary layers on all the tunnel walls and the corners, and in the process capture the SWBLI region.

A grid independence study was conducted to establish the convergence of the solution. This is discussed in detail in the *Results and Discussion* of Section I. From this study, grid independence was established at 17.93 million cells for the complete wind tunnel domain. The wind tunnel test section grid was divided into 300 divisions in length, 50 divisions each in height and width that resulted in its grid size being 3.11 million cells.

Table A.2.1 Inflation layer parameters (steady)

Inflation Layer Parameters	Values
First Layer Thickness	1×10^{-6} m
Growth Rate	1.2
Total number of layers	37

The inflation layer of the test section is shown in Fig. A.2.2 (b) and is further illustrated in Fig. A.2.2 (c).

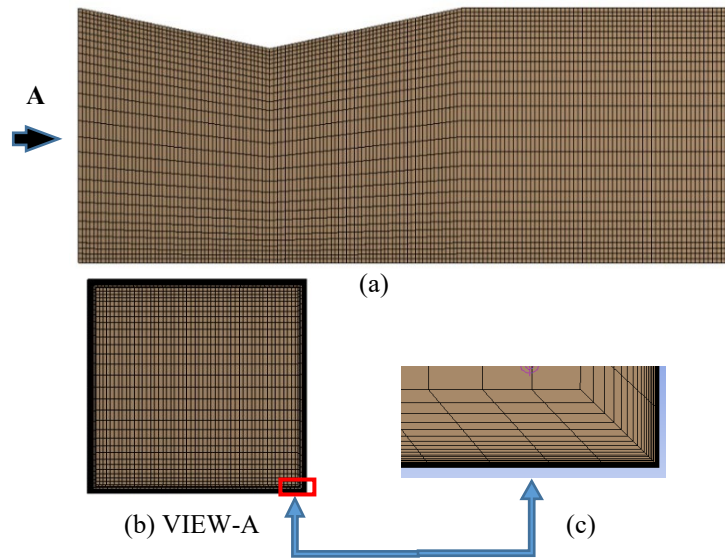


Figure A.2.2. ANSYS (FLUENT) test-section fluid domain grid (a) side-view (b) front-view (c) inflation layer to resolve boundary layer and SWBLI

Setup

- *General* - A steady-state, density-based solver was chosen in the ‘General’ option.

- Models - Reynolds stress (7 equation) model along with the energy equation were selected.

The Reynolds stress (R-S) model solves the Reynolds transport equation (Fig. A.2.3) for Reynolds stresses $\overline{\rho u'_i u'_j}$. Each of the terms of the equation are further modeled. The model was implemented with the default parameters (Fig. A.2.4). The values of the energy and wall Prandtl numbers (not shown in Fig. A.2.4) are 0.85 each.

$$\begin{aligned}
& \underbrace{\frac{\partial}{\partial t}(\rho \overline{u'_i u'_j})}_{\text{Local Time Derivative}} + \underbrace{\frac{\partial}{\partial x_k}(\rho u_k \overline{u'_i u'_j})}_{C_{ij} \equiv \text{Convection}} = - \underbrace{\frac{\partial}{\partial x_k} \left[\rho \overline{u'_i u'_j u'_k} + p (\delta_{kj} \overline{u'_i} + \delta_{ik} \overline{u'_j}) \right]}_{D_{T,ij} \equiv \text{Turbulent Diffusion}} \\
& + \underbrace{\frac{\partial}{\partial x_k} \left[\mu \frac{\partial}{\partial x_k} (\overline{u'_i u'_j}) \right]}_{D_{L,ij} \equiv \text{Molecular Diffusion}} - \underbrace{\rho \left(\overline{u'_i u'_k} \frac{\partial u_j}{\partial x_k} + \overline{u'_j u'_k} \frac{\partial u_i}{\partial x_k} \right)}_{P_{ij} \equiv \text{Stress Production}} - \underbrace{\rho \beta (\overline{g_i u'_j \theta} + \overline{g_j u'_i \theta})}_{G_{ij} \equiv \text{Buoyancy Production}} \\
& + \underbrace{p \left(\frac{\partial u'_i}{\partial x_j} + \frac{\partial u'_j}{\partial x_i} \right)}_{\phi_{ij} \equiv \text{Pressure Strain}} - \underbrace{2\mu \frac{\partial u'_i}{\partial x_k} \frac{\partial u'_j}{\partial x_k}}_{\epsilon_{ij} \equiv \text{Dissipation}} \\
& \underbrace{-2\rho \Omega_k (\overline{u'_j u'_m} \epsilon_{ikm} + \overline{u'_i u'_m} \epsilon_{jkm})}_{F_{ij} \equiv \text{Production by System Rotation}} + \underbrace{S_{\text{user}}}_{\text{User-Defined Source Term}}
\end{aligned}$$

Figure A.2.3. Reynolds transport equation

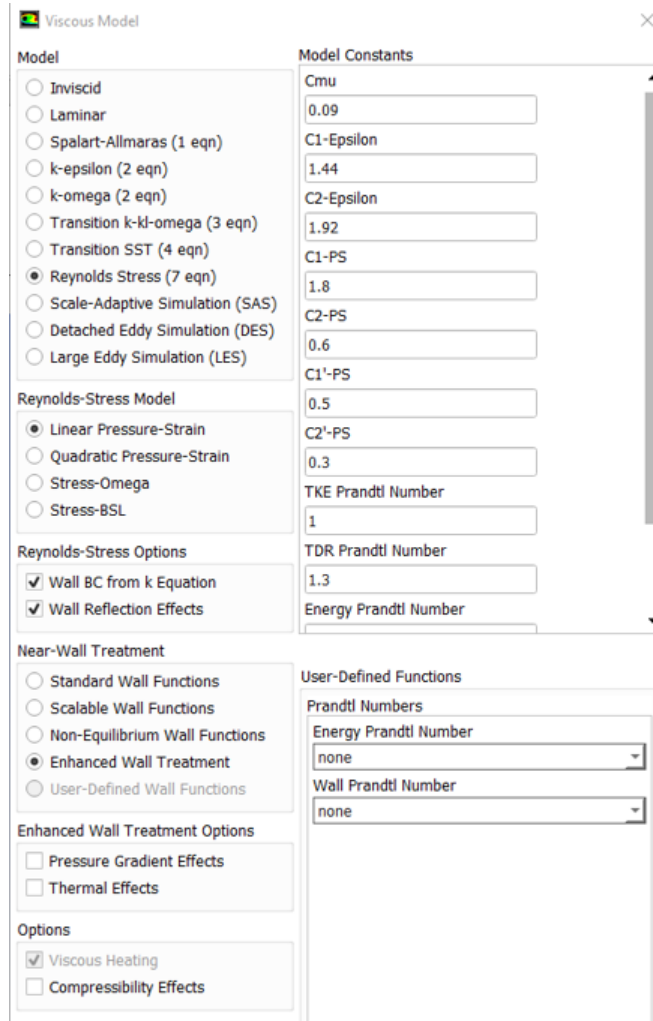


Figure A.2.4. Reynolds stress model parameters.

- Materials - Air was chosen as the fluid and was assigned the values for properties as shown in Fig A.2.5.

Create/Edit Materials

Name: air

Material Type: fluid

Chemical Formula:

Fluent Fluid Materials: air

Mixture: none

Order Materials by:

- Name
- Chemical Formula

Fluent Database...
User-Defined Database...

Properties

Density (kg/m ³)	ideal-gas	Edit...
Cp (Specific Heat) (j/kg-k)	constant	Edit...
	1006.43	
Thermal Conductivity (w/m-k)	constant	Edit...
	0.0242	
Viscosity (kg/m-s)	sutherland	Edit...
Molecular Weight (kg/kmol)	constant	Edit...
	28.966	

Figure A.2.5. Material properties

- Boundary Conditions
 - Inlet - The entrance of the inlet was defined as *Velocity Inlet*. The numerical values were assigned as shown in Fig. A.2.6.
 - Outlet - The exit of the diffuser was assigned as *Pressure Outlet* (Fig. A.2.7).
 - Wall - Each of the walls of the wind tunnel sections was defined as *Wall*.
 - Interface - The stream-wise interfaces of the three parts were defined as *Contact Region*.
 - Interior - The rest was by default defined as *Interior*.
- Mesh Interfaces and Dynamic Mesh - Default values were used.

Velocity Inlet ×

Zone Name
inlet

Momentum Thermal Radiation Species DPM Multiphase Potential UDS

Velocity Specification Method Magnitude, Normal to Boundary

Reference Frame Absolute

Velocity Magnitude (m/s) 622 constant

Supersonic/Initial Gauge Pressure (pascal) 0 constant

Outflow Gauge Pressure (pascal) 0 constant

Turbulence

Specification Method Intensity and Viscosity Ratio

Turbulent Intensity (%) 5

Turbulent Viscosity Ratio 10

Reynolds-Stress Specification Method K or Turbulent Intensity

Velocity Inlet ×

Zone Name
inlet

Momentum Thermal Radiation Species DPM Multiphase Potential UDS

Temperature (k) 107 constant

Figure A.2.61. Velocity inlet values

Pressure Outlet ×

Zone Name
outlet

Momentum Thermal Radiation Species DPM Multiphase Potential UDS

Backflow Reference Frame Absolute

Gauge Pressure (pascal) 0 constant

Pressure Profile Multiplier 1

Backflow Direction Specification Method Normal to Boundary

Backflow Pressure Specification Total Pressure

Radial Equilibrium Pressure Distribution

Average Pressure Specification

Averaging Method

Strong

Weak

Target Mass Flow Rate

Turbulence

Specification Method Intensity and Viscosity Ratio

Backflow Turbulent Intensity (%) 5

Backflow Turbulent Viscosity Ratio 10

Reynolds-Stress Specification Method K or Turbulent Intensity

Pressure Outlet ×

Zone Name
outlet

Momentum Thermal Radiation Species DPM Multiphase Potential UDS

Backflow Total Temperature (k) 300 constant

Figure A.2.7. Pressure outlet values

- *Reference Values* - Assigned as shown in Fig. A.2.8.

Reference Values

Compute from

Reference Values

Area (m2)	1
Density (kg/m3)	1.225
Enthalpy (j/kg)	0
Length (m)	1
Pressure (pascal)	0
Temperature (k)	288.16
Velocity (m/s)	1
Viscosity (kg/m-s)	1.7894e-05
Ratio of Specific Heats	1.4

Figure A.2.8. Reference values

Solution Methods

Formulation

Flux Type

Spatial Discretization

Gradient

Flow

Turbulent Kinetic Energy

Turbulent Dissipation Rate

Reynolds Stresses

Transient Formulation

Non-Iterative Time Advancement

Frozen Flux Formulation

Pseudo Transient

Warped-Face Gradient Correction

High Order Term Relaxation

Convergence Acceleration For Stretched Meshes

Solution Controls

Courant Number

Under-Relaxation Factors

Turbulent Kinetic Energy

Turbulent Dissipation Rate

Turbulent Viscosity

Reynolds Stresses

Solid

(a)

(b)

Figure A.2.9. (a) solution methods (b) solution controls

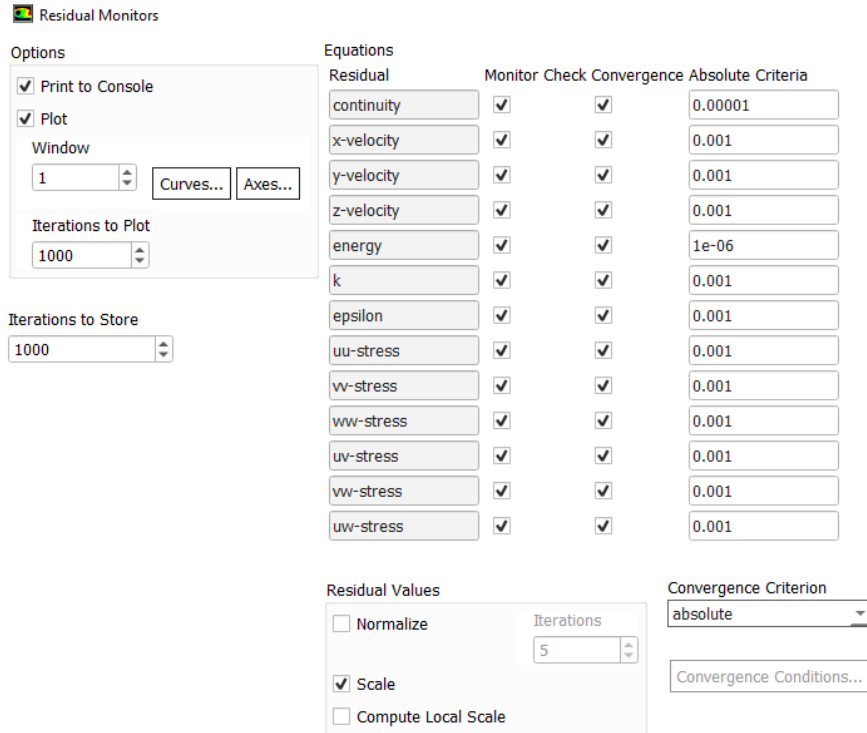


Figure A.2.10. Residual monitors

Solution

- Methods and Controls - Defined as shown in Figs. A.2.9 (a) and (b) respectively.
- Report Definitions, Report Files, Report Plots, Convergence Conditions, Cell Registers, and Calculation Activities - Set to default values.
- Monitors - Residuals were to values as shown in Fig. A.2.10.
- Initialization – Hybrid initialization was chosen.

The solution was then run for a few thousands of iterations till the residual values were achieved.

Procedure to Setup 2D Unsteady Simulation of IOSWBLI in ANSYS (FLUENT)

Geometry

In order to shorten the turnaround time of the simulation, unlike the steady-state simulation which involved the inclusion of the CAD model of the whole wind tunnel for the simulation, the unsteady simulation was run only for the test section. The CAD model of the test section (Fig A.2.11) was developed on *Design Modeler* in FLUENT. In this process, a certain offset distance

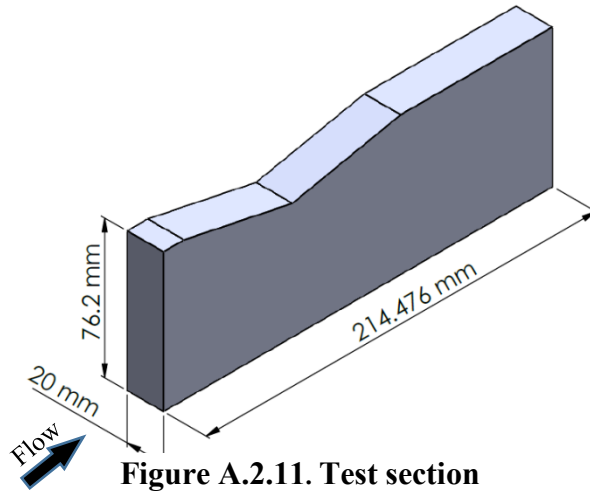


Figure A.2.11. Test section

was allocated upstream of the leading edge of the wedge. Given that the sidewalls of the test section were to be defined as periodic conditions, the distance between them was kept minimal to reduce the meshing time while keeping it large enough to avoid merging of sidewall boundary layers. All the other dimensions are identical to those of the test section from the steady state case

Mesh Generation

Like the steady-state simulation, a mesh was again generated using *Edge sizing* and *Multizone* features, in such a manner that it aligned with the flow direction (Fig. A.2.12 (a)). The *Inflation* layer details are as listed in Table A.2.2 and shown in Fig. A.2.12 (b) and Fig. A.2.12 (c). The longitudinal grid cell size (0.00067 m) of the steady state simulation at grid convergence was used as the guide to set the corresponding grid cell size of the unsteady simulation. A uniform cell

size of 0.0005 m resulted in a grid size of 4.02 million cells. This grid size was used for the simulation.

Table A.2.2 Inflation layer parameters (unsteady)

Inflation Layer Parameters	Values
First Layer Thickness	1×10^{-6} m
Growth Rate	1.15
Total number of layers	40

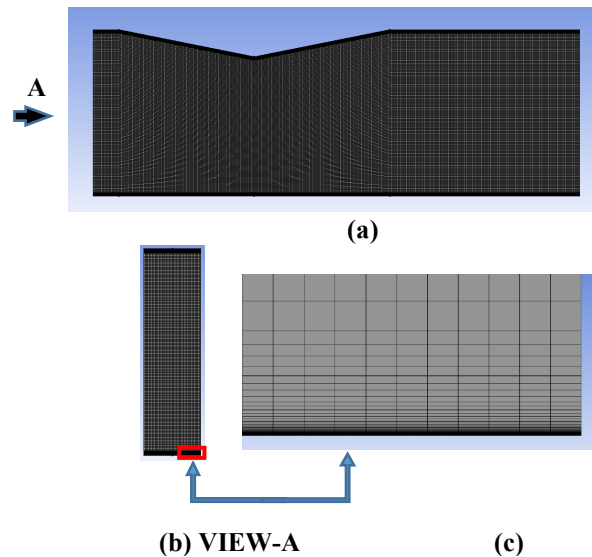
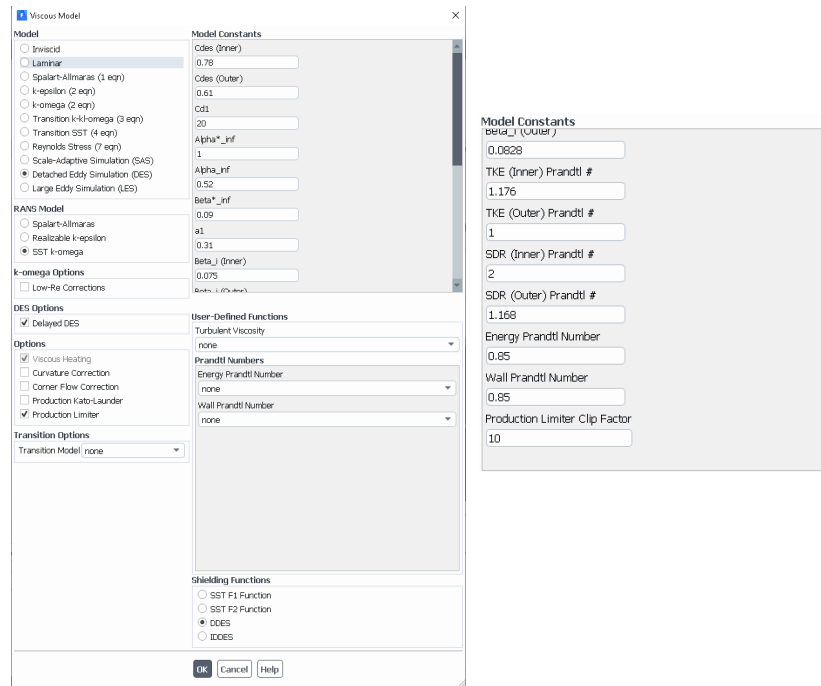


Figure A.2.12. ANSYS (FLUENT) test-section fluid domain grid (a) side-view (b) front-view (c) Inflation layer to resolve boundary layer and SWBLI

Setup

The simulation was run in two parts; a steady-state simulation was first run using the $R - S$ model till the period when the IOSWBLI was established in the fluid domain and the residuals fairly remained constant with increasing iterations. Thereafter, DDES turbulence model was chosen to run the unsteady simulation. The set-up discussed in this section only describes the process of implementing DDES model. The set-up for the $R - S$ model is the same as in the previous discussion of set-up of 3D steady-state simulation.

- General - A transient, density-based solver was chosen
- Models - ‘Detached Eddy Simulation’ along with the Energy equation were selected. The reader is referred to *ANSYS Documentation* for literature on the model. The model was implemented with the default parameters (Fig. A.2.13).



(a)

(b)

Figure A.2.132. (a) DDES model parameters (b) model constraints hidden in (a)

- Materials - Air was chosen as the fluid and property values were assigned as shown in Fig A.2.14.
- Cell Zone Conditions - Default values were used.

Figure A.2.14. Material properties

- a) Boundary Conditions - A profile that contains the values of flow properties at the centerline location which coincides with the entrance of the test section for the current simulation was imported from a steady state simulation that was run using the $k - \omega$ model. Inlet - The leading face of the test section was defined as *Velocity Inlet*. The values for the parameters were imported from the profile (Fig. A.2.15).

Figure A.2.15. Velocity inlet values

b) Interface - Each of the two sidewalls of the test section were defined as ‘Interface’

The two sidewalls were then transformed into periodic boundary conditions using the Text User Interface (TUI) on ANSYS console. The set of commands in Fig A.2.16 achieve this transformation. The id numbers of the sidewalls were entered for the ‘Periodic zone’ and ‘Shadow zone’ and the mesh-interface name was given a name.

```
> /define/grid-interfaces/make-periodic
Periodic zone [()]
Shadow zone [()]
Rotationally periodic? (if no, translationally) [yes] no
X-Translation (in [m]) [0]
Y-Translation (in [m]) [0]
Z-Translation (in [m]) [0.01999999955296516]
Create periodic zone? [yes]
mesh-interface name []
```

Figure A.2.16. TUI commands for periodicity

c) Outlet - The trailing face of the test section was defined as *Pressure Outlet*. The values for the parameters for *Pressure Outlet* were assigned as shown in Fig. A.2.17.

The image shows two screenshots of the ANSYS Fluent software interface for setting a Pressure Outlet boundary condition. The top screenshot shows the 'Pressure Outlet' dialog box with the following settings: Zone Name: outlet; Backflow Reference Frame: Absolute; Gauge Pressure [Pa]: -101320; Pressure Profile Multiplier: 1; Backflow Direction Specification Method: Normal to Boundary; Backflow Pressure Specification: Total Pressure; Prevent Reverse Flow: unchecked; Radial Equilibrium Pressure Distribution: unchecked; Average Pressure Specification: unchecked; Target Mass Flow Rate: unchecked; Turbulence Specification Method: Intensity and Viscosity Ratio; Backflow Turbulent Intensity [%]: 5; Backflow Turbulent Viscosity Ratio: 10; Acoustic Wave Model: Off. The bottom screenshot shows the same dialog box with the 'Backflow Total Temperature [K]' set to 300.

Figure A.2.17. Pressure outlet values

- Mesh Interfaces and Dynamic Mesh - Default values were assigned.

Reference Values

Compute from

Reference Values

Area (m ²)	1
Density (kg/m ³)	1.225
Enthalpy (j/kg)	0
Length (m)	1
Pressure (pascal)	0
Temperature (k)	288.16
Velocity (m/s)	1
Viscosity (kg/m-s)	1.7894e-05
Ratio of Specific Heats	1.4

Figure A.2.18. Reference values

- Reference Values – Values assigned as shown in Fig. A.2.18.

Solution

Methods and Controls - Defined as shown in Figs. A.2.19 (a) and (b).

Solution Methods

Formulation
Implicit

Flux Type
Roe-FDS

Spatial Discretization

Gradient
Least Squares Cell Based

Flow
Second Order Upwind

Turbulent Kinetic Energy
Second Order Upwind

Specific Dissipation Rate
Second Order Upwind

Transient Formulation
First Order Implicit

Non-Iterative Time Advancement

Frozen Flux Formulation

Warped-Face Gradient Correction

High Order Term Relaxation

Convergence Acceleration For Stretched Meshes

(a)

Solution Controls

Courant Number
200

Under-Relaxation Factors

Turbulent Kinetic Energy
0.8

Specific Dissipation Rate
0.8

Turbulent Viscosity
1

Solid
1

(b)

Figure A.2.19. (a) solution methods (b) solution controls

- Report Definitions - Parameters were chosen to be reported as shown in Fig. A.2.20.

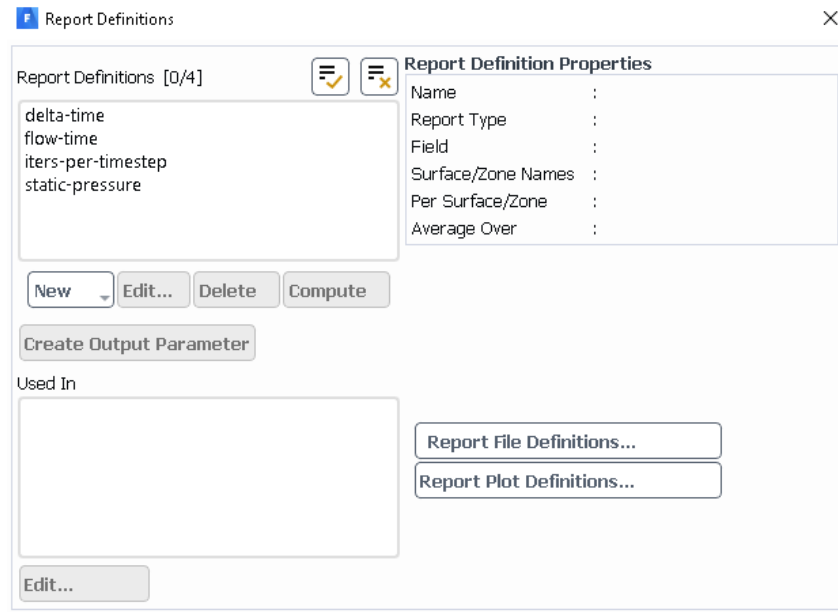


Figure A.2.20. Report definitions

- Monitors - Residuals were assigned as shown in Fig. A.2.21.

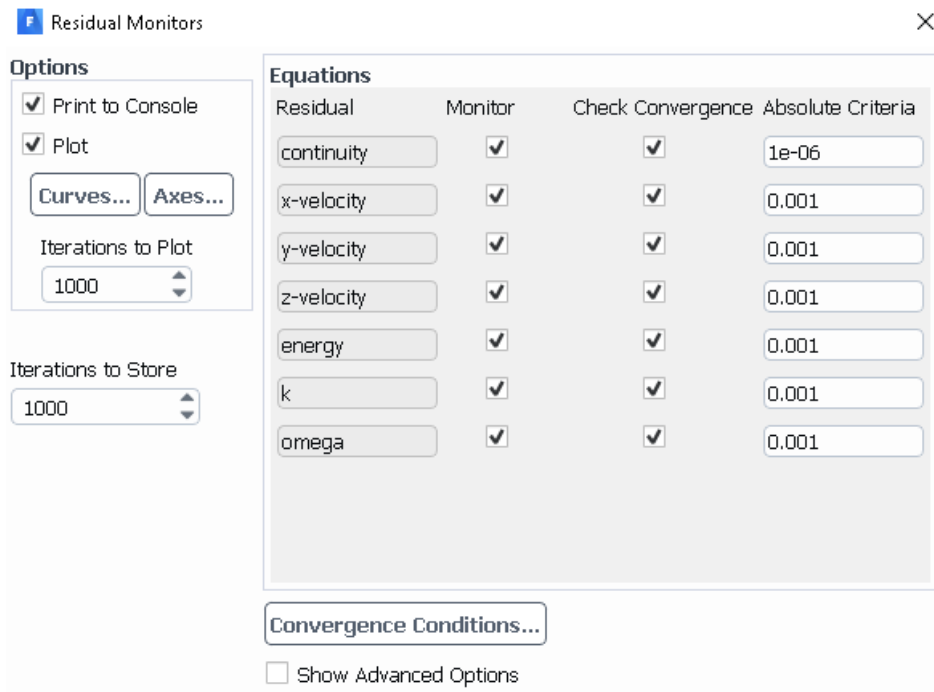


Figure A.2.21. Residual monitors

- Report Files and Report Plots - As shown in Fig. A.2.22.

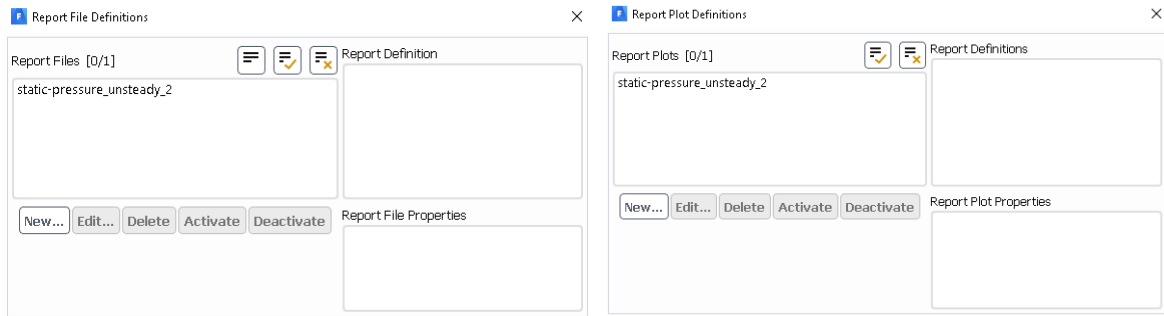


Figure A.2.22. (a) report file definitions (b) report plot definitions

- Convergence Conditions and Cell Registers - Default values were set
- Initialization - Hybrid Initialization was chosen
- Calculation Activities - A data (.dat) file was saved at every time step (Fig. A.2.23) which can be used for post processing in future

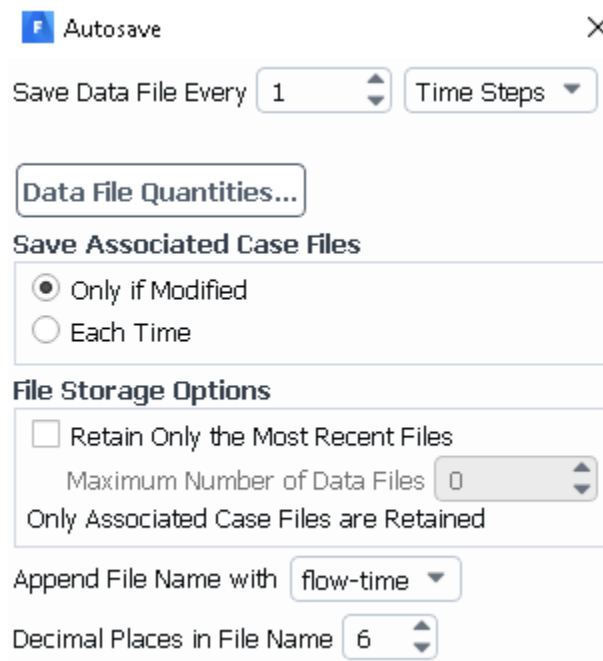


Figure A.2.23. Autosave of data files

- Run Calculation – The time step of the simulation was decided with guidance from literature regarding the separation shock frequencies. It was set to 6.667×10^{-5} s, which resulted in the data acquisition of 15 kHz. This was assumed to be high enough to capture the unsteady nature of the flow structures. The number of iterations per time step was set to 50. The solution was then run such that the data was acquired for a considerable amount of time.

Run Calculation

Check Case... Preview Mesh Motion...

Time Advancement

Type: Fixed Method: User-Specified

Parameters

Number of Time Steps: 100000 Time Step Size [s]: 6.6667e-5

Max Iterations/Time Step: 50 Reporting Interval: 1

Profile Update Interval: 1

Options

Extrapolate Variables
 Report Simulation Status
 Loosely Coupled Conjugate Heat Transfer

Solution Processing

Statistics

Data Sampling for Time Statistics

Data File Quantities...

Solution Advancement

Calculate

Figure A.2.24. Run calculation parameters

APPENDIX-III

KSC-2 Signal Conditioner Filter Settings

Serial Number	DerChan	Channel Name	Excitation Fault	Excitation Value (V)	Excitation Type	Sense	Balance Voltage (mV)	Subbalanc	Coupling	Shield	Input Mode	Overload Mode	Input Overload	Pregain	Filter Type	Filter Cutoff (Hz)	Resonance Compensation	Postgain	Output Overload (V)	Overloads	Settings
1.1	191146-022	8077-3-240		10.000	Bipolar	Local	-16.5312	Balance	DC	Ground	Operate	Continuous		32	None	50000	Enabled	3.0940	9.5	Clear	Save
1.2	191146-022	8077-3-240		10.000	Bipolar	Local	0.0273	Balance	DC	Ground	Operate	Continuous		32	None	50000	Enabled	1.6300	9.5	Clear	Save

Figure A.3.1. KSC-2 signal conditioner settings

APPENDIX -IV

MATLAB Program to calculate mean pressure and Prms (shown below for centerline)

```
clc
clear all
close all

% stdiables for aCE-062-100A

sensitivity1 = 0.00101;           % Sensitivity for Transducer
Pregain1= 32;
Postgain1=3.094;
factor1= sensitivity1*Pregain1*Postgain1;

% stdiables for aCS-062-15D
sensitivity2 = 0.012779;         % Coefficient for current
Transducer
Pregain2= 32;
Postgain2=1.630;
factor2= sensitivity2*Pregain2*Postgain2;

for a=1:19
    if a==1
        % Station 0_1
        A0 = csvread('residual_cent_Station_0_1.csv',3,0); %import data into stdiabile
        A1 = csvread('pf_cent_Station_0_1_trial_1.csv',3,0); %import data into
        stdiabile
        A2 = csvread('pf_cent_Station_0_1_trial_2.csv',3,0); %import data into
        stdiabile
        B0=A0(:,2);
        B1=A1(:,2);
        B2=A2(:,2);
        C1(a)=(mean(B1)-mean(B0))/factor1+14.7;
        C2(a)=(mean(B2)-mean(B0))/factor1+14.7;
        D0=A0(:,3);
        D1=A1(:,3);
        D2=A2(:,3);
        E1(a)=(mean(D1)-mean(D0))/factor2+14.7;
        E2(a)=(mean(D2)-mean(D0))/factor2+14.7;
        E(a)=E1(a);
        pwrms1(a)=std((B1(:,1)-mean(B0))/factor1+14.7);
        pwrms2(a)=std((B2(:,1)-mean(B0))/factor1+14.7);
        pwrms(a)=pwrms1(a);

    else
        if a==2
            % Station 0_2
```

```

A0 = csvread('residual_cent_Station_0_2.csv',3,0); %import data into stdiabile
A1 = csvread('pf_cent_Station_0_2_trial_1.csv',3,0); %import data into
stdiabile
A2 = csvread('pf_cent_Station_0_2_trial_2.csv',3,0); %import data into
stdiabile
B0=A0(:,2);
B1=A1(:,2);
B2=A2(:,2);
C1(a)=(mean(B1)-mean(B0))/factor1)+14.7;
C2(a)=(mean(B2)-mean(B0))/factor1)+14.7;
D0=A0(:,3);
D1=A1(:,3);
D2=A2(:,3);
E1(a)=(mean(D1)-mean(D0))/factor2)+14.7;
E2(a)=(mean(D2)-mean(D0))/factor2)+14.7;
E(a)=(E1(a)+E2(a))/2;
pwrms1(a)=std(((B1(:,1)-mean(B0))/factor1)+14.7);
pwrms2(a)=std(((B2(:,1)-mean(B0))/factor1)+14.7);
pwrms(a)=(pwrms1(a)+pwrms2(a))/2;

% A0 = csvread('residual_cent_Station_0_2.csv',3,0); %import data into
stdiabile
% A1 = csvread('pf_cent_Station_0_2_trial_1.csv',3,0); %import data into
stdiabile
% % A2 = csvread('pf_cent_Station_0_1_trial_2.csv',3,0); %import data into
stdiabile
% B0=A0(:,2);
% B1=A1(:,2);
% % B2=A2(:,2);
% C1(a)=(mean(B1)-mean(B0))/factor1)+14.7;
% % C2(a)=(mean(B2)-mean(B0))/factor1)+14.7;
% D0=A0(:,3);
% D1=A1(:,3);
% % D2=A2(:,3);
% E1(a)=(mean(D1)-mean(D0))/factor2)+14.7;
% % E2(a)=(mean(D2)-mean(D0))/factor2)+14.7;
% E(a)=E1(a);
% pwrms1(a)=std(((B1(:,1)-mean(B0))/factor1)+14.7);
% % pwrms2(a)=std(((B2(:,1)-mean(B0))/factor1)+14.7);
% pwrms(a)=pwrms1(a);
    else
        if a==3
            % Station 0_3
A0 = csvread('residual_cent_Station_0_3.csv',3,0); %import data into stdiabile
A1 = csvread('pf_cent_Station_0_3_trial_1.csv',3,0); %import data into
stdiabile
A2 = csvread('pf_cent_Station_0_3_trial_2.csv',3,0); %import data into
stdiabile
B0=A0(:,2);
B1=A1(:,2);
B2=A2(:,2);
C1(a)=(mean(B1)-mean(B0))/factor1)+14.7;
C2(a)=(mean(B2)-mean(B0))/factor1)+14.7;
D0=A0(:,3);
D1=A1(:,3);
D2=A2(:,3);
E1(a)=(mean(D1)-mean(D0))/factor2)+14.7;

```

```

E2(a)=(mean(D2)-mean(D0))/factor2)+14.7;
E(a)=(E1(a)+E2(a))/2;
pwrms1(a)=std(((B1(:,1)-mean(B0))/factor1)+14.7);
pwrms2(a)=std(((B2(:,1)-mean(B0))/factor1)+14.7);
pwrms(a)=(pwrms1(a)+pwrms2(a))/2;

% A0 = csvread('residual_cent_Station_0_3.csv',3,0); %import data into
stdiable
% A1 = csvread('pf_cent_Station_0_3_trial_1.csv',3,0); %import data into
stdiable
% % A2 = csvread('pf_cent_Station_0_1_trial_2.csv',3,0); %import data into
stdiable
% B0=A0(:,2);
% B1=A1(:,2);
% % B2=A2(:,2);
% C1(a)=(mean(B1)-mean(B0))/factor1)+14.7;
% % C2(a)=(mean(B2)-mean(B0))/factor1)+14.7;
% D0=A0(:,3);
% D1=A1(:,3);
% % D2=A2(:,3);
% E1(a)=(mean(D1)-mean(D0))/factor2)+14.7;
% % E2(a)=(mean(D2)-mean(D0))/factor2)+14.7;
% E(a)=E1(a);
% pwrms1(a)=std(((B1(:,1)-mean(B0))/factor1)+14.7);
% % pwrms2(a)=std(((B2(:,1)-mean(B0))/factor1)+14.7);
% pwrms(a)=pwrms1(a);

else
    if a==4
% Station 0_4
A0 = csvread('residual_cent_Station_0_4.csv',3,0); %import data into stdiable
A1 = csvread('pf_cent_Station_0_4_trial_1.csv',3,0); %import data into
stdiable
A2 = csvread('pf_cent_Station_0_4_trial_2.csv',3,0); %import data into
stdiable
B0=A0(:,2);
B1=A1(:,2);
B2=A2(:,2);
C1(a)=(mean(B1)-mean(B0))/factor1)+14.7;
C2(a)=(mean(B2)-mean(B0))/factor1)+14.7;
D0=A0(:,3);
D1=A1(:,3);
D2=A2(:,3);
E1(a)=(mean(D1)-mean(D0))/factor2)+14.7;
E2(a)=(mean(D2)-mean(D0))/factor2)+14.7;
E(a)=(E1(a)+E2(a))/2;
pwrms1(a)=std(((B1(:,1)-mean(B0))/factor1)+14.7);
pwrms2(a)=std(((B2(:,1)-mean(B0))/factor1)+14.7);
pwrms(a)=(pwrms1(a)+pwrms2(a))/2;

else
    if a==5
% Station 0_5
A0 = csvread('residual_cent_Station_0_5.csv',3,0); %import data into stdiable
A1 = csvread('pf_cent_Station_0_5_trial_1.csv',3,0); %import data into
stdiable

```

```

A2 = csvread('pf_cent_Station_0_5_trial_2.csv',3,0); %import data into
stdiable
B0=A0(:,2);
B1=A1(:,2);
B2=A2(:,2);
C1(a)=(mean(B1)-mean(B0))/factor1)+14.7;
C2(a)=(mean(B2)-mean(B0))/factor1)+14.7;
D0=A0(:,3);
D1=A1(:,3);
D2=A2(:,3);
E1(a)=(mean(D1)-mean(D0))/factor2)+14.7;
E2(a)=(mean(D2)-mean(D0))/factor2)+14.7;
E(a)=(E1(a)+E2(a))/2;
pwrms1(a)=std((B1(:,1)-mean(B0))/factor1)+14.7);
pwrms2(a)=std((B2(:,1)-mean(B0))/factor1)+14.7);
pwrms(a)=(pwrms1(a)+pwrms2(a))/2;

else
    if a==6
% Station 0_6
A0 = csvread('residual_cent_Station_0_6.csv',3,0); %import data into stdiable
A1 = csvread('pf_cent_Station_0_6_trial_1.csv',3,0); %import data into
stdiable
A2 = csvread('pf_cent_Station_0_6_trial_2.csv',3,0); %import data into
stdiable
B0=A0(:,2);
B1=A1(:,2);
B2=A2(:,2);
C1(a)=(mean(B1)-mean(B0))/factor1)+14.7;
C2(a)=(mean(B2)-mean(B0))/factor1)+14.7;
D0=A0(:,3);
D1=A1(:,3);
D2=A2(:,3);
E1(a)=(mean(D1)-mean(D0))/factor2)+14.7;
E2(a)=(mean(D2)-mean(D0))/factor2)+14.7;
E(a)=(E1(a)+E2(a))/2;
pwrms1(a)=std((B1(:,1)-mean(B0))/factor1)+14.7);
pwrms2(a)=std((B2(:,1)-mean(B0))/factor1)+14.7);
pwrms(a)=(pwrms1(a)+pwrms2(a))/2;

else
    if a==7
% Station 0_7
A0 = csvread('residual_cent_Station_0_7.csv',3,0); %import data into stdiable
A1 = csvread('pf_cent_Station_0_7_trial_1.csv',3,0); %import data into
stdiable
A2 = csvread('pf_cent_Station_0_7_trial_2.csv',3,0); %import data into
stdiable
B0=A0(:,2);
B1=A1(:,2);
B2=A2(:,2);
C1(a)=(mean(B1)-mean(B0))/factor1)+14.7;
C2(a)=(mean(B2)-mean(B0))/factor1)+14.7;
D0=A0(:,3);
D1=A1(:,3);
D2=A2(:,3);

```

```

E1(a)=(mean(D1)-mean(D0))/factor2)+14.7;
E2(a)=(mean(D2)-mean(D0))/factor2)+14.7;
E(a)=(E1(a)+E2(a))/2;
pwrms1(a)=std(((B1(:,1)-mean(B0))/factor1)+14.7);
pwrms2(a)=std(((B2(:,1)-mean(B0))/factor1)+14.7);
pwrms(a)=(pwrms1(a)+pwrms2(a))/2;

else
    if a==8
% Station 0_8
A0 = csvread('residual_cent_Station_0_8.csv',3,0); %import data into stdiabile
A1 = csvread('pf_cent_Station_0_8_trial_1.csv',3,0); %import data into
stdiabile
A2 = csvread('pf_cent_Station_0_8_trial_2.csv',3,0); %import data into
stdiabile
B0=A0(:,2);
B1=A1(:,2);
B2=A2(:,2);
C1(a)=(mean(B1)-mean(B0))/factor1)+14.7;
C2(a)=(mean(B2)-mean(B0))/factor1)+14.7;
D0=A0(:,3);
D1=A1(:,3);
D2=A2(:,3);
E1(a)=(mean(D1)-mean(D0))/factor2)+14.7;
E2(a)=(mean(D2)-mean(D0))/factor2)+14.7;
E(a)=(E1(a)+E2(a))/2;
pwrms1(a)=std(((B1(:,1)-mean(B0))/factor1)+14.7);
pwrms2(a)=std(((B2(:,1)-mean(B0))/factor1)+14.7);
pwrms(a)=(pwrms1(a)+pwrms2(a))/2;

else
    if a==9
% Station 0_9
A0 = csvread('residual_cent_Station_0_9.csv',3,0); %import data into stdiabile
A1 = csvread('pf_cent_Station_0_9_trial_1.csv',3,0); %import data into
stdiabile
A2 = csvread('pf_cent_Station_0_9_trial_2.csv',3,0); %import data into
stdiabile
B0=A0(:,2);
B1=A1(:,2);
B2=A2(:,2);
C1(a)=(mean(B1)-mean(B0))/factor1)+14.7;
C2(a)=(mean(B2)-mean(B0))/factor1)+14.7;
D0=A0(:,3);
D1=A1(:,3);
D2=A2(:,3);
E1(a)=(mean(D1)-mean(D0))/factor2)+14.7;
E2(a)=(mean(D2)-mean(D0))/factor2)+14.7;
E(a)=(E1(a)+E2(a))/2;
pwrms1(a)=std(((B1(:,1)-mean(B0))/factor1)+14.7);
pwrms2(a)=std(((B2(:,1)-mean(B0))/factor1)+14.7);
pwrms(a)=(pwrms1(a)+pwrms2(a))/2;

else
    if a==10
% Station 0_10

```

```

A0 = csvread('residual_cent_Station_0_10.csv',3,0); %import data into
stdiable
A1 = csvread('pf_cent_Station_0_10_trial_1.csv',3,0); %import data into
stdiable
A2 = csvread('pf_cent_Station_0_10_trial_2.csv',3,0); %import data into
stdiable
B0=A0(:,2);
B1=A1(:,2);
B2=A2(:,2);
C1(a)=(mean(B1)-mean(B0))/factor1)+14.7;
C2(a)=(mean(B2)-mean(B0))/factor1)+14.7;
D0=A0(:,3);
D1=A1(:,3);
D2=A2(:,3);
E1(a)=(mean(D1)-mean(D0))/factor2)+14.7;
E2(a)=(mean(D2)-mean(D0))/factor2)+14.7;
E(a)=(E1(a)+E2(a))/2;
pwrms1(a)=std(((B1(:,1)-mean(B0))/factor1)+14.7);
pwrms2(a)=std(((B2(:,1)-mean(B0))/factor1)+14.7);
pwrms(a)=(pwrms1(a)+pwrms2(a))/2;
else
    if a==11
        % Station 0_11
A0 = csvread('residual_cent_Station_0_11.csv',3,0); %import data into
stdiable
A1 = csvread('pf_cent_Station_0_11_trial_1.csv',3,0); %import data into
stdiable
A2 = csvread('pf_cent_Station_0_11_trial_2.csv',3,0); %import data into
stdiable
B0=A0(:,2);
B1=A1(:,2);
B2=A2(:,2);
C1(a)=(mean(B1)-mean(B0))/factor1)+14.7;
C2(a)=(mean(B2)-mean(B0))/factor1)+14.7;
D0=A0(:,3);
D1=A1(:,3);
D2=A2(:,3);
E1(a)=(mean(D1)-mean(D0))/factor2)+14.7;
E2(a)=(mean(D2)-mean(D0))/factor2)+14.7;
E(a)=(E1(a)+E2(a))/2;
pwrms1(a)=std(((B1(:,1)-mean(B0))/factor1)+14.7);
pwrms2(a)=std(((B2(:,1)-mean(B0))/factor1)+14.7);
pwrms(a)=(pwrms1(a)+pwrms2(a))/2;
else
    if a==12
        % Station 0_12
A0 = csvread('residual_cent_Station_0_12.csv',3,0); %import data into
stdiable
A1 = csvread('pf_cent_Station_0_12_trial_1.csv',3,0); %import data into
stdiable
A2 = csvread('pf_cent_Station_0_12_trial_2.csv',3,0); %import data into
stdiable
B0=A0(:,2);
B1=A1(:,2);
B2=A2(:,2);
C1(a)=(mean(B1)-mean(B0))/factor1)+14.7;
C2(a)=(mean(B2)-mean(B0))/factor1)+14.7;

```

```

D0=A0(:,3);
D1=A1(:,3);
D2=A2(:,3);
E1(a)=(mean(D1)-mean(D0))/factor2)+14.7;
E2(a)=(mean(D2)-mean(D0))/factor2)+14.7;
E(a)=(E1(a)+E2(a))/2;
pwrms1(a)=std(((B1(:,1)-mean(B0))/factor1)+14.7);
pwrms2(a)=std(((B2(:,1)-mean(B0))/factor1)+14.7);
pwrms(a)=(pwrms1(a)+pwrms2(a))/2;
else
    if a==13
        % Station 0_13
A0 = csvread('residual_cent_Station_0_13.csv',3,0); %import data into
stdiable
A1 = csvread('pf_cent_Station_0_13_trial_1.csv',3,0); %import data into
stdiable
A2 = csvread('pf_cent_Station_0_13_trial_2.csv',3,0); %import data into
stdiable
B0=A0(:,2);
B1=A1(:,2);
B2=A2(:,2);
C1(a)=(mean(B1)-mean(B0))/factor1)+14.7;
C2(a)=(mean(B2)-mean(B0))/factor1)+14.7;
D0=A0(:,3);
D1=A1(:,3);
D2=A2(:,3);
E1(a)=(mean(D1)-mean(D0))/factor2)+14.7;
E2(a)=(mean(D2)-mean(D0))/factor2)+14.7;
E(a)=(E1(a)+E2(a))/2;
pwrms1(a)=std(((B1(:,1)-mean(B0))/factor1)+14.7);
pwrms2(a)=std(((B2(:,1)-mean(B0))/factor1)+14.7);
pwrms(a)=(pwrms1(a)+pwrms2(a))/2;
else
    if a==14
        % Station 0_14
A0 = csvread('residual_cent_Station_0_14.csv',3,0); %import data into
stdiable
A1 = csvread('pf_cent_Station_0_14_trial_1.csv',3,0); %import data into
stdiable
A2 = csvread('pf_cent_Station_0_14_trial_2.csv',3,0); %import data into
stdiable
B0=A0(:,2);
B1=A1(:,2);
B2=A2(:,2);
C1(a)=(mean(B1)-mean(B0))/factor1)+14.7;
C2(a)=(mean(B2)-mean(B0))/factor1)+14.7;
D0=A0(:,3);
D1=A1(:,3);
D2=A2(:,3);
E1(a)=(mean(D1)-mean(D0))/factor2)+14.7;
E2(a)=(mean(D2)-mean(D0))/factor2)+14.7;
E(a)=(E1(a)+E2(a))/2;
pwrms1(a)=std(((B1(:,1)-mean(B0))/factor1)+14.7);
pwrms2(a)=std(((B2(:,1)-mean(B0))/factor1)+14.7);
pwrms(a)=(pwrms1(a)+pwrms2(a))/2;
else
    if a==15

```

```

        % Station 0_15
A0 = csvread('residual_cent_Station_0_15.csv',3,0); %import data into
stdiable
A1 = csvread('pf_cent_Station_0_15_trial_1.csv',3,0); %import data into
stdiable
A2 = csvread('pf_cent_Station_0_15_trial_2.csv',3,0); %import data into
stdiable
B0=A0(:,2);
B1=A1(:,2);
B2=A2(:,2);
C1(a)=(mean(B1)-mean(B0))/factor1+14.7;
C2(a)=(mean(B2)-mean(B0))/factor1+14.7;
D0=A0(:,3);
D1=A1(:,3);
D2=A2(:,3);
E1(a)=(mean(D1)-mean(D0))/factor2+14.7;
E2(a)=(mean(D2)-mean(D0))/factor2+14.7;
E(a)=(E1(a)+E2(a))/2;
pwrms1(a)=std((B1(:,1)-mean(B0))/factor1+14.7);
pwrms2(a)=std((B2(:,1)-mean(B0))/factor1+14.7);
pwrms(a)=(pwrms1(a)+pwrms2(a))/2;
else
    if a==16
        % Station 0_16
A0 = csvread('residual_cent_Station_0_16.csv',3,0); %import data into
stdiable
A1 = csvread('pf_cent_Station_0_16_trial_1.csv',3,0); %import data into
stdiable
A2 = csvread('pf_cent_Station_0_16_trial_2.csv',3,0); %import data into
stdiable
B0=A0(:,2);
B1=A1(:,2);
B2=A2(:,2);
C1(a)=(mean(B1)-mean(B0))/factor1+14.7;
C2(a)=(mean(B2)-mean(B0))/factor1+14.7;
D0=A0(:,3);
D1=A1(:,3);
D2=A2(:,3);
E1(a)=(mean(D1)-mean(D0))/factor2+14.7;
E2(a)=(mean(D2)-mean(D0))/factor2+14.7;
E(a)=(E1(a)+E2(a))/2;
pwrms1(a)=std((B1(:,1)-mean(B0))/factor1+14.7);
pwrms2(a)=std((B2(:,1)-mean(B0))/factor1+14.7);
pwrms(a)=(pwrms1(a)+pwrms2(a))/2;
else
    if a==17
        % Station 0_17
A0 = csvread('residual_cent_Station_0_17.csv',3,0); %import data into
stdiable
A1 = csvread('pf_cent_Station_0_17_trial_1.csv',3,0); %import data into
stdiable
A2 = csvread('pf_cent_Station_0_17_trial_2.csv',3,0); %import data into
stdiable
B0=A0(:,2);
B1=A1(:,2);
B2=A2(:,2);
C1(a)=(mean(B1)-mean(B0))/factor1+14.7;

```

```

C2(a)=(mean(B2)-mean(B0))/factor1)+14.7;
D0=A0(:,3);
D1=A1(:,3);
D2=A2(:,3);
E1(a)=(mean(D1)-mean(D0))/factor2)+14.7;
E2(a)=(mean(D2)-mean(D0))/factor2)+14.7;
E(a)=(E1(a)+E2(a))/2;
pwrms1(a)=std(((B1(:,1)-mean(B0))/factor1)+14.7);
pwrms2(a)=std(((B2(:,1)-mean(B0))/factor1)+14.7);
pwrms(a)=(pwrms1(a)+pwrms2(a))/2;

else
    if a==18
        % Station 0_18
A0 = csvread('residual_cent_Station_0_18.csv',3,0); %import data into
stdiabile
A1 = csvread('pf_cent_Station_0_18_trial_1.csv',3,0); %import data into
stdiabile
A2 = csvread('pf_cent_Station_0_18_trial_2.csv',3,0); %import data into
stdiabile
B0=A0(:,2);
B1=A1(:,2);
B2=A2(:,2);
C1(a)=(mean(B1)-mean(B0))/factor1)+14.7;
C2(a)=(mean(B2)-mean(B0))/factor1)+14.7;
D0=A0(:,3);
D1=A1(:,3);
D2=A2(:,3);
E1(a)=(mean(D1)-mean(D0))/factor2)+14.7;
E2(a)=(mean(D2)-mean(D0))/factor2)+14.7;
E(a)=(E1(a)+E2(a))/2;
pwrms1(a)=std(((B1(:,1)-mean(B0))/factor1)+14.7);
pwrms2(a)=std(((B2(:,1)-mean(B0))/factor1)+14.7);
pwrms(a)=(pwrms1(a)+pwrms2(a))/2;

else
    if a==19
        % Station 0_19
A0 = csvread('residual_cent_Station_0_19.csv',3,0); %import data into
stdiabile
A1 = csvread('pf_cent_Station_0_19_trial_1.csv',3,0); %import data into
stdiabile
A2 = csvread('pf_cent_Station_0_19_trial_2.csv',3,0); %import data into
stdiabile
B0=A0(:,2);
B1=A1(:,2);
B2=A2(:,2);
C1(a)=(mean(B1)-mean(B0))/factor1)+14.7;
C2(a)=(mean(B2)-mean(B0))/factor1)+14.7;
D0=A0(:,3);
D1=A1(:,3);
D2=A2(:,3);
E1(a)=(mean(D1)-mean(D0))/factor2)+14.7;
E2(a)=(mean(D2)-mean(D0))/factor2)+14.7;
E(a)=(E1(a)+E2(a))/2;
pwrms1(a)=std(((B1(:,1)-mean(B0))/factor1)+14.7);

```



```

plot(d,centrerms_mean,'-*','MarkerFaceColor','black','MarkerSize',5);
% labels_cornre=cellstr(num2str([1:1:19]));
% text(d,centrerms_mean,labels_cornre,'VerticalAlignment','bottom');
% title('Mean Streamwise Prms');
% xlabel('x/{\delta}');
% ylabel('{\sigma}/Pwall');
hold off

figure(2);
plot(d,p_rise1,'-o','MarkerFaceColor','black','MarkerSize',5);
labels_cornre=cellstr(num2str([1:1:19]));
text(d,p_rise1,labels_cornre,'VerticalAlignment','bottom');
title('Streamwise Pressure Rise-Pulse filter mode');
set(gca,'box','off');
set(gca,'TickDir','out')
xlabel('x/{\delta}');
ylabel('P/P_{\infty}');
set(gca,'XMinorTick','on','YMinorTick','on')
set(gca,'box','off');
hold on

plot(d,p_rise2,'-', 'MarkerFaceColor','black','MarkerSize',5);
% labels_cornre=cellstr(num2str([1:1:19]));
% text(d1,p,labels_cornre,'VerticalAlignment','bottom');
% title('Streamwise Pressure Rise-Flat filter mode');
% set(gca,'box','off');
% set(gca,'TickDir','out')
% xlabel('x/{\delta}');
% ylabel('P/P_{\infty}');
% set(gca,'XMinorTick','on','YMinorTick','on')
% set(gca,'box','off');

plot(d,p_rise_mean,'-*','MarkerFaceColor','black','MarkerSize',5);
% labels_cornre=cellstr(num2str([1:1:19]));
% text(d1,p,labels_cornre,'VerticalAlignment','bottom');
% title('Streamwise Pressure Rise-Flat filter mode');
% set(gca,'box','off');
% set(gca,'TickDir','out')
% xlabel('x/{\delta}');
% ylabel('P/P_{\infty}');
% set(gca,'XMinorTick','on','YMinorTick','on')
% set(gca,'box','off');

```

MATLAB Program to calculate PSD (shown below for centerline)

```
clc
clear all
close all

% *****Transducer-1

A0 = csvread('pf_vort_Station_0_1_trial_1.csv',3,0); %import data into
stdiable
A2 = csvread('pf_vort_Station_0_1_trial_2.csv',3,0);
for i=1:length(A0)
A1(i,1)=(A0(i,2)+A2(i,2))/2;
end
A=(A1(:,1)/0.1)+14.7;
t1 = A1(:,1);
Fs1 = 50000; % Sampling Frequency
FNyquist1 = Fs1/2; %Nyquist Frequency
B1 = 8192;
OverLapPer1 = 50; % of overlap you want
OverLap1 = 1-OverLapPer1/100; %convert to decimal
N1 = length(t1);
NP1 = 2^(nextpow2(N1)-1);
N1 = round(NP1/(B1*OverLap1));
Step1 = round(B1*OverLap1);
window1 = hann(B1);

[f1,Av1]=fftprog_1(A, N1, B1, Step1, window1, FNyquist1, 1);

A0 = csvread('pf_vort_Station_0_1_trial_1.csv',3,0); %import data into
stdiable
A2 = csvread('pf_vort_Station_0_1_trial_2.csv',3,0);
for i=1:length(A0)
A1(i,1)=(A0(i,2)+A2(i,2))/2;
end
A=(A1(:,1)/0.1)+14.7;
[f2,Av2]=fftprog_1(A, N1, B1, Step1, window1, FNyquist1, 1);

% *****Transducer-2

A0 = csvread('pf_vort_Station_0_2_trial_1.csv',3,0); %import data into
stdiable
A2 = csvread('pf_vort_Station_0_2_trial_2.csv',3,0);
for i=1:length(A0)
A1(i,1)=(A0(i,2)+A2(i,2))/2;
end
A=(A1(:,1)/0.1)+14.7;
[f3,Av3]=fftprog_1(A, N1, B1, Step1, window1, FNyquist1, 1);
```

```

A0 = csvread('pf_vort_Station_0_2_trial_1.csv',3,0); %import data into
stdiable
A2 = csvread('pf_vort_Station_0_2_trial_2.csv',3,0);
for i=1:length(A0)
A1(i,1)=(A0(i,2)+A2(i,2))/2;
end
A=(A1(:,1)/0.1)+14.7;
[f4,Av4]=fftprog_1(A, N1, B1, Step1, window1, FNyquist1, 1);

% *****Transducer-3

A0 = csvread('pf_vort_Station_0_3_trial_1.csv',3,0); %import data into
stdiable
A2 = csvread('pf_vort_Station_0_3_trial_2.csv',3,0);
for i=1:length(A0)
A1(i,1)=(A0(i,2)+A2(i,2))/2;
end
A=(A1(:,1)/0.1)+14.7;
[f5,Av5]=fftprog_1(A, N1, B1, Step1, window1, FNyquist1, 1);

A0 = csvread('pf_vort_Station_0_3_trial_1.csv',3,0); %import data into
stdiable
A2 = csvread('pf_vort_Station_0_3_trial_2.csv',3,0);
for i=1:length(A0)
A1(i,1)=(A0(i,2)+A2(i,2))/2;
end
A=(A1(:,1)/0.1)+14.7;
[f6,Av6]=fftprog_1(A, N1, B1, Step1, window1, FNyquist1, 1);

% *****Transducer-4

A0 = csvread('pf_vort_Station_0_4_trial_1.csv',3,0); %import data into
stdiable
A2 = csvread('pf_vort_Station_0_4_trial_2.csv',3,0);
for i=1:length(A0)
A1(i,1)=(A0(i,2)+A2(i,2))/2;
end
A=(A1(:,1)/0.1)+14.7;
[f7,Av7]=fftprog_1(A, N1, B1, Step1, window1, FNyquist1, 1);

A0 = csvread('pf_vort_Station_0_4_trial_1.csv',3,0); %import data into
stdiable
A2 = csvread('pf_vort_Station_0_4_trial_2.csv',3,0);
for i=1:length(A0)
A1(i,1)=(A0(i,2)+A2(i,2))/2;
end
A=(A1(:,1)/0.1)+14.7;
[f8,Av8]=fftprog_1(A, N1, B1, Step1, window1, FNyquist1, 1);

% *****Transducer-5

A0 = csvread('pf_vort_Station_0_5_trial_1.csv',3,0); %import data into
stdiable

```

```

A2 = csvread('pf_vort_Station_0_5_trial_2.csv',3,0);
for i=1:length(A0)
A1(i,1)=(A0(i,2)+A2(i,2))/2;
end
A=(A1(:,1)/0.1)+14.7;
[f9,Av9]=fftprog_1(A, N1, B1, Step1, window1, FNyquist1, 1);

A0 = csvread('pf_vort_Station_0_5_trial_1.csv',3,0); %import data into
stdiabile
A2 = csvread('pf_vort_Station_0_5_trial_2.csv',3,0);
for i=1:length(A0)
A1(i,1)=(A0(i,2)+A2(i,2))/2;
end
A=(A1(:,1)/0.1)+14.7;
[f10,Av10]=fftprog_1(A, N1, B1, Step1, window1, FNyquist1, 1);

% *****Transducer-6

A0 = csvread('pf_vort_Station_0_6_trial_1.csv',3,0); %import data into
stdiabile
A2 = csvread('pf_vort_Station_0_6_trial_2.csv',3,0);
for i=1:length(A0)
A1(i,1)=(A0(i,2)+A2(i,2))/2;
end
A=(A1(:,1)/0.1)+14.7;
[f11,Av11]=fftprog_1(A, N1, B1, Step1, window1, FNyquist1, 1);
A0 = csvread('pf_vort_Station_0_6_trial_1.csv',3,0); %import data into
stdiabile
A2 = csvread('pf_vort_Station_0_6_trial_2.csv',3,0);
for i=1:length(A0)
A1(i,1)=(A0(i,2)+A2(i,2))/2;
end
A=(A1(:,1)/0.1)+14.7;
[f12,Av12]=fftprog_1(A, N1, B1, Step1, window1, FNyquist1, 1);

% *****Transducer-7

A0 = csvread('pf_vort_Station_0_7_trial_1.csv',3,0); %import data into
stdiabile
A2 = csvread('pf_vort_Station_0_7_trial_2.csv',3,0);
for i=1:length(A0)
A1(i,1)=(A0(i,2)+A2(i,2))/2;
end
A=(A1(:,1)/0.1)+14.7;
[f13,Av13]=fftprog_1(A, N1, B1, Step1, window1, FNyquist1, 1);

A0 = csvread('pf_vort_Station_0_7_trial_1.csv',3,0); %import data into
stdiabile
A2 = csvread('pf_vort_Station_0_7_trial_2.csv',3,0);
for i=1:length(A0)
A1(i,1)=(A0(i,2)+A2(i,2))/2;
end
A=(A1(:,1)/0.1)+14.7;
[f14,Av14]=fftprog_1(A, N1, B1, Step1, window1, FNyquist1, 1);

% *****Transducer-8

```

```

A0 = csvread('pf_vort_Station_0_8_trial_1.csv',3,0); %import data into
stdiabile
A2 = csvread('pf_vort_Station_0_8_trial_2.csv',3,0);
for i=1:length(A0)
A1(i,1)=(A0(i,2)+A2(i,2))/2;
end
A=(A1(:,1)/0.1)+14.7;
[f15,Av15]=fftprog_1(A, N1, B1, Step1, window1, FNyquist1, 1);

A0 = csvread('pf_vort_Station_0_8_trial_1.csv',3,0); %import data into
stdiabile
A2 = csvread('pf_vort_Station_0_8_trial_2.csv',3,0);
for i=1:length(A0)
A1(i,1)=(A0(i,2)+A2(i,2))/2;
end
A=(A1(:,1)/0.1)+14.7;
[f16,Av16]=fftprog_1(A, N1, B1, Step1, window1, FNyquist1, 1);

% *****Transducer-9

A0 = csvread('pf_vort_Station_0_9_trial_1.csv',3,0); %import data into
stdiabile
A2 = csvread('pf_vort_Station_0_9_trial_2.csv',3,0);
for i=1:length(A0)
A1(i,1)=(A0(i,2)+A2(i,2))/2;
end
A=(A1(:,1)/0.1)+14.7;
[f17,Av17]=fftprog_1(A, N1, B1, Step1, window1, FNyquist1, 1);

A0 = csvread('pf_vort_Station_0_9_trial_1.csv',3,0); %import data into
stdiabile
A2 = csvread('pf_vort_Station_0_9_trial_2.csv',3,0);
for i=1:length(A0)
A1(i,1)=(A0(i,2)+A2(i,2))/2;
end
A=(A1(:,1)/0.1)+14.7;
[f18,Av18]=fftprog_1(A, N1, B1, Step1, window1, FNyquist1, 1);

% *****Transducer-10

A0 = csvread('pf_vort_Station_0_10_trial_1.csv',3,0); %import data into
stdiabile
A2 = csvread('pf_vort_Station_0_10_trial_2.csv',3,0);
for i=1:length(A0)
A1(i,1)=(A0(i,2)+A2(i,2))/2;
end
A=(A1(:,1)/0.1)+14.7;
[f19,Av19]=fftprog_1(A, N1, B1, Step1, window1, FNyquist1, 1);

A0 = csvread('pf_vort_Station_0_10_trial_1.csv',3,0); %import data into
stdiabile
A2 = csvread('pf_vort_Station_0_10_trial_2.csv',3,0);
for i=1:length(A0)
A1(i,1)=(A0(i,2)+A2(i,2))/2;

```

```

end
A=(A1(:,1)/0.1)+14.7;
[f20,Av20]=fftprog_1(A, N1, B1, Step1, window1, FNyquist1, 1);

% *****Transducer-11

A0 = csvread('pf_vort_Station_0_11_trial_1.csv',3,0); %import data into
stdiabile
A2 = csvread('pf_vort_Station_0_11_trial_2.csv',3,0);
for i=1:length(A0)
A1(i,1)=(A0(i,2)+A2(i,2))/2;
end
A=(A1(:,1)/0.1)+14.7;
[f21,Av21]=fftprog_1(A, N1, B1, Step1, window1, FNyquist1, 1);

A0 = csvread('pf_vort_Station_0_11_trial_1.csv',3,0); %import data into
stdiabile
A2 = csvread('pf_vort_Station_0_11_trial_2.csv',3,0);
for i=1:length(A0)
A1(i,1)=(A0(i,2)+A2(i,2))/2;
end
A=(A1(:,1)/0.1)+14.7;
[f22,Av22]=fftprog_1(A, N1, B1, Step1, window1, FNyquist1, 1);

% *****Transducer-12

A0 = csvread('pf_vort_Station_0_12_trial_1.csv',3,0); %import data into
stdiabile
A2 = csvread('pf_vort_Station_0_12_trial_2.csv',3,0);
for i=1:length(A0)
A1(i,1)=(A0(i,2)+A2(i,2))/2;
end
A=(A1(:,1)/0.1)+14.7;
[f23,Av23]=fftprog_1(A, N1, B1, Step1, window1, FNyquist1, 1);

A0 = csvread('pf_vort_Station_0_12_trial_1.csv',3,0); %import data into
stdiabile
A2 = csvread('pf_vort_Station_0_12_trial_2.csv',3,0);
for i=1:length(A0)
A1(i,1)=(A0(i,2)+A2(i,2))/2;
end
A=(A1(:,1)/0.1)+14.7;
[f24,Av24]=fftprog_1(A, N1, B1, Step1, window1, FNyquist1, 1);

% *****Transducer-13

A0 = csvread('pf_vort_Station_0_13_trial_1.csv',3,0); %import data into
stdiabile
A2 = csvread('pf_vort_Station_0_13_trial_2.csv',3,0);
for i=1:length(A0)
A1(i,1)=(A0(i,2)+A2(i,2))/2;
end
A=(A1(:,1)/0.1)+14.7;
[f25,Av25]=fftprog_1(A, N1, B1, Step1, window1, FNyquist1, 1);

```

```

A0 = csvread('pf_vort_Station_0_13_trial_1.csv',3,0); %import data into
stdiable
A2 = csvread('pf_vort_Station_0_13_trial_2.csv',3,0);
for i=1:length(A0)
A1(i,1)=(A0(i,2)+A2(i,2))/2;
end
A=(A1(:,1)/0.1)+14.7;
[f26,Av26]=fftprog_1(A, N1, B1, Step1, window1, FNyquist1, 1);

% *****Transducer-14

A0 = csvread('pf_vort_Station_0_14_trial_1.csv',3,0); %import data into
stdiable
A2 = csvread('pf_vort_Station_0_14_trial_2.csv',3,0);
for i=1:length(A0)
A1(i,1)=(A0(i,2)+A2(i,2))/2;
end
A=(A1(:,1)/0.1)+14.7;
[f27,Av27]=fftprog_1(A, N1, B1, Step1, window1, FNyquist1, 1);

A0 = csvread('pf_vort_Station_0_14_trial_1.csv',3,0); %import data into
stdiable
A2 = csvread('pf_vort_Station_0_14_trial_2.csv',3,0);
for i=1:length(A0)
A1(i,1)=(A0(i,2)+A2(i,2))/2;
end
A=(A1(:,1)/0.1)+14.7;
[f28,Av28]=fftprog_1(A, N1, B1, Step1, window1, FNyquist1, 1);

% *****Transducer-15

A0 = csvread('pf_vort_Station_0_15_trial_1.csv',3,0); %import data into
stdiable
A2 = csvread('pf_vort_Station_0_15_trial_2.csv',3,0);
for i=1:length(A0)
A1(i,1)=(A0(i,2)+A2(i,2))/2;
end
A=(A1(:,1)/0.1)+14.7;
[f29,Av29]=fftprog_1(A, N1, B1, Step1, window1, FNyquist1, 1);

A0 = csvread('pf_vort_Station_0_15_trial_1.csv',3,0); %import data into
stdiable
A2 = csvread('pf_vort_Station_0_15_trial_2.csv',3,0);
for i=1:length(A0)
A1(i,1)=(A0(i,2)+A2(i,2))/2;
end
A=(A1(:,1)/0.1)+14.7;
[f30,Av30]=fftprog_1(A, N1, B1, Step1, window1, FNyquist1, 1);

% *****Transducer-16

A0 = csvread('pf_vort_Station_0_16_trial_1.csv',3,0); %import data into
stdiable
A2 = csvread('pf_vort_Station_0_16_trial_2.csv',3,0);
for i=1:length(A0)

```

```

A1(i,1)=(A0(i,2)+A2(i,2))/2;
end
A=(A1(:,1)/0.1)+14.7;
[f31,Av31]=fftprog_1(A, N1, B1, Step1, window1, FNyquist1, 1);

A0 = csvread('pf_vort_Station_0_16_trial_1.csv',3,0); %import data into
stdiabile
A2 = csvread('pf_vort_Station_0_16_trial_2.csv',3,0);
for i=1:length(A0)
A1(i,1)=(A0(i,2)+A2(i,2))/2;
end
A=(A1(:,1)/0.1)+14.7;
[f32,Av32]=fftprog_1(A, N1, B1, Step1, window1, FNyquist1, 1);

% *****Transducer-17

A0 = csvread('pf_vort_Station_0_17_trial_1.csv',3,0); %import data into
stdiabile
A2 = csvread('pf_vort_Station_0_17_trial_2.csv',3,0);
for i=1:length(A0)
A1(i,1)=(A0(i,2)+A2(i,2))/2;
end
A=(A1(:,1)/0.1)+14.7;
[f33,Av33]=fftprog_1(A, N1, B1, Step1, window1, FNyquist1, 1);

A0 = csvread('pf_vort_Station_0_17_trial_1.csv',3,0); %import data into
stdiabile
A2 = csvread('pf_vort_Station_0_17_trial_2.csv',3,0);
for i=1:length(A0)
A1(i,1)=(A0(i,2)+A2(i,2))/2;
end
A=(A1(:,1)/0.1)+14.7;
[f34,Av34]=fftprog_1(A, N1, B1, Step1, window1, FNyquist1, 1);

% *****Transducer-18

A0 = csvread('pf_vort_Station_0_18_trial_1.csv',3,0); %import data into
stdiabile
A2 = csvread('pf_vort_Station_0_18_trial_2.csv',3,0);
for i=1:length(A0)
A1(i,1)=(A0(i,2)+A2(i,2))/2;
end
A=(A1(:,1)/0.1)+14.7;
[f35,Av35]=fftprog_1(A, N1, B1, Step1, window1, FNyquist1, 1);

A0 = csvread('pf_vort_Station_0_18_trial_1.csv',3,0); %import data into
stdiabile
A2 = csvread('pf_vort_Station_0_18_trial_2.csv',3,0);
for i=1:length(A0)
A1(i,1)=(A0(i,2)+A2(i,2))/2;
end
A=(A1(:,1)/0.1)+14.7;
[f36,Av36]=fftprog_1(A, N1, B1, Step1, window1, FNyquist1, 1);

% *****Transducer-19

```

```

A0 = csvread('pf_vort_Station_0_19_trial_1.csv',3,0); %import data into
stdiabile
A2 = csvread('pf_vort_Station_0_19_trial_2.csv',3,0);
for i=1:length(A0)
A1(i,1)=(A0(i,2)+A2(i,2))/2;
end
A=(A1(:,1)/0.1)+14.7;
[f37,Av37]=fftprog_1(A, N1, B1, Step1, window1, FNyquist1, 1);

A0 = csvread('pf_vort_Station_0_19_trial_1.csv',3,0); %import data into
stdiabile
A2 = csvread('pf_vort_Station_0_19_trial_2.csv',3,0);
for i=1:length(A0)
A1(i,1)=(A0(i,2)+A2(i,2))/2;
end
A=(A1(:,1)/0.1)+14.7;
[f38,Av38]=fftprog_1(A, N1, B1, Step1, window1, FNyquist1, 1);

% *****Transducer-20

A0 = csvread('pf_vort_Station_0_20_trial_1.csv',3,0); %import data into
stdiabile
A2 = csvread('pf_vort_Station_0_20_trial_2.csv',3,0);
for i=1:length(A0)
A1(i,1)=(A0(i,2)+A2(i,2))/2;
end
A=(A1(:,1)/0.1)+14.7;
[f39,Av39]=fftprog_1(A, N1, B1, Step1, window1, FNyquist1, 1);

A0 = csvread('pf_vort_Station_0_20_trial_1.csv',3,0); %import data into
stdiabile
A2 = csvread('pf_vort_Station_0_20_trial_2.csv',3,0);
for i=1:length(A0)
A1(i,1)=(A0(i,2)+A2(i,2))/2;
end
A=(A1(:,1)/0.1)+14.7;
[f40,Av40]=fftprog_1(A, N1, B1, Step1, window1, FNyquist1, 1);

f=f1';

for i=1:20
    if i==1
Ah{i}(:,1)=(Av1)/(0.3955*0.3955);
    else
    if i==2
Ah{i}(:,1)=(Av3)/(0.3955*0.3955);%-Ah{1}(1,:);
    else
    if i==3
Ah{i}(:,1)=(Av5)/(0.3955*0.3955);%-Ah{1}(1,:);
    else
    if i==4
Ah{i}(:,1)=(Av7)/(0.3955*0.3955);%-Ah{1}(1,:);
    else
    if i==5

```



```

end
end
end
end
end
end
end
end
end

% f=f1';
figure(1)
semilogx(f1,Ah{1}, 'LineWidth',2)
hold on
% for i=1:17
% if i==1
% p{i} = polyfit(f(1:500,1),Ah{8}(1:500,1),25);
% a{i} = polyval(p{i},f(1:500,1));
% q{1}(1:500)=a{i}(:,1);
% else
%     if i==17
% k=(i-1)*500;
% p{i} = polyfit(f(k+1:length(Av1),1),Ah{8}(k+1:j,1),25);
% a{i} = polyval(p{i},f(k+1:length(Av1),1));
% q{1}(k+1:length(Av1))=a{i}(:,1);
%     else
% j=i*500;
% k=(i-1)*500;
% p{i} = polyfit(f(k+1:j,1),Ah{8}(k+1:j,1),25);
% a{i} = polyval(p{i},f(k+1:j,1));
% q{1}(k+1:j)=a{i}(:,1);
% end
% end
% end
% semilogx(f,q,'Color',[0,1,0],'LineWidth',2);
% p1 = polyfit(f1,Ah1,25);
% a1 = polyval(p1,f1);
% semilogx(f1,a1,'LineWidth',2);
% hold on

% semilogx(f1,Ah2,'LineWidth',2)
% % p2 = polyfit(f1,Ah2,25);
% % a2 = polyval(p2,f1);
% % semilogx(f1,a2,'LineWidth',2);
%
% semilogx(f1,Ah3,'LineWidth',2)
% % p3 = polyfit(f1,Ah3,25);
% % a3 = polyval(p3,f1);
% % semilogx(f1,a3,'LineWidth',2);
%
% semilogx(f1,Ah4,'LineWidth',2)
% % p4 = polyfit(f1,Ah4,25);
% % a4 = polyval(p4,f1);
% % semilogx(f1,a4,'LineWidth',2);
%
% semilogx(f1,Ah5,'LineWidth',2)
% % p5 = polyfit(f1,Ah5,25);

```

```

% % a5 = polyval(p5,f1);
% % % semilogx(f1,a5,'LineWidth',2);
% %
% semilogx(f1,Ah6,'LineWidth',2)
% % p6 = polyfit(f1,Ah6,25);
% % a6 = polyval(p6,f1);
% % semilogx(f1,a6,'LineWidth',2);
% %
% semilogx(f1,Ah7,'LineWidth',2)
% % p7 = polyfit(f1,Ah7,25);
% % a7 = polyval(p7,f1);
% % semilogx(f1,a7,'LineWidth',2);
Q=fix(length(Av1)/500);
for x=1:20
    if x==1
semilogx(f,Ah{1},'LineWidth',2)
for i=1:Q
if i==1
p{i} = polyfit(f(1:500,1),Ah{1}(1:500,1),25);
a{i} = polyval(p{i},f(1:500,1));
q{x}(1:500,1)=a{i}(:,1);
        else
j=i*500;
k=(i-1)*500;
p{i} = polyfit(f(k+1:j,1),Ah{1}(k+1:j,1),25);
a{i} = polyval(p{i},f(k+1:j,1));
q{x}(k+1:j,1)=a{i}(:,1);
        end
end
k=(i-1)*500;
p{i} = polyfit(f(k+1:length(Av1),1),Ah{1}(k+1:length(Av1),1),25);
a{i} = polyval(p{i},f(k+1:length(Av1),1));
q{x}(k+1:length(Av1),1)=a{i}(:,1);
semilogx(f(:,1),q{x}(:,1),'Color',[0,1,0],'LineWidth',2);
        else
            if x==2
semilogx(f,Ah{2},'LineWidth',2)
for i=1:Q
if i==1
p{i} = polyfit(f(1:500,1),Ah{2}(1:500,1),25);
a{i} = polyval(p{i},f(1:500,1));
q{x}(1:500,1)=a{i}(:,1);
        else
j=i*500;
k=(i-1)*500;
p{i} = polyfit(f(k+1:j,1),Ah{2}(k+1:j,1),25);
a{i} = polyval(p{i},f(k+1:j,1));
q{x}(k+1:j,1)=a{i}(:,1);
        end
end
k=(i-1)*500;
p{i} = polyfit(f(k+1:length(Av1),1),Ah{2}(k+1:length(Av1),1),25);
a{i} = polyval(p{i},f(k+1:length(Av1),1));
q{x}(k+1:length(Av1),1)=a{i}(:,1);
semilogx(f(:,1),q{x}(:,1),'Color',[0,1,0],'LineWidth',2);
            else
                if x==3

```

```

semilogx(f,Ah{3}, 'LineWidth', 2)
for i=1:Q
if i==1
p{i} = polyfit(f(1:500,1),Ah{3}(1:500,1),25);
a{i} = polyval(p{i},f(1:500,1));
q{x}(1:500,1)=a{i}(:,1);
else
j=i*500;
k=(i-1)*500;
p{i} = polyfit(f(k+1:j,1),Ah{3}(k+1:j,1),25);
a{i} = polyval(p{i},f(k+1:j,1));
q{x}(k+1:j,1)=a{i}(:,1);
end
end
k=(i-1)*500;
p{i} = polyfit(f(k+1:length(Av1),1),Ah{3}(k+1:length(Av1),1),25);
a{i} = polyval(p{i},f(k+1:length(Av1),1));
q{x}(k+1:length(Av1),1)=a{i}(:,1);
semilogx(f(:,1),q{x}(:,1), 'Color', [0,1,0], 'LineWidth', 2);
else
if x==4
semilogx(f,Ah{4}, 'LineWidth', 2)
for i=1:Q
if i==1
p{i} = polyfit(f(1:500,1),Ah{4}(1:500,1),25);
a{i} = polyval(p{i},f(1:500,1));
q{x}(1:500,1)=a{i}(:,1);
else
j=i*500;
k=(i-1)*500;
p{i} = polyfit(f(k+1:j,1),Ah{4}(k+1:j,1),25);
a{i} = polyval(p{i},f(k+1:j,1));
q{x}(k+1:j,1)=a{i}(:,1);
end
end
k=(i-1)*500;
p{i} = polyfit(f(k+1:length(Av1),1),Ah{4}(k+1:length(Av1),1),25);
a{i} = polyval(p{i},f(k+1:length(Av1),1));
q{x}(k+1:length(Av1),1)=a{i}(:,1);
semilogx(f(:,1),q{x}(:,1), 'Color', [0,1,0], 'LineWidth', 2);
else
if x==5
semilogx(f,Ah{5}, 'LineWidth', 2)
for i=1:Q
if i==1
p{i} = polyfit(f(1:500,1),Ah{5}(1:500,1),25);
a{i} = polyval(p{i},f(1:500,1));
q{x}(1:500,1)=a{i}(:,1);
else
j=i*500;
k=(i-1)*500;
p{i} = polyfit(f(k+1:j,1),Ah{5}(k+1:j,1),25);
a{i} = polyval(p{i},f(k+1:j,1));
q{x}(k+1:j,1)=a{i}(:,1);
end
end
k=(i-1)*500;

```

```

p{i} = polyfit(f(k+1:length(Av1),1),Ah{5}(k+1:length(Av1),1),25);
a{i} = polyval(p{i},f(k+1:length(Av1),1));
q{x}(k+1:length(Av1),1)=a{i}(:,1);
semilogx(f(:,1),q{x}(:,1),'Color',[0,1,0],'LineWidth',2);
else
    if x==6
semilogx(f,Ah{6},'LineWidth',2)
for i=1:Q
if i==1
p{i} = polyfit(f(1:500,1),Ah{6}(1:500,1),25);
a{i} = polyval(p{i},f(1:500,1));
q{x}(1:500,1)=a{i}(:,1);
else
j=i*500;
k=(i-1)*500;
p{i} = polyfit(f(k+1:j,1),Ah{6}(k+1:j,1),25);
a{i} = polyval(p{i},f(k+1:j,1));
q{x}(k+1:j,1)=a{i}(:,1);
end
end
k=(i-1)*500;
p{i} = polyfit(f(k+1:length(Av1),1),Ah{6}(k+1:length(Av1),1),25);
a{i} = polyval(p{i},f(k+1:length(Av1),1));
q{x}(k+1:length(Av1),1)=a{i}(:,1);
semilogx(f(:,1),q{x}(:,1),'Color',[0,1,0],'LineWidth',2);
else
    if x==7
semilogx(f,Ah{7},'LineWidth',2)
for i=1:Q
if i==1
p{i} = polyfit(f(1:500,1),Ah{7}(1:500,1),25);
a{i} = polyval(p{i},f(1:500,1));
q{x}(1:500,1)=a{i}(:,1);
else
j=i*500;
k=(i-1)*500;
p{i} = polyfit(f(k+1:j,1),Ah{7}(k+1:j,1),25);
a{i} = polyval(p{i},f(k+1:j,1));
q{x}(k+1:j,1)=a{i}(:,1);
end
end
k=(i-1)*500;
p{i} = polyfit(f(k+1:length(Av1),1),Ah{7}(k+1:length(Av1),1),25);
a{i} = polyval(p{i},f(k+1:length(Av1),1));
q{x}(k+1:length(Av1),1)=a{i}(:,1);
semilogx(f(:,1),q{x}(:,1),'Color',[0,1,0],'LineWidth',2);
else
    if x==8
semilogx(f,Ah{8},'LineWidth',2)
for i=1:Q
if i==1
p{i} = polyfit(f(1:500,1),Ah{8}(1:500,1),25);
a{i} = polyval(p{i},f(1:500,1));
q{x}(1:500,1)=a{i}(:,1);
else
j=i*500;
k=(i-1)*500;

```

```

p{i} = polyfit(f(k+1:j,1),Ah{8}(k+1:j,1),25);
a{i} = polyval(p{i},f(k+1:j,1));
q{x}(k+1:j,1)=a{i}(:,1);
end
end
k=(i-1)*500;
p{i} = polyfit(f(k+1:length(Av1),1),Ah{8}(k+1:length(Av1),1),25);
a{i} = polyval(p{i},f(k+1:length(Av1),1));
q{x}(k+1:length(Av1),1)=a{i}(:,1);
semilogx(f(:,1),q{x}(:,1),'Color',[0,1,0],'LineWidth',2);
    else
        if x==9
semilogx(f,Ah{9},'LineWidth',2)
for i=1:Q
if i==1
p{i} = polyfit(f(1:500,1),Ah{9}(1:500,1),25);
a{i} = polyval(p{i},f(1:500,1));
q{x}(1:500,1)=a{i}(:,1);
        else
j=i*500;
k=(i-1)*500;
p{i} = polyfit(f(k+1:j,1),Ah{9}(k+1:j,1),25);
a{i} = polyval(p{i},f(k+1:j,1));
q{x}(k+1:j,1)=a{i}(:,1);
end
end
k=(i-1)*500;
p{i} = polyfit(f(k+1:length(Av1),1),Ah{9}(k+1:length(Av1),1),25);
a{i} = polyval(p{i},f(k+1:length(Av1),1));
q{x}(k+1:length(Av1),1)=a{i}(:,1);
semilogx(f(:,1),q{x}(:,1),'Color',[0,1,0],'LineWidth',2);
    else
        if x==10
semilogx(f,Ah{10},'LineWidth',2)
for i=1:Q
if i==1
p{i} = polyfit(f(1:500,1),Ah{10}(1:500,1),25);
a{i} = polyval(p{i},f(1:500,1));
q{x}(1:500,1)=a{i}(:,1);
        else
j=i*500;
k=(i-1)*500;
p{i} = polyfit(f(k+1:j,1),Ah{10}(k+1:j,1),25);
a{i} = polyval(p{i},f(k+1:j,1));
q{x}(k+1:j,1)=a{i}(:,1);
end
end
k=(i-1)*500;
p{i} = polyfit(f(k+1:length(Av1),1),Ah{10}(k+1:length(Av1),1),25);
a{i} = polyval(p{i},f(k+1:length(Av1),1));
q{x}(k+1:length(Av1),1)=a{i}(:,1);
semilogx(f(:,1),q{x}(:,1),'Color',[0,1,0],'LineWidth',2);
    else
        if x==11
semilogx(f,Ah{11},'LineWidth',2)
for i=1:Q
if i==1

```

```

p{i} = polyfit(f(1:500,1),Ah{11}(1:500,1),25);
a{i} = polyval(p{i},f(1:500,1));
q{x}(1:500,1)=a{i}(:,1);
    else
j=i*500;
k=(i-1)*500;
p{i} = polyfit(f(k+1:j,1),Ah{11}(k+1:j,1),25);
a{i} = polyval(p{i},f(k+1:j,1));
q{x}(k+1:j,1)=a{i}(:,1);
end
end
k=(i-1)*500;
p{i} = polyfit(f(k+1:length(Av1),1),Ah{11}(k+1:length(Av1),1),25);
a{i} = polyval(p{i},f(k+1:length(Av1),1));
q{x}(k+1:length(Av1),1)=a{i}(:,1);
semilogx(f(:,1),q{x}(:,1),'Color',[0,1,0],'LineWidth',2);
    else
if x==12
semilogx(f,Ah{12},'LineWidth',2)
for i=1:Q
if i==1
p{i} = polyfit(f(1:500,1),Ah{12}(1:500,1),25);
a{i} = polyval(p{i},f(1:500,1));
q{x}(1:500,1)=a{i}(:,1);
        else
j=i*500;
k=(i-1)*500;
p{i} = polyfit(f(k+1:j,1),Ah{12}(k+1:j,1),25);
a{i} = polyval(p{i},f(k+1:j,1));
q{x}(k+1:j,1)=a{i}(:,1);
end
end
k=(i-1)*500;
p{i} = polyfit(f(k+1:length(Av1),1),Ah{12}(k+1:length(Av1),1),25);
a{i} = polyval(p{i},f(k+1:length(Av1),1));
q{x}(k+1:length(Av1),1)=a{i}(:,1);
semilogx(f(:,1),q{x}(:,1),'Color',[0,1,0],'LineWidth',2);
        else
            if x==13
semilogx(f,Ah{13},'LineWidth',2)
for i=1:Q
if i==1
p{i} = polyfit(f(1:500,1),Ah{13}(1:500,1),25);
a{i} = polyval(p{i},f(1:500,1));
q{x}(1:500,1)=a{i}(:,1);
                else
j=i*500;
k=(i-1)*500;
p{i} = polyfit(f(k+1:j,1),Ah{13}(k+1:j,1),25);
a{i} = polyval(p{i},f(k+1:j,1));
q{x}(k+1:j,1)=a{i}(:,1);
end
end
k=(i-1)*500;
p{i} = polyfit(f(k+1:length(Av1),1),Ah{13}(k+1:length(Av1),1),25);
a{i} = polyval(p{i},f(k+1:length(Av1),1));
q{x}(k+1:length(Av1),1)=a{i}(:,1);

```

```

semilogx(f(:,1),q{x}(:,1),'Color',[0,1,0],'LineWidth',2);
else
    if x==14
semilogx(f,Ah{14},'LineWidth',2)
for i=1:Q
if i==1
p{i} = polyfit(f(1:500,1),Ah{14}(1:500,1),25);
a{i} = polyval(p{i},f(1:500,1));
q{x}(1:500,1)=a{i}(:,1);
    else
j=i*500;
k=(i-1)*500;
p{i} = polyfit(f(k+1:j,1),Ah{14}(k+1:j,1),25);
a{i} = polyval(p{i},f(k+1:j,1));
q{x}(k+1:j,1)=a{i}(:,1);
end
end
k=(i-1)*500;
p{i} = polyfit(f(k+1:length(Av1),1),Ah{14}(k+1:length(Av1),1),25);
a{i} = polyval(p{i},f(k+1:length(Av1),1));
q{x}(k+1:length(Av1),1)=a{i}(:,1);
semilogx(f(:,1),q{x}(:,1),'Color',[0,1,0],'LineWidth',2);
else
    if x==15
semilogx(f,Ah{15},'LineWidth',2)
for i=1:Q
if i==1
p{i} = polyfit(f(1:500,1),Ah{15}(1:500,1),25);
a{i} = polyval(p{i},f(1:500,1));
q{x}(1:500,1)=a{i}(:,1);
    else
j=i*500;
k=(i-1)*500;
p{i} = polyfit(f(k+1:j,1),Ah{15}(k+1:j,1),25);
a{i} = polyval(p{i},f(k+1:j,1));
q{x}(k+1:j,1)=a{i}(:,1);
end
end
k=(i-1)*500;
p{i} = polyfit(f(k+1:length(Av1),1),Ah{15}(k+1:length(Av1),1),25);
a{i} = polyval(p{i},f(k+1:length(Av1),1));
q{x}(k+1:length(Av1),1)=a{i}(:,1);
semilogx(f(:,1),q{x}(:,1),'Color',[0,1,0],'LineWidth',2);
else
    if x==16
semilogx(f,Ah{16},'LineWidth',2)
for i=1:Q
if i==1
p{i} = polyfit(f(1:500,1),Ah{16}(1:500,1),25);
a{i} = polyval(p{i},f(1:500,1));
q{x}(1:500,1)=a{i}(:,1);
    else
j=i*500;
k=(i-1)*500;
p{i} = polyfit(f(k+1:j,1),Ah{16}(k+1:j,1),25);
a{i} = polyval(p{i},f(k+1:j,1));
q{x}(k+1:j,1)=a{i}(:,1);

```

```

end
end
k=(i-1)*500;
p{i} = polyfit(f(k+1:length(Av1),1),Ah{16}(k+1:length(Av1),1),25);
a{i} = polyval(p{i},f(k+1:length(Av1),1));
q{x}(k+1:length(Av1),1)=a{i}(:,1);
semilogx(f(:,1),q{x}(:,1),'Color',[0,1,0],'LineWidth',2);
else
    if x==17
semilogx(f,Ah{17},'LineWidth',2)
for i=1:Q
if i==1
p{i} = polyfit(f(1:500,1),Ah{17}(1:500,1),25);
a{i} = polyval(p{i},f(1:500,1));
q{x}(1:500,1)=a{i}(:,1);
    else
j=i*500;
k=(i-1)*500;
p{i} = polyfit(f(k+1:j,1),Ah{17}(k+1:j,1),25);
a{i} = polyval(p{i},f(k+1:j,1));
q{x}(k+1:j,1)=a{i}(:,1);
end
end
k=(i-1)*500;
p{i} = polyfit(f(k+1:length(Av1),1),Ah{17}(k+1:length(Av1),1),25);
a{i} = polyval(p{i},f(k+1:length(Av1),1));
q{x}(k+1:length(Av1),1)=a{i}(:,1);
semilogx(f(:,1),q{x}(:,1),'Color',[0,1,0],'LineWidth',2);
else
    if x==18
semilogx(f,Ah{18},'LineWidth',2)
for i=1:Q
if i==1
p{i} = polyfit(f(1:500,1),Ah{18}(1:500,1),25);
a{i} = polyval(p{i},f(1:500,1));
q{x}(1:500,1)=a{i}(:,1);
    else
j=i*500;
k=(i-1)*500;
p{i} = polyfit(f(k+1:j,1),Ah{18}(k+1:j,1),25);
a{i} = polyval(p{i},f(k+1:j,1));
q{x}(k+1:j,1)=a{i}(:,1);
end
end
k=(i-1)*500;
p{i} = polyfit(f(k+1:length(Av1),1),Ah{18}(k+1:length(Av1),1),25);
a{i} = polyval(p{i},f(k+1:length(Av1),1));
q{x}(k+1:length(Av1),1)=a{i}(:,1);
semilogx(f(:,1),q{x}(:,1),'Color',[0,1,0],'LineWidth',2);
    else
        if x==19
semilogx(f,Ah{19},'LineWidth',2)
for i=1:Q
if i==1
p{i} = polyfit(f(1:500,1),Ah{19}(1:500,1),25);
a{i} = polyval(p{i},f(1:500,1));
q{x}(1:500,1)=a{i}(:,1);

```



```

%
% % Output=zeros(2,length(f1));
% % p=1;
% % for i=1:2
% % for j=1:length(f1)
% %     str1=(sprintf('Ah%d',i));
% %     Output(p,j)=strcat(str1,str2);
% % end
% % p=p+1;
% % end
%
legend('Transducer-1','Transducer-2','Transducer-3','Transducer-
4','Transducer-5','Transducer-6','Transducer-7','Transducer-8','Transducer-
9','Transducer-10','Transducer-11','Transducer-12','Transducer-
13','Transducer-14','Transducer-15','Transducer-16','Transducer-
17','Transducer-18','Transducer-19','Transducer-20');
% % legend('Transducer-5','Transducer-6','Transducer-7','Transducer-
8','Transducer-9','Transducer-10','Transducer-11','Transducer-
12','Transducer-13','Transducer-14','Transducer-15','Transducer-
16','Transducer-17','Transducer-18','Transducer-19');
% % legend('Transducer-5','Transducer-6','Transducer-7','Transducer-
8','Transducer-9','Transducer-16','Transducer-17','Transducer-
18','Transducer-19');

csvwrite('name8.csv', Ah);
csvwrite('name9.csv', q);

```

Function

```

function [f1,Av]=fftprog_1(A, N1, B1, Step1, window1, FNyquist1, i)
t1 = A(:,i);
t1m = mean(t1);
t1 = t1-t1m;
[b,a] = butter(7,0.004,'high'); % Setting up an 8th order butterworth filter
t1 = filtfilt(b,a,t1); % filter the data

% Blocks = zeros(NumBlocks,Fs); %used to pad blocks and result in bins for
each hz
for i = 1:N1
    Blocks1(i,1:B1) = t1(((i-1)*Step1+i):((i-1)*Step1+i+B1-1));
for j = 1:B1
Blocks1(i,j) = Blocks1(i,j)*window1(j); %apply the hanning window
end
end

for i = 1:N1
FDoubleSided1(i,:) = fft(Blocks1(i,:));
end

% N = length(x);
% xdft = fft(x);

```

```

% xdft = xdft(1:N/2+1);
% psdx = (1/(Fs*N)) * abs(xdft).^2;
% psdx(2:end-1) = 2*psdx(2:end-1);
% freq = 0:Fs/length(x):Fs/2;

for i=1:N1
P2(i,:)=(1/((FNyquist1*2)*8192))*abs(FDoubleSided1(i,:)).^2;
P1(i,:) = 2*P2(i,1:B1/2+1);
end

% for i=1:N1
% P2(i,:)=abs(FDoubleSided1(i,+)/B1);
% P1(i,:)=2*P2(i,1:B1/2+1);
% end

tot=zeros(B1/2+1);

for i=1:N1
    for j=1:B1/2+1
        tot(j)=tot(j)+P1(i,j);
    end
end

for j=1:B1/2+1
Av(j)=tot(j)/N1;
end

f1=FNyquist1*2*(0:(B1/2))/B1;

end

```

APPENDIX-V

Wind Tunnel Operation

Following is the wind tunnel operating procedure:

- In order to operate the compressors to fill the tank bring the switch to the position shown below to turn on the compressors. Switch can be found in the room behind the storage tank (Fig.A.5.1).



Figure A.5.1. Switch to turn on the compressor

- Press the Start button the control panel of the compressors.



Figure A.5.2. Compressor panel

- Turn on the dehumidifier to the Dryer on position.



Figure A.5.3. Dryer dehumidifier panel

- It is advised to charge the tank to atleast 140 psi for optimum usage of the supersonic wind tunnel for the existing assembly (Mach 3 nozzle, wedge on the bottom of test section for SWBLI).



Figure A.5.4. Storage tank panel



Figure A.5.5. (From left to right) butterfly valve pneumatic line, filters, and pressure gage

- Open the valve, which is located at the corner of the supersonic tunnel lab to supply air to the butterfly control valve. Clear the filters at regular intervals to avoid moisture or water entering the butterfly valve. Pressure gage should read 45 psi which is required to control the valve.
- Pressure regulator (Fig. A.5.6) should be maintained at 65 psig for current assembly.



Figure A.5.6. Pressure regulator



Figure A.5.7. Storage tank valve

- Open the valve on the 1000 ft³ storage tank to let the air supply into the supersonic wind tunnel.

- Use the button on the rectangular box to control the butterfly valve present on top of the meshed pipe.



Figure A.5.8. (From left to right) control console and butterfly valve

- Once the tunnel usage is completed, turn off the air supply from the storage tank by turning of the valve as explained earlier. Turn off the air supply to the butterfly valve which is located at the corner of the room.
- If moisture or water enters the butterfly valve, it would not operate normally, so carefully dry it before operating.
- If water enters the pressure regulator, the tunnel would not operate normally, in that situation, remove the top portion of the pressure regulator and dry it carefully. Once it is dried replace the lid with the nuts and bolts without altering the diaphragm's (present inside the regulator) location.

APPENDIX - VI

Operation of KSC-2 Signal Conditioner and Picoscope

The pressure transducer is operated through a combination of settings on the KSC-2 signal conditioner and Picoscope. A maximum of two transducers can be connected to the signal conditioner. Both the instruments have the corresponding software to operate them. The

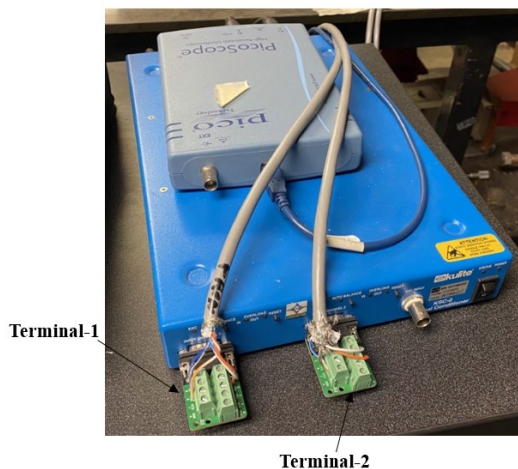


Figure. A.6.1 Picoscope and KSC-2 Signal conditioner

instruments in the have been set up in the lab as shown below. Transducers can be connected either to Terminal 1 or Terminal 2.

A few operations on the signal conditioner can be performed either using the instrument or the software

- Switch on the signal conditioner and start the software
- The *Exc* and *Overload (In and Out)* will adjust based on the integrity of the transducer, i.e., if the transducer is damaged, the overload button will light up red.

- Press the *Autobalance* button on the instrument or *Balance* button in the software. This zeroes the voltage on the transducer by balancing the Wheatstone bridge in the instrument



Dev.Chan	Serial Number	Channel Name	Excitation Fault	Excitation Value (V)	Excitation Type	Sense	Balance Voltage (mV)	utobalanc	Coupling	Shield	Input Mode	Overload Mode	Input Overload	Pregain	Filter Type	Filter Cutoff (Hz)	Resonance compensatio	Postgain	Output Overload (V)	Overloads	Settings
1:1	191148-022	8077-3-240		10.000	Bipolar	Local	-14.5312	Balance	DC	Ground	Operate	Continuous		32	None	50000	Enabled	3.0940	9.5	Clear	Save
1:2	191148-022	8077-3-240		10.000	Bipolar	Local	0.5273	Balance	DC	Ground	Operate	Continuous		32	None	50000	Enabled	1.6300	9.5	Clear	Save

Figure. A.6.2 KSC-2 signal conditioner (top); KSC-2 software control panel (below)

- Input the pre-filter and post filter gain the software panel utilizing the values advised by Kulite (Fig. A.6.2) and set the cut-off frequency as required.
- Leave the *Coupling*, *Shield*, *Input Mode*, *Overload Mode* at the default settings
- The Picoscope has no separate power button and switches on through the USB connection to the computer
- The Picoscope software panel is as shown in Fig. A.6.3. While the software has several settings that can be controlled individually, this discussion is restricted only to the procedure adopted to acquire the pressure from the transducer for the experiments under consideration. In the panel, the X-axis represents time and Y-axis is the voltage from the. *Button-1* and *Button-3* can be adjusted to scale the Y- and X-axis. *Button-2* is adjusted to acquire AC/DC signal. For the experiments, it was left at DC setting. *Button-4* is used to

adjust the number of acquired samples. *Button-5* is pressed to start and stop the signal acquisition. Hence, for example, by setting *Button-3* to 1 s/div (results in X-axis being divided into 10 s) and *Button-4* to 100 samples, the acquisition frequency is 10 Hz.

- The output of the transducers is in voltage which is calculated as

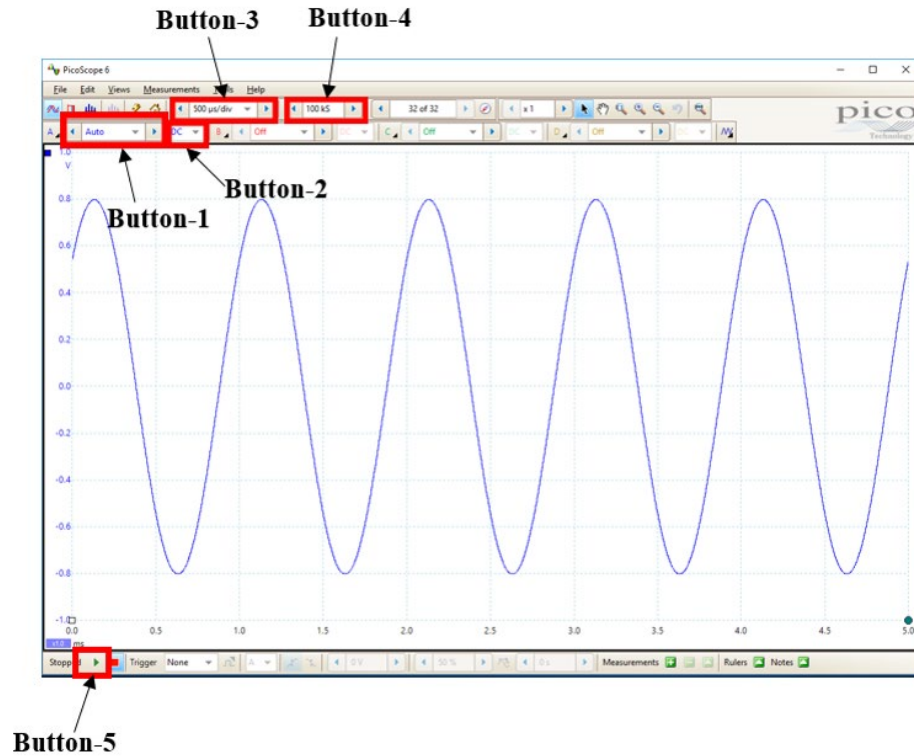


Figure. A.6.3 Picoscope software panel

Voltage = Pressure * Sensitivity * Pre-filter gain * Post filter gain

For example if the sensed pressure is 4 psia by a transducer with a sensitivity of 0.025136 V/psi then with a pre and post filter gains of 32 and 2.486 respectively,

Voltage = (4 psia)*(0.025136 V/psi)*(pre-filter gain)*(post filter gain)

Voltage = 4*0.025136*32*2.486

Voltage = 8 V

With no scaling, this should be the voltage reading visible on Picoscope software. Hence, by reading the voltage, the pressure can be calculated by re-arranging the terms in the above equation